

REF ID: A214 643

TRW

(2)

AD-A214 643

NONLINEAR OPTICS TECHNOLOGY PHASE II FINAL REPORT

AREA I: FOUR WAVE MIXING TECHNOLOGY

AREA II: PHASE CONJUGATED SOLID STATE
LASER TECHNOLOGY

J. BROCK, M. CAPONI, L. FRANTZ, G. HARPOLE, C. HOEFER,
H. INJEYAN, F. PATTERSON, D. SHEMWEILL, J. TYMINSKI

DISTRIBUTION STATEMENT A

Approved for public release;
Distribution Unlimited

SPONSORED BY:
DEFENSE ADVANCED RESEARCH PROJECTS AGENCY

MONITORED BY:
OFFICE OF NAVAL RESEARCH
CONTRACT #N00014-85-C-0257

DTIC
ELECTE
NOV 20 1989
S D & D

The views and conclusions contained in this document are those of the authors and should not be interpreted as necessarily representing the official policies, either expressed or implied, of the Defense Advanced Research Projects Agency or the U. S. Government.

TRW SPACE AND TECHNOLOGY GROUP
APPLIED TECHNOLOGY DIVISION
ONE SPACE PARK
REDONDO BEACH, CA 90278

89 11 20 008



NONLINEAR OPTICS TECHNOLOGY PHASE II FINAL REPORT

**AREA I: FOUR WAVE MIXING TECHNOLOGY
AREA II: PHASE CONJUGATED SOLID STATE
LASER TECHNOLOGY**

**J. BROCK, M. CAPONI, L. FRANTZ, G. HARPOLE, C. HOEFER,
H. INJEYAN, F. PATTERSON, D. SHEMWELL, J. TYMINSKI**

**SPONSORED BY:
DEFENSE ADVANCED RESEARCH PROJECTS AGENCY**

**MONITORED BY:
OFFICE OF NAVAL RESEARCH
CONTRACT #N00014-85-C-0257**

The views and conclusions contained in this document are those of the authors and should not be interpreted as necessarily representing the official policies, either expressed or implied, of the Defense Advanced Research Projects Agency or the U. S. Government.

**TRW SPACE AND TECHNOLOGY GROUP
APPLIED TECHNOLOGY DIVISION
ONE SPACE PARK
REDONDO BEACH, CA 90278**

REPORT DOCUMENTATION PAGE

1a REPORT SECURITY CLASSIFICATION Unclassified			1b. RESTRICTIVE MARKINGS		
2a SECURITY CLASSIFICATION AUTHORITY			3 DISTRIBUTION / AVAILABILITY OF REPORT Unclassified/unlimited		
2b DECLASSIFICATION / DOWNGRADING SCHEDULE					
4 PERFORMING ORGANIZATION REPORT NUMBER(S)			5 MONITORING ORGANIZATION REPORT NUMBER(S)		
6a. NAME OF PERFORMING ORGANIZATION TRW Space & Technology		6b. OFFICE SYMBOL (if applicable)	7a NAME OF MONITORING ORGANIZATION Office of Naval Research		
6c ADDRESS (City, State, and ZIP Code) One Space Park Redondo Beach, CA 90278			7b ADDRESS (City, State, and ZIP Code) 759 East Walnut St. Pasadena, CA 91101		
8a NAME OF FUNDING / SPONSORING ORGANIZATION DARPA		8b OFFICE SYMBOL (if applicable) DEO	9 PROCUREMENT INSTRUMENT IDENTIFICATION NUMBER N00014-85-C-0257		
9c ADDRESS (City, State, and ZIP Code) 1400 Wilson Blvd. Arlington, VA 22209-2308			10 SOURCE OF FUNDING NUMBERS		
			PROGRAM ELEMENT NO.	PROJECT NO.	TASK NO.
					WORK UNIT ACCESSION NO.
11 TITLE (Include Security Classification) Nonlinear Optics Technology Phase II Final Report					
12 PERSONAL AUTHOR(S) J. Brock, M. Caponi, L. Frantz, G. Harpole, C. Hoefer, H. Injeyan, F. Patterson (TRW); D. Shemwell, J. Tyminski (Spectra Technology, Inc.)					
13a TYPE OF REPORT Phase II Final		13b TIME COVERED FROM 86 Sept TO 88 Jan		14 DATE OF REPORT (Year, Month, Day) 88 Jan 15	
15 PAGE COUNT					
16 SUPPLEMENTARY NOTATION					
17 COSATI CODES			18 SUBJECT TERMS (Continue on reverse if necessary and identify by block number)		
FIELD	GROUP	SUB-GROUP	four-wave Mixing, cesium, semiconductors, multiquantum wells, diode lasers, phase conjugation, detectivity, conjugated harmonic doubling, stimulated Brillouin scattering, ring oscillator, conjugated amplifier, slab laser, astigmatism, rapid turn-on		
19 ABSTRACT (Continue on reverse if necessary and identify by block number) Four wave mixing (FWM) phase conjugation was investigated in materials that can operate at diode laser wavelengths. Investigated were atomic cesium vapor, bulk GaAs, multiquantum well (MQW) GaAs/AlGaAs, and intracavity FWM in diode laser waveguides operating above threshold. Conjugate reflectivities up to 154% were observed in cesium for cw pumping at ~100W/cm ² , with signal observed over a 30 GHz bandwidth around the 852 nm hyperfine transitions. Self focusing and angular response were also investigated. Backward FWM phase conjugation at room temperature was demonstrated in bulk GaAs and MQW GaAs/AlGaAs for the first time. Reflectivities of ~0.1% were observed in both materials for 4 kW/cm ² pumping. Results show that the stronger excitonic effects in MQW samples do not help FWM performance when high reflectivity (>10%) is desired because the pump fields required strongly saturate the excitonic component. Conjugate reflectivities > 2x10 ⁶ % were observed for FWM inside the waveguide cavity of (Continued on reverse side)					
20 DISTRIBUTION / AVAILABILITY OF ABSTRACT <input checked="" type="checkbox"/> UNCLASSIFIED/UNLIMITED <input type="checkbox"/> SAME AS RPT <input type="checkbox"/> DTIC USERS			21 ABSTRACT SECURITY CLASSIFICATION Unclassified		
22a NAME OF RESPONSIBLE INDIVIDUAL V. Smiley			22b TELEPHONE (Include Area Code) (818) 795-5971		22c OFFICE SYMBOL ONR/Pasadena

Block 19. Abstract (Continuation)

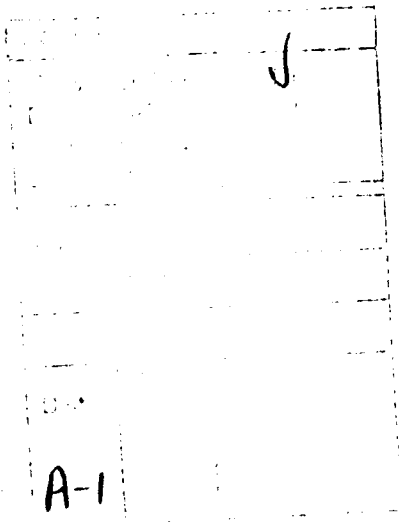
diode lasers operating above threshold. The first demonstration of a conjugation capability in diode laser FWM, piston conjugation to correct optical path differences, was also accomplished.

Detectivity of FWM was investigated to determine minimum input conditions. For strong, classical pumps, the FWM process is noisy due to fluctuations of the input probe field, fluctuations at the empty port corresponding to the conjugate field input, and fluctuations due to the medium response associated with absorption and emission. Analysis shows that good conjugate fidelity is achieved when the number of input quanta is larger than $(1+(\alpha/\kappa)^2)$ where α is the medium absorption coefficient and κ is the nonlinear coupling coefficient.

A ring oscillator, conjugated power amplifier was constructed and tested. Using a Nd:YAG slab, this configuration produced 30 mJ output with near diffraction limited beam quality independent of pulse repetition over a range from 1-50 Hz.

Phase conjugated doubling to produce high beam quality of the second harmonic when there are aberrations in the doubling medium was demonstrated and analyzed theoretically. The capability of SBS to correct astigmatic aberrations characteristic of high power solid state laser components was investigated experimentally and modeled successfully with the BRIWON code.

Rapid turn-on of a solid state laser was modeled to estimate thermal gradients and resulting optical distortion 2 s after start from a standby mode. All components except the doubler come to steady state. Thermally induced phase mismatching of the doubler was identified as a rapid turn-on issue. Also presented is a design approach for a conjugated 10 J solid state laser to illustrate methodology for component sizing.





NONLINEAR OPTICS TECHNOLOGY PHASE II FINAL REPORT

**AREA I: FOUR WAVE MIXING TECHNOLOGY
AREA II: PHASE CONJUGATED SOLID STATE
LASER TECHNOLOGY**

**J. BROCK, M. CAPONI, L. FRANTZ, G. HARPOLE, C. HOEFER,
H. INJEYAN, F. PATTERSON, D. SHEMWELL, J. TYMINSKI**

**SPONSORED BY:
DEFENSE ADVANCED RESEARCH PROJECTS AGENCY**

**MONITORED BY:
OFFICE OF NAVAL RESEARCH
CONTRACT #N00014-85-C-0257**

The views and conclusions contained in this document are those of the authors and should not be interpreted as necessarily representing the official policies, either expressed or implied, of the Defense Advanced Research Projects Agency or the U. S. Government.

**TRW SPACE AND TECHNOLOGY GROUP
APPLIED TECHNOLOGY DIVISION
ONE SPACE PARK
REDONDO BEACH, CA 90278**

PREFACE

This final report describes efforts performed during the second phase of the Nonlinear Optics Technology Program. This program was funded by the Defense Advanced Research Projects Agency and monitored by the Office of Naval Research under contract No. N00014-85-C-0257.

Most of the work was performed by TRW Space and Technology Group, Applied Technology Division, Redondo Beach, CA. The effort described in Section 5 was performed under subcontract by Spectra Technology, Inc., Bellevue WA. The program was managed by J. Brock. M. Caponi managed the Area I nonlinear optics work and H. Injeyan managed the solid state laser efforts. Other personnel making important contributions to the technical effort were L. Frantz, G. Harpole, C. Hoefer, A. Horwitz, F. Patterson, and R. St. Pierre. The laboratory assistance of W. Carrion, K. Davis, A. Edmon, K. Kell, and B. Zukowski was vital to the successful completion of experimental work. R. Chan and M. Nguyen-Vo provided superb modeling support. The technical and managerial guidance of L. Marabella is also gratefully acknowledged, along with the capable secretarial support provided by J. C. Miller and P. Bessenbacher. Project administration was handled smoothly by P. Weber, project control, M. Piehler and P. Brockmeier, contracts, and J. Hyland and J. Brady, subcontracts. The Spectra Technology subcontract was managed by D. Shemwell, with technical contributions from J. Tyminski, L. DeShazer, and J. Eggleston.

The work on this contract was administered by S. Shey of the DARPA Directed Energy Office, and monitored by R. Behringer and V. Smiley of the Office of Naval Research. Their support and assistance contributed greatly to the success of this program.

TABLE OF CONTENTS

	Page
List of Figures	vii
Area I: FWM Technology	
1.0 Introduction	1
1.1 NLOT Program Structure	1
1.2 Phase II Program Overview	2
1.2.1 Area I: FWM Technology	2
1.2.2 Area II: Phase Conjugated Solid State Laser Technology ..	5
1.3 References	6
2.0 Four Wave Mixing in Cesium Vapor	7
2.1 Introduction	7
2.2 Cesium Spectroscopy	8
2.3 Experimental Configuration	15
2.4 DFWM Spectroscopy of Cesium Vapor	18
2.4.1 Frequency Dependence of DFWM in Cesium Vapor	18
2.4.2 Temperature Dependence of FWM Signal	22
2.4.3 Optical Intensity Dependence of FWM Signal	22
2.5 Self-focusing Effects in Cesium FWM ...	24
2.5.1 Effects of Self-focusing on Optical Beam Profiles	26
2.6 Cesium Vapor FWM Field of View	31
2.7 Conclusions	35
2.8 References	35
3.0 Degenerate Four Wave Mixing in Semiconductors	36
3.1 General Description	36
3.2 Intracavity NDFWM in Single Mode Diode Lasers:	
Reflectivity Results	37
3.2.1 Experimental Setup	38
3.2.2 Intracavity FWM Results	43
3.3 Intracavity FWM in Single Mode Diode Lasers:	
Piston Error Correction	50
3.3.1 Piston Correction Experimental Setup	50
3.3.2 Piston Error Correction Results	54
3.4 CW DFWM in Bulk GaAs and MQW GaAs	59
3.4.1 Spectroscopy of GaAs and AlGaAs MQW Materials	59
3.4.2 Experimental Setup	74
3.4.3 Experimental Results	76
3.5 Modeling	87
3.6 References	95
4.0 Four Wave Mixing Detectivity	97
4.1 Introduction	97
4.2 Formalism	98
4.3 Lossless Four Wave Mixing Phase Conjugator Quantum Noise ...	104
4.3.1 Action of a Degenerate FWM PC	104
4.3.2 Action of a Non-degenerate FWM PC	106
4.4 Quantum Noise in a Lossy Medium	111
4.5 Mode Combination as a Noise Source Detector	117
4.6 References	120

	Page
Area II: Phase Conjugated Solid State Laser Technology	121
5.0 Ring Oscillator Power Amplifier	
Final Report of Spectra Technology, Inc.....	121a
5.1 Introduction	121a
5.2 Experimental Configuration	124
5.2.1 Ring Oscillator Power Amplifier	124
5.2.2 The Oscillator Wave Front	127
5.2.3 SBS Cell Characteristics	127
5.2.4 Diagnostics	127
5.3 System Performance	132
5.3.1 Oscillator Performance	132
5.3.2 Amplifier Performance	146
5.3.3 ROPA Performance	155
5.4 Discussion	163
5.5 Conclusions	165
5.6 References	167
6.0 Phase Conjugated Doubling	169
6.1 Introduction	169
6.2 Stimulated Brillouin Scattering Experiment	169
6.2.1 Stimulated Brillouin Scattering Experimental Arrangement	169
6.2.2 Stimulated Brillouin Scattering Experimental Results ...	172
6.3 Phase CONjugated Doubling Experiment	176
6.3.1 Phase Conjugated Doubling Experiment Setup	179
6.3.2 Phase Conjugated Doubling Experimental Results	183
6.4 Stimulated Brillouin Scattering Modeling of Astigmatic Beams	185
6.4.1 Model Description	185
6.4.2 Modeling Results	189
6.5 Conclusions	195
7.0 50 W Wavelength Agile Nd:YAG Laser Rapid Turn-on Analysis	197
7.1 Thermal Gradient Analysis	198
7.2 Thermal Profiles in the Laser Slab	200
7.3 Thermal Effects in the Doubling Crystal	200
7.4 Thermal Gradients in the Raman Cell	203
7.5 Conclusions	205
7.6 References	206
8.0 10 Joule Nd:glass MOPA Design	207
References	218
Appendices:	
Appendix A: Abstracts and Summaries of other NLOT Final Report	
Volumes	220
Phase I, Area I	221
Phase I, Area II	229
Appendix B: Theory of Phase Conjugation in Frequency Doubling ..	234
Appendix C: Derivation of the Frantz-Nodvik Equation for a	
Zig-zag Slab Amplifier	247

LIST OF FIGURES

Figure	Title	Page
2-1	Energy level diagram and hyperfine transition frequency spectrum of the cesium D_2 line at 852.112 nm.	9
2-2	Relative line intensities, Einstein coefficients, and transition dipole moments for the hyperfine components of the cesium first resonance lines	11
2-3	Comparison of the Doppler-broadened (T=400K) spectra of the sodium and cesium D_2 line	12
2-4	Spectral overlap of the three transitions originating from each of the two ground state hyperfine levels	14
2-5	Basic experimental setup for DFWM experiments in cesium	16
2-6	Typical frequency spectrum of DFWM reflectivity in cesium vapor under high reflectivity conditions	19
2-7	Overlap of the DFWM reflectivity spectrum and the Doppler-broadened absorption spectrum	21
2-8	Change in DFWM frequency spectrum as temperature and cesium density are increased	23
2-9	Impact of increasing probe/pump ratio on observed conjugate reflectivity	25
2-10	Effect of increasing pump intensity on DFWM reflectivity in cesium vapor	25
2-11	Experimental configuration for determining impact of self-focusing on conjugate beam profiles	27
2-12	Observed self-focusing effects during DFWM experiments in cesium vapor	29
2-13	Observed probe beam profile as a function of conjugate reflectivity	30
2-14	Experimental setup for determining the angular dependence of DFWM in cesium vapor	33
2-15	Observed angular dependence of DFWM reflectivity	34
3-1	Experimental setup for the demonstration of intracavity NDFWM in single mode diode lasers	39
3-2	Transverse profiles of the focused beam at the LD2 facet	40

Figure	Title	Page
3-3	Photograph of an oscilloscope trace displaying the output of the 8 GHz free spectral range etalon	42
3-4	Conjugate reflectivity (R) and probe amplification (A) as a function of the probe-pump detuning, δ , for an incident probe power of 0.51 mW	44
3-5	Same as in Figure 3-4, except for an incident probe power of 1.4 mW	44
3-6	Plot of the square of the frequency detuning at which the maximum signal occurs, Δ^2 , versus the lasing output of the FWM diode	46
3-7	The strong intracavity laser field splits the two-level diode lasing transition into a series of four resonances through the ac Stark effect	47
3-8	Plot of the maximum reflectivity and probe amplification obtained at the minimum detuning	49
3-9	Plot of conjugate reflectivity and probe amplification as a function of input probe power for three different detunings: $\delta = -4, -5, -6$ GHz	51
3-10	Experimental setup for demonstrating phase conjugation of piston error using diode laser intracavity NDFWM	52
3-11	Interference patterns of the outputs of FWM1 and FWM2	55
3-12	Photograph of an oscilloscope trace displaying the output of the 8 GHz free spectral range etalon	56
3-13	Interference patterns generated between the outputs of FWM1 and FWM2	58
3-14	Plots of the energy dispersion characteristics of the density of states and the absorption coefficient using a free electron model of a semiconductor.....	61
3-15	Same as Figure 3-14, but the effects of the electron-hole Coulomb interaction have been included	63
3-16	Schematic and experimental absorption spectra near the band edge of room temperature bulk GaAs	65
3-17	Diagrams relevant to GaAs/AlGaAs multiple quantum well sample	66
3-18	Plots of the energy dispersion characteristic in the density of states and the absorption coefficient using a free electron model and particle-in-a-box model for MQWs	68

Figure	Title	Page
3-19	Schematic and experimental absorption spectra near the band edge of room temperature GaAs/AlGaAs MQWs	70
3-20	Energy dispersion characteristic and potential structure for the MQW when the effects of light and heavy holes are accounted for	72
3-21	Schematic and experimental absorption spectra near the band edge of room temperature GaAs/AlGaAs MQWs including the effects of light and heavy holes	73
3-22	Experimental setup for the CW backward DFWM experiments in room temperature bulk GaAs and GaAs/AlGaAs MQWs	75
3-23	Linear absorption spectrum and FWM spectrum at three pump powers for the MQW sample discussed in the text	77
3-24	Log-log plot of the MQW FWM signal versus pump intensity	78
3-25	Table of slopes of the Log(R)-Log(I) plots for various wavelengths near the MQW band edge	78
3-26	The slopes of Figure 3-25 are labeled onto the MQW linear spectrum	79
3-27	Part A: ΔA and Δn are calculated for the MQW sample using a model of a frequency-independent saturation intensity. Part B: the square of Δn is plotted on the same graph as the FWM spectrum	82
3-28	For the purpose of comparison, data from Reference 3.23 is shown here	84
3-29	Room temperature linear absorption spectrum for a bulk GaAs sample	86
3-30	Intensity dependence of the bulk GaAs FWM signal at 865 nm ..	86
3-31	FWM reflectivity as a function of the ratio of the pump intensity to the saturation intensity, I_{sat}	88
3-32	FWM reflectivity as a function of pump intensity and frequency detuning, δ , calculated using a simple free electron model for the saturable nonlinearity	91
3-33	Analytical fitting of the observed spectrum for incorporating in the FWM model	93
3-34	FWM reflectivity as a function of wavelength for various values of I/I_{sat} using the GaAs FWM model	94
4-1	Schematic diagram of four-wave mixing	100

Figure	Title	Page
4-2	Relative variance in the output conjugate quadrature and reflectivity versus the nonlinear coupling coefficient, κL ...	107
4-3	Schematic diagram of nondegenerate four wave mixing	107
4-4	Relative variance of one output conjugate quadrature versus detuning parameter $\phi = \Delta kL/2\pi$ for various values of nonlinear coupling coefficient κL	109
4-5	Relative variance of one of the output conjugate quadratures versus detuning parameter ϕ for $\kappa L = \pi/2$ and various values of input noise	110
4-6	Variance of one output conjugate quadrature as a function of the nonlinear coupling κL for $\phi = 0$ (DFWM) and $\phi = 0.3$	110
4-7	Relative variance of the output conjugate quadrature as a function of the real absorption coefficient, αL	115
4-8	Relative variance of the output conjugate and FWM reflectivity as a function of the nonlinear coupling coefficient, κL for two values of real absorption	115
4-9	Comparison of contribution to the output conjugate quadrature variance from amplified input noise and atomic fluctuations	116
4-10	Relative contributions to the output conjugate quadrature variance from the amplified empty port noise, the amplified input probe, and the atomic fluctuations for a system where the empty port is not a vacuum state	116
4-11	Mode combination scheme for characterizing noise sources in FWM media	118
5-1	Schematic of a ROPA identifying all major components	122
5-2	The ROPA configuration	125
5-3	The reflectivity of the SBS cell filled with methane under 1400 PSI pressure	128
5-4	The point diffraction interferometer used to diagnose the wave fronts	130
5-5	The extraction of the energy from the ring cavity defined by the 6 mm aperture	133
5-6	The extraction of the energy from the ring cavity defined by the 6 mm aperture and the spatial filter	134
5-7	The oscilloscope trace from a fast photodiode looking at the oscillator output	136

Figure	Title	Page
5-8	The extraction of the energy from the oscillator versus the repetition rate	138
5-9	The wavefront interferograms at the output aperture of the intracavity spatial filter	140
5-10	The wavefront interferograms at the output aperture of the oscillator	142
5-11	The wavefront interferograms at the output aperture of the oscillator	143
5-12	The relative transmission of the oscillator output through the subdiffraction limited pinhole versus the system repetition rate	144
5-13	The oscillator output versus the cavity detuning angle	145
5-14	The extraction of the energy from the amplifier	148
5-15	The extraction of the energy from the amplifier versus the system repetition rate	150
5-16	The wavefront interferograms at the output aperture of the amplifier	152
5-17	The relative transmission of the amplifier output through the subdiffraction limited pinhole versus the system repetition rate	153
5-18	The amplifier output versus the cavity detuning angle	154
5-19	The extraction of the energy from the ROPA system	156
5-20	ROPA output energy as a function of system repetition rate ..	157
5-21	The wavefront interferograms at the output aperture of the ROPA	159
5-22	The wavefront interferograms at the output aperture of the amplifier	160
5-23	The relative transmission of the ROPA output through the subdiffraction limited pinhole versus the system repetition rate	161
5-24	The ROPA output versus the cavity detuning angle	162
5-25	Diffraction loss as a function of spherical aberration for two generic ring cavities	166
6-1	Experimental schematic for SBS reflectivity and fidelity in methane	170

Figure	Title	Page
6-2	SBS reflectivity as a function of input energy for various cylindrical aberrators	173
6-3	Table of SBS threshold and aberrator power for cylindrical and He aberrators	173
6-4	Input and SBS return fringes for various cylindrical lens aberrators	174
6-5	Input and output beam quality as a function of input energy for various cylindrical aberrators	175
6-6	Reflectivity as a function of input energy for two helium jet aberrations	175
6-7	Input fringes and SBS return fringes for the He-jet aberrator.....	177
6-8	Input and return beam quality as a function of energy for He-jet aberrators	178
6-9	Schematic for harmonic doubling experiments	180
6-10	Type I doubling efficiency for CD [*] A	180
6-11	SBS reflectivity as a function of input energy with and without CD [*] A doubler	181
6-12	Correction of doubler aberration	182
6-13	SBS reflectivity, doubler with corrector in place, as a function of input energy for various cylindrical aberrators	184
6-14	Table of thresholds for various cylindrical aberrators obtained during the phase conjugated doubling experiment	184
6-15	Input and doubled return fringes for various cylindrical lens aberrators	186
6-16	Input and output beam quality as a function of input energy for two cylindrical aberrators	187
6-17	Input and return beam quality for various cylindrical and spherical lenses	188
6-18	Focusing geometry and pump beam intensity profile	190
6-19	Model outputs for intensity, phase and farfield intensity ..	192
6-20	Reflectance and relative increase of SBS threshold as a function of astigmatism	193
6-21	Stokes beam quality as a function of astigmatism	194

Figure	Title	Page
6-22	Stokes beam quality as a function of input power	194
6-23	Comparison of theoretical and experimental results: reflectance as a function of cylindrical aberrator power	196
6-24	Comparison of theoretical and experimental results: relative threshold as a function of cylindrical aberrator power	196
7-1	Predicted thermal performance of various components of 50 W solid state laser	199
7-2	Temperatures in the slab $-b < x < b$ with constant heat production at the rate A per unit volume and zero surface temperature	201
7-3	Thermal properties of component materials	201
7-4	Center-to-edge thermal profile in steady state for an edge-cooled slab with two different thicknesses of RTV insulation	202
7-5	Refractive indices of the two candidate doubling materials at the fundamental and second harmonic wavelengths	204
7-6	Conversion efficiency as a function of interaction length in the two candidate doubling materials	204
8-1	Schematic layout of 10 J Nd:glass MOPA analysis	208
8-2	Input and propagation geometry of the optical beam through a zig-zag slab medium	208
8-3	Ray propagation in the slab and the equivalent geometry used for the derivation of a modified Frantz-Nodvik equation	210
8-4	Geometry of the pumping region showing the vertical face area, A , and the pumping length, L	210
8-5	Table of parameters used for the 10 J MOPA design	211
8-6	Extracted energy and extraction efficiency in the Nd:YLF pre-amplifier as a function of the slab cross-sectional area ...	213
8-7	Folding geometries of the two Nd:glass slab amplifiers	217
8-8	Summary of 10 J MOPA design parameters	219
B-1	Uneven surface of crystal segment	236
C-1	Geometry of derivation of modified Frantz-Nodvik equation for beam propagation in a zig-zag slab medium	248

1.0 Introduction

This final report describes results obtained during the second phase of the Nonlinear Optics Technology (NLOT) program, a two phase, two year effort to investigate optical phase conjugation for enhancing performance of electro-optical systems.

1.1 NLOT Program Structure

The overall objective of the NLOT program has been to characterize and develop nonlinear optical techniques and materials that will improve the performance of electrooptical systems. A basic approach to this is to focus on improving the performance of laser transmitters already under active development. This can entail the use of a nonlinear material as an integral part of the laser transmitter itself to produce an output with high beam quality and improved brightness. It can also involve developing a phase conjugating material that operates efficiently and with high conjugate reflectivity at the lasing wavelength of particularly promising laser transmitters. Such conjugators can be used to coherently couple multiple laser apertures, or can be used to correct propagation path aberrations so that transmitter output energy is more efficiently utilized. Thus, this conjugation technology can apply not only to the lasers themselves, but also to a wide range of laser-based phase conjugated electrooptical systems.

The first year (Phase I) of the NLOT program examined two different areas. Area I examined four wave mixing characteristics of sodium vapor under conditions of high phase conjugate reflectivity. Area II involved the design of nonlinear optical experiments for phase conjugating and coherently beam combining large CW chemical lasers, effort that has since developed into a major effort, the APACHE program. Results of the first year (Phase I) of the program are contained in two separate volumes, Nonlinear Optics Technology Area I: FWM Technology, Phase I Final Report (Reference 1-1), and Nonlinear Optics Technology, Phase I, Area 2 (Reference 1-2). Because these volumes are separate and complete unto themselves, their contents have not been presented again but constitute by reference a part of the NLOT program final report. Abstracts of both of these volumes are presented as Appendix A.

Phase II of the NLOT program also consisted of two areas. Area I again examined four wave mixing (FWM) physics with the objective of understanding and developing four wave mixing phase conjugators that could be used in conjunction with diode lasers. Studied were cesium vapor near its 852 nm first resonance line, bulk GaAs, multiple quantum well GaAs/AlGaAs, and four wave mixing intracavity to diode lasers themselves. Also examined was FWM detectivity, i.e., the noise performance of a FWM conjugator for low light level inputs.

The second area of the NLOT Phase II program investigated phase conjugated solid state laser technology. One effort, performed under subcontract by Spectra Technology, Incorporated, was the demonstration of a novel phase conjugated master oscillator with excellent beam quality and high output pulse energy. Another effort investigated phase conjugated second harmonic generation, demonstrating that optical aberrations in nonlinear harmonic generator materials can be corrected as part of the conversion process itself. As part of this effort, work to characterize the types and magnitude of aberrations that can be reliably corrected using stimulated Brillouin scattering (SBS) was also performed. An analysis of solid state laser rapid turn-on issues and the conceptual design of a 10 J solid state laser were also a part of the Area II effort.

1.2 Phase II Program Overview

1.2.1 Area I: FWM Technology

Area I concentrated on identifying and characterizing FWM materials that could be used in conjunction with diode lasers, a rapidly developing laser source technology. In particular, recent advances in developing two-dimensional arrays of laser diodes offer the possibility of compact, efficient, high power transmitter sources. Performance of such arrays can be significantly improved if the individual laser apertures comprising the array can be coherently coupled to provide a uniform phase output. Phase conjugation has been demonstrated to accomplish such coupling (Reference 1.1 and 1.2); implementation for diode laser arrays requires a suitable material operating in the 800 - 860 nm region. The purpose of this effort was to characterize practical FWM materials that offer the possibility of direct, monolithic integration with the laser arrays.

Because diode lasers are compact, efficient, and mechanically rugged, they are attractive transmitters on optical links for communication, IFF, target illumination, etc. In many cases, such applications can benefit from enhanced capabilities afforded by phase conjugation. These include automatic link tracking and correction of propagation path aberrations. For this reason, the work reported here also has focussed on identifying potential conjugator materials for such applications and characterizing their performance in terms of system parameters such as field-of-view, pump intensity, spectral response, and conjugation fidelity.

The Area I approach to developing diode laser wavelength conjugators has been to investigate both a near term candidate, cesium vapor, and longer term semiconductor-based approaches that may offer more attractive performance and the possibility of monolithic integration but are further from implementation.

The cesium work, described in Section 2, is a natural extension of the sodium vapor research performed during Phase I. Being a metal vapor with a strong, spectrally narrow transition at 852 nm (and 894 nm), cesium offers essentially the same advantages (very strong nonlinearity, easy implementation) and disadvantages (self-focusing, limited field of view) as sodium vapor. Because the basic nonlinear optical physics governing the performance characteristics of cesium vapor are essentially the same as for the well characterized sodium vapor, and because an atomic vapor conjugator is straightforward to construct, cesium vapor offers a near term approach for a diode wavelength conjugator with high performance, albeit over a limited range of input conditions. The work reported here demonstrated FWM phase conjugation in cesium vapor for the first time, with low pump power conjugate reflectivities up to 154% observed. Limited tuning of the degenerate FWM response over a 30 GHz bandwidth also was demonstrated. An improved experiment to determine the FWM angular response showed similar results as in sodium, with an observed field-of-view of 20 mrad at the half response points. Self-focusing effects were observed to be similar to those in sodium vapor, with an onset of increased conjugate divergence for reflectivities greater than about 25%.

Limitations of atomic vapor phase conjugators, however, motivated the rest of the effort in Area I: development of an efficient, high performance phase conjugator with potential for monolithic integration with the

diode laser transmitter. Semiconductor materials are one obvious approach; results of efforts in this area are presented in Section 3. FWM experiments had been performed previously in a number of semiconductor materials, but generally for very short pulses or at very low pump intensities at cryogenic temperatures. Experiments and analysis reported here examined backward FWM phase conjugation at room temperature in both bulk GaAs and multiquantum well GaAs/AlGaAs material under cw pumping conditions. These experiments, the first reported at room temperature, and the first for bulk GaAs, resulted in conjugate reflectivities of $10^{-1}\%$ for pump intensities of several kW/cm^2 . Comparison of the the results indicates that excitonic enhancement in multiquantum well materials will contribute to the optical nonlinearity only at very low powers, and is not likely to contribute at the pump intensities present in monolithic configurations.

Another more advanced approach, using the actively pumped gain medium intracavity to a diode laser as the FWM phase conjugating medium, is also discussed in Section 3. Good wave mixing efficiency, coupled with strong intracavity pump fields and saturable gain for amplifying the generated signal, provide very high conjugate reflectivities ($R \geq 2 \times 10^6\%$) for nondegenerate FWM experiments. These reflectivities, when coupled with optical path difference correction demonstrated in this work, show the potential of this approach to a large aperture phase conjugator operating at diode laser wavelengths. The optical path difference correction experiment is the first to demonstrate actual phase conjugation capabilities of diode laser intracavity FWM.

Section 4 presents a general discussion of FWM detectivity delineating the impact of various noise sources on the conjugate fidelity. This is an important system consideration that is needed to establish requirements on incoming signal levels and permissible noise performance of FWM materials. Quantum noise in FWM interactions due to field fluctuations is treated extensively, showing that there is noise added to the signal due to fluctuations of the initial state of the fourth, generated wave. This noise affects both the phase and intensity quadratures of the signal. Analysis shows that a minimum input of 10 quanta is necessary for reasonable conjugation fidelity at high reflectivity. Impact of noise due to medium properties such as absorption and spontaneous emission is also analyzed. Such phenomena increase the

noise in the intensity quadrature. A short discussion is presented to show how squeezed states can be used to characterize the noise contributions of potential FWM materials.

1.2.2 Area II: Phase Conjugated Solid State Laser Technology

Area II of the program sought to develop solid state laser technology through the novel application of phase conjugation. Because solid state lasers are generally pulsed with substantial peak power, phase conjugation using stimulated Brillouin scattering (SBS) was the basic technical approach. Two major subjects were investigated.

The first subject is the development of a phase conjugated master oscillator technology combining both high beam quality and good pulse energy. These oscillator characteristics are important when low gain solid state materials with high saturation intensities are used in power amplifier stages. The approach has been to demonstrate a ROPA, a spatially filtered ring oscillator integrated with a double pass, phase conjugated power amplifier, where the oscillator and amplifier share the same active gain region. The work is presented in Section 5, the final report of Spectra Technology, Inc., who originated the ROPA concept and performed the demonstration under subcontract to TRW. ROPA output of 30 mJ was obtained, with constant, near diffraction limited beam quality for repetition frequencies up to 50 Hz.

The second major subject, presented in Section 6 of this report, deals with phase conjugated second harmonic generation. Many solid state laser applications require operation in the visible, often requiring second harmonic conversion in crystalline materials with moderate to severe optical aberrations, both intrinsic and thermally induced. Effort on this program demonstrates that these aberrations can be sensed using the fundamental wavelength, which when phase conjugated provides the correct intensity pattern to produce a high quality second harmonic beam at the exit of the doubling crystal.

The work reported here not only successfully demonstrates the principles of this concept, but also investigates SBS conjugation characteristics for astigmatic aberrations likely to be encountered in high power doubling applications. Modeling of astigmatic aberrations using the BRIWON code shows good agreement with experimental results.

Two related topics are treated in Sections 7 and 8. Section 7 presents results of analysis on issues involving the rapid turn-on of a medium power solid state laser configured for visible operation. Primarily thermal in nature, start up transients can adversely affect the first output pulses of a solid state laser unless they are compensated in some manner. The system considered consisted of a 50 W slab laser, doubling crystal, and Raman converter. Results show that all components except the doubler come to thermal steady state in less than two seconds. Predicted thermal profiles and optical path differences are presented for all components, and thermally-induced phase mismatch leading to reduced doubling efficiency is analyzed.

Section 8 presents a conceptual design for a 10 J solid state laser with nonlinear optical compensation of thermally-induced aberrations in a gain medium with slab geometry. Derived is a modified Frantz-Nodvik equation to describe optical gain in zig-zag slab amplifiers; this equation is then used to establish slab dimensions, input/out energies, and efficiency for the 10 J system.

1.3 References

- 1.1 J. Brock, G. Holleman, F. Patterson, J. Fukumoto, L. Frantz, M. Valley, "Nonlinear Optics Technology Area I: FWM Technology", Phase I Final Report for DARPA/ONR Contract #N00014-85-C-0257, Defense Technical Information Center Report #ADA 174112, September, 1986.
- 1.2 S. Meisenholder, J. Doyle, R. Hilyard, C. Koop, D. Sower, S. Fisher, "Nonlinear Optics Technology, Phase I, Area 2", final report on Phase I activities on DARPA/ONR Contract #N00014-85-C-0257. Submitted January, 1988.

2.0 FOUR WAVE MIXING IN CESIUM VAPOR

2.1 Introduction

Near term demonstrations of diode laser systems using phase conjugation for coherent coupling, beam cleanup, automatic link tracking, or propagation path correction require an efficient, well characterized phase conjugator that is easily implemented. Possible candidates operating in the 820-860 nm region include photorefractive materials (Reference 2.1), organic dyes (Reference 2.2), cesium vapor, and the semiconductor materials that are the subject of Section 3 of this report. The semiconductor materials, while offering long term promise, are still far from practical implementation. Of the other candidate materials, only cesium vapor offers a low power time response (30 MHz) fast enough to handle the characteristic atmospheric fluctuations ($\tau_a \approx 3$ msec) and accommodate small frequency nondegeneracies among input signals and the FWM pump beams.

As an atomic metal vapor saturable absorber, cesium vapor offers many advantages. First, the atomic spectrum is characterized by very narrow spectral features associated with exceptionally strong transitions. The very large oscillator strengths associated with the dipole-allowed first resonance atomic transitions at 852.112 nm and 894.4 nm are distributed over homogeneous linewidths of $\Delta\nu \approx 4.7$ MHz, resulting in exceptionally low saturation intensities. This in turn leads to strong four wave mixing even at pump intensities of a few watts/cm².

Additionally, cesium has a relatively high vapor pressure so that adequate vapor densities can be achieved for cell temperatures on the order of 400 K. As a result, implementation of a cesium vapor conjugator is not a significant engineering problem. The material is readily available and by its nature does not constrain the potential aperture size of the conjugator.

A final and significant advantage is that the underlying physics of nonlinear optical interactions in cesium vapor are the same as for sodium vapor, a well studied system. Four wave mixing in sodium vapor has been studied in the low power, Doppler limit by a number of investigators (Reference 2.3), and has also been extensively characterized in the high reflectivity regime during the first phase of the NLOT contract. Results of this characterization are detailed in Reference 1.1, the final report

covering Phase I. A general discussion of FWM interactions in inhomogeneously-broadened saturable absorbers is presented in Section 3 of that report; the reader is referred to that section for a more complete discussion of the basic physics operative in cesium vapor in the high reflectivity regime of interest for a practical conjugator.

2.2 Cesium Spectroscopy

Many of the experimental results presented in this section depend strongly on the characteristics of the particular cesium transition used in these studies. Because the underlying objective was to develop a conjugator for diode lasers, the work reported here was performed at or near the $6^2S_{1/2} - 6^2P_{3/2}$ resonance transition at $\lambda_{\text{air}} = 852.112$ nm. This is a strong transition with transition dipole moment of 1.6×10^{-17} esu*cm, slightly stronger than the corresponding D_2 transition in sodium vapor. Because cesium has a nuclear spin of $I=7/2$, the purely electronic transition is split into six hyperfine components, each with a different transition moment, linear absorption, saturation intensity, etc. The net result is that different, weighted combinations of these hyperfine transitions contribute to the FWM interaction depending on the absolute frequency and bandwidth of the optical fields.

Figure 2-1 presents the cesium 852 nm line hyperfine structure and a stick spectrum showing the frequencies and relative line strengths of the six dipole-allowed transitions. The ground state consists of two hyperfine levels, $F=3$ and $F=4$, separated by $\Delta\nu = 9.2$ GHz. This splitting in the ground state separates the hyperfine spectrum into two groups of three closely spaced transitions, the $F=3$ to $F'=2,3,4$ group and the $F=4$ to $F'=3,4,5$. This second group is stronger in absorption because the individual component transition dipoles are larger and because the $F=4$ state has 9/16 of the ground state population due to the relative magnetic sublevel degeneracies of the two ground state hyperfine levels. Two sets of upper level splittings are shown in Figure 2-1, one based on the saturation experiments of Hori, et. al (Reference 2.4), and the other based on spectral calculations using hyperfine splitting coefficients reported by Nakayama (Reference 2.5) and others (Reference 2.6). The differences are small compared to the Doppler width, and so are not important in the results reported here.

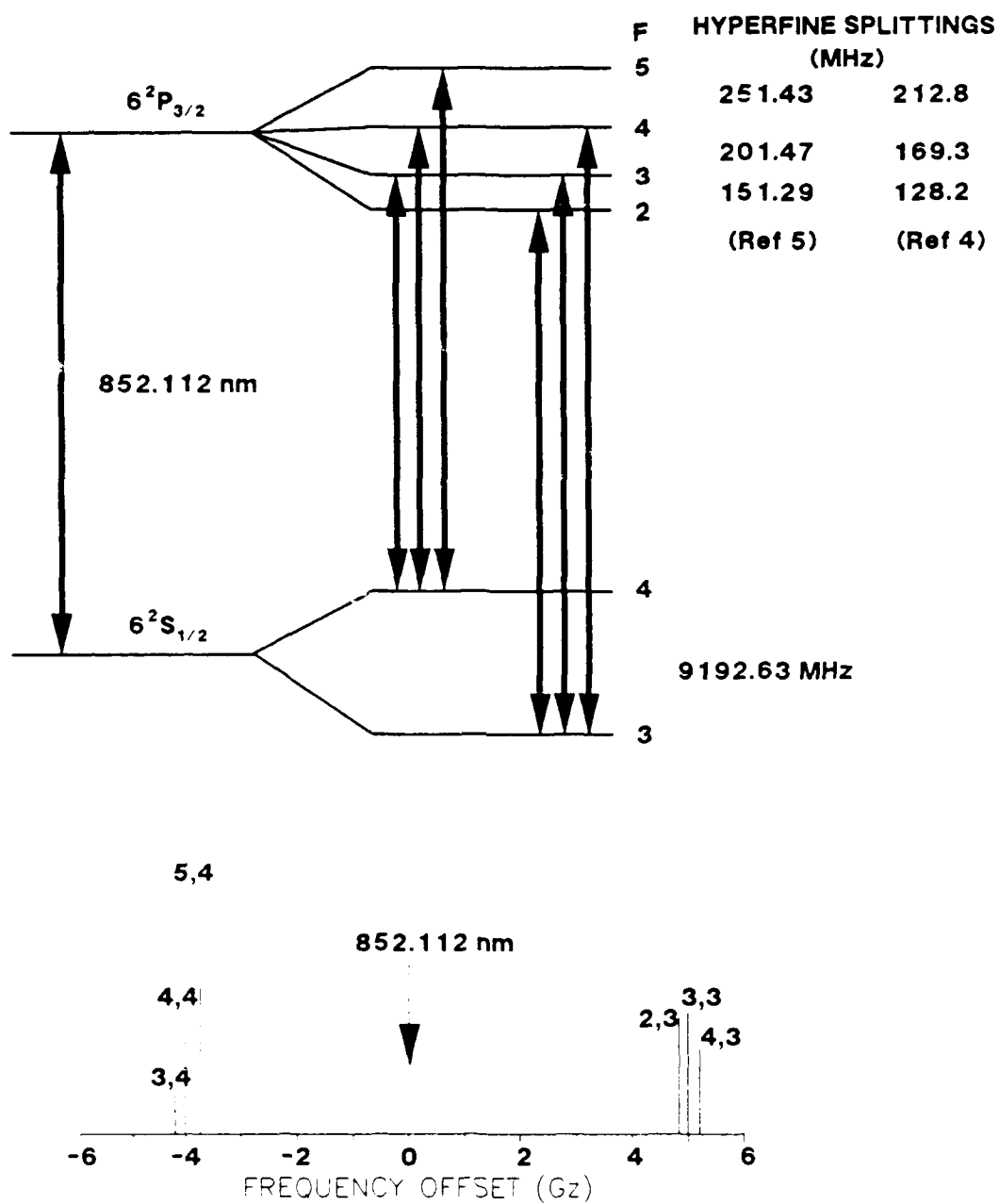


Figure 2-1. Energy level diagram and hyperfine transition frequency spectrum of the cesium D₂ line at 852.112 nm.

Relative line intensities, effective Einstein A coefficients, and transition dipole moments of the six hyperfine components are listed in Figure 2-2. Note that while the magnetic sublevels within each hyperfine level are degenerate in zero external field, they must be considered when calculating the correct transition moment because of the dependence of the magnetic sublevel selection rules on the polarization state of the optical fields, i.e. $\Delta M=0$ for linear polarization, $+1$ for right circularly polarized, and -1 for left circular polarization.

It is the ground state splitting of 9 GHz that most affects the cesium spectrum, both for linear absorption, and as will be shown in Section 2.4 for FWM phase conjugation. This splitting is large compared to the Doppler linewidth at 400 K ($\Delta\nu_{\text{Dop}} \approx 440$ MHz), leading to two distinct frequency regions for absorption and nonlinear mixing. This is in contrast to sodium vapor where the ground state splitting of 1.8 GHz is comparable to the Doppler broadening. Figure 2-3 shows the Doppler broadened absorption spectrum for cesium and sodium to illustrate the impact of the larger ground state hyperfine splitting.

The frequency splittings among the upper hyperfine levels are also larger than in sodium, but are still smaller than the Doppler broadening. As a result, even the narrow band ($\Delta\nu_L \approx 1$ MHz) laser source used during most of the experiments usually excites more than one hyperfine transition. Each hyperfine component will contribute to the FWM response at the laser angular frequency, ω_L , according to its transition dipole moment and $\Delta\omega = \omega_L - \omega_0$, the frequency offset of the laser from the zero velocity transition frequency. This frequency offset determines which velocity group, and hence population fraction, is simultaneously resonant with one of the FWM pump beams and incoming signal beam. Since this velocity group is $2\Delta\omega$ out of resonance with the other counterpropagating pump beam (also at ω_L), the frequency offset also determines the effective strength of the induced nonlinearity, i.e. the amount of susceptibility saturation at the Doppler-shifted back pump frequency. This nonlinearity detuning effect is discussed in Sections 3.1.1 and 3.1.2 of the Phase I report.

Figure 2-3 shows that the ground state hyperfine splitting in cesium is large enough to completely isolate the $F=3 \rightarrow F'$ from the $F=4 \rightarrow F'$ transitions except for extremely strong optical fields ($I > 10^7 I_{\text{sat}}$)

ATOMIC SPECIES - CESIUM 8521.12 Angstrom Line

UPPER STATE ELECTRONIC ANG. MOMTM - 1.5
 LOWER STATE ELECTRONIC ANG. MOMTM - .5
 NUCLEAR MOMTM - 3.5
 ELECTRONIC TRANSITION A COEFFICIENT (1/SEC) - 3.24E+07
 TOTAL ELTRNC. TRANS DIPOLE MOMENT (ESU*CM)- 1.595525E-17

F-upper	F-lower	Rel. Int.	Compt. A	Dipole Momnt (ESU*CM)
2.0000E+00	3.0000E+00	1.5625E-01	3.2400E+07	1.7839E-17
3.0000E+00	3.0000E+00	1.6406E-01	2.4300E+07	1.8279E-17
3.0000E+00	4.0000E+00	5.4688E-02	8.1000E+06	1.0553E-17
4.0000E+00	3.0000E+00	1.1719E-01	1.3500E+07	1.5449E-17
4.0000E+00	4.0000E+00	1.6406E-01	1.8900E+07	1.8279E-17
5.0000E+00	4.0000E+00	3.4375E-01	3.2400E+07	2.6459E-17

SUM OF CALC. LINE INTENSITIES - 384
 TOTAL NUMBER OF HYPERFINE LINES - 6

ATOMIC SPECIES - CESIUM 8944 Angstrom Line

UPPER STATE ELECTRONIC ANG. MOMTM - .5
 LOWER STATE ELECTRONIC ANG. MOMTM - .5
 NUCLEAR MOMTM - 3.5
 ELECTRONIC TRANSITION A COEFFICIENT (1/SEC) - 2.89E+07
 TOTAL ELTRNC. TRANS DIPOLE MOMENT (ESU*CM)- 1.145823E-17

F-upper	F-lower	Rel. Int.	Compt. A	Dipole Momnt (ESU*CM)
3.0000E+00	4.0000E+00	3.2813E-01	2.1675E+07	1.8564E-17
3.0000E+00	3.0000E+00	1.0938E-01	7.2250E+06	1.0718E-17
4.0000E+00	3.0000E+00	3.2813E-01	1.6858E+07	1.8564E-17
4.0000E+00	4.0000E+00	2.3438E-01	1.2042E+07	1.5690E-17

SUM OF CALC. LINE INTENSITIES - 48
 TOTAL NUMBER OF HYPERFINE LINES - 4

Figure 2-2. Relative line intensities, Einstein coefficients, and transition dipole moments for the hyperfine components of the cesium first resonance lines.

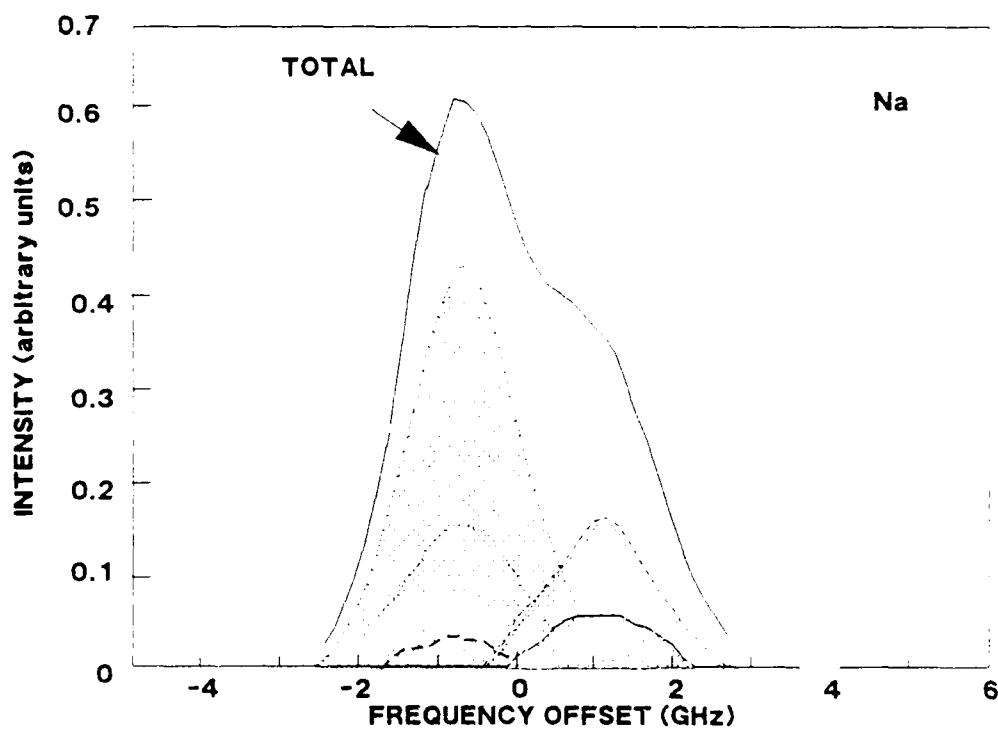
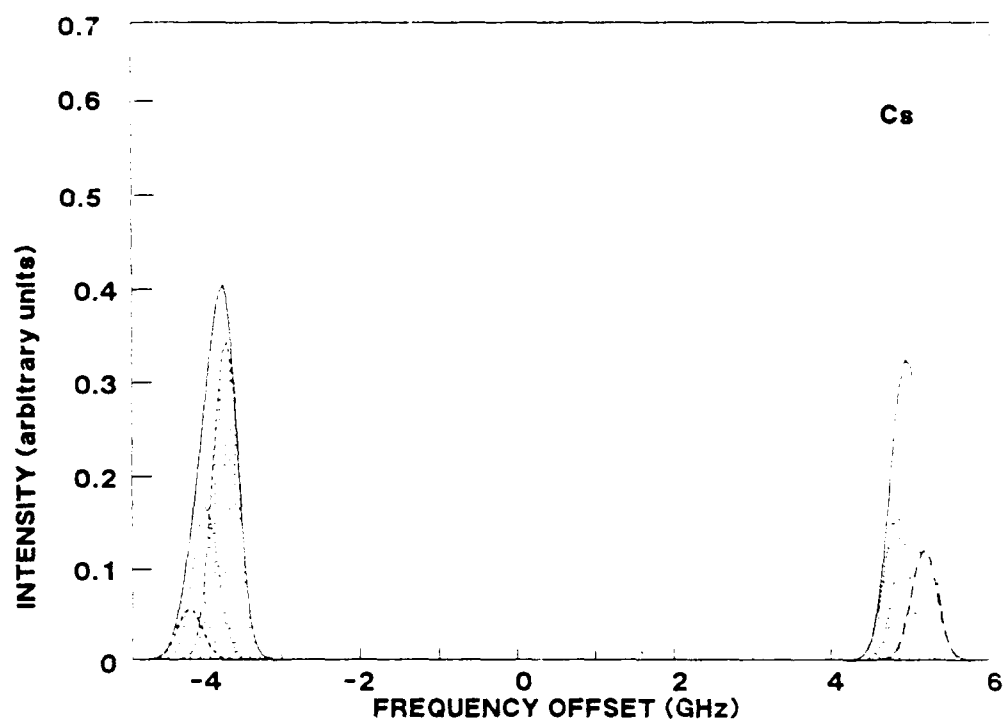


Figure 2-3. Comparison of the Doppler-broadened ($T=400\text{K}$) spectra of the sodium and cesium D_2 lines.

where power broadening is comparable to the zero-field ground state hyperfine splitting. Since this requires optical intensities of greater than 10^4 W/cm^2 , this regime was not investigated in this work.

There is overlap, however, of the three transitions originating from each of the ground state hyperfine levels. Figure 2-4 shows the Doppler broadened profiles ($T=400\text{K}$) for each of the hyperfine components illustrating that multiple transitions can contribute to the four wave mixing interaction at most frequencies. The contribution due to four of the transitions to the FWM interaction is reduced, however, by the impact of optical pumping (Reference 2.7).

Optical pumping arises when population pumped by an optical field from a ground state hyperfine level into a particular excited state hyperfine level can radiate back to other than the original ground state level. For example, population pumped from the $F=3$ level to the $F'=3$ or 4 level radiates back to both the $F=3$ and $F=4$ levels. Since population entering the $F=4$ level no longer is in resonance with the optical field, the net effect is to pump population from $F=3$ to $F=4$, depleting the $F=3$ level population. The $F=3$ population is removed in those velocity groups where the $3 \rightarrow 3$ and $3 \rightarrow 4$ transitions are resonant with the laser.

The $F=3 \rightarrow F'=2$ and $F=4 \rightarrow F'=5$ transitions are not optically pumped because only $\Delta F = 0$ or ± 1 transitions are dipole allowed. The $F'=2$ level can only emit to the $F=3$ level and the $F'=5$ level can only emit to the $F=4$ level. For this reason, these transitions, shaded in Figure 2-4, are the dominant contributors in cw FWM experiments in cesium vapor. The optically pumped transitions, however, do have small contributions because population does feed into the depleted level due to diffusion of cesium atoms from unilluminated regions into the optically-pumped region. Their contribution depends on the relative magnitude of the optical pumping rate and thermal diffusion.

In the spectral region near the $F=4 \rightarrow F'$ transitions, the non-optically pumped $F=4 \rightarrow F'=5$ transition dominates the FWM spectroscopy because it is also the strongest transition of that trio. The $F=3 \rightarrow F'=2$ transition also is not optically pumped, but diffusion-fed contributions from the $3 \rightarrow 3$ and $3 \rightarrow 4$ are more important because their oscillator strengths are comparable. For low optical power degenerate four wave mixing (DFWM) experiments, the FWM signal would be expected to occur

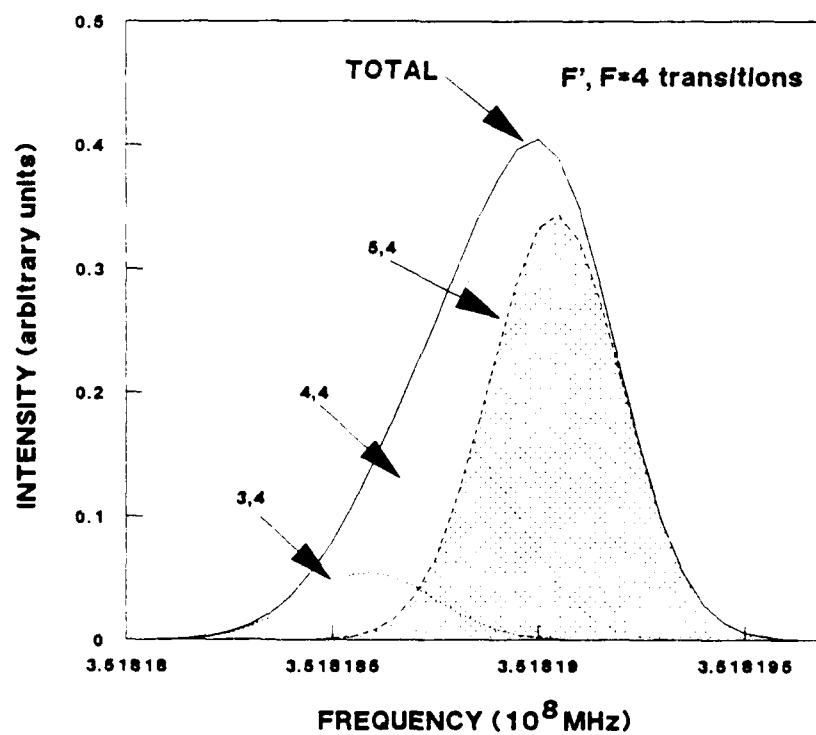
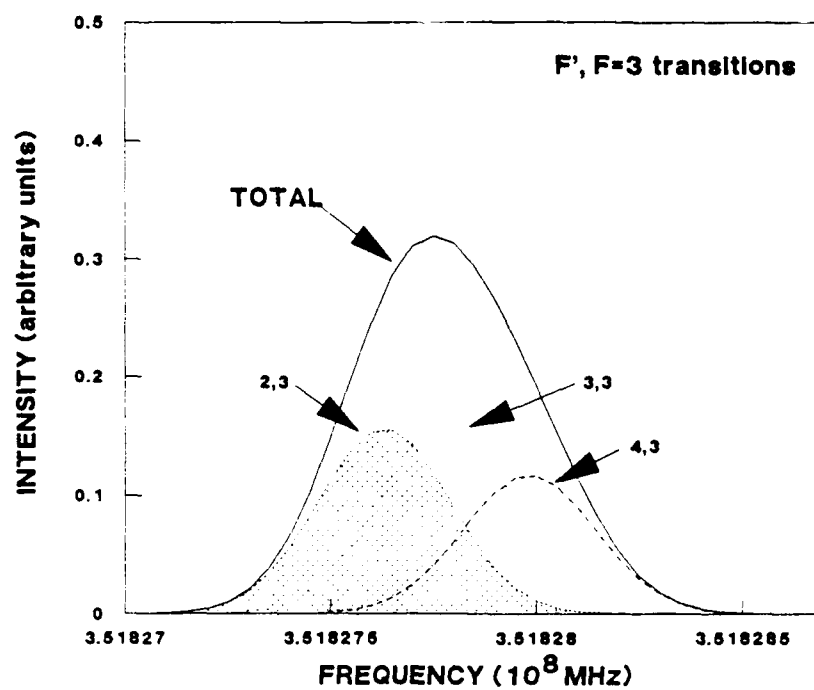


Figure 2-4. Spectral overlap of the three transitions originating from each of the two ground state hyperfine levels. The shaded transitions are the two that are not optically pumped.

exactly on resonance to the $F=3 \rightarrow F'=2$ transition because the nonlinearities from the $3 \rightarrow 3$ and $3 \rightarrow 4$ transitions are being sampled off resonance by some $2\Delta\omega = 300$ MHz and 700 MHz respectively. Since these shifts are larger than or comparable to the Doppler width, the contribution of these transitions is reduced even further.

At higher optical powers, the $F=3 \rightarrow F'=3,4$ transitions become more important for at least two reasons. First, as discussed in Sections 3.2 and 4.3.3 of the Phase I report, the optimum frequency detuning of ω_L from ω_0 depends on the ratio I/I_{sat} so that the frequency offsets of the $3 \rightarrow 3$ and $3 \rightarrow 4$ transitions actually become more favorable. Secondly, power broadening can lead to significant increase in the frequency overlap of the three transitions. A balance exists in that increased optical power aids in the dispersive contribution of the optically pumped transitions, but reduces the steady state population established by optical pumping and thermal diffusion.

2.3 Experimental Configuration

All degenerate four wave mixing experiments performed in cesium vapor are done using the same skeletal arrangement which is shown in Figure 2-5. A Coherent 20 W Ar⁺ laser is used to pump a 699-21 ring dye laser which is set up to operate with Styrl-9 dye. In this configuration, ~250 mW of 852 nm radiation is produced to pump the $6^2S_{1/2}$ to $6^2P_{3/2}$ transition in Cs vapor. The bandwidth of the dye laser output has been measured to be < 1.5 MHz yielding a coherence length of ~30 meters. The output of the dye laser is s-polarized to the reflecting mirror surfaces to insure a high degree of co-polarization in the interaction region of the Cs cell, and to minimize losses at the turning mirror surfaces. The turning mirrors (M) are dielectric coated for 850 nm at the specific angle of use. To align the counter-propagating pump beams exactly colinearly through the Cs cell without allowing feedback radiation from entering back into the dye laser, a Faraday optical isolator is inserted into the beam path close to the laser outcoupler. Losses induced by the isolator are kept to < 12% by AR coating the associated optics and polarizers. A half wave plate, also AR coated for 850 nm, is placed after the isolator to preserve the s-polarization of the beam.

Several pick off beam splitters are used in the setup to allow for Lamb dip frequency diagnostics, and to define separate pump and probe beams. The first beam splitter (BS1) slices out 4% of the main beam to use as a reference and probe beam for real time, on-line Lamb dip diagnostic. The Lamb dip experiment is similar to that of Hansch et al (Reference 2-8) where equal intensity reference and probe beams are directed through a 10 cm Cs cell which is typically operated at 120 C. A third saturating beam is sent through the cell in a counter-propagating direction to the reference and probe beams and made to overlap with them. The transmitted reference and probe beams are detected by a matched pair of photodiodes and monitored on a high sensitivity differential amplifier whose output is displayed on an oscilloscope. With proper cell temperature and beam alignment, the scanning of the dye laser can be used to identify the line center on the transitions originating from the hyperfine splitting of the $6^2S_{1/2}$ state of Cs. This in turn is used for calibration of the pumping frequency during the FWM experiments. The inset in Figure 2-5 shows the observed Lamb dips and crossover resonances on the Doppler absorption profiles indicating the two dips corresponding to the $F=4 \rightarrow F'=5$ and $F=3 \rightarrow F'=2$ transitions. These two Lamb dips were used to establish absolute frequency position and calibrate frequency scales.

A second beam is spliced from the main beam using a variable beam splitter (VBS) to produce the probe beam. This beam splitter is typically adjusted to extract ~ 5% of the main beam to be used as the probe. The remainder of the main beam serves to generate the two pump beams for the Cs FWM cell. A 50-50 beamsplitter (BS2) is inserted into the beam and angle tuned to match the power in both the transmitted (backward pump, B Pump) and reflected (forward pump, F Pump) legs of the resulting beams to within 5%. Lens L1 which is inserted into the beam prior to the beam splitter, typically a 90 cm focal length, serves to co-focus the two counter-propagating legs of the split beam to the same position in the Cs cell with the same beam spot size. The spot size for this configuration is measured to be ~400 microns in diameter at the $1/e^2$ point which gives a Rayleigh range of ~15 cm. This insures that the overlapped beams in the 1 cm long Cs cell are both focused to a minimum beam waist.

The Cs cell is made of Pyrex with a 1 cm long cavity. The Cs is inserted into the cell under a vacuum of $\sim 1 \times 10^{-3}$ torr. Temperature

control of the cell is done using a thermocouple controlled heating tape wrapped around a copper casing with the cell inserted into its center.

2.4 DFWM Spectroscopy of Cesium Vapor

This section presents data on the spectral, temperature, and power dependences of the DFWM in cesium vapor near the 852 nm resonance line.

2.4.1 Frequency Dependence of DFWM in Cesium Vapor

Figure 2-6 presents a DFWM spectrum of cesium vapor obtained under conditions of high phase conjugate reflectivity. In this case, the observed phase conjugate reflectivity, defined as $I_{\text{conjugate}}/I_{\text{signal}}$, was 124%. Reflectivities as high as 154% were also obtained with spectra displaying the same basic four-peaked structure, although relative peak intensities did vary.

The observed spectrum is much as one would anticipate based on the 852 nm line spectroscopy discussed in Section 2.1 and the appearance of the sodium D_2 line FWM spectrum reported in Section 4.3.1 of the Phase I report. The quadruple-peaked structure can be understood as follows. The two double-peaked structures are separated by $\Delta\nu \approx 8.5$ GHz, measured between the the reflectivity minimums, using the indicated Lamb dip frequency markers and assuming the larger upper state hyperfine splittings presented in Figure 2-1. As can be seen, this frequency separation corresponds very closely to the separation of the $F=2 \rightarrow F'=3$ and $F=4 \rightarrow F'=5$ transitions, the two hyperfine transitions contributing most to the FWM signal because they are not optically pumped.

The additional "splitting" to yield a FWM reflectivity minimum at the transition frequencies of the two dominant transitions is not a spectral splitting at all. Observed in the sodium spectrum as well, the double peak feature arises both because of strong saturation of the absorptive component of the transition and residual absorption of generated FWM signal. This minimum at resonance is a characteristic feature identifying the spectrum at higher reflectivities where strongly saturating pump fields are employed. At low powers, the FWM spectrum is essentially the inverse of Figure 2-6, with reflectivity only on resonance where the absorptive component to the susceptibility is strongest (Reference 2.3). At high powers, however, the absorptive component saturates and it is the

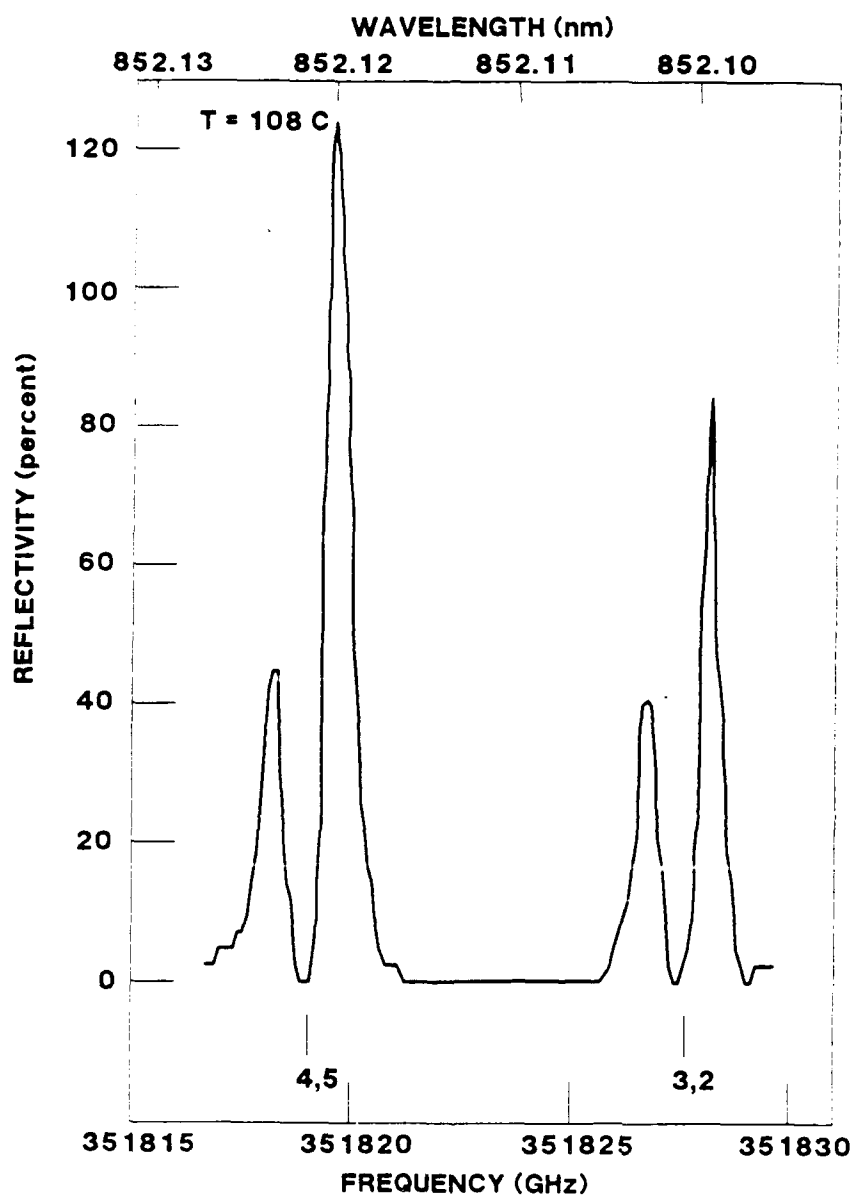


Figure 2-6. Typical frequency spectrum of DFWM reflectivity in cesium vapor under high reflectivity conditions.

dispersive component of the susceptibility that dominates. The dispersive contribution is zero on resonance, accounting for the dip in the FWM spectrum at high power.

A second factor contributing to the reflectivity minimum near the dominant transition resonances is linear absorption. The small signal absorption near resonance is of order 100 cm^{-1} at the cesium vapor densities used in our experiments, and so even though strongly saturating fields are present, residual absorption of several cm^{-1} remains to attenuate signal generated at frequencies within the absorption bands.

Figure 2-7 presents the DFWM spectrum overlaid with the Doppler broadened absorption spectrum. A close examination of Figure 2-7 shows the impact of both processes contributing to the minimum reflectivity at the $F=4 \rightarrow F'=5$ and $F=3 \rightarrow F'=2$ resonances. FWM reflectivity does go to zero as the transition frequency of the $F=4 \rightarrow F'=5$ transition is approached from higher frequency; reflectivity just below the transition frequency remains negligible due to linear absorption. The apparent asymmetry of the absorption band within the FWM reflectivity hole may be due to reflectivity enhancement on the high frequency side due to self-focusing effects discussed below and in Section 2.5. A similar explanation can be applied to the $F=3$ transitions. The minimum occurs right at the $F=3 \rightarrow F'=2$ transition frequency, with signal generated on the high frequency side better able to counter the effect of absorption.

The relative intensities of the peaks in Figure 2-6 are qualitatively in accordance with expectations. The largest peak corresponds to frequencies on the high frequency side of the $F=4 \rightarrow F'=5$ transition, the stronger of the two dominant hyperfine transitions. This transition has a dipole moment approximately 1.5 times as large as the $F=3 \rightarrow F'=2$ transition giving rise to the other doublet feature. Since FWM response goes as the fourth power of the dipole moment, a first order expectation would be for a relative signal ratio of about 5:1.

This ratio is not observed, however, and the ratio of the higher frequency peaks of both doublets has been observed to range from $< 1:1$ to about the 1.4:1 ratio displayed in Figure 2-6. A clue to the cause of this behavior is the pronounced asymmetry of the two peaks associated with a single transition. The high frequency side usually is much larger, an observation attributed to self-focusing of the pump beams that produces

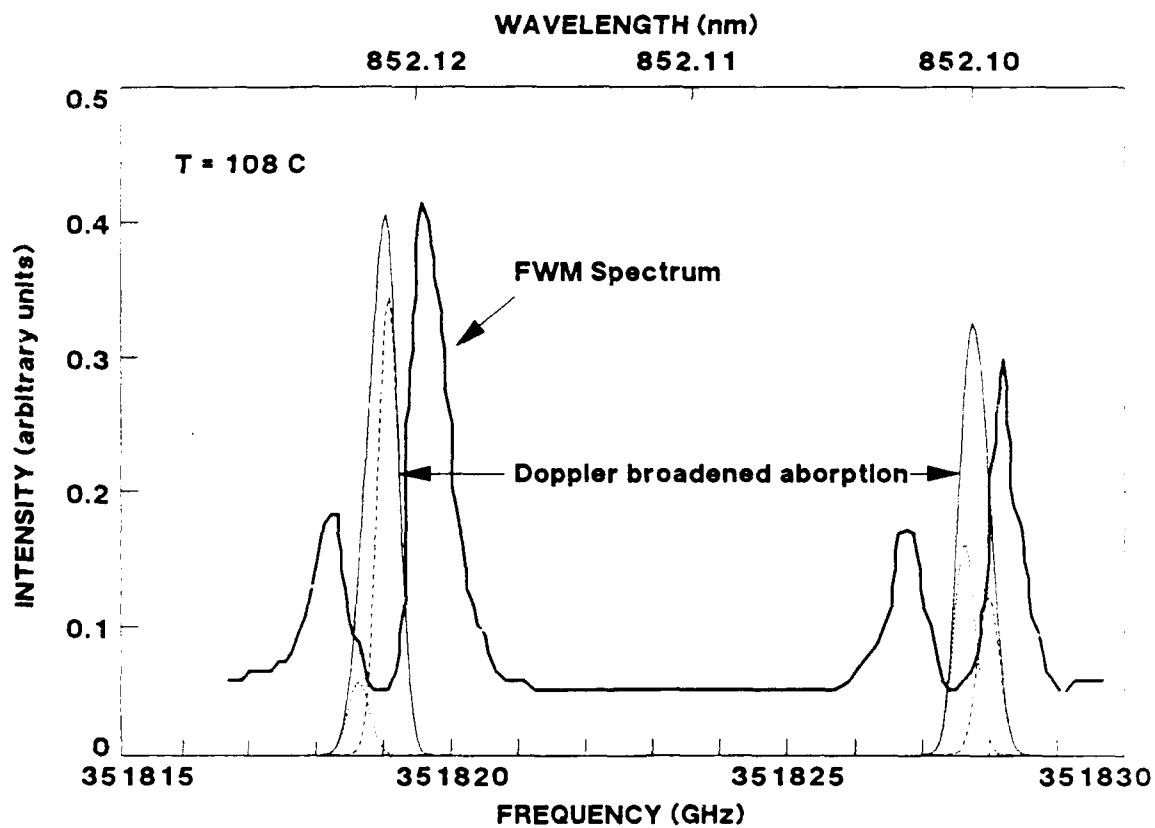


Figure 2-7. Overlap of the DFWM reflectivity spectrum and the Doppler-broadened absorption spectrum illustrating the major contributions of the non-optically pumped hyperfine transitions and the impact of linear absorption.

higher pump intensities. This effect and its consequence on conjugate fidelity are discussed in detail in Section 2.5 and Sections 4.3.1-2 of the Phase I report. The net impact on the relative peak intensities in the frequency spectrum is to place more importance on the $F=3 \rightarrow F'=2$ transition in the high pump power, high reflectivity regime. Self-focusing on the high frequency side of this line increases FWM response at those frequencies, while self-defocusing on the low frequency side counteracts somewhat the self-focusing on the high side of the $F=4 \rightarrow F'=5$ transition.

2.4.2 Temperature Dependence of FWM Signal

The large ground state hyperfine level splitting in cesium vapor affords the possibility of limited frequency tuning by adjusting the Doppler absorption spectrum and optical density via temperature. As the cesium density and Doppler broadening increase, the absorptive hole in each of the two double-peaked features broadens, moving FWM reflectivity away on both sides from the transition frequency. As the temperature increases, the broadening can lead to FWM response at frequencies throughout the $\Delta\nu = 8.5$ GHz region between the two dominant hyperfine transitions. Additional tuning range is realized by the broadening because response is also generated at frequencies in the "outside" wings of the dominant transitions.

This effect has been observed in cesium vapor. Figure 2-8 presents the observed temperature dependence of the DFWM frequency spectrum, showing FWM response over approximately $\Delta\nu \approx 30$ GHz. The spectrum has been normalized at each temperature for clarity; the actual reflectivity was observed to decrease as the temperature of the cesium cell was increased. In practice, operational conditions such as cell temperature and pump intensity would need to be adjusted to achieve the best reflectivity at a particular frequency, limiting the range over which rapid frequency tuning can be achieved to much less than the 30 GHz response region.

2.4.3 Optical Intensity Dependence of Cesium FWM Signal

In an effort to provide some guidance for establishing suitable operating conditions for a cesium conjugator, FWM reflectivity was

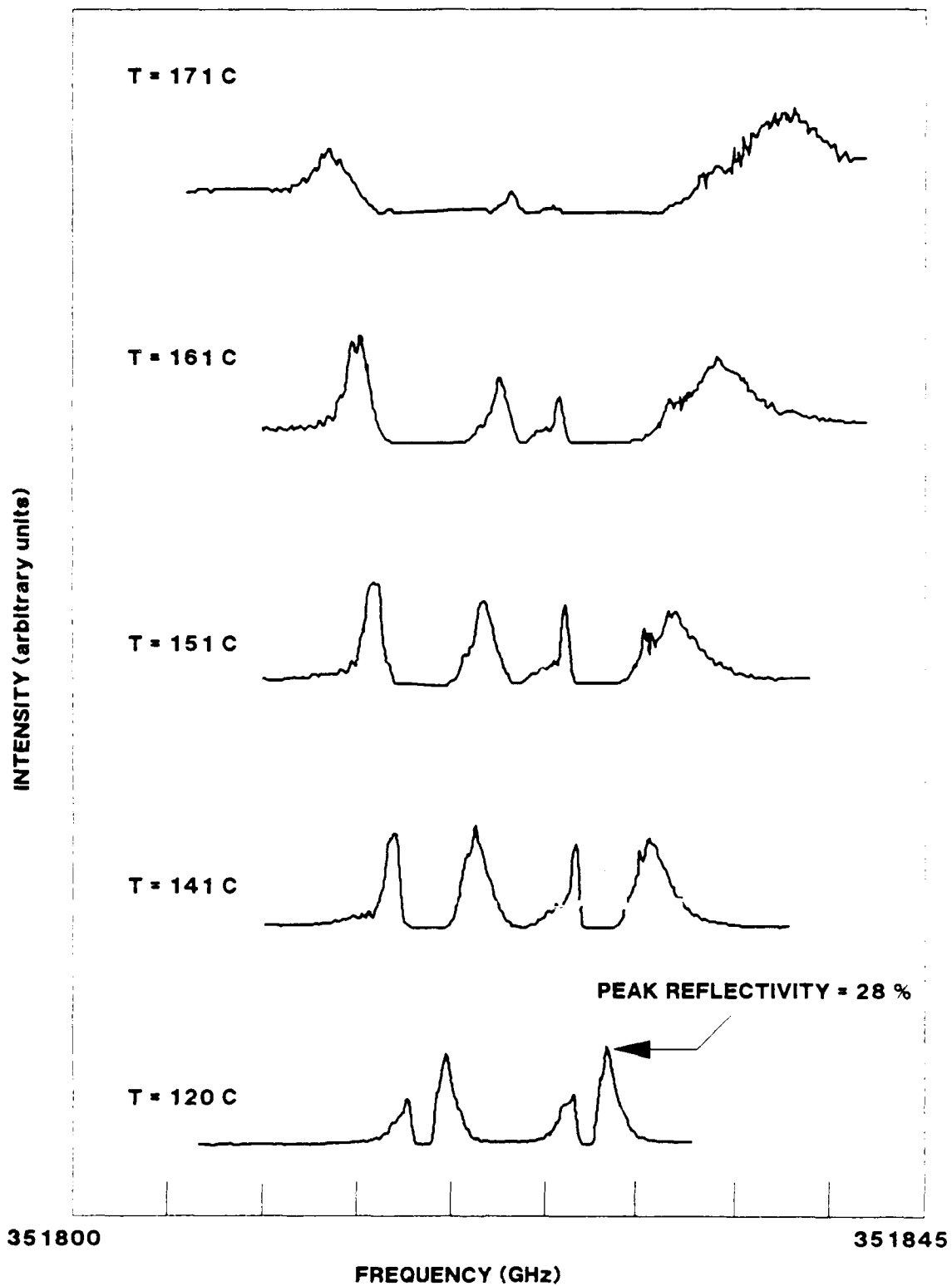


Figure 2-8. Change in DFWM frequency spectrum as temperature and cesium density are increased.

measured as a function of input optical field intensities. Figure 2-9 shows the observed dependence of FWM reflectivity on input probe field power at constant pump field intensity. Figure 2-10 shows reflectivity as a function of pump power for fixed input probe intensity.

Figure 2-9 shows a steady decline in reflectivity with increasing probe intensity. This effect is consistent with pump depletion effects, which are predicted to affect reflectivity for probe/pump ratios as low as a few percent (Reference 2.9). Although there is some scatter in the data at low pump intensities, it is clear that depletion effects are adversely impacting FWM reflectivity for probe intensities larger than 3%-4% of the pump intensity. This probe/pump ratio for the onset of pump depletion effects is the same as was observed for sodium vapor.

Figure 2-10 also shows the impact of pump depletion at low pump intensities. Increasing the pump intensity does overcome this effect and leads to increased reflectivity, but the reflectivity is expected to roll over and decline at very high pump intensities because the refractive nonlinearity becomes highly saturated. Such behavior is predicted theoretically in Reference 2.10; experimental limitations prevented a clear observation of the reflectivity roll over.

2.5 Self-Focusing Effects in Cesium FWM

In nonlinear media, intensity dependent changes in the material's refractive index cause self-focusing or self-defocusing of propagating laser beams that have nonuniform intensity profiles. The equation describing the nonlinear index change (Δn) for Gaussian laser beams propagating in resonant media is:

$$\Delta n = \frac{-\pi N |\mu|^4 E_0^2}{[\hbar(\omega_0 - \omega_L)]^3} \quad (2-1)$$

where μ is the transition dipole moment, N is the (atomic) number density, ω_L is the laser frequency, ω_0 is the transition frequency and E_0 is the electric field amplitude. It can be seen from this equation that when the laser is tuned to a frequency above the transition frequency, $\Delta n > 0$. This corresponds to a positive lens and the nonlinear medium will have a tendency to focus the laser beam. For laser frequencies below the

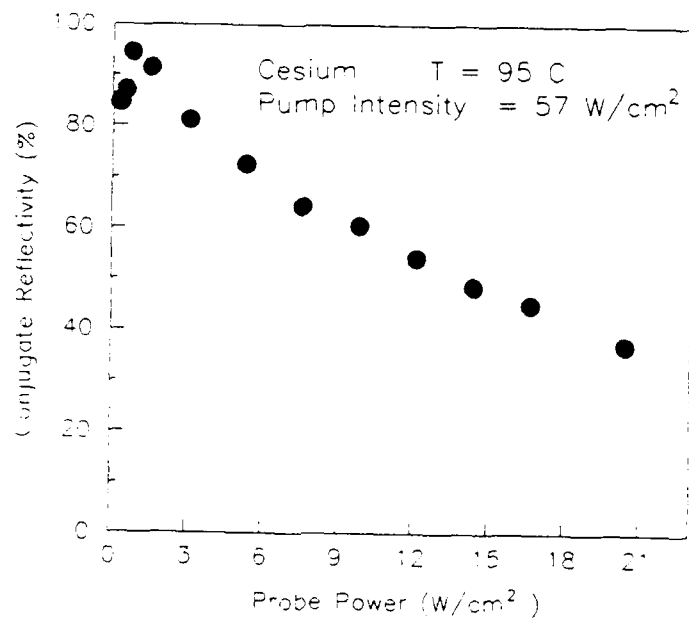


Figure 2-9. Impact of increasing probe/pump ratio on observed conjugate reflectivity.

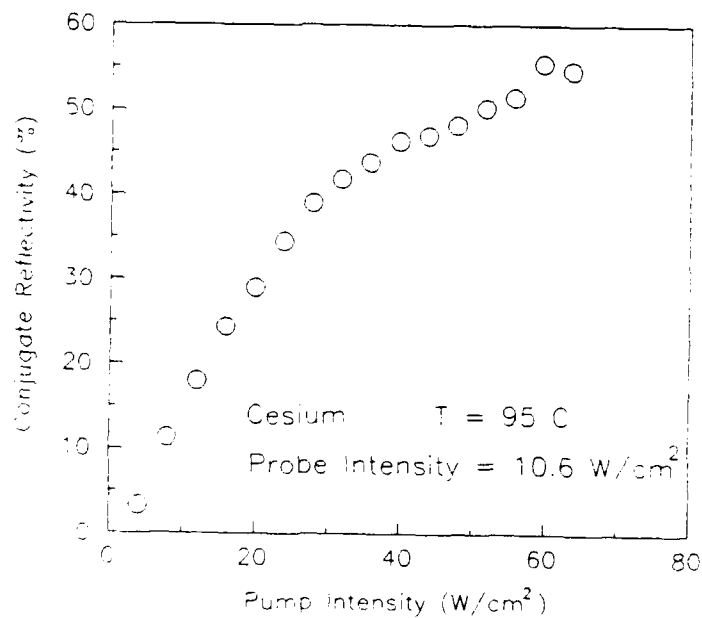


Figure 2-10. Effect of increasing pump intensity on DFWM reflectivity in cesium vapor.

transition frequency $\Delta n < 0$ and the nonlinear medium will act as a negative lens, tending to defocus the propagating laser beams. Furthermore, it has been shown (Reference 2.11) that the minimum power for self-focusing to affect a Gaussian laser beam is given by:

$$P_{sf} = \frac{3.174 \times 10^{-3} \lambda_0^2 c}{n_2} \quad (2-2)$$

where λ_0 is the vacuum wavelength of the laser, c is the speed of light, and $n_2 = 2\Delta n/|E_0|^2$. P_{sf} is on the order of 100 μW for the conditions in the experiments presented here.

The DFWM pump powers employed in TRW's experiments were in the range of 50-100 mW, so self-focusing (self-defocusing) is expected to impact the observed spectral behavior. The F-3 \rightarrow F'-2 transition has a larger reflectivity peak than expected which grows relative to the F-4 \rightarrow F'-5 peaks as pump power increases because self-focusing increases the effective pump intensity and hence DFWM reflectivity. Note that self-defocusing is inherently a self limiting process and so is not expected to play a significant role in determining the FWM reflectivity on the low frequency side of the F-4 \rightarrow F'-5 transition. Defocus due to the F-3 \rightarrow F'-2 transition may mitigate somewhat focusing on the high frequency side of the F-4 \rightarrow F'-5 transition.

Further evidence in support of this explanation of the role of self action effects on the FWM spectrum of cesium comes from both previous observations of self-focusing and self-defocusing in sodium vapor (Reference 2.12 and Phase I report, Section 4.3.2) and from observations of greatly increased beam divergences in the present experiments. This is discussed in more detail in the next section.

2.5.1 Effects of Self-Focusing on Optical Beam Profiles

Because the effects of self-focusing are apparent in the FWM spectrum even at moderate reflectivities, an experiment was performed to characterize its impact in backward FWM phase conjugation experiments. This experiment was essentially the same as the work reported in Section 4.3.2 of the Phase I report; the setup is shown schematically in Figure 2-11.

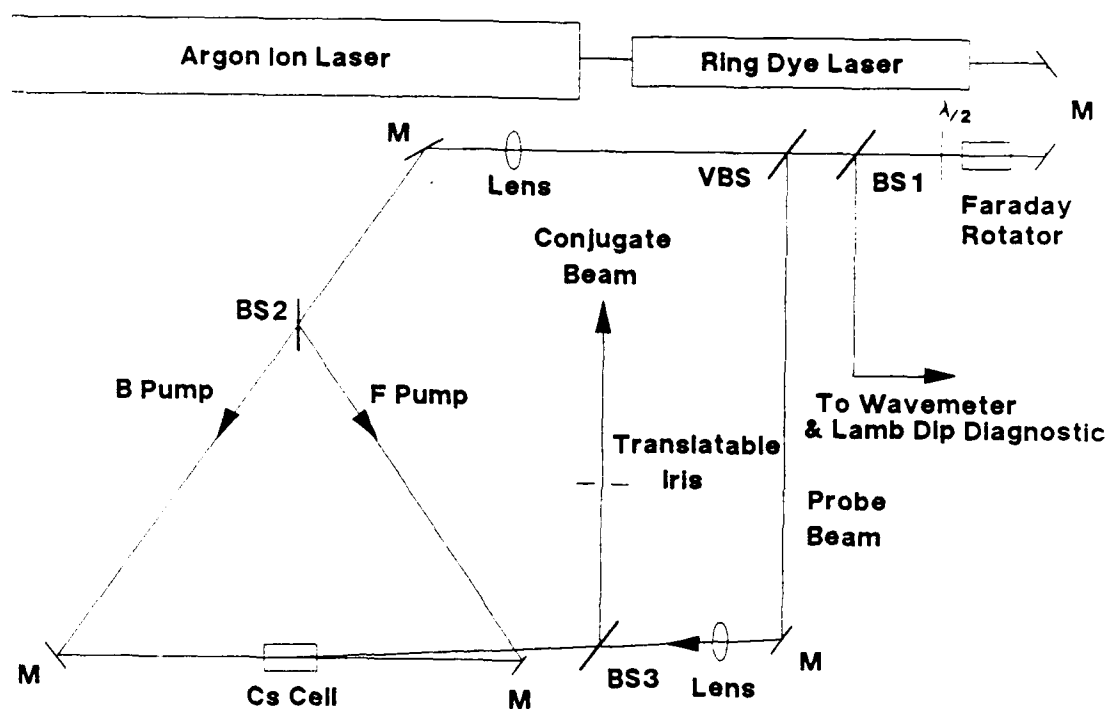
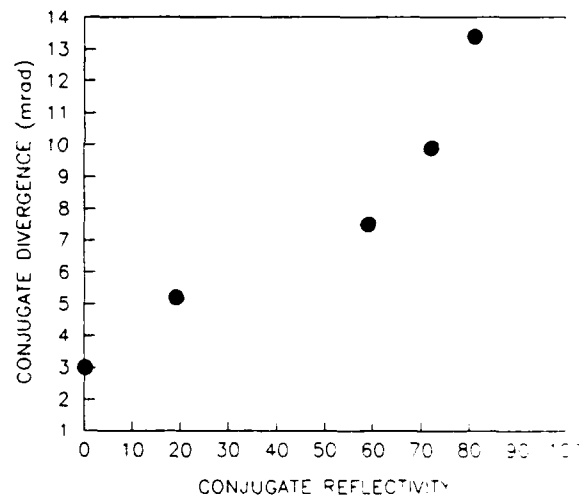
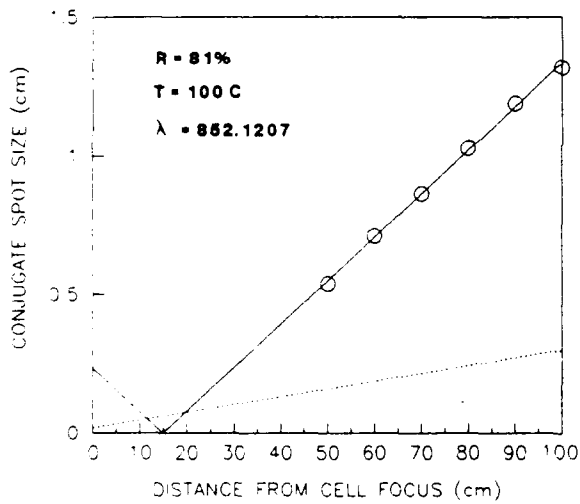
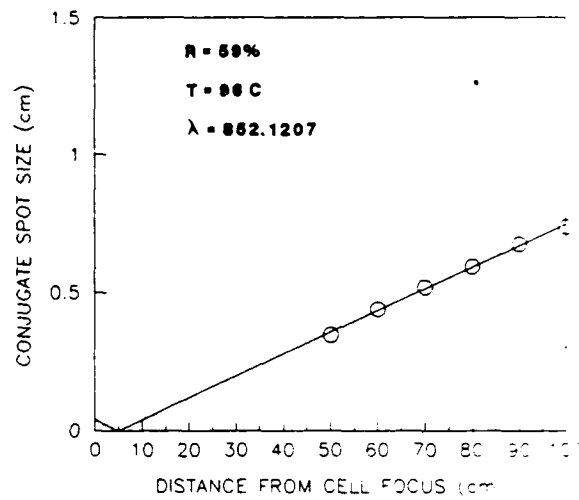
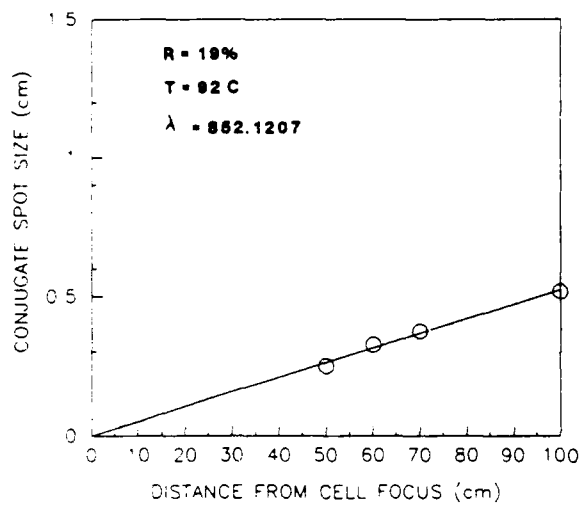


Figure 2-11. Experimental configuration for determining impact of self-focusing on conjugate beam profiles.

It consisted of the standard backward phase conjugating configuration with the conjugate return beam passing through a translatable variable aperture iris for determining the $1/e^2$ diameter of the conjugate beam.

Figure 2-12 presents measured beam diameter of the conjugate return beam as a function of distance from the cesium cell at three different reflectivities. The wavelength of the experiment was 852.1207 nm (air), which corresponds to the FWM reflectivity peak on the high frequency side of the $F=4 \rightarrow F'=5$ transition. Pump intensity was held constant; increasing reflectivity was achieved by increasing the cell temperature and correspondingly the cesium density. Measured data points are shown as open circles. The thin, dotted line illustrates the beam diameter of the incoming probe beam. The thicker line is a best fit beam diameter for a Gaussian beam with divergence that matches the observed beam diameter data. Also shown is a plot of observed divergence as a function of reflectivity. Figure 2-13 shows that self-focusing effects were also observed on the transmitted probe beam.

The data clearly show the influence of self-focusing as the cesium density and FWM reflectivity increase. The best fit Gaussian indicates that the conjugate beam is converging to a waist a short distance from the cesium cell, a region where geometric constraints prevented data collection. Such a focus is anticipated if the pump beams are focusing. However, the best fit Gaussian beam diameter at the cesium cell is calculated to be unrealistically large for reflectivities greater than 30%, indicating that the beam is not propagating as a Gaussian in this region, or that the influence of self-focusing in the cesium cell is more complex than a simple focusing. From the sodium work, 30% reflectivity is about where the impact of self-focusing would be expected to manifest itself. At lower reflectivities, the increased divergence of the conjugate over the incoming probe is believed to be due to an aperturing effect rather than nonlinear self-focusing. This aperturing effect arises because the overlap of the three input Gaussian beams, coupled with the strong pump intensity dependence of the FWM interaction, generates an effective conjugating "aperture" that is smaller than the probe beam itself. The sodium vapor results presented in Figure 4-7 of the Phase I report support this hypothesis because measurements on the defocus side of the line showed a divergence larger than that of the probe but identical to the focus side divergence for reflectivities up to 41%.



○ Raw Data

— Best Fit

Proce

Figure 2-12. Observed self-focusing effects during DFWM experiments in cesium vapor. a,b,c: observed conjugate beam diameters at different conjugate reflectivities, d: observed conjugate beam divergence as a function of DFWM conjugate reflectivity. The various lines are explained in the text.

TRANSMITTED PROBE BEAM PROFILE

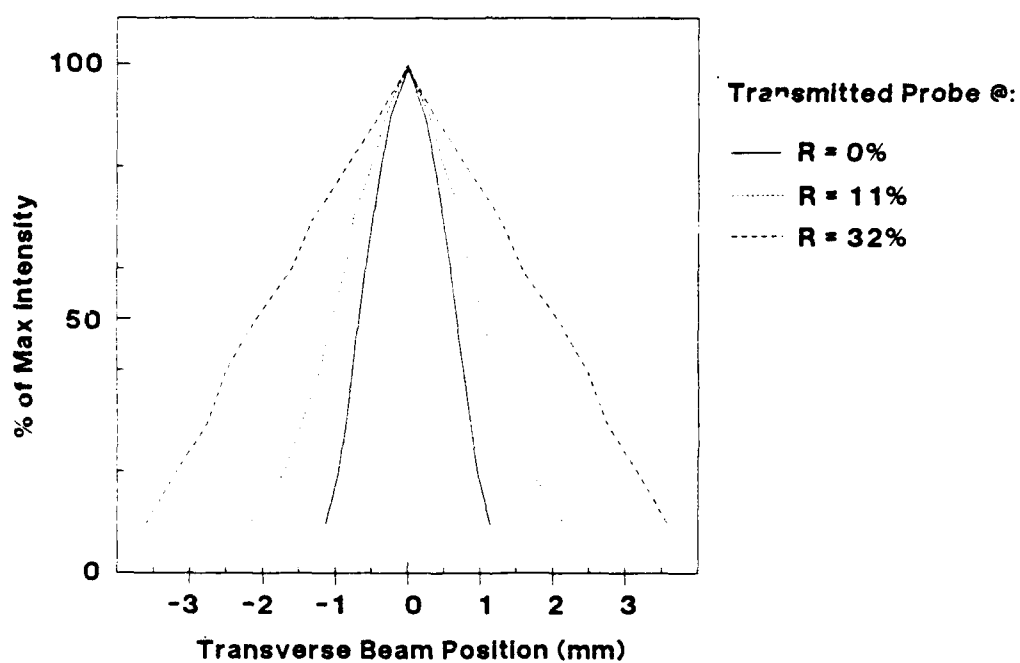


Figure 2-13. Observed probe beam profile as a function of conjugate reflectivity. Measured 70 cm beyond the cesium cell.

2.6 Cesium Vapor FWM Field of View

A detailed discussion of the dependence of FWM reflectivity on θ_{fs} , the angle between the forward pump beam and the incoming signal, has been presented in Section 4.3.4 of the Phase I report for FWM media that are inhomogeneously broadened saturable absorbers subject to the effects of thermal motion. Cesium vapor is such a medium.

Briefly, FWM reflectivity is expected to be angularly independent for very small θ_{fs} , where the spacing of the interference grating produced by the forward pump and signal beam is so large that the grating lifetime is limited only by the excited state lifetime of the $6^2P_{3/2}$ state (34 nsec). As θ_{fs} increases, the grating spacing decreases and thermal diffusion of cesium atoms between light and dark regions becomes an important mechanism for destroying the grating. In this regime, the angular dependence of reflectivity is predicted to be $\sin^{-2}(\theta_{fs}/2)$ because of the $\sin^{-1}(\theta_{fs}/2)$ dependence of the grating population spacing and the N^2 dependence of reflectivity on the grating population. For visible wavelengths, where grating spacings can be small, and at thermal velocities of atomic species, this effect is important for small angles where $\sin^{-2}\theta \approx 4\theta^{-2}$. Calculations based on the average grating destroying velocity in the Doppler limit, $\langle v_{gd} \rangle_D$ given by

$$\langle v_{gd} \rangle_D = ((2RT/(\pi M))^{1/2} \frac{(1 - \exp[-M\Gamma^2/(2RTk^2 \sin^2(\theta/2))])}{\text{erf}[M^{1/2}\Gamma/((2RT)^{1/2}k \sin(\theta/2))])} \quad (2-3)$$

and the time required for absorbers to travel one-half the interference grating fringe spacing, t_{washout} i.e.,

$$t_{\text{washout}} = \lambda/[4 \sin(\theta/2) \langle v_{gd} \rangle] \quad (2-4)$$

indicated that the transition from angle independence to θ^{-2} dependence would occur around 15 mrad for sodium vapor; a similar calculation in cesium vapor indicates a transition around 25 mrad. Equations 2-3 and 2-4 are derived in Section 3 of the Phase I report. This increase is due to the larger grating spacing at the longer wavelength and the slower thermal velocity of cesium atoms, two effects that more than compensate for the longer excited state lifetime of cesium.

Inhomogeneously broadened systems are predicted to exhibit a third regime at much larger values of θ_{fs} because of decreasing population of the velocity group that is simultaneously resonant with the forward pump and signal beam. This population effect was shown to add another $\sin^{-2}\theta_{fs}$ dependence for angles larger than the ratio of the homogeneous to inhomogeneous linewidths.

The cesium FWM reflectivity angular dependence, i.e. the field of view, was measured experimentally with the arrangement shown in Figure 2-14. The probe beam was directed off of a sweep mirror onto a spherical mirror located a radius of curvature away from the cesium cell. This allowed sweeping θ_{fs} while minimizing changes in the interaction volume because the probe swung about its intersection point with the pump beams. One significant change in this experimental arrangement from that used in the sodium experiments was the use of a Faraday optical rotator to isolate the dye laser from the FWM experiment. This allowed the two FWM pump beams to be exactly coaligned, removing a source of phase mismatch that was suspected of distorting small angle data in our sodium experiment.

Results are presented in Figure 2-15. The results are roughly as expected, with a θ^{-2} dependence indicated by the solid line. Evident is the trend towards angular independence for small angles, although the transition appears to occur at smaller angles than the 25 mrad predicted by considerations of thermal washout. This may be due to an under-estimation of $\langle v_{gd} \rangle$ by using Equation 4-3, which is strictly valid only in the Doppler limit. The more general form, presented as Equation 3-9 in the Phase I report, would provide a better estimate in the cesium experiments because power broadening was comparable to the Doppler width. This equation is quite cumbersome, however, and so was not used in our first order estimate of the transition to angular dependence.

Within the scatter of the data, the θ^{-2} dependence appears to hold throughout most of the angular region investigated. The one positive angle point that is significantly below the line is suspect because it is not reproduced by the negative angle data and a transition to stronger angular dependence due to population effects is not expected to be observed in our experiments because the power-broadened homogeneous width is calculated to be in excess of the inhomogeneous Doppler broadening.

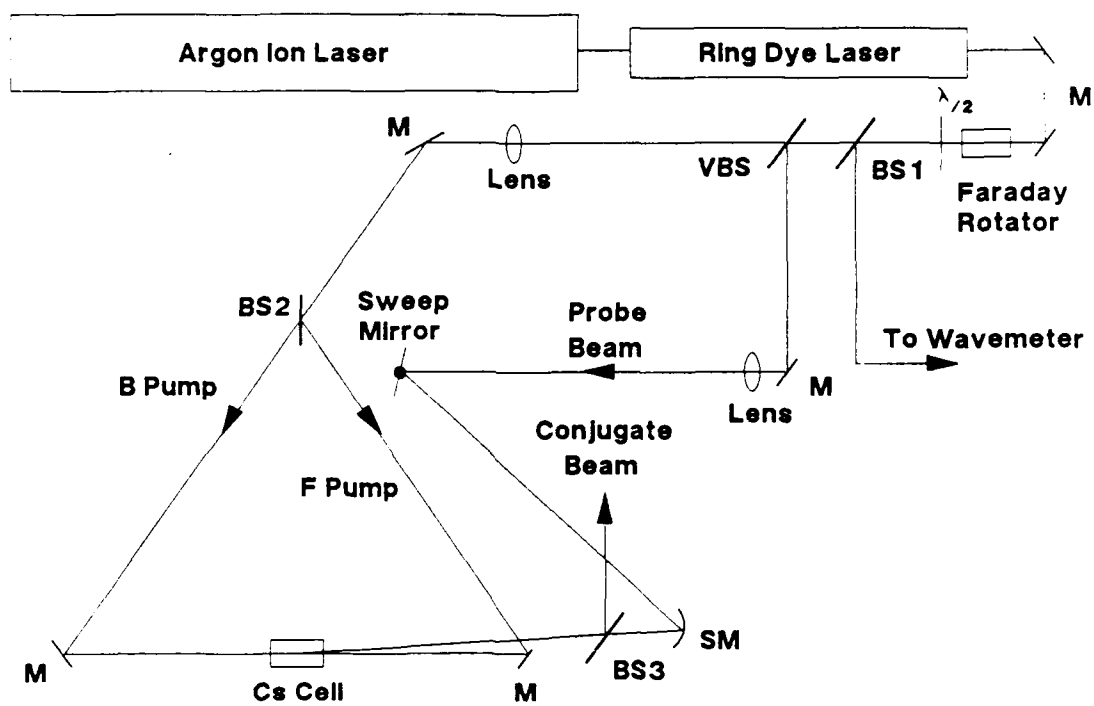


Figure 2-14. Experimental setup for determining the angular dependence of DFWM in cesium vapor.

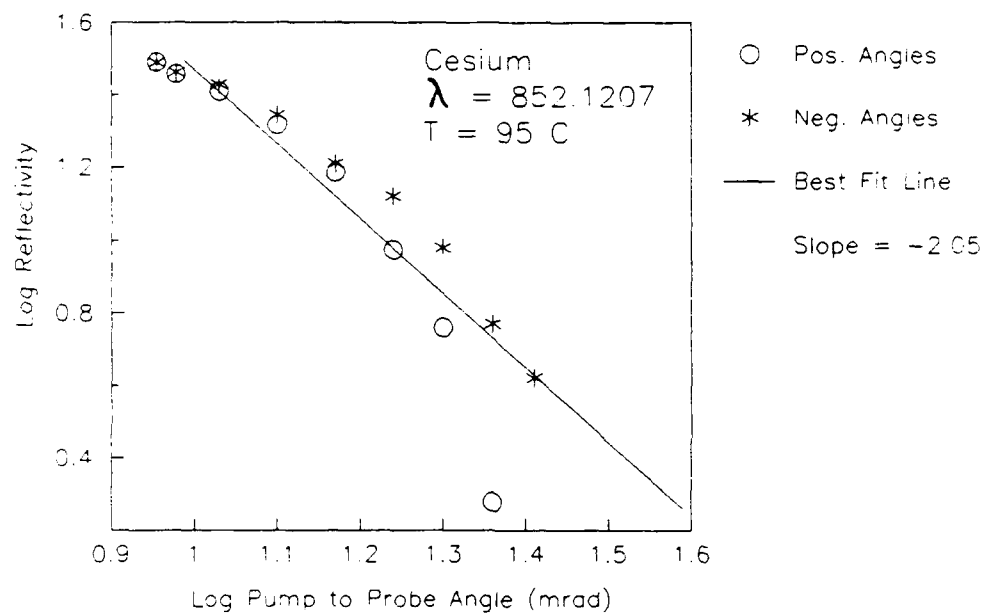


Figure 2-15. Observed angular dependence of DFWM reflectivity. The dependence is consistent with thermal washout effects being the dominant mechanism determining angular response.

2.7 Conclusions

The experimental results obtained here demonstrate that cesium vapor is a viable near-term phase conjugating medium operating at a wavelength compatible with diode lasers. As a FWM medium, cesium is characterized by excellent phase conjugate reflectivity at low pump intensities, and because of the details of its hyperfine splitting, offers response over a spectral range substantially larger than that provided by sodium vapor. Like sodium vapor, however, cesium displays a limited angular response and induces other nonlinear optical effects that can degrade conjugation fidelity of transverse phase information. However, such undesirable nonlinear effects would not be expected to degrade piston error correction, an important capability for conjugators operating at diode laser wavelengths.

2.8 References

- 2.1 R. R. Stephens, R. C. Lind, C. R. Giuliano, Appl. Phys. Lett. 50, 647 (1987); A. M. Glass, Opt. Eng. 17, 470 (1978).
- 2.2 H. J. Hoffman, J. Opt. Soc. Am. B 3, 253 (1986).
- 2.3 J. F. Lam, D. G. Steel, R. A. McFarlane, R. C. Lind, Appl. Phys. Lett. 38, 977 (1981); D. G. Steel and R. A. McFarlane, Phys. Rev. A27, 1687 (1983).
- 2.4 H. Hori, Y. Kitayama, M. Kitano, T. Yabuzaki, T. Ogawa, IEEE J. Quantum Electron QE-19, 169 (1983).
- 2.5 Shigeru Nakayama, Japan. J. Appl. Phys. 23, 879 (1984).
- 2.6 H. Bucka, Z. Phys. 151, 328 (1958); S. Svanberg and G. Berlin, Z. Phys. 251, 1 (1972).
- 2.7 D. G. Steel and R. A. McFarlane, Phys. Rev. A27, 1687 (1983); *ibid*, Phys. Rev. A27, 1217 (1983).
- 2.8 T. W. Hansch, M. D. Levenson, A. L. Schalow, Phys. Rev Lett. 26, 946 (1971).
- 2.9 W. P. Brown, J. Opt. Soc. Am. 73, 629 (1983); M. T. Gruneisen, A. L. Gaeta, R. W. Boyd, IEEE J. Quantum Electron. QE-18, 1095 (1986).
- 2.10 R. C. Lind, D. G. Steel, G. J. Dunning, Opt. Eng. 21, 190 (1982).
- 2.11 E. L. Dawes and J. H. Marburger, Phys. Rev. 179, 86 (1969).
- 2.12 J. E. Bjorkholm and A. Askin, Phys. Rev. Lett. 32, 129 (1974).

3.0 DEGENERATE FOUR WAVE MIXING IN SEMICONDUCTORS

3.1 General Description

Development of basic four wave mixing technology (FWM) leading to efficient, high reflectivity phase conjugators is important for realizing the benefits of optical phase conjugation in electro-optical systems. More specifically, low power diode laser phase conjugation is a potentially powerful technique, with applications such as communication via a phase conjugated link, spatial filtering with gain, and coherently coupled diode laser arrays where frequency matched FWM in the same semiconductor material provides an attractive means to achieve the necessary phase coupling and piston error correction. In Section 3, we describe FWM experiments performed in several different semiconductor materials in the 800-900 nm wavelength region. These materials, which offer the potential for monolithic integration, are candidates for the phase conjugation of GaAs/AlGaAs diode lasers which lase in this same wavelength region. The present work investigates two different approaches: systems exhibiting saturable gain and materials with saturable absorptions. There are advantages and disadvantages to both of these nonlinear materials.

High saturable gain is provided by intracavity FWM in diode lasers. Using this technique, very large conjugate signal reflectivities have been achieved with incident probe powers of $< 1 \mu\text{W}$. In Section 3.2 we report intracavity FWM reflectivities $\sim 5 \times 10^4$, an order of magnitude greater than previously reported values (Reference 3.1). The dependence of the FWM signal on: 1) the pump-probe frequency detuning, 2) the intracavity pump power, and 3) the incident probe power, is discussed.

To date, FWM in diode lasers has been limited to single (longitudinal and transverse) mode lasers which are inherently one dimensional (1D) waveguides. Since the dimensions of their active emitting areas are comparable to the wavelength of the laser light ($\sim 0.8 \mu\text{m}$), it is impossible to retain and phase conjugate any spatial information contained on the input probe beam. Thus, the advantage of saturable gain provided by diode lasers is somewhat offset by the inability of a single waveguide to perform image conjugation. However, intracavity FWM in diode lasers does

have an important conjugation capability. In Section 3.3, we present the first experimental verification of the phase conjugation properties of the intracavity FWM process in laser diodes: correction of an optical path length difference (OPD), or piston error, inserted into the incident probe beam.

Bulk semiconductor materials do not suffer from the spatial frequency limitation imposed by the diode laser waveguide, and do offer a saturable absorption for nonlinear optical interactions. Nonlinear saturable absorbers have been extensively studied for use as FWM optical phase conjugators (Reference 3.2). To use a saturable absorber as a FWM phase conjugator, it must have a strong dipole transition at the wavelength of interest. In the case of diode laser phase conjugator materials, the resonant medium which composes the diode laser is a logical candidate since it has a strong transition at the appropriate wavelength. For diode lasers operating in the near infrared (800-900 nm), the semiconductor GaAs is indicated. Of particular interest is the role of exciton transitions at room temperature and at moderate pump intensities.

We have studied FWM in two different forms of GaAs: bulk GaAs and GaAs/AlGaAs multiple quantum wells (MQW). These materials can be grown epitaxially in thin ($\sim 2 \mu\text{m}$), large area (several cm^2) uniform wafers. Thus, in contrast to the single mode diode lasers discussed above, the GaAs semiconductor materials could serve as large area phase conjugators with the possibility of image processing applications. FWM reflectivities, however, are much smaller: only $\sim 10^{-3}$ was observed with CW pump beams at 4 kW/cm^2 . An analysis of FWM (Section 3.5) indicates that the reflectivity is limited by the optical thickness of these materials. Reflectivities greater than 100% should be obtainable with samples with optical path lengths of $\geq 40 \mu\text{m}$ for pump intensities large compared to the saturation intensity.

The results of CW FWM in bulk GaAs and GaAs MQW samples is discussed in Section 3.4. Excitonic enhancement of the MQW optical nonlinearity and its role in CW FWM at moderate pump intensities is compared and contrasted to that of bulk GaAs.

3.2 Intracavity NDFWM in Single Mode Diode Lasers: Reflectivity Results

Nondegenerate four wave mixing (NDFWM) inside single mode laser diode cavities has recently been accomplished (References 3.1 and 3.3). In this

system the inverted laser medium provides saturable gain. The laser medium can be operated either above or below lasing threshold (Reference 3.4). Above threshold, the laser standing wave acts as the counter-propagating pump fields in the FWM experiment. Below threshold, external pump fields are injected into the diode cavity. In either case, an external probe beam detuned by a few GHz is injected into the diode cavity. The advantage of an amplifying medium over the saturable absorber case is obvious: reflectivities greater than 5000 have been obtained inside of a single diode laser cavity (Reference 3.1).

3.2.1 Experimental Setup

Figure 3-1 is a diagram of the experimental setup used to examine the NDFWM reflectivity characteristics of a diode laser cavity. Two identical single mode laser diodes (Mitsubishi ML5101A) are mounted on thermoelectric cooling elements and temperature stabilized to $\sim .02^\circ\text{C}$. The diodes are operated CW with stabilized current supplies ($\sim 10\ \mu\text{A}$ stability) near 820 nm. With a proper choice of operating temperatures and currents, the two diodes lase at exactly the same wavelength. The FWM diode laser (LD2 in Figure 3-1) is operated at frequency ν and the probe diode laser, LD1, at a frequency ν_p detuned from ν by $\pm 1-10\ \text{GHz}$. The output of LD1 is efficiently collimated ($\sim 90\%$) with a 0.5 numerical aperture, 8 mm focal length diffraction limited lens (L1), specifically designed for diode lasers. The LD1 light beam is then passed through a 2 mm aperture Faraday optical isolator (FOI) providing isolation $> 10^3$ to prevent optical feedback of LD2 into LD1. Since the collimated output beam of LD1 is very large ($\sim 4 \times 8\ \text{mm}$), most of this light does not transmit through the FOI aperture. This loss is not a problem because only a few μW of probe light need to be injected into the FWM diode. To reduce optical alignment requirements, the front facet of LD2 is flooded with LD1 light by weakly focusing with a 40 cm lens (L2). Figure 3-2 shows the measured transverse intensity pattern of this focussed spot at the LD2 facet position. Figure 3-2A shows the spot is approximately Gaussian in the horizontal direction with a spot diameter ($1/e^2$) of $340\ \mu\text{m}$ and Figure 3-2B shows that the spot is also Gaussian in the vertical direction but with a spot diameter of $130\ \mu\text{m}$. The output of LD1 is separated from the LD1-LD2 direction by the 50% beamsplitter (BS) shown in the figure. The LD1 output light reflected

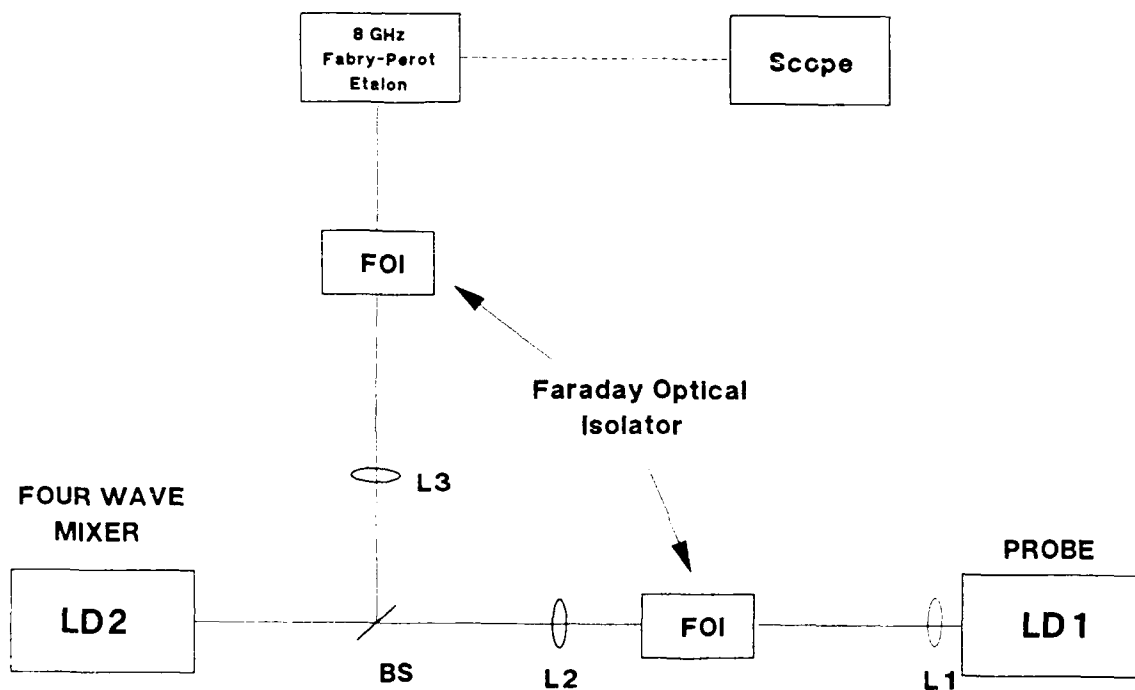
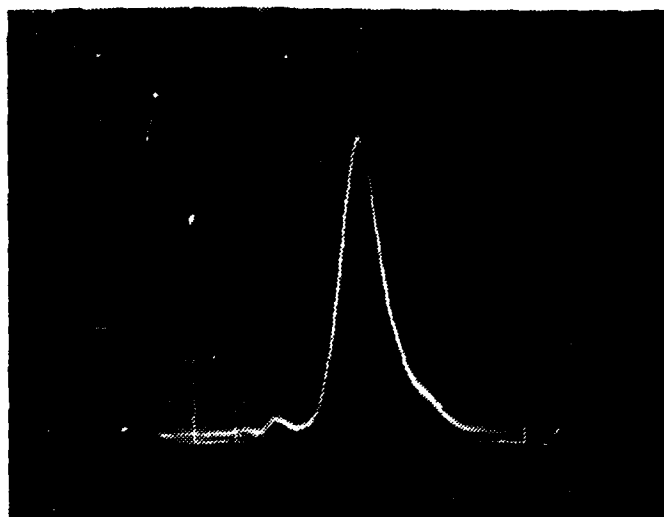
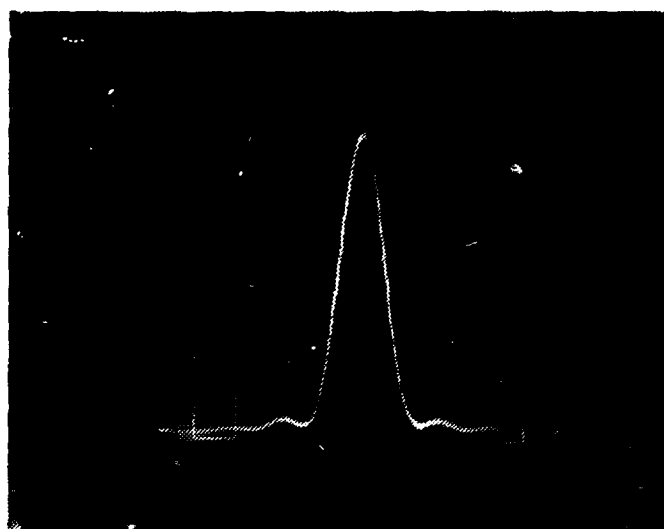


Figure 3-1. Experimental setup for the demonstration of intracavity NDFWM in single mode diode lasers. LD1 and LD2 are Mitsubishi ML5101A single mode diodes, L1 = 8 mm focal length lens, L2 = 40 cm focal length lens, L3 = 10 cm focal length lens, and BS is a 50% beamsplitter.



A



B

Figure 4-2. Transverse profiles of the focused beam at the LD2 facet. A: horizontal beam profile, B: vertical beam profile.

from BS is collimated with a 10 cm lens (L3), directed through a large aperture (5 mm) FOI and into an 8 GHz free spectral range, high finesse (~200) scanning confocal Fabry-Perot etalon.

As a result of the one dimensional waveguide nature of single mode diode lasers, the pump, amplified probe and conjugate output beams are all exactly colinear with one another. To isolate the signal beams, the FWM experiment is performed nondegenerately with the probe detuned by an amount $\delta = \nu_p - \nu$ sufficient to permit spectral resolution using a Fabry-Perot etalon ($\delta \sim 1-10$ GHz). The cavity length of the etalon is piezo-electrically scanned and the pump (ν), probe ($\nu_p = \nu + \delta$), and conjugate ($\nu_c = \nu - \delta$) outputs are all detected by a photodiode and viewed on an oscilloscope with horizontal sweep driven by the same ramp which drives the etalon cavity length.

Figure 3-3 shows a photograph of a typical oscilloscope trace. The top trace is a x50 magnification of the bottom trace. The large peak in the center of the trace corresponds to the pump beam, the peak on the left corresponds to the probe beam tuned 3.3 GHz to the red of ν , and the peak on the right corresponds to the conjugate signal frequency, ν_c . The spacing between adjacent etalon peaks (8 GHz) is used to calibrate the horizontal (frequency) scale of each photograph. The vertical scale of the oscilloscope is calibrated by blocking the LD1 probe diode and measuring the amplitude of the pump beam on the scope. Since the power output of the pump from the FWM diode is known, the number of millivolts on the scope per mW of light input can be calculated. The absolute powers of the probe and conjugate signals are thus easily obtained.

To calculate the magnitude of the FWM reflectivity, it is necessary to know the amount of probe power coupled into LD2. In the present experimental setup this is determined as follows. From the theory developed for weakly guided 1D waveguides, the ratio of the power coupled into the diode (P_d) to the incident power (P_i) is given by (Reference 3.5):

$$P_d/P_i = \frac{T \cdot \left| \int dA E_{ix} e_{tx} \right|^2}{\int dA |e_{tx}|^2 \cdot \int dA |E_{ix}|^2} \quad (3-1)$$

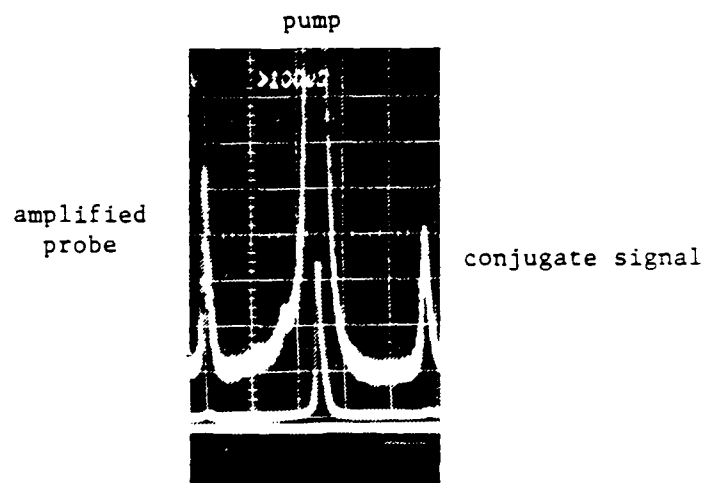


Figure 3-3. Photograph of an oscilloscope trace displaying the output of the 8 GHz free spectral range etalon. The top trace is a x50 magnification of the bottom trace. The large central peak is the pump beam, the smaller peak on the left is the amplified probe beam, and the peak on the right is the conjugate signal. The probe-pump detuning, δ , is about 3.3 GHz. The photo has been cropped to remove peaks from other etalon orders.

where E_{ix} is the x transverse spatial dependence of the incident E-field, e_{tx} is the x spatial dependence of the fundamental waveguide mode, and A is the area of the waveguide facet. T is a transmission factor, determined in many cases by Fresnel reflection at the waveguide surface. Here, the 1D diode is also a (low finesse) Fabry-Perot etalon. Since the transmission band pass (~ 1 Å or 45 GHz) for the diode etalon is large compared to the probe detuning, we assume that the probe is exactly on cavity resonance and take $T=1$. Equation 3-1 is basically a normalized convolution integral of the 1D fundamental waveguide mode with the incident spatial mode structure. The 1D waveguide mode of the diode is back-calculated from a measurement of the far-field radiation pattern of the diode. This procedure gives an effective diode mode size of $0.7 \mu\text{m} \times 2 \mu\text{m}$. Using this, along with the spots sizes obtained from Figure 3-2 ($240 \mu\text{m}$ and $130 \mu\text{m}$) for the incident beam, yields a power coupling ratio of $\sim 3 \times 10^{-5}$. This factor determines the magnitude of the FWM reflectivity, and is the source of greatest uncertainty in the calculation.

3.2.2 Intracavity FWM Results

The largest probe amplification ($\sim 1.4 \times 10^5$) and FWM reflectivity ($\sim 5.2 \times 10^4$) are observed for an incident probe power (before coupling losses) of 0.14 mW and a detuning of -0.6 GHz. These values for FWM reflectivity and probe amplification are an order of magnitude larger than those reported previously in Reference 3.1. The difference may be due to a combination of two factors: 1) the pump power employed here, measured external to the cavity at 15 mW, is approximately twice as large as that in Reference 3.1 (8.7 mW) and 2) the length of the active diode medium in the Mitsubishi diodes is 1.5 times longer than in the Hitachi diodes used in Reference 3.1. The NDFWM spectrum is presented in Figure 3-4, which shows the probe amplification, A , and the conjugate reflectivity, R , as a function of detuning, δ , for an incident probe intensity of 0.51 mW and LD2 diode pump power of 15 mW. Under these conditions, the maximum probe amplification ($\sim 4.6 \times 10^4$) and conjugate reflectivity ($\sim 2.4 \times 10^4$) occur at a probe detuning of $\delta = -1.2$ GHz.

In Figure 3-4 the conjugate signal is symmetric with respect to the probe detuning ($\pm\delta$), whereas the probe amplification is observed to be asymmetric, with larger values found at negative detunings ($\delta < 0$). In

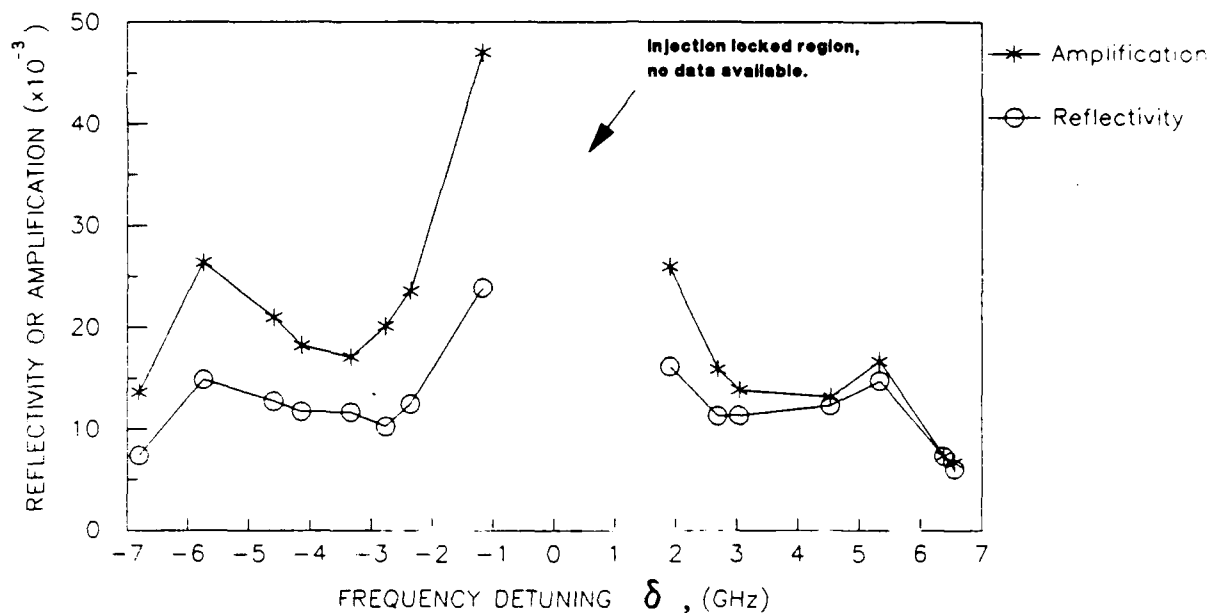


Figure 3-4. Conjugate reflectivity (R) and probe amplification (A) as a function of the probe-pump detuning, δ , for an incident probe power of .51 mW. In the frequency region near zero, the FWM diode is injection locked to the input probe frequency and NDFWM does not occur.

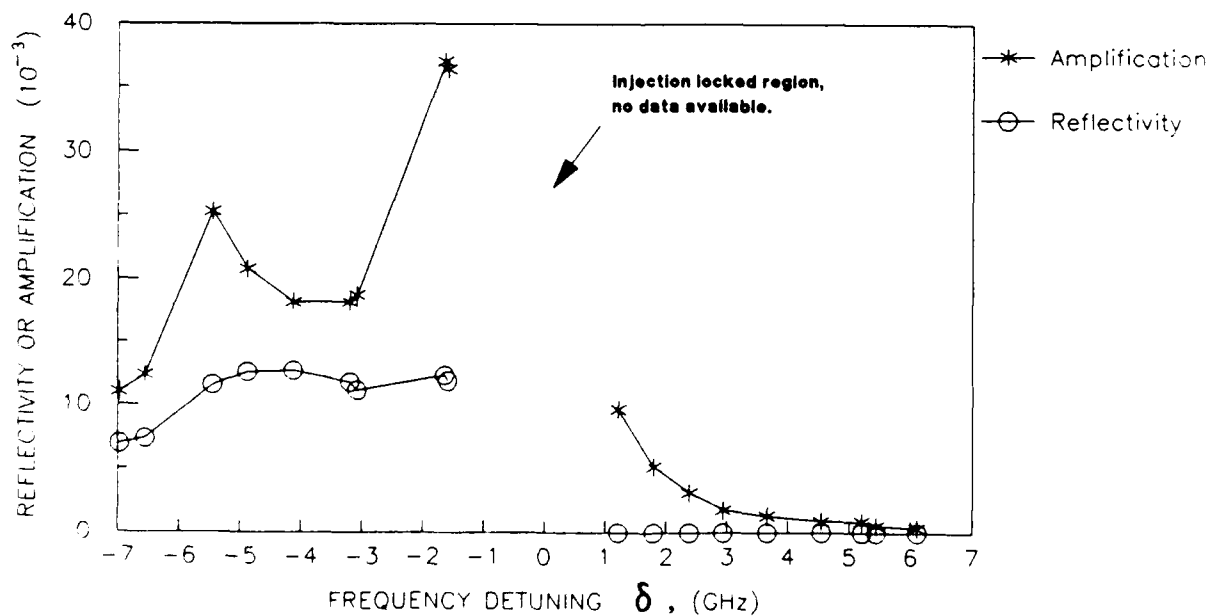


Figure 3-5. Same as Figure 3-4, except for an incident probe power of 1.4 mW.

Figure 3-5, the asymmetry of the probe amplification with δ is even more pronounced. Also, in Figure 3-5 the conjugate reflectivity displays an interesting asymmetry; no detectable conjugate is observed for $\delta > 0$ detunings. These asymmetries in the frequency-dependent FWM data are not completely understood, however, they may be related to a similar effect in below-threshold diode FWM which has been predicted theoretically (Reference 3.6) and observed experimentally (Reference 3.3). In those studies, the conjugate is symmetric with respect to detuning, but the probe signals are asymmetric with larger magnitudes for negative detunings, similar to the results presented in Figure 3-4. The results of References 3.6 and 3.3 were interpreted as due to an asymmetry in the gain lineshape for the probe beam which occurs independently of the FWM interaction. The corresponding gain lineshape is symmetric for the conjugate signal. Although these results are strictly valid only for FWM in diodes below threshold, a similar asymmetry in the amplifier gain is anticipated for operation of the FWM cavity above threshold. This can explain the results of Figure 3-4. An explanation for the asymmetry of the conjugate signal observed in Figure 3-5 is presently lacking. The FWM evolution equations for the case where the diode laser is operated above threshold have not yet been investigated.

Another interesting feature of the probe detuning experiments can be seen in Figure 3-4. A secondary maximum is observed for both the conjugate and the probe signals at a detuning of $\delta = \pm 5.8$ GHz. This secondary peak is observed in all of the nondegenerate FWM data. The probe detuning δ at which the peak occurs, denoted by $\delta = \Delta$, is observed to shift to larger detunings as the diode pump power is increased. This effect can be seen clearly in Figure 3-6, which shows a plot of Δ^2 versus the LD2 pump power. The plot shows a linear dependence of Δ^2 on pump power. This effect may be understood qualitatively by considering the behavior of a two-level atom in a strong field of frequency ν tuned near resonance, ν_0 . The population will undergo strong oscillation between the two levels at a frequency given by the generalized Rabi frequency, $\nu_{GR} = [(\nu - \nu_0)^2 + (\nu_R)^2]^{1/2}$, where $\nu_R = \mu E / \hbar$, μ is the transition dipole moment and E the field strength of the incident optical field. This effect can be viewed as a splitting of each level into two levels separated by an energy $\hbar \nu_{GR}$, and is known as the ac Stark shift. As shown in Figure 3-7, three transition frequencies are expected, with

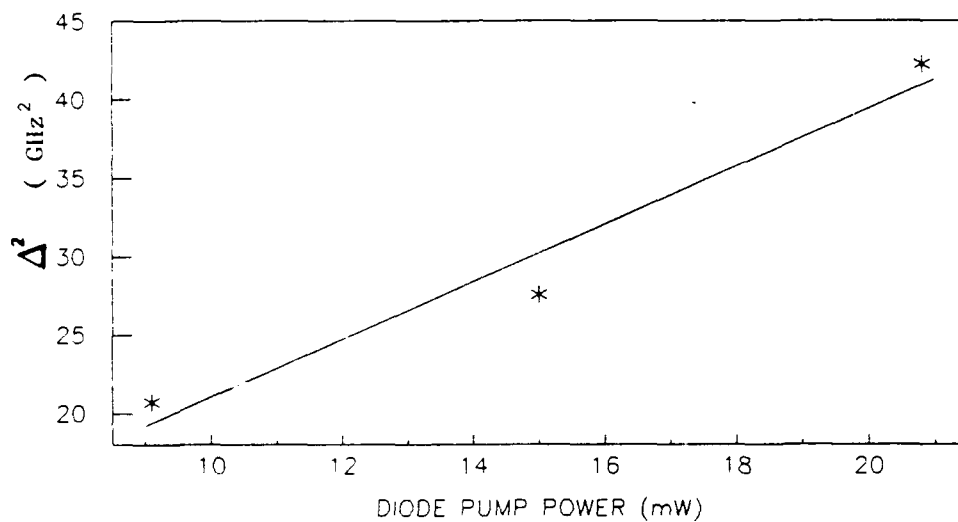


Figure 3-6. Plot of the square of the frequency detuning at which the maximum signal occurs, Δ^2 , versus the lasing output of the FWM diode. The linear relationship displayed in this plot indicates that the ac Stark effect causes a splitting of the lasing transition, resulting in resonantly enhanced signal contributions at $\delta=0, \pm\Delta$. In the text it is shown that $\Delta=\nu_R$, the Rabi frequency.

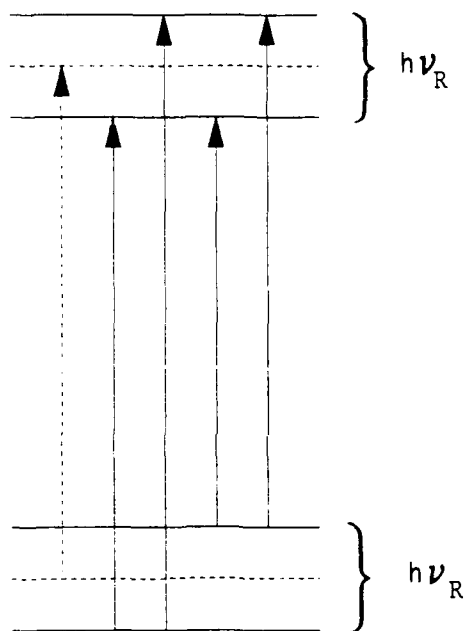


Figure 3-7. The strong intracavity laser field splits the two-level diode lasing transition (dotted lines) into a series of four resonances through the ac Stark effect (solid lines). Three resonant conditions are now possible: $\delta = 0, \pm \nu_R$ where ν_R is the Rabi frequency.

resonances at ν_0 and $\nu_0 \pm \nu_R$. We can use this simple analysis in the diode system studied here, by making the following identifications: ν_0 is the diode cavity resonance, $\nu (= \nu_0)$ is the diode pump frequency as defined above, and $I = (\epsilon_0 c / 2) E^2$ is the intracavity diode pump intensity. Thus, we expect the resonant media inside the diode laser cavity to split into three resonances (as in Figure 3-7) by the ac Stark shift, with a splittings given by $\Delta = 0, \pm \nu_R$. In the case of FWM, resonant enhancement of the gain will occur at these side band resonances. Furthermore, since $\nu_R \propto I^{1/2}$, it is expected that the position of the resonantly enhanced FWM peak moves as $\Delta^2 \propto I$ as observed in Figure 3-6.

In the probe detuning experiments discussed above, the minimum probe detuning is limited by injection locking of the LD2 diode pumps to the probe frequency (References 3.1 and 3.7). While injection locking does not interfere intrinsically with the FWM process, it is undesirable because the conjugate becomes degenerate with the strong pump fields and cannot be separated for practical use. The detuning at which injection locking occurs depends upon the power incident in the probe beam. The smaller the incident probe power, the smaller the value of δ at which injection locking occurs. In Figure 3-4, injection locking occurs at $\delta \sim 1$ GHz. It can be seen from the figure that both the probe amplification and the reflectivity increase monotonically as the probe is tuned closer to the pump frequency, ν . Thus, for given pump and probe powers, the FWM reflectivity is limited by the minimum detuning allowed before injection locking of the FWM diode occurs.

The incident probe power will also have an effect on the measured amplification/reflectivity in the pump depletion regime. With large injected probe powers and high reflectivity (and high probe amplification), a substantial fraction of pump photons will be converted into the amplified probe and conjugate beams. The effective pump intensity will be reduced, resulting in a corresponding decrease in the reflectivity (amplification). Thus, the maximum reflectivity (amplification) should occur at low probe powers where a minimum probe detuning, as well as the absence of pump depletion effects are possible. Figure 3-8 is a plot of the maximum reflectivity (amplification) obtained at minimum probe detuning, versus incident probe power. Contrary to the analysis just presented, the reflectivity (amplification) is observed initially to increase in magnitude with probe power but then to begin decreasing as

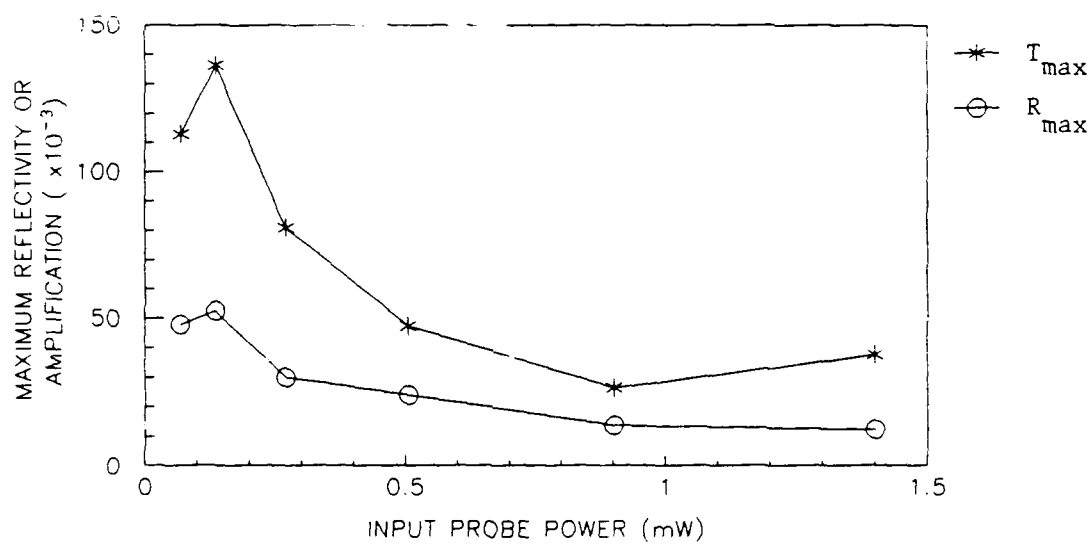


Figure 3-8. Plot of the maximum reflectivity (\circ) and probe amplification ($*$) obtained at the minimum detuning (determined by the point of injection locking), versus incident probe power.

expected. A similar dependence on probe power is seen when the reflectivity (amplification) is plotted at other, constant probe detunings. This can be seen in Figure 3-9, where R and A are plotted for $\delta = -4, -5$ and -6 GHz. These plots have qualitatively the same shape as that of Figure 3-8. This initial increase in reflectivity (amplification) is not presently understood. However, the decrease at higher incident probe powers is almost certainly due to pump depletion. Under these conditions, the amplitude of the pump beam, which is monitored simultaneously with the FWM as in Figure 3-4, is observed to decrease substantially.

3.3 Intracavity FWM in Single Mode Diode Lasers: Piston Error Correction

FWM in the inverted lasing medium of single mode diode lasers, previously demonstrated in Section 3.2 and Reference 3.1, has several advantages over FWM in non inverted materials. Most notably, TRW has recently obtained FWM reflectivities greater than 10^4 (Section 3.2). However, in these previously reported diode FWM experiments, only the amplitude and probe frequency detuning properties of the FWM process have been characterized. Single mode diode lasers are inherently one dimensional (1D) waveguides, so transverse or spatial phase information is destroyed. The 1D waveguide nature of single mode diode lasers and the consequent spatial filtering of injected light beams (e.g., the probe beam), makes it impossible to demonstrate aberration correction via FWM in the usual manner, i.e., by image correction. The spatial frequencies which make up an image do not survive the injection process into the diode waveguide.

In the experiment described here, an important capability of phase conjugation that can be accomplished by intracavity NDFWM is directly verified for the first time by demonstrating the correction of piston error in the conjugate beam when an optical path length difference (OPD) is introduced into the probe beam. For further information on the basic properties of NDFWM in diode lasers see Section 3.2.

3.3.1 Piston Correction Experimental Setup

Figure 3-10 shows the experimental setup for demonstrating phase conjugation of piston error using diode laser intracavity FWM. In order

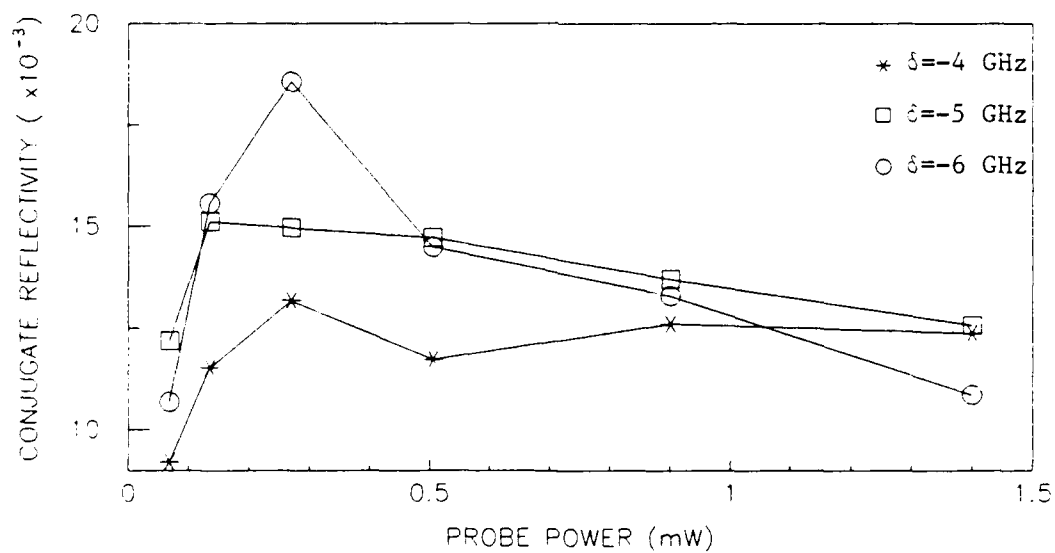
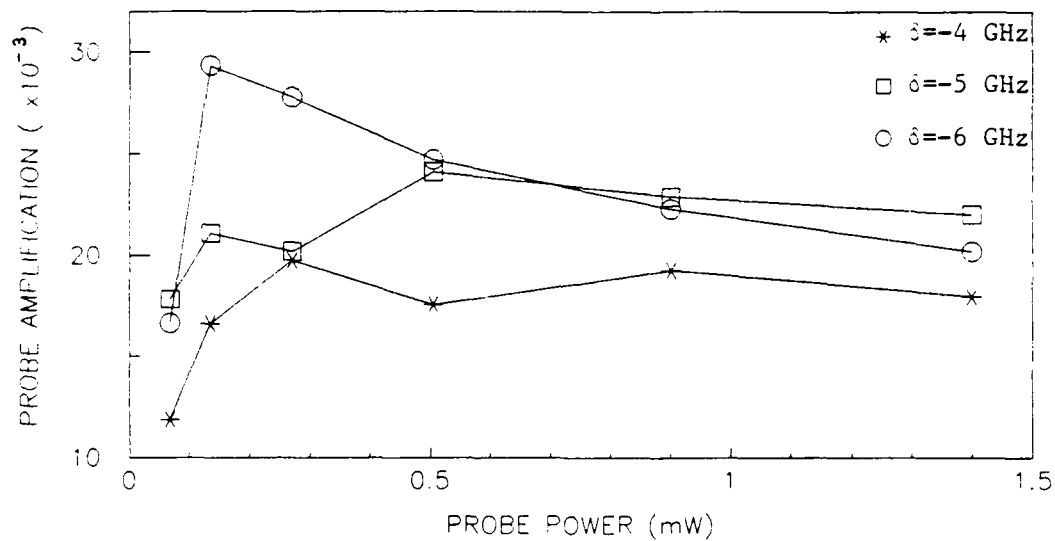


Figure 3-9. Plot of conjugate reflectivity and probe amplification as a function of input probe power for three different detunings: $\delta = -4, -5, -6$ GHz.

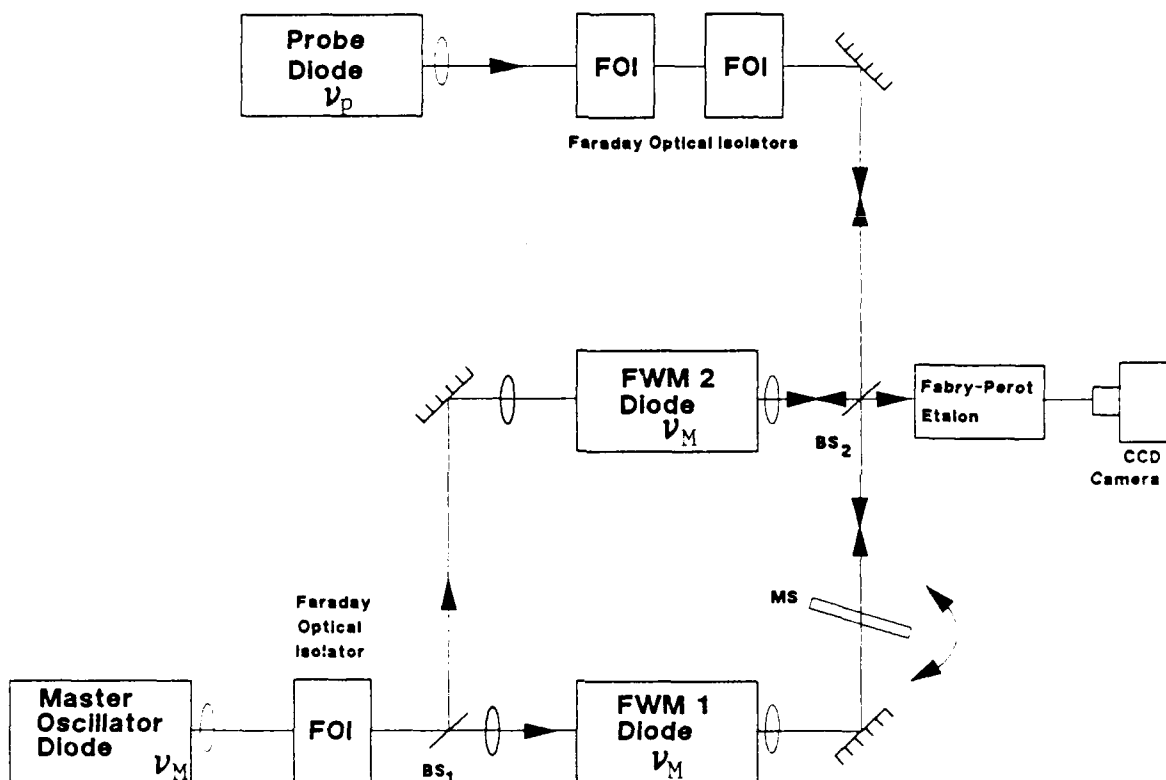


Figure 3-10. Experimental setup for demonstrating phase conjugation of piston error using diode laser intracavity NDFWM.

to observe the correction of piston error on the conjugate beam by using an interferometric technique, it is necessary to have a phase-locked reference wave at the conjugate frequency. This is accomplished as follows. Four identical single mode laser diodes (Hitachi HLP1400) are temperature stabilized to -0.02°C and operated CW with stabilized current supplies ($\sim 10\text{ }\mu\text{A}$ stability). With a proper choice of operating temperatures and currents, all four single mode diodes lase at exactly the same wavelength (near 831 nm). The coherence length of these diodes, previously measured to be $\sim 15\text{ m}$ (Reference 3.7), is so long that no special care in the matching of optical pathlengths is necessary. One of the diodes is operated as a master oscillator (frequency ν_M) to simultaneously injection lock two of the other diodes (FWM1 and FWM2) at the same frequency (Figure 3-10). In order to accomplish injection locking, it is necessary to inject only a few μW (Reference 3.8). Therefore, to reduce some of the stringent alignment requirements in this experiment, the master oscillator diode output is flooded onto the rear facets of FWM1 and FWM2 by focusing weakly with 8 cm focal length lenses.

In contrast, the input probe beam is focused with near diffraction limited quality onto the front facets of FWM1 and FWM2. This is necessary because of geometric constraints which require that the probe beam be focused with the same lenses that collimate the outputs of FWM1 and FWM2. Furthermore, efficient collimation of FWM1 and FWM2 is required to obtain enough conjugate signal power out of these diodes after filtering to detect the interference pattern on a CCD camera. Thus, the outputs of FWM1 and FWM2 are efficiently ($> 90\%$) collimated using 0.5 numerical aperture, 8 mm focal length diffraction limited lenses specifically designed for collimating diode lasers. Initially the master oscillator diode was not optically isolated from the other diodes because it was felt that the low efficiency of the 8 cm lenses would provide sufficient isolation. However, feedback effects did occur, and the injection locking was found to be much more stable after the addition of a Faraday optical isolator (FOI) into the master oscillator beam path. Isolation is greater than 1000:1.

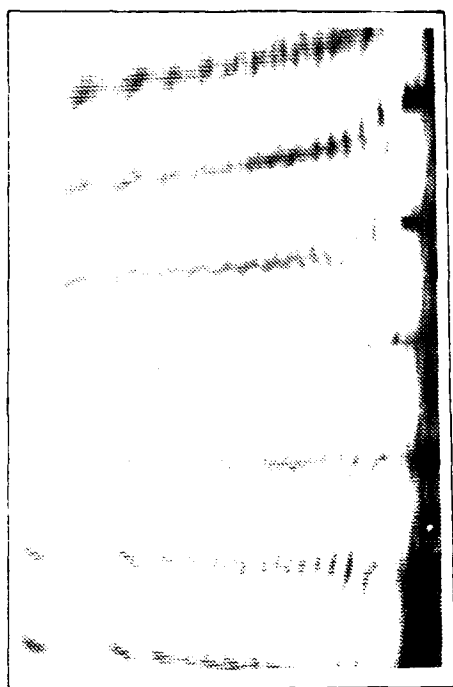
The simultaneous injection locking of FWM1 and FWM2 is verified in a Mach-Zehnder type interferometer where a high contrast, stationary interference pattern is observed between the outputs of FWM1 and FWM2. In order to obtain this pattern, it is necessary to misalign the two beams

from perfect colinearly. The two beams are slightly tilted from one another in the vertical direction, thus generating the series of horizontal light-dark fringes shown in Figure 3-11A. When the two diodes are fully injection locked, a very clear and stable fringe pattern is obtained (Figure 3-11A). This fringe pattern disappears completely when the master oscillator is blocked (Figure 3-11B), indicating that the free running modes of FWM1 and FWM2 are not phase coherent. In the intermediate regime, the pattern is observed to fluctuate if either FWM1 or FWM2 is incompletely injection locked. Thus, this interference pattern serves as a very sensitive indicator of the simultaneous injection locking of the two laser diodes to a common (ν_M) FWM pump frequency.

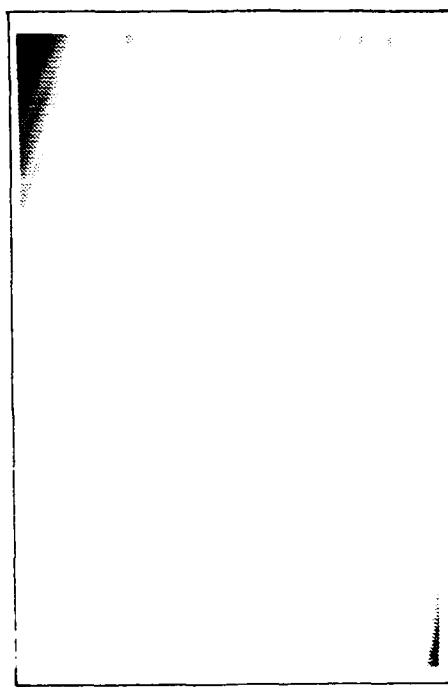
The FWM probe beam is incorporated into the setup by directing the output of the probe diode through the backside of the beamsplitter which forms part of the Mach-Zehnder interferometer (BS_2 in Figure 3-10). The probe beam is split and imaged onto the facets of FWM1 and FWM2 as described above. Since the injected probe beam is anti colinear to the outputs of FWM1 and FWM2, their output beams are both automatically imaged onto the probe diode facet. To prevent optical feedback from these beams into the probe source, two Faraday optical isolators are inserted serially into the probe beam. This provides isolation of greater than $10^6:1$. After combining the FWM1 and FWM2 outputs with a beamsplitter (BS_2 in Figure 3-10), the probe and conjugate signals are isolated with a high finesse planar Fabry-Perot etalon and directed into a CCD camera. This is necessary because the outputs of FWM1 and FWM2 contain the pump light at the master oscillator frequency and the probe light, in addition to the conjugate signal. By piezo-electrically tuning the etalon mirror separation, interference patterns at any of the three frequencies can be observed. A 6 GHz detuning, δ , of the probe diode laser, frequency ν_p , to the red of frequency ν_M allowed excellent resolution and separation of the conjugate and probe beams from the much more intense pump beams.

3.3.2 Piston Error Correction Results

NDFWM with the experimental setup described above can be seen in Figure 3-12. This figure is a photograph of an oscilloscope trace displaying the output of a scanning Fabry-Perot etalon. The central large peak is due to the pump beam (ν_M) and the two smaller peaks equidistant

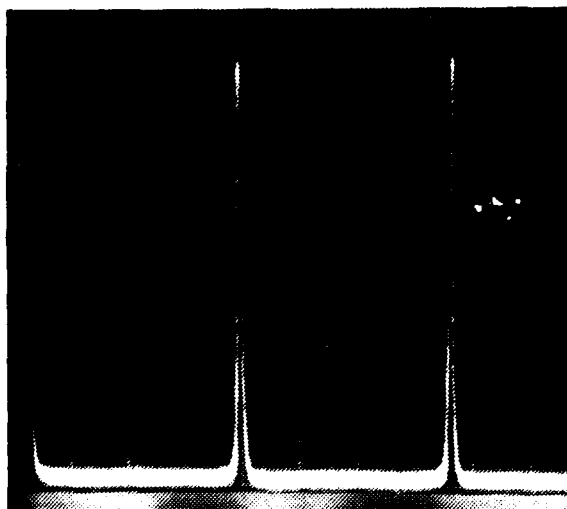


A

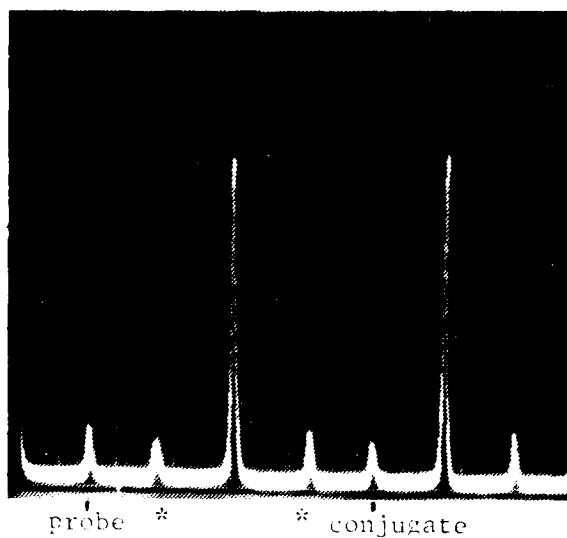


B

Figure 3-11. Interference patterns of the outputs of FWM1 and FWM2. In A, the clear, stationary fringes indicate complete injection locking of FWM1 and FWM2 to the master oscillator. In B, the master oscillator has been blocked, allowing FWM1 and FWM2 to oscillate freely. The interference pattern disappears, washed out because of a frequency mismatch between FWM1 and FWM2.



A



B

* = peaks from
other etalon modes

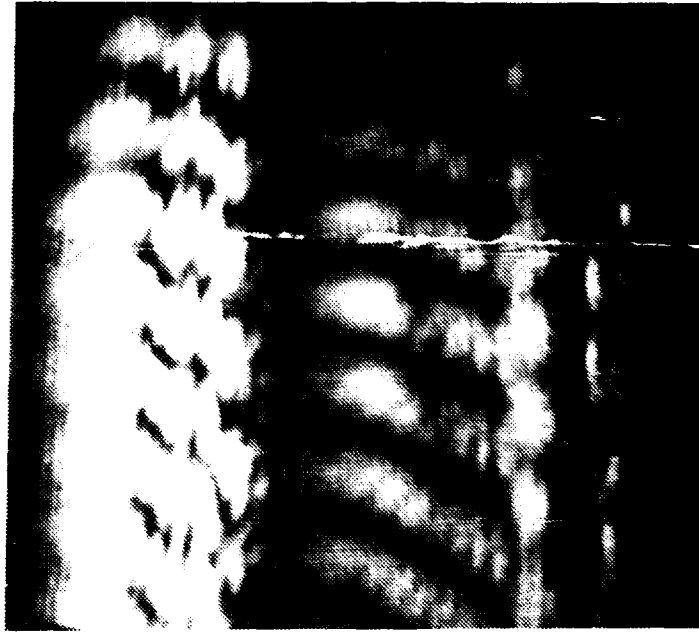
Figure 3-12. Photograph of an oscilloscope trace displaying the output of the 8 GHz free spectral range etalon. In A, the input probe beam is blocked so that only the pump frequency is observed. The two peaks correspond to two adjacent transmission modes of the etalon. Large NDFWM signals are observed when the probe input is unblocked (B). The probe detuning is 5.5 GHz and the peaks are as labeled in the figure.

on each side of the pump are the probe (ν_p , left) and conjugate ($\nu_c = 2\nu_M - \nu_p$, right). The probe detuning is approximately 5.5 GHz. The FWM reflectivity in Hitachi HLP1400 laser diodes was similar to that reported in Section 3.2. It can also be seen from Figure 3-12 that the probe and conjugate signal beams are a significant fraction of the pump beam amplitude, ~15% and 12% respectively, indicating that substantial pump depletion is occurring. A comparison of the pump amplitude seen in the figure to the amplitude of the pump beam with the probe beam blocked, indicates that the pump beams are depleted by ~23%.

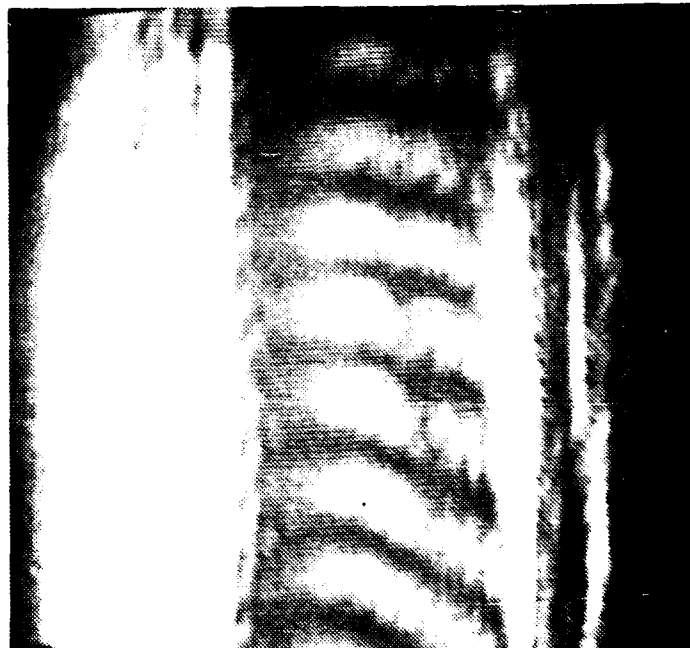
The results of piston error correction can be seen in the series of interference patterns shown in Figure 3-13. Due to significant wavefront curvature of the diode beams in the horizontal direction, only a narrow horizontal portion of each beam is transmitted through the plane-parallel etalon, i.e., the etalon acts as a wavefront filter. This results in the interference patterns of Figure 3-13 which have a vertical slit-like appearance. At certain etalon cavity lengths it is possible to simultaneously view spatially distinct interference patterns from more than one of the three incident frequencies at a time. This simultaneous transmission of different vertical slit sections from each beam is possible as there is a tradeoff between laser frequency and the incidence angle of the various light rays in the wavefront in meeting the etalon cavity condition.

Figure 3-13A shows the interference patterns at the pump frequency ν_M (left) and conjugate frequency (ν_c , right). The pump interference pattern is not quite as clear as that of the conjugate because the pump beam is much more intense and saturation of the CCD camera occurs under the conditions used here to optimize simultaneous viewing of both beams. A somewhat distorted probe beam fringe pattern is also visible just to the right of the conjugate pattern. These interference patterns are very stable and jitter free, as long as FWM1 and FWM2 are well injection locked.

Changing phase (OPD), introduced by tilting a microscope slide in one leg of the Mach-Zehnder interferometer, results in a spatial shifting of the interference fringe pattern. However, if changing phase on the incoming probe is conjugated during FWM, the variable phase is exactly corrected when the conjugate return passes back through the slide, i.e., there is no variation of piston where the interference pattern is



A



B

Figure 3-13. Interference patterns generated between the outputs of FWM1 and FWM2. The pump beam interference is on the left, the conjugate in the center, and the probe pattern can be dimly seen on the right. In A, all optical paths are stationary, so all beams form stationary fringes. In B, a glass slide modulates the optical path difference between FWM1 and FWM2. Only the conjugate fringes remain stationary.

written. This is not true for the pumps (single pass through slide) or the probe beam, where the double pass doubles the OPD piston added by the glass slide. As a result, only the interference pattern written by the two conjugate beams should be stationary when the slide is rotated in front of one of the FWM diodes. Figure 3-13B shows fringes when a tilting microscope slide has been inserted into the path of the light emerging from FWM1. It can be seen that the interference pattern due to the pump beams is completely obliterated, whereas that of the conjugate beams is not affected. Identical results are obtained when the slide is inserted into the beam path of FWM2.

The microscope slide is modulated by hand at several different rates. In all cases, the conjugate interference pattern is not affected whereas that of the pump beam jumps tremendously and at high modulation rates is observed to disappear completely. When the microscope slide is tilted slowly, the pump fringes do not disappear but instead are observed to sweep up and down across the TV monitor. The obliteration of the pump interference pattern occurs at high modulation rates because the dark lines are averaged out as a result of the (slow) response time of the CCD camera. A close inspection of Figure 3-13 shows that the amplified probe beam interference pattern also is obliterated as expected when the OPD is modulated with the microscope slide. The latter effect is very clearly seen when the Fabry-Perot is tuned to maximize the probe beam transmission. This experiment has been recorded on video tape, where the various effects of the tilting microscope slide are easily seen. The results presented above show that the OPD phase shift of the microscope slide is completely corrected in the intracavity NDFWM optical phase conjugation process occurring in single mode diode lasers.

3.4 CW DFWM in Bulk GaAs and MQW GaAs

3.4.1 Spectroscopy of GaAs and AlGaAs MQW Materials

In this section, the background information necessary to understand the relevant band gap physics of the bulk GaAs and GaAs/AlGaAs MQW semiconductor samples will be briefly reviewed. First, a simple free electron model will be used to explain many of the bulk GaAs spectral

features. The relevant equations for this system are as follows (Reference 3.9):

$$E_{c,v}(k) = \hbar^2 k^2 / 2m_{c,v}^* \quad \text{band energy} \quad (3-2)$$

$$D(E) = (V/2\pi^2 a^3 R_y) \cdot [(E-E_G)/R_y]^{1/2} \quad \text{density of states} \quad (3-3)$$

$$A(E) = C \cdot |p_{cv}|^2 \cdot [(E-E_G)/R_y]^{1/2} \quad \text{absorption coeff.} \quad (3-4)$$

where c and v refer to the conduction and valence bands, respectively, k is the free electron wave vector, $m_{c,v}^*$ the electron effective mass for the energy band indicated by the subscript, V is the crystal volume, $a = \epsilon \hbar^2 / \mu e^2$ is the exciton Bohr radius discussed later, $R_y = e^4 \mu / 2 \epsilon^2 \hbar^2$ is analogous to the Rydberg energy for a hydrogen atom, μ is the effective reduced mass, E and E_G are respectively the photon energy and the band gap energy (E must be $> E_G$), C is a constant, and $|p_{cv}|^2$, the square of the momentum matrix element between the valence and conduction bands, describes the band to band transition probability. Plots of the (parabolic) dispersion curve ($E_{c,v}$ versus k), the density of states, $D(E)$, and the absorption coefficient, $A(E)$, for the free electron model are shown in Figure 3-14. Note that this simple model predicts an absorption spectrum proportional to the square root of the difference in energy between the incident photon and the band gap (Equation 3-4). Since the observed absorption spectrum for bulk GaAs does not have this simple spectral dependence, the simple free electron model alone is not capable of describing the system.

When a photon of light is absorbed and an electron is promoted to the conduction band, a positively charged hole (h) is left behind in the valence band. The Coulomb interaction between the excited electron and hole modifies the band gap absorption spectrum. Below the band gap ($E < E_g$) bound exciton states exist. These are discrete energy states with hydrogen-like wave function solutions. In contrast to the hydrogen atom this interaction is weak: the exciton binding energy ($-R_y$) of $\sim 4 \times 10^{-3}$ eV is small compared to 13.6 eV for hydrogen and the exciton Bohr radius, a , of ~ 15 nm is very large compared to .053 nm for hydrogen. For energies greater than the band gap, the Coulomb interaction gives rise to states that are analogous to the continuum states of the hydrogen atom. These

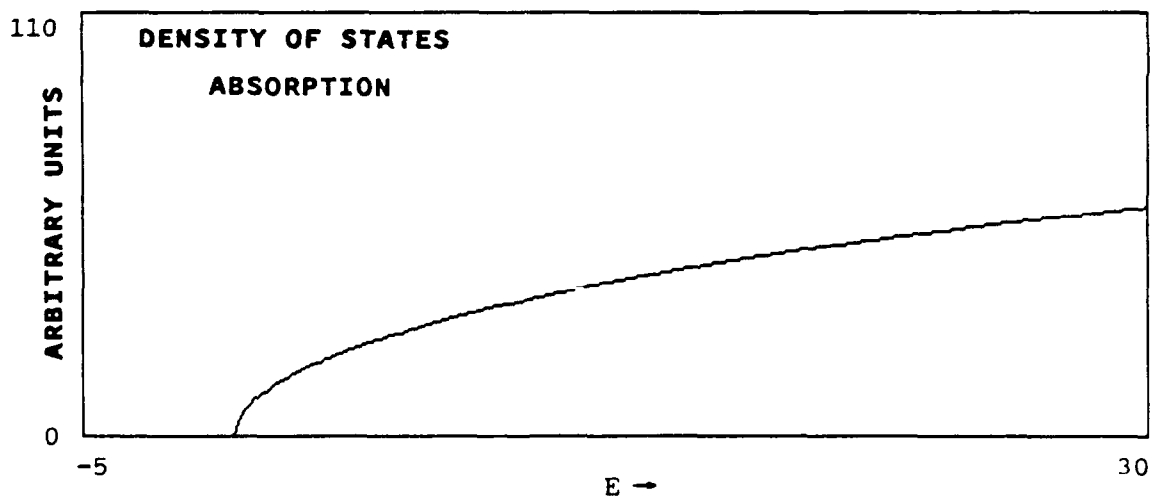
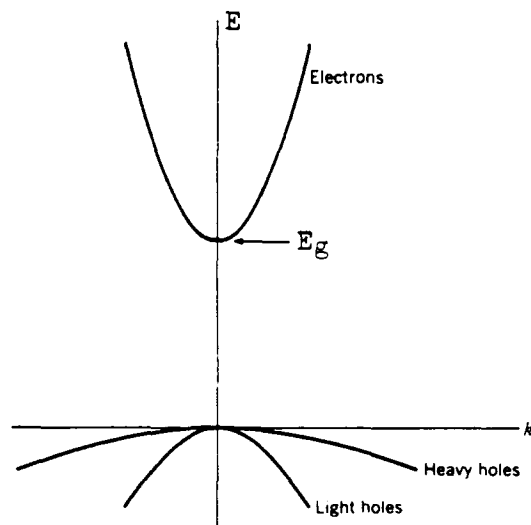


Figure 3-14. Plots of the energy dispersion characteristic (E vs. k), the density of states (D), and the absorption coefficient (A) using a free electron model of a semiconductor.

states result in a broad absorption that enhances that due to free electron band to band transitions.

Despite the relatively weak Coulomb interactions between electrons and holes in semiconductors compared to that of the hydrogen atom, large effects on the physics and spectroscopy in the band edge region are seen. The relevant equations are as follows (References 3.10 and 3.11):

$$E_l = -R_y/l^2; \quad l \geq 1 \quad \text{exciton energy} \quad (3-5)$$

$$f_l = (2|p_{cv}|^2/\pi m_0 a^3 h\nu) \cdot l^{-3} \quad \text{exciton oscillator strength} \quad (3-6)$$

$$K = (B|p_{cv}|^2/\nu) \cdot [(E-E_g)/R_y]^{1/2} \cdot (\pi\alpha \exp(\pi\alpha)/\sinh(\pi\alpha)) \quad (3-7)$$

where K is the absorption coefficient above the band edge, l is an integer quantum number, m_0 is the free electron mass, ν is the photon frequency, B is a constant and $\alpha = (R_y/E)^{1/2}$. From Equation 3-5 it can be seen that the exciton ground state binding energy ($l=1$) is equal to $-R_y$. For bulk GaAs, R_y has been measured to be $\sim 4.2 \times 10^{-3}$ eV (Reference 3.12). Equations 3-5 and 3-6 show that the excited exciton levels ($l > 1$) are much less important since the binding energy decreases as l^{-2} and the oscillator strength decreases as l^{-3} for these levels. These excited exciton levels are difficult to observe and have never been observed at room temperature.

The absorption coefficient, K , includes the effects of the Coulomb enhancement on the conduction band continuum of states. These effects, as well as the effects of the discrete exciton levels on the absorption coefficient, can be seen in Figure 3-15. An absorption spectrum much different than the simple parabolic dependence of Equation 3-4 is predicted. Note the large increase in absorption just above the band edge, and also the excitonic resonances which carry a substantial oscillator strength in a narrow region of frequency space. The spectrum shown in the figure is still somewhat artificial and incomplete. An infinitely sharp absorption band edge, as depicted in the figure, is never observed. Inhomogeneities such as impurities and strains result in microscopic fluctuations in the crystalline local electric fields. These fluctuations result in a distribution of slightly different band gap

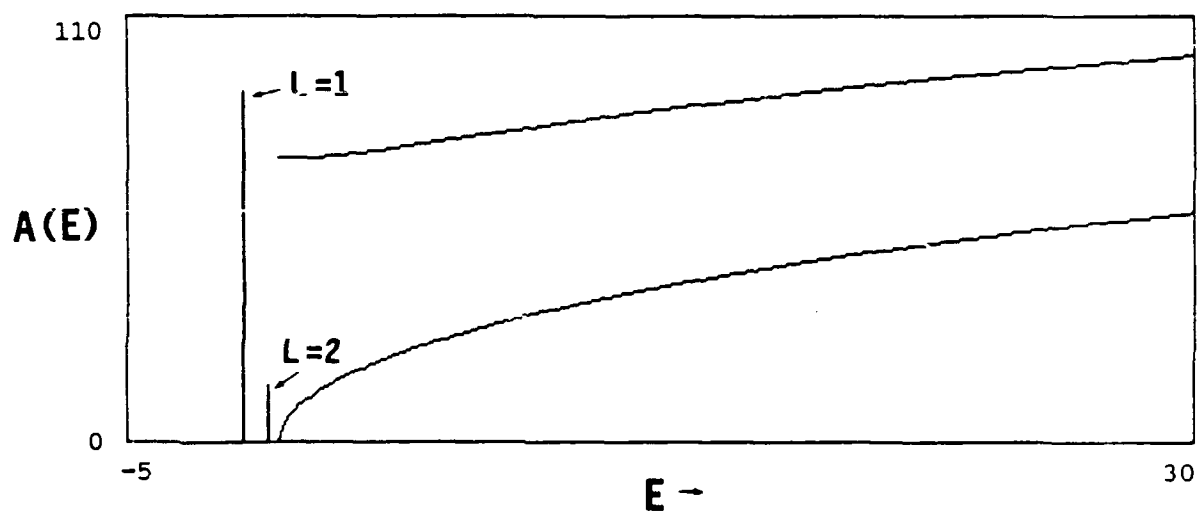


Figure 3-15. Same as Figure 3-14, but the effects of the electron-hole Coulomb interaction have been included.

energies in the sample and an exponential absorption tail (Urbach tail) is observed in the band gap wavelength region (Reference 3.13). Furthermore, line broadening of the (narrow) exciton resonances result from phonon scattering processes, particularly at room temperature. When all of the effects which have been discussed above are included in the analysis, a satisfactory explanation for the bulk GaAs absorption spectrum is obtained. Figure 3-16 shows both a schematic absorption spectrum depicting the individual contributions to the absorption, as well as an experimental spectrum (Reference 3.15) which clearly shows the excitonic absorption feature. At room temperature, large amounts of inhomogeneities and screening of the exciton interaction by impurity ions can blur the resolution of the exciton absorption feature. This will be discussed in more detail later.

The band gap physics relevant to the GaAs/AlGaAs MQW samples will now be discussed. The MQW growth structure is shown in Figure 3-17A. Thin (~10 nm) alternating layers of $\text{Al}_x\text{Ga}_{1-x}\text{As}$ and GaAs are grown epitaxially and capped on each end with thick (~1 μm) $\text{Al}_x\text{Ga}_{1-x}\text{As}$ layers. Typically ~70 alternating periods are grown. Figures 3-17B and 3-17C show that since the band gap of the AlGaAs layers is much greater than that of the GaAs layers, a periodic potential well structure is formed in the MQW sample. Provided that the AlGaAs layers are thick enough to prevent the interaction between neighboring GaAs wells (~10 nm), the result of this potential well structure is to confine the conduction band electrons and valence band holes within the GaAs layers in which they are generated. This confinement effect can cause a substantial reduction in the average e-h distance compared to the bulk GaAs material. The smaller e-h distance results in a larger Coulomb interaction energy and, consequently, a larger exciton binding energy in the MQW ($R_y \propto a^{-2}$). In bulk GaAs, the average distance between the electron and hole comprising the exciton, the exciton Bohr radius, a , is ~15 nm. Thus, more tightly bound excitons are expected in MQW samples when the GaAs well thickness is less than ~15 nm. Excitons in MQW samples will be discussed in more detail shortly. First, another effect of particle confinement in the GaAs layers needs to be addressed.

When the GaAs layers in MQW samples are made sufficiently thin to obtain excitonic enhancement (~10 nm), quantum size effects become important in the growth direction (z in Figure 3-17) and produce large

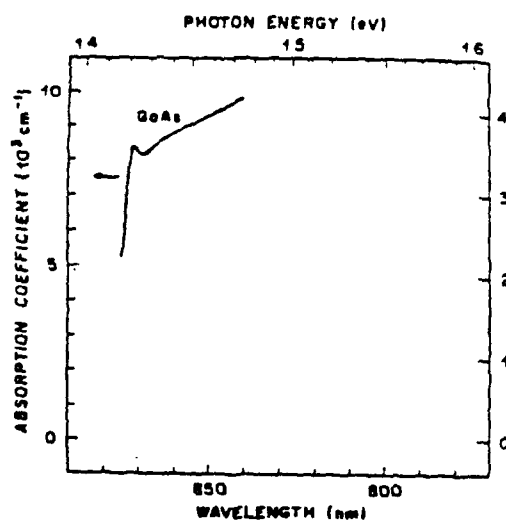
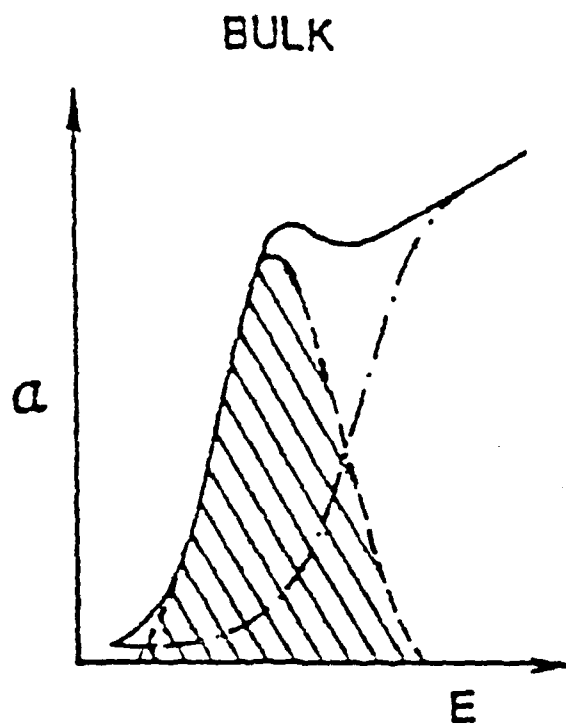
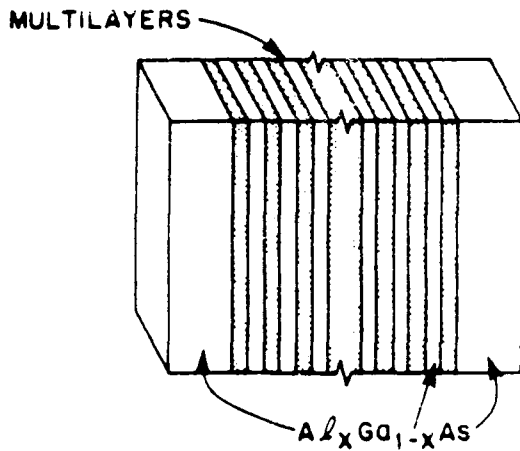
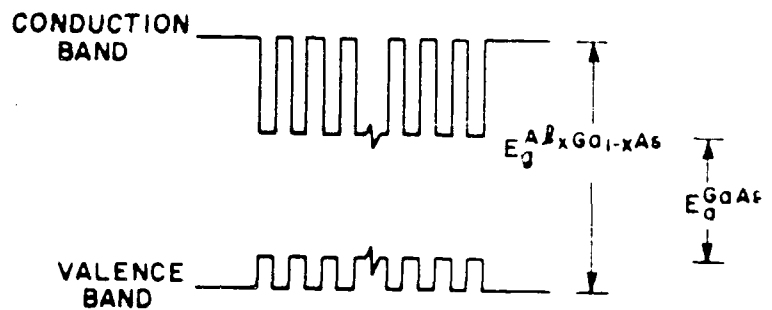


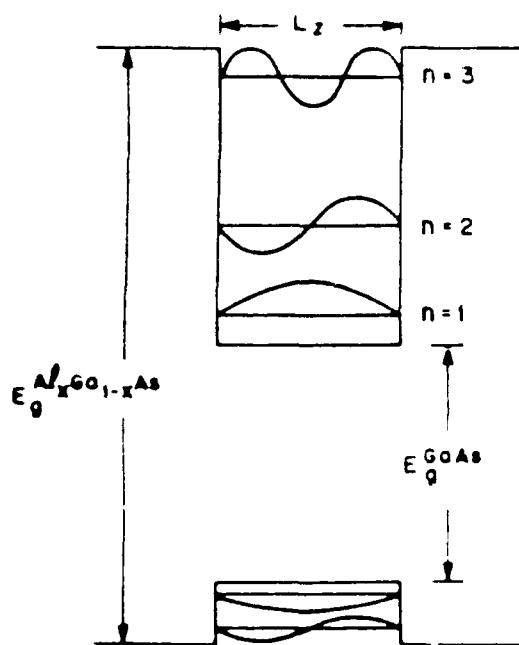
Figure 3-16. Schematic (top) and experimental (bottom) absorption spectra near the band edge of room temperature bulk GaAs.



A



B



C

Figure 3-17. Diagrams relevant to GaAs/AlGaAs multiple quantum well sample (MQW). Part A shows the growth structure, Part B shows the periodicity of the conduction band and valence band potential wells, and Part C shows the particle-in-a-box solutions for the system.

changes in the band gap physics. Temporarily ignoring the effects of the e-h Coulomb interaction, simple particle-in-a-box theory can be used to describe the electrons and holes in the z direction and the free electron theory can be used to describe their behavior in the x and y directions. The result of particle confinement in the z direction is to quantize the energy in this direction. The equations describing the solution of this model are as follows (Reference 3.15):

$$E_{c,v}(k) = (\hbar^2/2m_{c,v}^*) \cdot (k_x^2 + k_y^2) + E_{n_c, n_v} \quad \text{band energy} \quad (3-8)$$

$$E_{n_c, n_v} = (\hbar^2/2m_{c,v}^*) \cdot (n_c, n_v \cdot \pi/L_z)^2; \quad n_c, n_v \geq 1 \quad \text{z-energy} \quad (3-9)$$

$$D(E) = (S/2\pi a^2 R_y) \cdot \theta[E - (E_g + E_c + E_v)] \quad \text{density of states} \quad (3-10)$$

$$A(E) = C \cdot |p_{cv}|^2 \cdot D(E); \quad \Delta n = n_c - n_v = 0 \quad \text{absorption coeff.} \quad (3-11)$$

where L_z is the GaAs layer thickness, n_c and n_v are integer quantum numbers for conduction and valence bands in the z direction, S is the area of the MQW layers, and θ is the Heaviside step function. Figure 3-17C shows schematically the particle in a box energy levels and wave functions for both the valence and conduction bands. Note that since the effective mass for the holes is negative, the potential well appears inverted for the valence band. As a result of the parity of the particle-in-a-box wave functions, only transitions with $n_c = n_v$ are allowed. Thus, quantization in the z direction results in a series of transitions between the bound discrete levels of the conduction and valence band potential wells. At the low energy edge of each of these transitions k_x and k_y equal zero, i.e., this corresponds to the band edge for the x and y directions. Thus, a series of band edges will be observed for the absorption coefficient and the density of states. These step-like functions are shown in Figure 3-18. For purposes of comparison, the dotted line in the figure indicates the corresponding function for the parabolic band of the bulk semiconductor material (neglecting Coulomb effects).

As in the case of bulk GaAs, Coulomb interactions modify the MQW band gap physics. For the MQW there are two important differences. First of all, there are several band edge transitions so excitonic effects will be

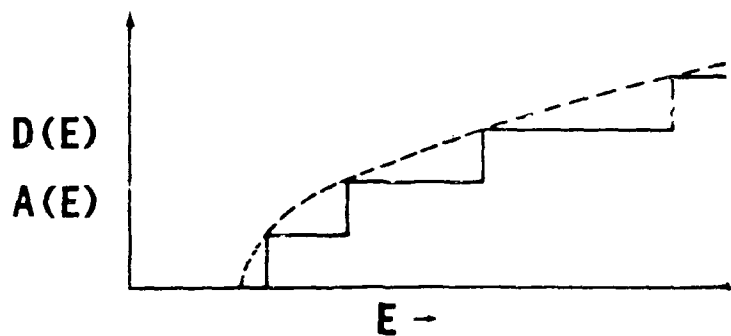
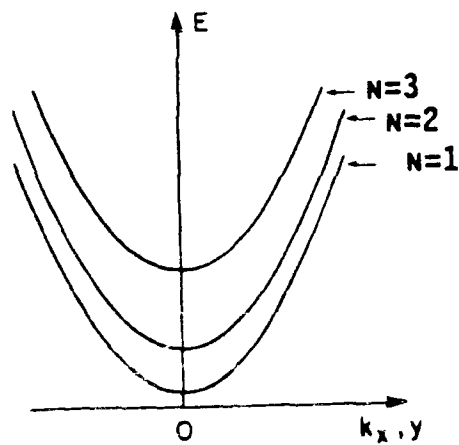


Figure 3-18. Plots of the energy dispersion characteristic (E vs. k), the density of states (D), and the absorption coefficient (A) using a free electron model and a particle-in-a-box model for MQW s.

evident at each of them. This effect can be seen in Figure 3-19, which shows a schematic drawing of the quantization and exciton effects in MQW's, as well as an experimental absorption spectrum from Reference 3.16. As mentioned above, the other difference between the MQW and bulk material results from the decrease in the average e-h distance due to particle confinement in the GaAs layers. The effects of this can be seen from the following two equations (Reference 3.11):

$$E_{\ell} = -R_y/(\ell+1/2)^2; \ell \geq 0 \quad \text{MQW exciton energy (3-12)}$$

$$f_{\ell} = (2|p_{cv}|^2/\pi m_0 a^2 \hbar \nu)/(\ell+1/2)^3; \ell \geq 0 \quad \text{oscillator strength (3-13)}$$

where ℓ , the exciton quantum number, can be zero or a positive integer. The differences between Equations 3-12 and 3-13 for MQW's and Equations 3-5 and 3-6 for bulk GaAs, are due to the fact that a 2-D hydrogen model is used to describe the e-h motion in MQWs, and a 3-D model is used for bulk GaAs. This difference in boundary conditions results in the different functional forms for the exciton energies and oscillator strengths, as well as the different range for the quantum number, ℓ . From Equation 3-12 it is seen that the MQW exciton binding energy ($\ell = 0$) equals $-4R_y$, i.e., four times greater than that for the bulk material. Furthermore, a comparison of Equations 3-13 and 3-6 shows that the oscillator strength of the ground state exciton in the MQW is eight times greater than that of the bulk exciton. This increased excitonic oscillator strength in the MQW is easily seen experimentally. A comparison of the bulk GaAs absorption spectrum (Figure 3-16) and the MQW spectrum of Figure 3-19 clearly shows the increase prominence of the exciton in the absorption spectrum. The ratio of the excitonic absorption to the conduction band absorption is much greater in the MQW sample. As discussed below, the increased excitonic absorption found in MQWs results in a much larger optical nonlinearity compared to that of the bulk material under certain conditions.

One final modification must be made to the above MQW model. In Figure 3-14, it can be seen that the valence band of GaAs is degenerate. Holes with two different effective masses are possible, giving rise to two differently shaped valence energy bands, known as the light and heavy hole

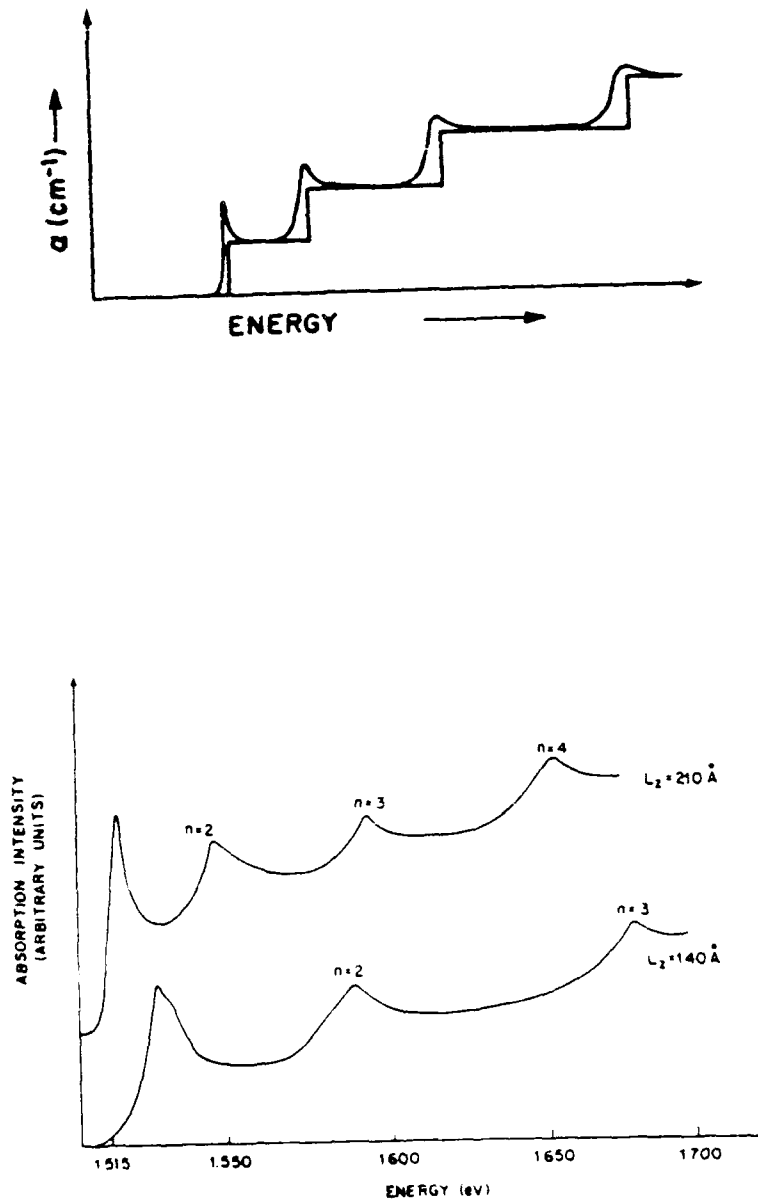


Figure 3-19. Schematic (top) and experimental (bottom) absorption spectra near the band edge of room temperature GaAs/AlGaAs MQWs. Compared to Figure 3-16, the excitonic enhancement of the MQW absorption is clearly evident.

bands. In bulk GaAs, the effects of this degeneracy are not manifested in the spectrum since the absorption band edge occurs at $k=0$ where the two bands are isoenergetic. In the MQW case, however, there is a forbidden region of k -space ($k \geq k_z$) which results in a lifting of the degeneracy of the light and heavy hole valence band energies at the band edge transition energy. These effects are shown schematically in Figure 3-20. Thus, each band edge of the MQW is actually split into a doublet with an energy separation given by the difference in energy of the light and heavy holes. Furthermore, at each of these doublet band edges an excitonic enhancement results: light and heavy exciton peaks are observed at each band edge. The latter can be seen experimentally in the absorption spectrum of Figure 3-21 (Reference 3.11). Here, a high resolution spectrum for the $n_v = 1$ to $n_c = 1$ band to band transition clearly shows the light and heavy hole exciton peaks.

The result of the above analysis is that the room temperature optical nonlinearity ($\chi^{(3)}$) near the GaAs MQW band edge is expected to be very large. Compared to bulk GaAs, the MQW $\chi^{(3)}$ associated with the exciton should be a factor of sixty-four times larger since $f_{MQW} = 8f_{GaAs}$ and $\chi^{(3)} \propto f^2$. Indeed, CW FWM has been performed on a room temperature MQW sample at pump intensities of a few W/cm^2 (Reference 3.17). However, since the saturation intensity, I_{sat} , for a resonant system is proportional to f^{-1} , the MQW's are expected to saturate at much lower pump intensities than the bulk material. In the experiment just referred to, saturation of the MQW FWM signal occurs at $\sim 15 W/cm^2$. Thus, the attractiveness of MQW material for monolithically integrated diode laser phase conjugators may be limited because the intensity incident at the phase conjugator would be of the same order as the intensity at the laser diode facet (tens of kW/cm^2). At such large intensities, the MQW excitonic nonlinearity may be fully saturated and may not contribute to the phase conjugate signal intensity.

The purpose of the set of experiments described in this report is to examine and compare the FWM characteristics of bulk GaAs and GaAs MQW's at moderately high CW laser intensities. The role of the excitonic enhancement of the optical nonlinearity in the two materials is assessed under these conditions.

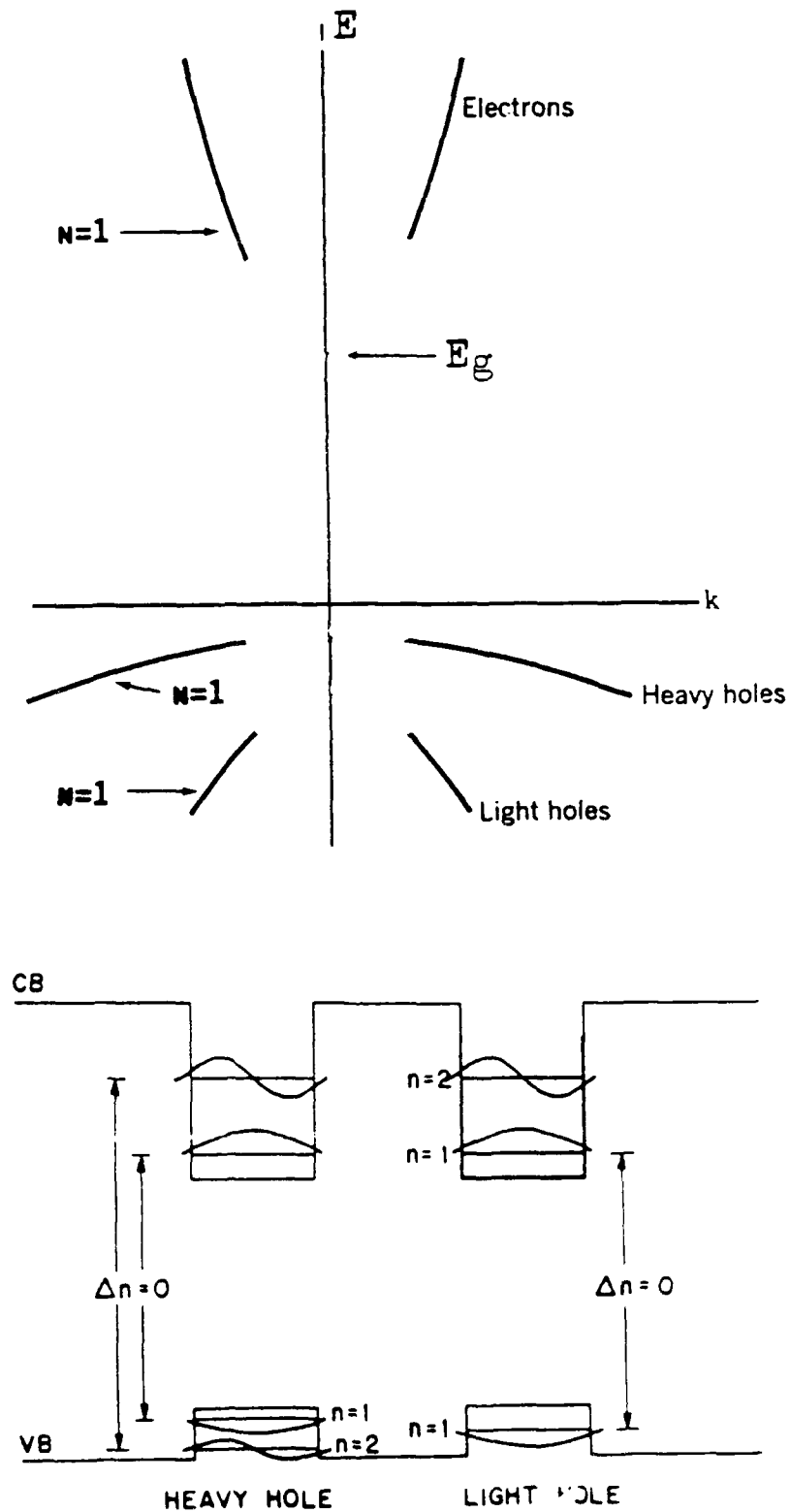


Figure 3-20. Energy dispersion characteristic and potential structure for the MQW when the effects of light and heavy holes are accounted for. In the top figure, a forbidden region of k -space exists since the minimum possible k is $k_z = n\pi/L_z$.

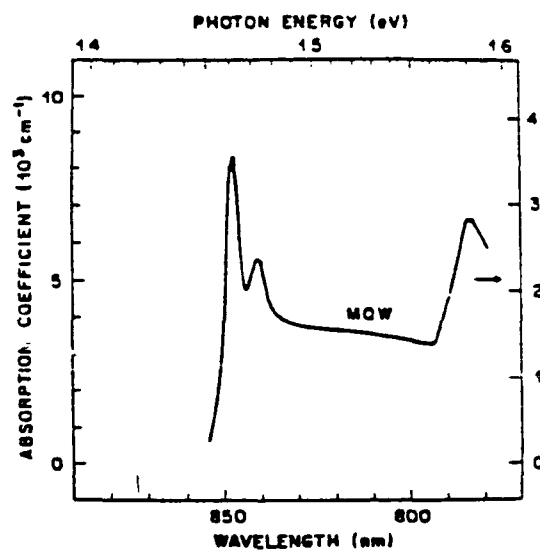
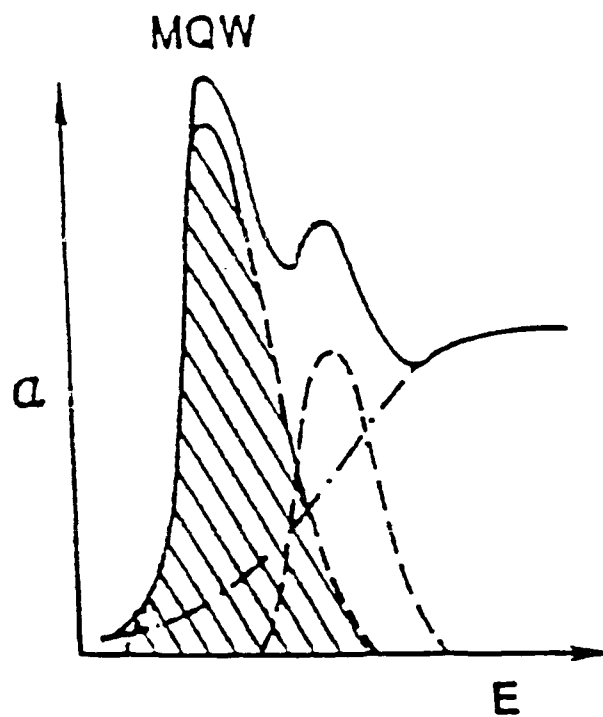


Figure 3-21. Schematic (top) and experimental (bottom) absorption spectra near the band edge of room temperature GaAs/AlGaAs MQW's including the effects of light and heavy holes.

3.4.2 Experimental Setup

The backward DFWM experimental setup for characterizing semiconductor materials is shown in Figure 3-22. A commercial, Ar^+ pumped, ring dye laser system provides 200 to 300 mW over the MQW spectral region (810-836 nm) with a frequency bandwidth of ~ 2 GHz. An acousto-optic modulator (AOM) is used to reduce the duty cycle of the CW dye laser. Laser pulses of 1 to 2 μsec and repetition rates of ~ 1 kHz are employed to eliminate heat deposition in the samples which can result in thermal shifts in the band gap energies and thermal contributions to the FWM signal (Reference 3.18). The proper operating conditions were determined by adjustment of the laser excitation energy and repetition rate until the band gap wavelength shift was eliminated. A series of half-wave plates and polarizing beamsplitter cubes produces the three co-polarized input beams in a manner which allows their intensity ratios to be easily adjusted. The conjugate signal beam is spatially separated from the counterpropagating probe beam by BS1. As the scattered light level is typically twenty times greater than the signal level, a double chopper, double lock-in amplifier technique is employed to permit noise discrimination (Reference 3.17). The backward pump beam is chopped at 300 Hz and the forward pump beam is chopped at 13 Hz. Only the conjugate signal beam is modulated at both frequencies and detected after the photodiode signal is serially processed through two lock-in amplifiers referenced at 300 Hz and 13 Hz. In the experiments described here, the forward pump-probe angle is fixed at ~ 35 mrad and the spot sizes of all three input beam are matched at $\sim 80 \mu\text{m}$ ($1/e^2$ beam diameter).

Both the MQW and bulk samples are epitaxial GaAs/AlGaAs layers on a GaAs substrate. They are grown by the metal organic chemical vapor deposition (MOCVD) technique. The MQW sample consists of 65 periods of GaAs quantum well layers 5 nm thick, alternated with $\text{Al}_{0.32}\text{Ga}_{0.68}\text{As}$ barrier layers 10 nm thick. The MQW active region is sandwiched between two $1 \mu\text{m}$ layers of $\text{Al}_{0.32}\text{Ga}_{0.68}\text{As}$. The bulk GaAs sample consists of a single $\sim 3 \mu\text{m}$ layer of GaAs sandwiched between two $1 \mu\text{m}$ layers of $\text{Al}_{0.32}\text{Ga}_{0.68}\text{As}$. After the growth, the substrate is removed using a jet thinning machine. Low temperature single layer anti-reflection coatings applied to both sides of the samples resulted in $\sim 3\%$ and 6% reflectivity per side for the MQW and bulk GaAs samples, respectively.

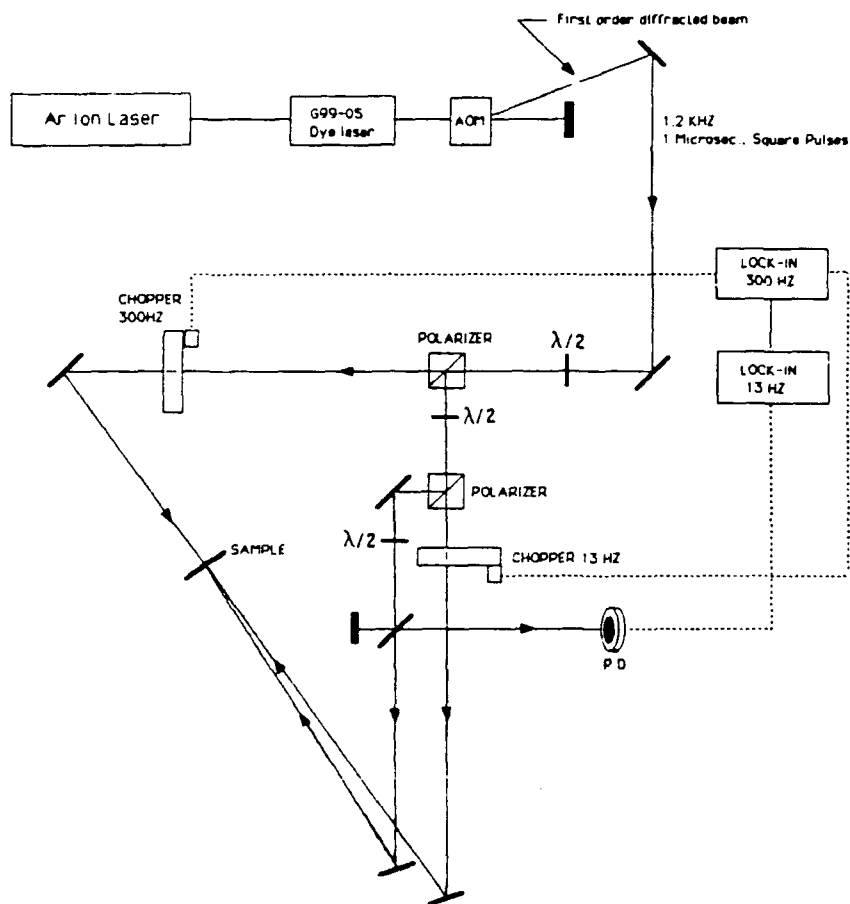


Figure 3-22. Experimental setup for the CW backward DFWM experiments in room temperature bulk GaAs and GaAs/AlGaAs MQW s.

3.4.3 Experimental Results

Figure 3-23A shows a linear (small signal) absorption spectrum for the MQW sample. In contrast to the spectra reported in Reference 3.14 for MBE-grown samples and those reported in Reference 3.19 for MOCVD samples, the light and heavy hole exciton resonances cannot be resolved: a broad enhanced absorption bump is observed at the band edge. This feature will be explained below. Figure 3-23B shows the wavelength dependence of the DFWM signal in the band edge region of the MQW sample for three different incident laser intensities. This data represents the first ever demonstration of CW backward FWM in a MQW. Similar FWM spectra are observed for each of the three intensities shown in the figure: two well resolved peaks with a near zero signal region in between and approximately a 2 to 1 peak ratio with the largest peak on the red side of the bandgap wavelength. Note that the wavelength at which the minimum FWM signal occurs corresponds to the peak of the MQW absorption spectrum. This FWM spectrum will be discussed in more detail below. The largest FWM reflectivity observed in this sample was $\sim 10^{-3}$.

An intensity dependence of the FWM signal was performed at each of the wavelengths shown in Figure 3-23B. Figure 3-24 shows a typical data set for the laser wavelength 815 nm. In this figure, the log of the FWM signal is plotted versus the log of the total laser intensity. In the absence of saturation, a straight line with a slope of three (nonsaturable optical Kerr medium) is expected since in this experiment the probe intensity is varied proportionately with that of the pump beams. In all of the cases described here, the log-log plots are highly linear with slopes between two and three, indicating that the intensity dependence of the FWM signal follows a simple I^n dependence over the intensity region studied here. Experimentally, the minimum I is determined by the signal to noise ratio and the maximum I by the maximum dye laser output. The slopes of these log-log plots can be used as a sensitive indication of the degree of saturation at each of the FWM wavelengths. Thus, in Figure 3-24, a slope of 1.8 is observed, indicating substantial saturation of the FWM signal at this wavelength. Figure 3-25 lists the average slopes obtained from several data sets at each wavelength. The wavelength dependent saturation can be seen more clearly in Figure 3-26 where the tabulated slopes are labelled onto the MQW absorption spectrum at the

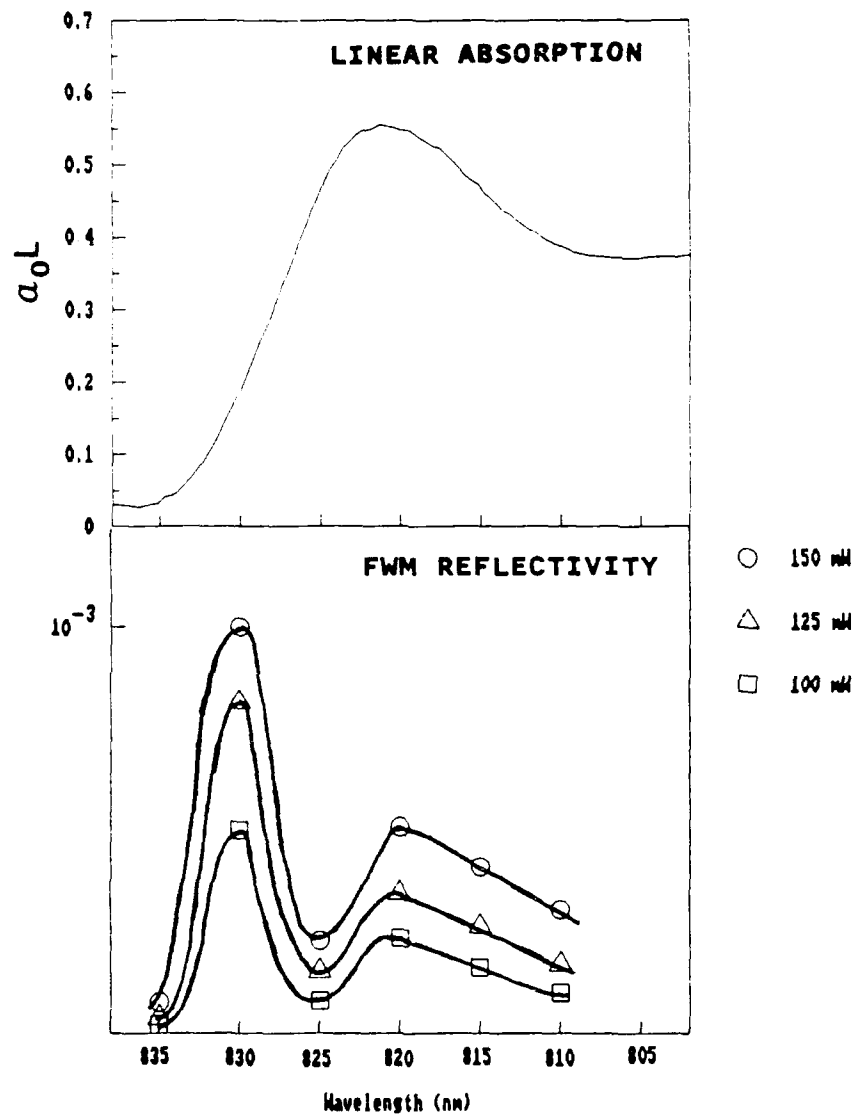


Figure 3-23. Linear absorption spectrum and FWM spectrum at three pump powers for the MQW sample discussed in the text.

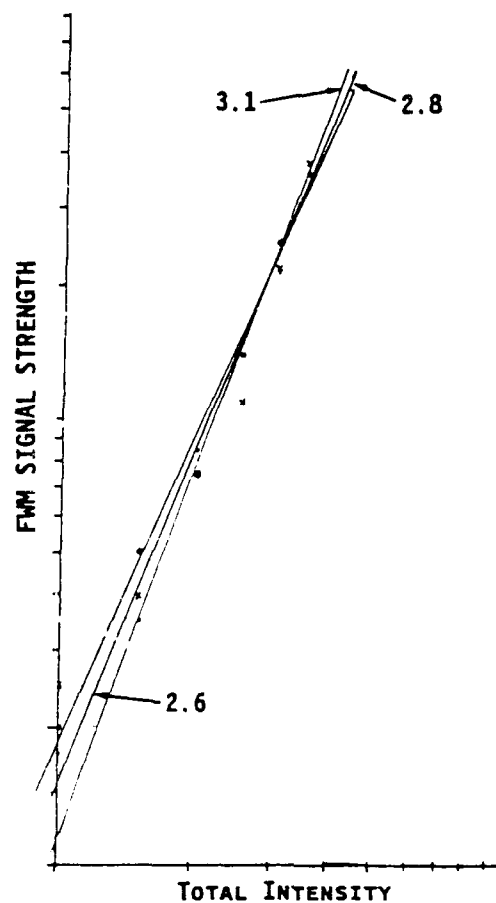


Figure 3-24. Log-Log plot of the MQW FWM signal versus pump intensity. A slope of three on this plot indicates the lack of saturation of the FWM signal.

WAVELENGTH (Å)	DATA SET #				AV.	S.D.
	1ST	2ND	3RD	4TH		
8050	2.8	3.1	2.6		2.8	+ .25
8100	2.1	2.6	2.8	2.5	2.5	+ .29
8150	2.2	1.9	1.9		1.99	+ .19
8200	2.3	2.3	2.7		2.4	+ .23
8250	2.5	2.0			2.25	+ .35
8300	3.1	2.9	2.7		2.9	+ .2

Figure 3-25. Table of the slopes of the Log(R)-Log(I) plots for various wavelengths near the MQW band edge.

FWM SLOPES AT DIFFERENT WAVE LENGTHS

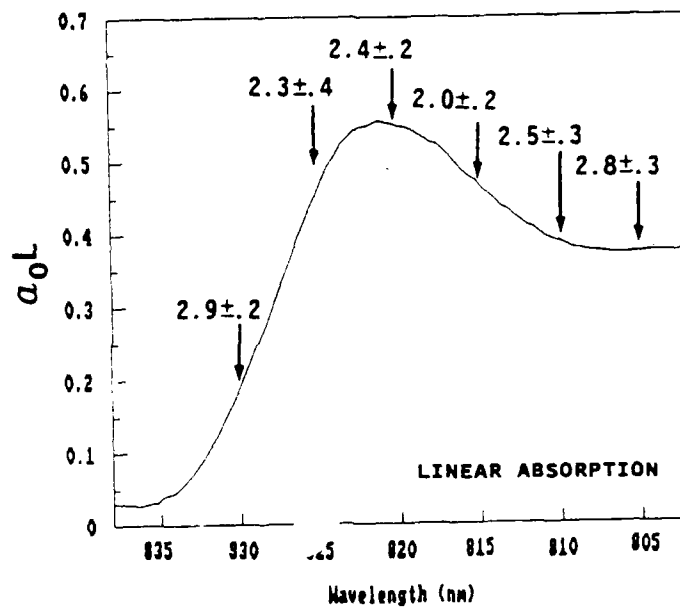


Figure 3-26. The slopes of Figure 3-25 are labeled onto the MQW linear spectrum.

appropriate wavelength. Note that substantial saturation occurs in the region of the exciton resonance but to the red and blue of this wavelength region the slope -3 , indicating no appreciable saturation up to the highest pump intensities used here, 4 kW/cm^2 .

The two-peaked FWM spectrum and the FWM saturation data in the exciton wavelength region suggest that the FWM signal is due to the light and heavy hole exciton peaks even though these peaks are not resolved in the linear absorption spectrum. However, there are several reasons to believe that in the MQW sample studied here that excitonic contributions to the optical nonlinearity are negligible. First of all, a saturated absorption experiment performed on the sample at the same wavelengths as the FWM signal (805-835 nm), showed no saturation of absorption up to the highest laser intensities available, 8 kW/cm^2 , indicating that $I_{\text{sat}} > 25 \text{ kW/cm}^2$. Furthermore, in the intensity-dependent FWM data, e.g. Figure 3-24, the signal is seen to increase monotonically for pump intensities up to 2 kW/cm^2 . The latter two experimental observations are inconsistent with excitonically enhanced MQW samples which have been shown to have saturation intensities of $\sim 500 \text{ W/cm}^2$ (Reference 3.12). In this case, not only should the absorption be highly saturated at the intensities employed, but the FWM signal should peak and begin to decrease in magnitude with increasing pump intensities on the order of I_{sat} or larger (Reference 3.2).

It has previously been shown in MOCVD-grown GaAs/AlGaAs MQW samples that the growth temperature has an important effect on the background carrier concentration (Reference 3.19). A high background carrier concentration results in a plasma screening of the electron-hole Coulomb interaction and a decrease in the probability of bound exciton states (References 3.20 and 3.21). In this case, the room temperature excitonic absorption is effectively saturated at zero pump intensity and well-resolved exciton peaks are absent. Evidence in support of this comes from a comparison of the absorption spectra in Reference 3.19 and those obtained for the MQW sample used in this study. In Reference 3.19, the linear absorption spectra of MQW samples with a high background carrier concentration ($\sim 4 \times 10^{16}/\text{cm}^3$) are seen to mimic the highly saturated absorption spectra of a sample with a low background carrier concentration ($\sim 6 \times 10^{14}/\text{cm}^3$). In both cases, the relevant spectra display broad enhanced absorption bumps in the exciton wavelength region but light and

heavy hole absorption peaks are completely blurred and cannot be distinguished. The linear absorption of the MQW sample studied here has a similar broad bump-like appearance (Figure 3-23). The spectrum of this sample looks similar to the saturated absorption spectrum from Reference 3.19 taken at an intensity three times greater than the saturation intensity for that sample.

This evidence, in conjunction with the saturated absorption results, suggests that excitons in the sample are screened and saturated by free background carriers, generated in this case as a result of impurity ions implanted into the sample during the growth process. Free carrier screening of excitons can also result from the large number of free carriers which are optically generated at high laser intensities (free electron-hole pairs). Thus, our MQW sample with impurity-induced high background concentrations serves as a model system for the study of nonlinear optical effects under high optical pump intensities expected in monolithically-integrated configurations.

Although no quantitative FWM model is available for comparison to the experimental data, the FWM spectrum can be explained well by dispersive contributions to the signal. The dispersive optical nonlinearity is most commonly determined from measurements of the saturated absorption (e.g., References 3.12, 3.18, and 3.20). A Kramers-Kronig transformation of $\Delta A(I, \nu) = A(0, \nu) - A(I, \nu)$, the change in the absorption coefficient due to an incident intensity I , gives $\Delta n(I, \nu)$, the nonlinear index change due to intensity I . The dispersive contribution to the FWM spectrum will be proportional to Δn^2 (Reference 3.12). As mentioned above, the MQW sample studied here displayed no saturated absorption. However, if we assume a frequency-independent model for the saturation intensity I_{sat} , then an approximation to $\Delta n(\nu)$ can be obtained from a Kramers-Kronig transformation of the MQW linear absorption spectrum.

The result of this calculation is shown in Figure 3-27A. In Figure 3-27B, Δn^2 and the experimental FWM data points have been plotted as a function of the laser photon energy. From this figure it can be that the dispersive optical nonlinearity qualitatively reproduces many of the main FWM spectral features: 1) the two-peaked appearance of the spectrum is correctly predicted 2) the positions of the signal peaks and null are approximately accounted for and 3) the relative ratio of the peak amplitudes is predicted fairly well. Note that the above procedure is

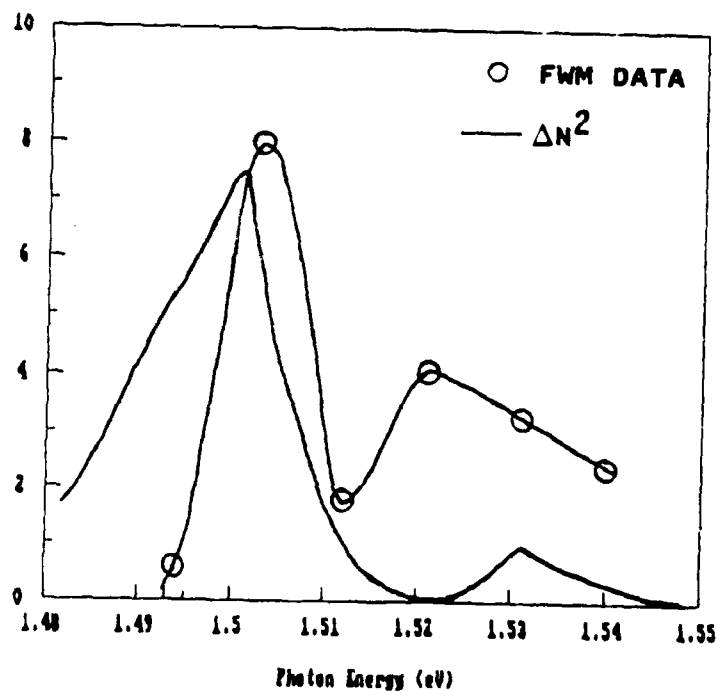
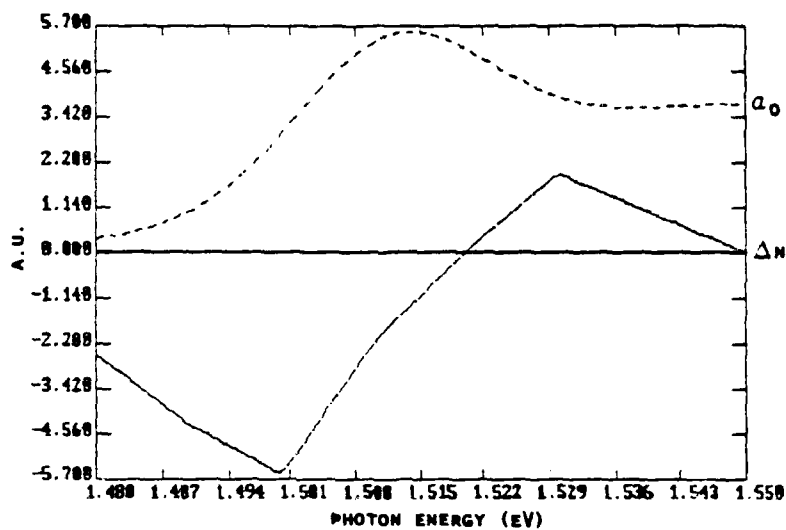


Figure 3-27. Part A: ΔA and Δn are calculated for the MQW sample using a model of a frequency-independent saturation intensity. Part B: the square of Δn is plotted on the same graph as the FWM spectrum.

strictly empirical in nature; no knowledge of the mechanisms responsible for the optical nonlinearity is necessary to arrive at the conclusion that the signal is dominantly dispersive.

A more quantitative fit to the FWM spectrum requires accounting for the effects of absorption on the FWM signal. Absorption impacts the signal through two mechanisms: 1) reduction of the effective pump intensities along the propagation directions of the optically thick sample and 2) absorption of the (amplified) probe and FWM signal. An exact FWM calculation including both dispersive and absorptive effects (which must be solved numerically) has been performed in the case of a homogeneously-broadened two level system with a Lorentzian line shape (Reference 3.22). In the case being discussed here, however, an expression for the dispersive nonlinearity is not readily available. An approximation has been incorporated into a 1D FWM code developed at TRW in order to make a preliminary study of the effects of absorption on FWM in semiconductor nonlinear materials. This approximation is described in the next section, 3.5.

For the purposes of comparing FWM response in semiconductors for two different pump intensity regimes, Figure 3-28 (from Reference 3.23) shows the FWM intensity-dependence (Figure 3-28A) and frequency-dependence (Figure 3-28B) for a MQW sample under conditions where the signal is generated by the excitonic optical nonlinearity, i.e., low pump intensities and a low background carrier concentration. In Figure 3-28A it can be seen that the FWM signal begins to saturate at very low pump powers, $\sim 13 \text{ W/cm}^2$ (I_{sat} for this sample is $\sim 580 \text{ W/cm}^2$). Thus, at the intensities found at the facets of laser diodes (tens of kW/cm^2), any excitonic contributions to the FWM signal are expected to be negligible, both because excitonic absorption is completely saturated and because of optically-induced free carrier screening of excitons. This supports our contention that the MQW sample studied here provides a model for what one would expect for FWM at laser diode facet intensities, even for samples displaying large excitonic enhancements. In Figure 3-28B it can be seen that, in contrast to the high power FWM spectra of this study (Figure 3-23B), absorptive contributions dominate the FWM spectrum at powers where the exciton is expected to contribute.

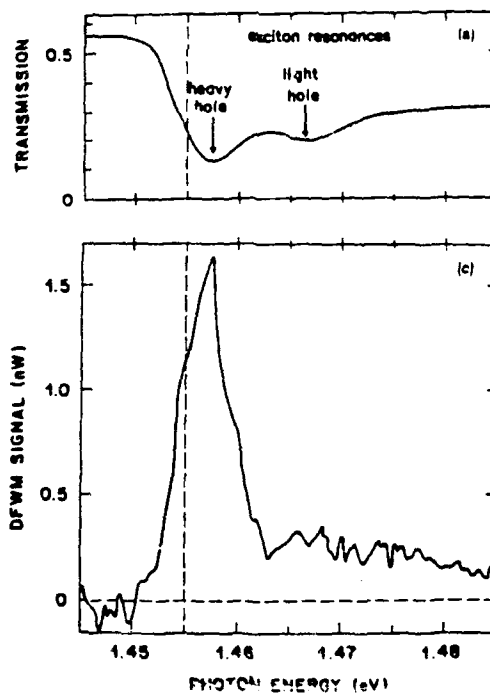
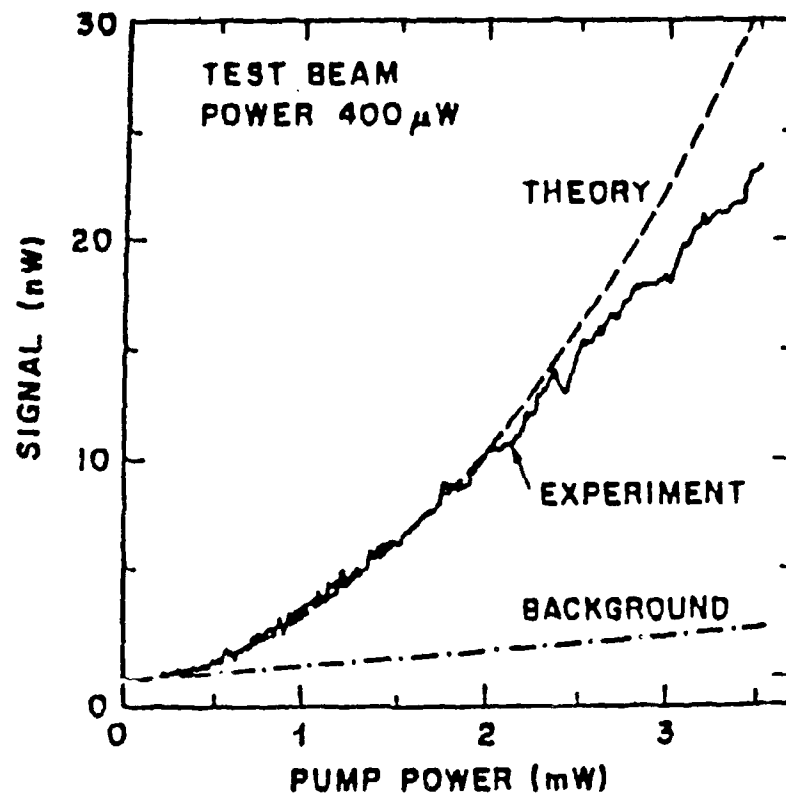


Figure 3-28. For the purpose of comparison, data from Reference 3.23 is shown here. Part A shows the FWM intensity dependence and Part B the frequency dependence.

This result is analogous to the results obtained in low power, low density sodium vapor FWM experiments where only small resonant signals are obtained (Reference 3.24). In the case of sodium vapor, large FWM signals can be obtained at higher pump intensities, provided that the optical absorption is increased appropriately (Reference 3.25).

This brief and simple analysis suggests that the excitonic enhancement found in semiconductor MQW materials cannot be effectively utilized at high pump intensities ($\geq 100 \text{ W/cm}^2$) to obtain large FWM signals. Low power pumping with longer interaction lengths is not a practical approach because the MQW optical path length is severely limited (to $\sim 3 \mu\text{m}$) by the growth process.

Some preliminary FWM results obtained in bulk GaAs will now be discussed. In this study, CW FWM is performed for the first time ever in bulk GaAs. The details of the experimental setup are identical to those for the MQW sample discussed above. Figure 3-29 shows a room temperature linear absorption spectrum for a $3 \mu\text{m}$ thick sample. In contrast to the MBE-grown sample of Reference 3.14, an exciton peak cannot be resolved in the spectrum. This is not surprising since the exciton binding energy for bulk GaAs is a factor of four weaker than that of the MQW (Reference 3.12). As discussed above, the weaker bulk GaAs exciton binding energy results in an oscillator strength for the excitonic transition which is eight times weaker compared to that of the MQW excitonic transition. In addition, since the bulk GaAs samples and the MQW samples are prepared under identical conditions, it is expected that a high background carrier concentration will be present in the bulk samples as well. This high background carrier concentration will be even more effective in screening the weaker bulk exciton than it is the MQW case. Thus, as in the case of the MQW sample discussed above, it is expected that excitonic effects will not be important in the interpretation of the FWM data. Conduction band transitions are responsible for generating the FWM signal.

Figure 3-30 is a log-log plot of the FWM signal versus incident pump intensity at a laser wavelength of 865 nm. Note that unlike the MQW data of Figure 3-24 where the total incident intensity is varied, only the pump intensity is varied in the experiment of Figure 3-30. In this case, an unsaturated, optical Kerr-like FWM signal is expected to vary as the square of the pump intensity giving a slope of two on a log-log plot. The slope of three obtained in this experiment indicates that absorptive

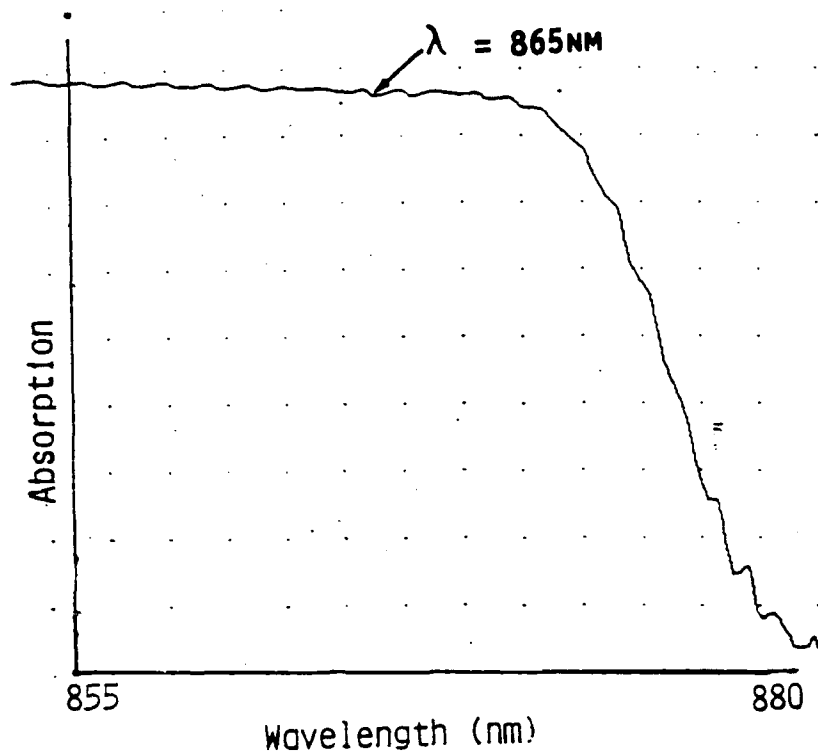


Figure 3-29. Room temperature linear absorption spectrum for a bulk GaAs sample.

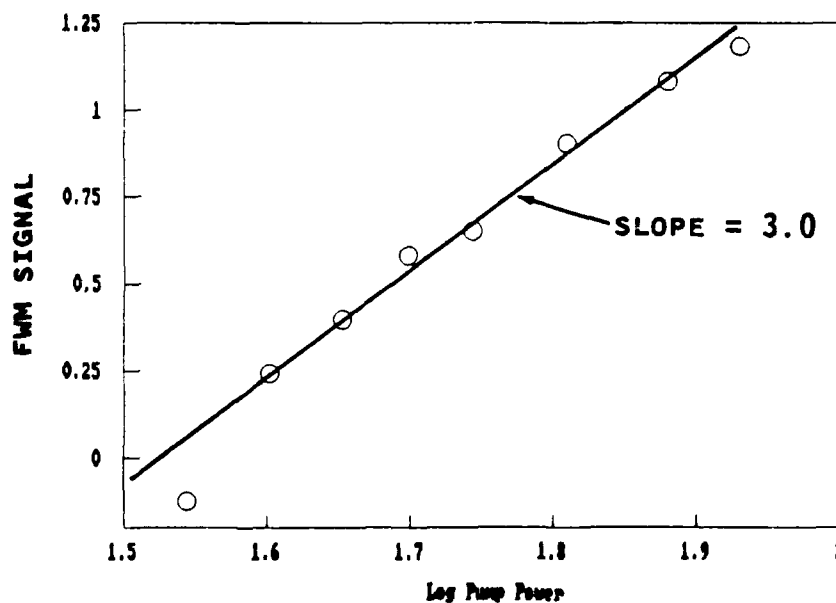


Figure 3-30. Intensity dependence of the bulk GaAs FWM signal at 865 nm. On the Log-Log plot shown here, a slope of two would indicate no saturation of the FWM signal. The steeper slope of three which is observed indicates that the effects of pump and signal absorption need to be included in any attempt to model the system.

effects need to be accounted for in order to explain the data; a slope greater than two is not possible otherwise.

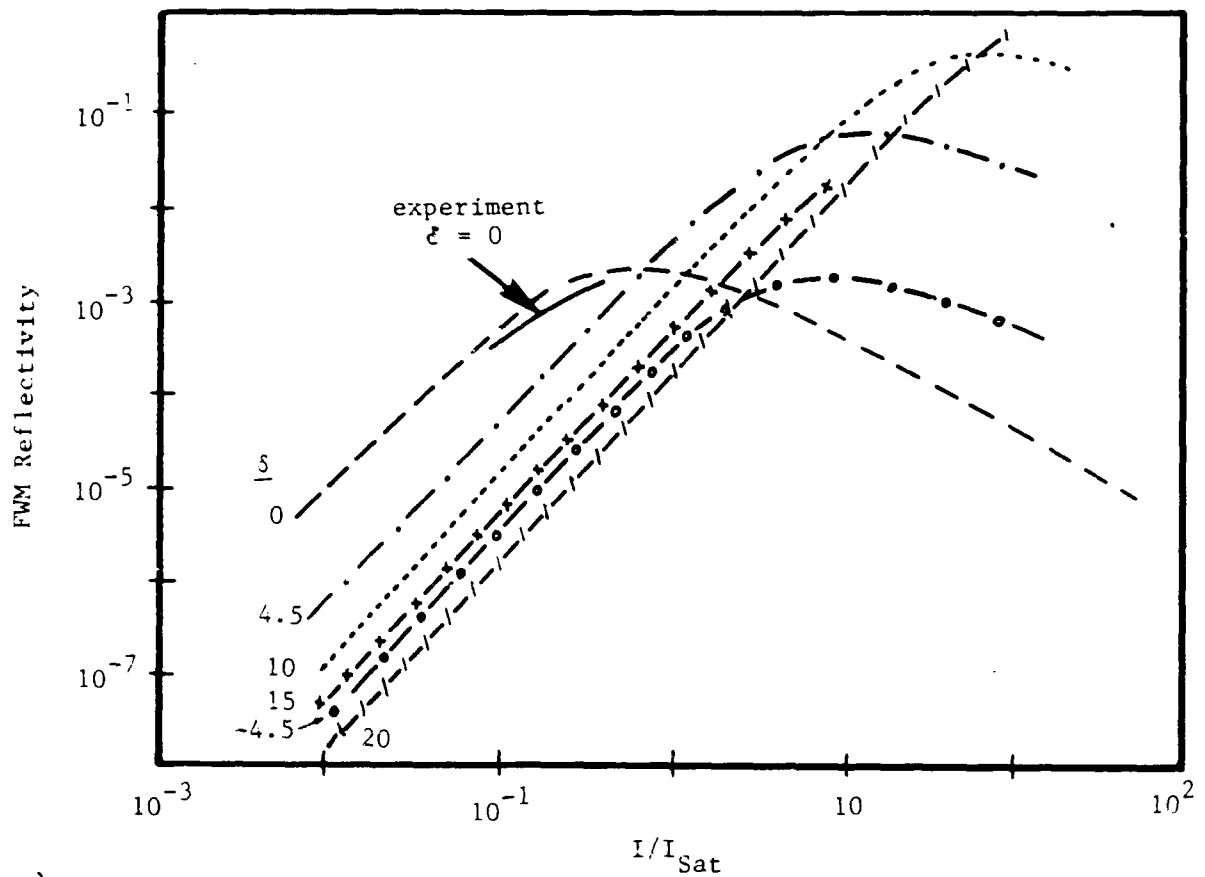
Absorptive effects are anticipated, however, because the experimental wavelength is well above the band edge. It has been shown previously that when the effects of absorption are included in a model for FWM in a homogeneously-broadened two level system, the intensity dependence of the FWM signal can have an arbitrary functional form (Reference 3.22). In this case, an intensity dependence stronger than I^2 is possible. Results of the TRW FWM code are in agreement with this interpretation. This can be seen in Figure 3-31.

Qualitative results have also been obtained for the wavelength dependence of the FWM signal. As the laser is tuned across the band edge region, the maximum signal is obtained at 865 nm. This result is uncorrected for the variation in dye laser intensity as the laser is scanned, but since the laser power decreases towards the longer wavelengths it can safely be stated that the maximum FWM signal is obtained within ~ 10 nm of the band edge and not far into the conduction band. Also, an approximate estimate for the FWM bandwidth is ~ 10 nm. This is substantially smaller than the FWM bandwidth for the MQW sample (~ 30 nm, Figure 3-23B).

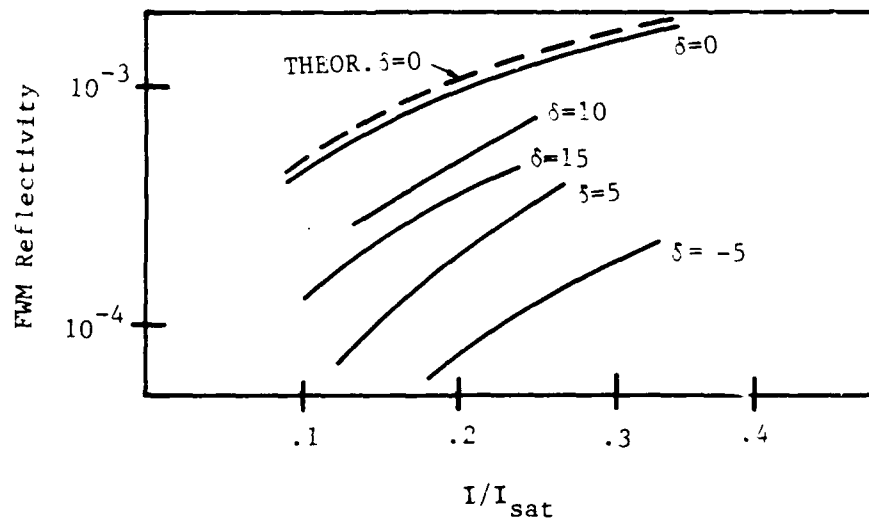
The maximum FWM reflectivity obtained for the bulk GaAs sample is, within experimental error, identical to that obtained for the MQW sample, $\sim 10^{-3}$. This result provides further evidence to support the contention that excitons do not contribute to the FWM signal in the MQW sample discussed above. The implication is that in the absence of excitonic effects, the nature of the conduction band transitions in both samples is similar. Thus, the quantum confinement effect of the MQW does not enhance the optical nonlinearity above that of the bulk GaAs material in the moderate pump intensity regime studied here. However, MQWs still provide at least one advantage over the bulk material: the wavelength position of the MQW band edge can be tailored during the growth process to meet specific system requirements. This advantage must be traded off against manufacturing constraints imposed by the MQW structure.

3.5 Modeling

In the previous section a general theoretical background of the relevant band gap physics for bulk GaAs and GaAs/AlGaAs MQW was



a)



b)

Figure 3-31. FWM reflectivity as a function of the ratio of pump intensity to the saturation intensity, I_{sat} . Solid lines are experimental data and dashed lines are analytical results. Model results for different detunings $\delta = (E_{\text{photon}} (\text{eV}) - 1.51) / .004$ are shown in a); experimental measurements at different δ are presented in b).

summarized. In this section we describe how those theories were modified and utilized in an effort to model the experimental results and predict trends for future experiments. We should stress at the outset that although we were able to develop a formalism that can model the FWM behavior of semiconductors quite adequately, due to the complexity of the problem we were only moderately successful in utilizing the model for a detailed data analysis.

The modeling of DFWM in semiconductors requires a description of the nonlinear polarization and its insertion into the wave equations through appropriate integrations over a wavelength so that the slowly varying envelope approximation (SVEA) remains valid (Reference 3.2). A rigorous derivation, valid even for high intensities (of the order or larger than the saturation intensity of the material), involves the use of a perturbative approach in a density matrix calculation similar to that developed for a saturable absorber consisting of two-level atoms (Reference 3.24).

For semiconductors, the presence of a quasi continuum of states and the lack of detailed information on the matrix elements and dephasing rates makes this approach cumbersome. The two next best possible approaches are to either a) assume that the radiation induced changes (if any) in the population of the energy levels are small or b) modify the SVEA equations with a phenomenological theoretical description for two-level atoms saturable absorbers.

The first approach involves estimating the magnitudes and signs of the various orders of the nonlinear susceptibility. The order of the susceptibilities involved, however, depends on the specifics of the nonlinear interactions. Hence for this approach to provide a simplification, the nonlinear interaction must be such that only the third order susceptibilities are dominant. This will, in general, restrict the results to low light intensities and special cases of two-photon transitions from the valence to the conduction band. In the approach b) the intensity dependence of the nonlinear polarization is assumed to be similar to that of the two-level saturable absorber. Afterwards, the absorptive (imaginary part of the third order susceptibility) and dispersive (real part) contributions for $I \ll I_{\text{sat}}$ are replaced by those obtained for semiconductors. These contributions are basically the

absorption coefficient and the refractive index that can be obtained from the frequency spectrum of the absorption coefficient by the appropriate Kramer-Kronig transformation. In our modeling we have adopted the later approach.

We were not able to include in the description of the dispersive part of the susceptibility the effect of the Coulomb interactions and the exciton contributions as derived by the various theories (Reference 3.10 and 3.27) due to the numerical complexity associated with the Kramer-Kronig integrals and the solution of the differential equations. A formalism that utilized simplified functional forms for the absorption coefficient was developed but only carried through to predict the index of refraction and not the DFWM signal (cf. Figure 3-27).

When a simple free electron model is utilized, the absorption coefficient has a simple energy dependence, quite similar to that of the two level atom saturable absorbers (cf. Equation 3.7). In this case, it is quite straight forward to obtain an analytical expression for the index of refraction to substitute in the full SVEA equations that predict the DFWM signal (cf. Reference 3.2, pages 332-335). We find that for a simple free electron model the equations developed for saturable absorbers consisting of two level atoms can be utilized with minor modifications to predict the DFWM signal. Initially, we utilized this model to obtain a parametric dependence of the reflectivity with intensity for various values of the absorption parameter αL . Figure 3-32 shows the results obtained with that model. The DFWM code developed during the first phase of the contract was utilized to solve the SVEA equations for the pump, probe and conjugate. The code includes pump absorption but neglects pump depletion. We believe that the results obtained in this form are only valid for zero detuning.

As discussed in the previous section, a simple comparison of the experimental absorption spectra with the theoretical one obtained from Equation 3.7 shows that the simple electron model is not a good description of the semiconductor systems near their band edges. Absorption enhancement in the conduction band continuum of states due to Coulomb interactions and the excitonic resonances must be taken into account to describe both the bulk GaAs and the MQW absorption spectra. Further, for those cases where the carrier density is very large (as we suspect to be the case in our samples), the optically generated

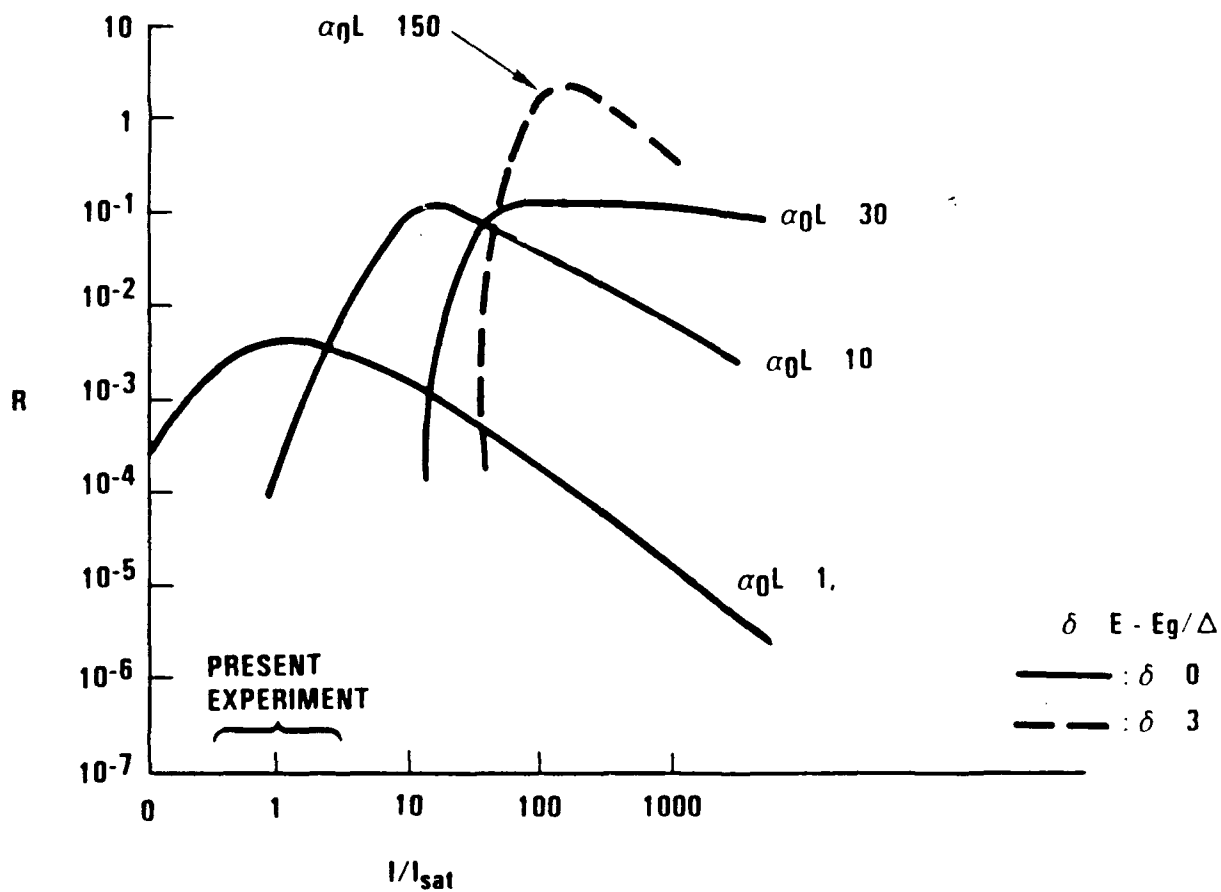


Figure 3-32. FWM reflectivity as a function of pump intensity and frequency detuning, δ , calculated using a simple free electron model for the saturable nonlinearity.

electron-hole pairs will interact with the electron-hole plasma, a screening of the potential will occur and the Coulomb enhancement will be decreased.

We have utilized a phenomenological formula that contains all the previously described phenomena to model the absorption spectra (Reference 3.18) and modified the DFWM code by substituting this formula for the absorption spectra, in both the absorptive and dispersive parts. Thus, the dispersive description of the code does not include a complete Kramer-Kronig transformation. In this case the results would be valid as long as the absorptive part contributions are dominant.

The general formula utilized to describe the absorption spectra for both the bulk and MQW GaAs samples is of the form:

$$A \tanh(a_1 \delta + a_2) \bullet [(1/\cosh(a_3 \delta + a_4) + \gamma(1/\cosh(a_5 \delta + a_6) + \dots \quad 3.14$$

where the effects of nonzero temperature and plasma screening are included in the tanh term. In general a_1 and a_2 can be associated with the chemical potential and a_3 , a_4 , et.. with the gap energy renormalized due to the presence of the Coulomb potential. We have obtained values for the parameters a_i by fitting the formula to our experimental spectra. It turns out that there are only a few combinations of parameters that can fit the data and be physically acceptable. Figure 3-33 shows an example of our analytical fit to the AlGaAs MQW absorption spectra data. Figure 3-33b shows the contributions from the different terms in Equation 3.14.

An example of the results obtained with this model are shown in Figures 3-31 and 3-34 where we have plotted reflectivity versus intensity and reflectivity versus wavelength respectively for the MQW case. In Figure 3-31 we compare the results with the data for zero detuning $\delta=0$, that shows good agreement.

The experimental results for $\delta \neq 0$, however show peaks that are not predicted by the theory, although the δ asymmetry is expected. Those peaks can be associated with the dispersive contribution to the signal. In fact, although a Kramer-Kronig transformation of an equation of the type of 3.14 is quite complicated, we have found that the same functional form can be reproduced with the sum of three Gaussians of appropriate mean and variance. In this case, the Kramer-Kronig transformation can be easily performed. The results for the dispersive part obtained in that

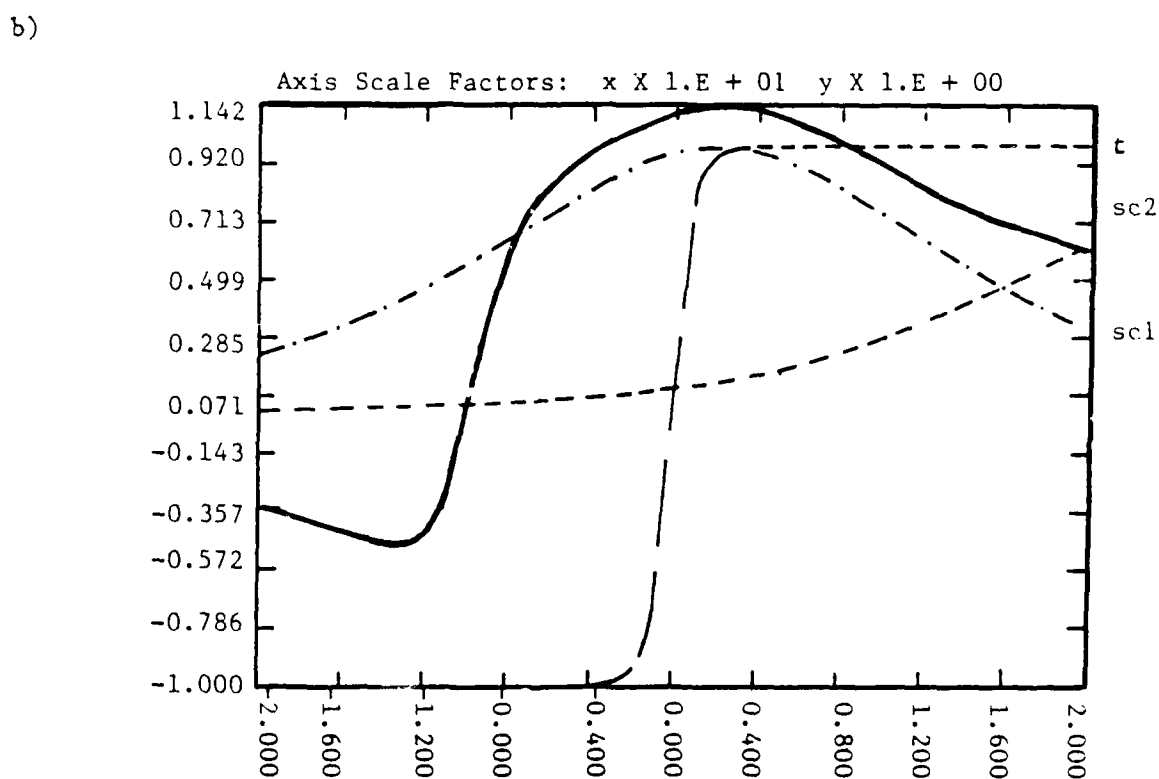
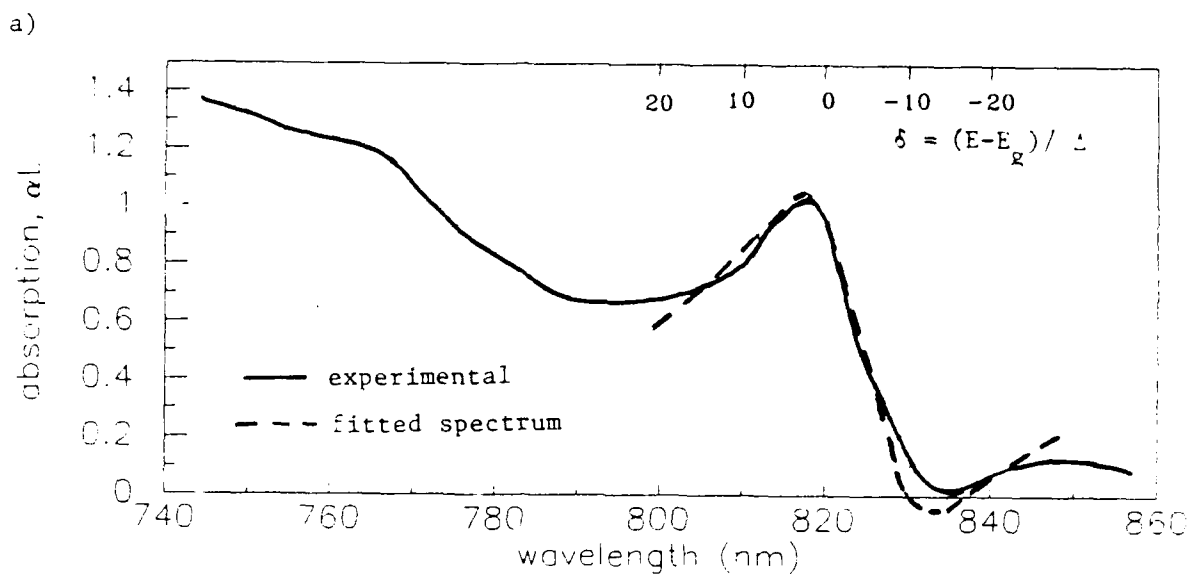


Figure 3-33. Analytical fitting of the observed absorption spectrum for incorporating in the FWM model: a) shows the observed and model absorption used in the model. b) shows the relative contributions from the tanh (t) and two cosh (sc) terms in Equation 3.14.

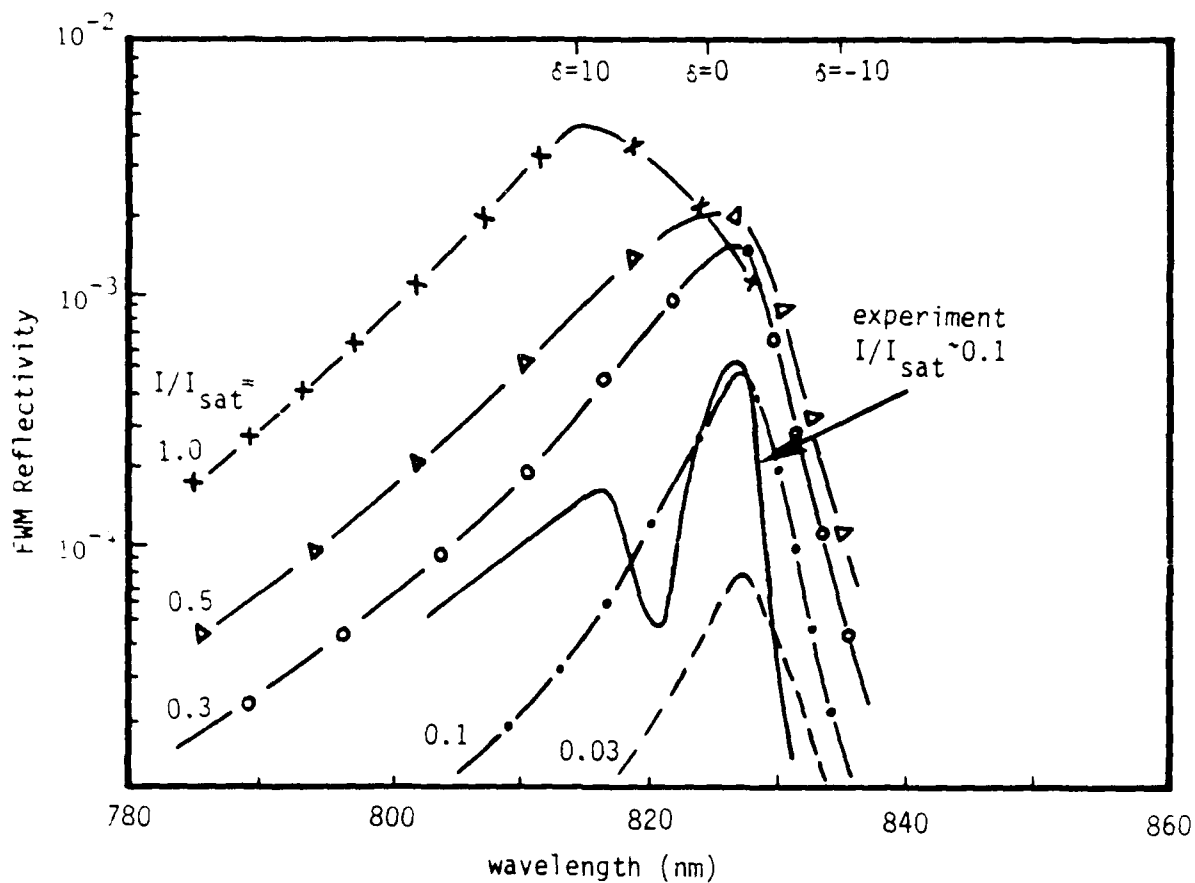


Figure 3-34. FWM reflectivity as a function of wavelength for various values of I/I_{sat} using the GaAs FWM model. The solid line shows experimental results.

manner have been shown in Figure 3-27. As described in Section 3.4.3, the index of refraction shows a number of peaks of similar relative intensity and closely located in energy to those obtained experimentally.

From the discussion above we conclude that a suitable model can be achieved by including a dispersive part obtained by transforming an absorption spectra represented by Gaussians. However, we were unable to complete calculations for conditions that would permit verification by comparison with our experimental results.

3.6 References

- 3.1 H. Nakajima and R. Frey, IEEE J. Quantum Electron. QE-22, 1349(1986); *ibid.*, Appl. Phys. Lett. 47, 769 (1985); *ibid.*, Phys. Rev. Lett. 54, 1798 (1985).
- 3.2 R.A. Fisher, ed., Optical Phase Conjugation (Academic, New York, 1983), and references therein.
- 3.3 K. Inoue, T. Mukai, and T. Saitoh, Appl. Phys. Lett. 51, 1051 (1987).
- 3.4 J. Reinjtes and L. J. Palumbo, IEEE J. Quantum Electron. QE-18, 1934 (1982).
- 3.5 A.W. Snyder and J.D. Love, Optical Waveguide Theory (Chapman and Hall, London, 1983).
- 3.6 G. Agrawal, Optics Letters 12, 260 (1987).
- 3.7 K. Creath, Applied Optics 24, 1291 (1985).
- 3.8 S. Kobayashi and T. Kimura, IEEE J. Quantum Electron. QE-17, 681 (1981).
- 3.9 C. Kittel, Introduction to Solid State Physics (John Wiley and Sons, Inc., New York, 1976).
- 3.10 R.J. Elliot, Phys. Rev. 108, 1384 (1957).
- 3.11 M. Shinada and S. Sugano, J. Phys. Soc. Jap. 21, 1936 (1966).
- 3.12 D.S. Chemla, D.A.B. Miller, P.W. Smith, A.C. Gossard, and W. Wiegmann, IEEE J. Quantum Electron. QE-20, 265 (1984).
- 3.13 J.S. Blakemore, J. Appl. Phys. 53, R123 (1982).
- 3.14 D.A.B. Miller, D.S. Chemla, D.J. Eilenberger, P.W. Smith, A.C. Gossard, and W.T. Tsang, Appl. Phys. Lett. 41, 679 (1982).

- 3.15 D.S. Chemla, Helvetica Physica Acta 56, 607 (1983).
- 3.16 R. Dingle, Festkorperprobleme XV, 21 (1975).
- 3.17 D.A.B. Miller, D.S. Chemla, A.C. Gossard, and W. Wiegmann, Optics Letters 8, 477 (1983).
- 3.18 Y.H. Lee, A. Chavez-Pirson, B.K. Rhee, H.M. Gibbs, A.C. Gossard, and W. Wiegmann, Appl. Phys. Lett. 49, 1505 (1986).
- 3.19 H.C. Lee, A. Hariz, P.D. Dapkus, A. Kost, M. Kawase, and E. Garmire, Appl. Phys. Lett. 50, 1182 (1987).
- 3.20 L. Banyai and S.W. Koch, Z. Phys. B63, 283 (1986).
- 3.21 Y.H. Lee, A. Chavez-Pirson, S.W. Koch, H.M. Gibbs, S.H. Park, J. Morhange, A. Jeffery, N. Peyghambarian, L. Banyai, A.C. Gossard, and W. Wiegmann, Phys. Rev. Lett. 57, 2446 (1986).
- 3.22 M.T. Gruneisen, A.L. Gaeta, and R.W. Boyd, J. Opt. Soc. Am. B 2, 117 (1985); A.L. Gaeta, M.T. Gruneisen, and R.W. Boyd, IEEE J. Quantum Electron., QE-18, 1095 (1986).
- 3.23 D.A.B. Miller, D.S. Chemla, D.J. Eilenberger, P.W. Smith, A.C. Gossard, and W. Wiegmann, Appl. Phys. Lett. 42, 925 (1983).
- 3.24 J.F. Lam, D.G. Steel, R.A. McFarlane, R.C. Lind, Appl. Phys. Lett. 38, 977 (1981); D.G. Steel and R.A. McFarlane, Phys. Rev. A27, 1687 (1983).
- 3.25 J.P. Woerdmann and M.F.H. Shuurmans, Opt. Lett. 6, 239 (1981).

4.0 Four-Wave Mixing Detectivity

4.1 Introduction

A number of four-wave mixing (FWM) applications require the phase conjugation (PC) of a very small input signal or probe. In some cases this PC wave must be amplified and high gains are required. Because the PC fidelity can be degraded by the presence of even a small amount of noise, and the noise can also be amplified, noise generation imposes limitations on the minimum input signal that can be conjugated and the gain amplification.

There are three main sources of noise that can introduce non-correctable phase errors and limit the conjugate fidelity : a) noise added by the FWM PC process itself, b) the noise added by the nonlinear medium fluctuations and c) the noise due to the detection system. In each case the noise can be further classified as i) additive noise: noise added to the output signal independent of the input signal or ii) multiplicative noise proportional to the input signal.

In this chapter we analyze the limitations imposed by additive noise, which is the most restrictive for very small input signals. Further, we have concerned ourselves first only with the minimum additive noise or quantum noise limit due to the FWM PC process itself, "ideal noise". Afterwards, we calculate the modification of the results introduced by the medium fluctuations such as absorption and spontaneous emission. We have found that the FWM PC process itself is quite noisy, adding one "noise" photon per N photons reflected, where N is the number of input photons. This quantum "ideal noise" imposes a limitation on the minimum power per unit bandwidth $\Pi_m = P_m/\Delta\omega$ that can be conjugated with fidelity : $\Pi_m \gg \hbar\omega$ ($\Pi_m \sim 10\hbar\omega$) for high gains, and $\Pi_m \rightarrow \infty$ for zero gain. The minimum power limitation can be increased by medium fluctuations that affect accurate determination of the output conjugate intensity or in the case where the empty port, defined below, is not a vacuum state. In these cases the limitation is increased to $\Pi_m \gg (1 + (\alpha/\kappa)^2)\hbar\omega$ for high gains, where α is the absorption coefficient and κ is the nonlinear coupling coefficient.

For the ideal noise case we have traced the main source of noise added to the conjugated phase to the presence of quantum fluctuations in

the empty port of a FWM, and to the FWM PC process itself for the unwanted variations of the conjugated wave intensity. This suggests that the limitation imposed by the quantum noise on the output quadratures (amplitude and phase) could be decreased with the use of a single-ended optical cavity, a possibility that needs further investigation..

In addition, we have also found that the use of a beam splitter to produce a suitable combination of the input and output modes (as that utilized in the generation of squeezed states) might provide a mechanism to detect the source of noise: FWM conjugation, empty port, or medium fluctuations. We have not explored detection noise as a further source of added noise since that noise is not linked to the nonlinear optical interactions themselves.

4.2 Formalism

The analysis utilized to calculate the quantum noise limits follows the formalism developed by C. M. Caves (Reference 4.1) to evaluate the quantum noise limit in linear amplifiers as well as the quantum theory of four wave mixing evolved by various authors (Reference 4.2) to model squeezing by four wave mixing.

The basic idea is to treat the FWM PC as a PC mirror (PCM) that reflects the input signal with some gain, i.e., like a reflecting linear amplifier with a complex reflectivity or "gain". An amplifier is defined as a device that takes an input signal, carried by a collection of bosonic modes, and processes the input to produce an output signal also carried by a (possibly different) collection of bosonic modes (Reference 4.1). In a linear amplifier the output signal is linearly related to the input signal. Further, the FWM PC can be treated as a phase insensitive linear amplifier, a linear device for which a phase shift of the input produces the same or the opposite phase shift (the case for PC) of the output. The advantage of identifying a FWM PC with a phase insensitive linear amplifier is that in that case the quantum limit can be expressed in terms of a single noise number A which satisfies:

$$A > |1 + G^{-1}|/2 \quad 4.1$$

where A is the noise added to the signal, referred to the amplified input

noise or the output conjugate intensity and given in units of number of quanta. Thus $A \hbar \omega$ is the added noise energy per unit bandwidth, (Joules) /amplification of the input noise. G , is the amplifier gain in units of number of quanta. In Section 4.2 we will show in detail for the ideal degenerate FWM (DFWM) case that a FWM PC satisfies the inequality in Equation 4.1. Here, we give a brief description of a FWM PC that leads to the characterization of its quantum noise and to Equation 4.1.

A FWM PC can be considered as a mirror device that takes an input signal and after interaction with the mirror internal degrees of freedom produces an output signal. The output can be taken as the reflected Hermitian conjugate of the input with some complex reflectivity, $R^{1/2} = G^{1/2} \exp(i\phi)$. Because both input and output are electromagnetic fields they can be represented by boson operators.

The relation between input and output operators can be obtained through the solution of a set of "evolution equations" that depend on the particular characteristics of the FWM PC. A simple prescription to find this set of operator evolution equations is to replace the classical phasor A , (amplitude and phase) and its conjugate A^* , by the quantum mechanical set of annihilation and creation operators a, a^+ in the set of classical coupled-mode equations that represent the FWM interaction (Reference 4.3). The equations obtained by this simple method are valid in the limit of "ideal noise", with additional fluctuation terms required to describe the quantization of the medium. These fluctuation terms are obtained from Langevin noise operators and will be described in Section 4.3 (cf. Reference 4.4).

The evolution equations must be consistent with the boson character of the input and output operator, i.e., they must preserve the appropriate commutation and anticommutation relations. Thus, in general if we identify the input wave or probe to a FWM PC with an operator pair a_4, a_4^+ and the output wave or conjugate with a pair a_3, a_3^+ (cf. Figure 4.1), related through some complex reflectivity, we find that the evolution equations must also contain an additional or "noise" term to satisfy the commutation relations. In particular, for a single mode description, the pairs a_1, a_1^+ satisfy:

$$[a_i, a_j] = 0 \quad 4.2a$$

$$[a_i, a_j^+] = \delta_{ij} \quad 4.2b$$

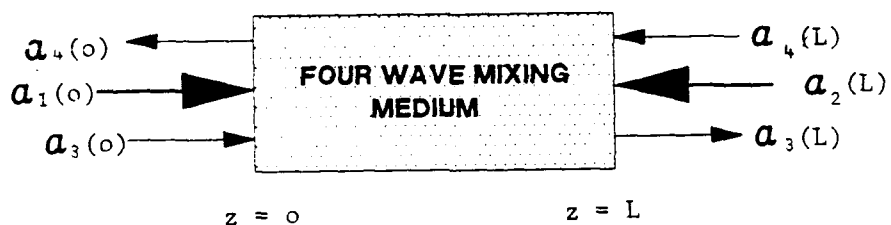


Figure 4-1. Schematic diagram of degenerate four-wave mixing. a_j represents the complex vector potentials associated with the electromagnetic waves. The indices 1,2 represent the classical pumps and 3,4 correspond to the conjugate and probe respectively.

Hence, $a_3(0)$ (output conjugate wave) is related to $a_4(0)$ (input probe) through

$$a_3(0) = a_4(0)^+ G^{1/2} \exp(i\phi) + F \quad 4.3$$

where in order to satisfy Equation 4.2 for a_3 , F must be different from 0 and satisfy in turn

$$[F, F^+] = 1 + G \quad 4.4$$

The complexities of a particular single moded FWM device are now buried in the single operator F which is responsible for added "ideal" noise (in the absence of losses or fluctuations in the medium).

4.2.1 Ideal Noise Characterization

The unitarity condition, Equation 4.4, places a lower limit on the fluctuations associated with F . In fact, by splitting F into its Hermitian real and imaginary parts, which are in turn associated with the annihilation and creation operators F , we have:

$$F = F_1 + iF_2 = [(F + F^+) + i(F^+ - F)]/2.$$

The mean square fluctuation of F can then be written as

$$|\Delta F|^2 = [\langle FF^+ + F^+ F \rangle / 2] - \langle F \rangle \langle F^+ \rangle = \Delta F_1^2 + \Delta F_2^2 \quad 4.5$$

The lower limit in the quantum noise fluctuations is set by the generalized uncertainty principle:

$$|\Delta F|^2 \geq 2|\Delta F_1 \Delta F_2| \geq |\langle [F_1, F_2] \rangle| \geq |\langle [F, F^+] \rangle| / 2 = |1 + G| / 2 \quad 4.6$$

Equations 4.3 through 4.6 show that if G is known for a FWM device, the quantum noise limit can be easily calculated. In particular, the noise can be further characterized and its physical meaning clarified by introducing complex amplitude components for the input and output operators. Thus defining $a_i = X_i + iY_i$, where X_i and Y_i are referred as the mode i

operator quadratures, we can rewrite the evolution equations as

$$X_3(0) = G^{1/2}(\cos(\phi)X_4(0) + \sin(\phi)Y_4(0)) + F_1 \quad 4.7a$$

$$Y_3(0) = G^{1/2}(\sin(\phi)X_4(0) - \cos(\phi)Y_4(0)) + F_2 \quad 4.7b$$

Note that the operator quadratures can in turn be associated with measurable quantities such as the normal ordering intensity $\langle W \rangle = \langle a_i a_i^\dagger \rangle$, and the phase associated with $\langle Y_i \rangle / \langle W \rangle$.

When the evolution equations are written in the form 4.7, and assuming $\phi = 3\pi/2$ (which we show later is the case for DFWM), the uncertainties in the output quadratures have a simple form:

$$\Delta X_3(0)^2 = G \Delta Y_4(0)^2 + \Delta F_1^2 \quad 4.8a$$

$$\Delta Y_3(0)^2 = G \Delta X_4(0)^2 + \Delta F_2^2 \quad 4.8b$$

Equations 4.8 show that only one number is needed to characterize the quantum noise if $\Delta F_1 = \Delta F_2 = \Delta F$. Further, the added noise can now be conveniently characterized by an "added noise number" $A = |\Delta F|^2 / G = |1+G|/2G$, referred to the input and measured in units of number of quanta (Reference 4.1). A represents the ratio of the added noise to the amplification of the input probe noise. This number is also proportional to the ratio of the added noise to the probe amplification. Note that the ratio of the amplified input noise to the amplified probe intensity (and output conjugate intensity) is independent of the gain and is only proportional to the ratio of the input noise to the input intensity. For high reflectivity FWM PC, $A \rightarrow 1/2$, which for the minimum fluctuations $\Delta X = \Delta Y = 1/4$ associated with a vacuum state or a number state, limits the input probe to values that are at least 10 quanta or larger (the input probe power per unit bandwidth to values that are at least $10\hbar\omega$ Joules).

Another way to characterize the effect of the noise in the output conjugate is by calculating the output number operator and its variance which are directly related to measurable quantities such as power or intensity. The number operator is defined as $n_i = a_i^\dagger a_i$. Using the evolution Equations 4.3 we find that:

$$\langle n_3 \rangle = G(\langle n_4 \rangle + 1) + G^{1/2} [\exp(-i\phi) \langle a_4 F \rangle + \exp(i\phi) \langle F^\dagger a_4^\dagger \rangle] + \langle F^\dagger F \rangle \quad 4.9$$

Even for the ideal case where F is a vacuum state with average value $\langle n_f \rangle = \langle F^\dagger F \rangle = 0$, and there are no mixed states ($\langle a_4 F \rangle = \langle F^\dagger a_4^\dagger \rangle = 0$), we find that $\langle n_3(0) \rangle = G(\langle n_4(0) \rangle + 1)$. This result shows that an additional number of G photons are put into the output mode independent of the number of input photons, one extra noise photon per $\langle n_4 \rangle$ input photons. This characteristic is a result of the "conjugation" properties of the system and the commutation properties of bosons, i.e., the fact that the output operator a_3 depends on a_4^\dagger and Equations 4.3. Further, the output photon number variance can be calculated using Equation 4.9 and

$$\langle n_3^2 \rangle = \langle a_3^\dagger a_3 a_3^\dagger a_3 \rangle = \langle a_3^{\dagger 2} a_3^2 \rangle + \langle n_3 \rangle$$

to be :

$$\Delta n_3^2 = \langle n_3^2 \rangle - \langle n_3 \rangle^2 = G^2 \Delta n_4^2 + G(G+1)(\langle n_4 \rangle + 1) \quad 4.10$$

The normal ordering variance, associated with the normal ordering intensity $W_i = a_i^\dagger a_i$, is:

$$\begin{aligned} \Delta W^2 &= \langle W^2 \rangle - \langle W \rangle^2 = \langle :n_3(0)^2: \rangle - \langle :n_3(0): \rangle^2 \\ &= \langle a_3^\dagger a_3^\dagger a_3 a_3 \rangle = G^2 (\Delta n_4(0)^2 + \langle n_4(0) \rangle + 1) \end{aligned} \quad 4.11$$

The last term in both Equations 4.10 and 4.11 can be associated with added noise due to the conjugation process itself, independent of fluctuations in any of the inputs (the probe or the added noise F). It is interesting to note from Equations 4.8 and 4.10, 4.11, that the noise associated with the FWM process itself only affects the output intensity variance, whereas the variance of the output quadratures are affected by the noise associated with the empty port.

The previous description, although valid for "ideal noise", is also valid when the medium fluctuations are included. In that case, the operator F can be associated in part with the empty port and in part with the medium noise. The main modification results in an effect on the intensity because the part associated with the medium fluctuations of the

average value $\langle FF^+ \rangle$ is finite and modifies Equations 4.10 and 4.11 and the value of $\langle n_3(0) \rangle$. The modifications introduced by the medium fluctuations are discussed in Section 4.4.

The description above can be extended to a multimode system by an appropriate generalization of the evolution equations, commutation relations and variances. The main difference in the results is that the analog to the added noise number is an added noise spectral density, which has the same general form as A but depends on $G(\omega)$ or the reflectivity at each frequency, so that the added noise fluctuations are not uniform in frequency. This frequency dependence of the noise can play an important role in systems that utilize nondegenerate FWM PC.

In the next sections we calculate the added noise for particular FWM PC examples.

4.3 Lossless Four Wave Mixing Phase Conjugator Quantum Noise

4.3.1 Action of a Degenerate FWM PC

In this section we will demonstrate that the noise characterization described in the previous section is in fact satisfied by an ideal DFWM PC and will calculate the quadrature variances as a function of the PC characteristics. In order to simplify the calculation we make the following idealized assumptions:

1. Kerr nonlinear media
2. Single mode. Degenerate FWM
3. Large pump intensity: $I_{\text{pump}} \gg I_{\text{probe}}$. Pumps are treated classically
4. Negligible fluctuations in the nonlinear media
5. Small probe and pump intensities, treated with quantum mechanics
6. Absorption and pump depletion neglected
7. Quantum fluctuations in both the input probe and the conjugate empty input port.

Following the prescription from the previous section we transform the propagation equations for the probe and conjugate amplitudes and phase into operator propagation equations. Thus,

$$\begin{aligned} \frac{da_3}{dz} &= i\kappa^* a_4^+ & \frac{da_4^+}{dz} &= i\kappa a_3 \end{aligned} \quad 4.12$$

where the nonlinear coupling coefficient κ^* is related to the third order susceptibility $\chi^{(3)}$ and the pump intensity I through

$$\kappa^* = 2\pi\omega(I_1 I_2) \chi / cn.$$

The solutions to Equations 4.12 at the ends of the FWM cell (cf. Fig 4.1) are:

$$a_3(0) = \sec(\kappa L) a_3(L) - i(\kappa^*/|\kappa|)\tan(\kappa L) a_4^+(0) \quad 4.13a$$

$$a_4(L) = \sec(\kappa L) a_4(0) - i(\kappa^*/|\kappa|)\tan(\kappa L) a_3^+(L) \quad 4.13b$$

The output operators $a_3(0)$ and $a_4(L)$ satisfy the commutation relations, Equations 4.2, if the input operators do also. In fact by inspection of 4.13a, we can identify;

$$F = \sec(\kappa L) a_3(L) \quad 4.14$$

and

$$R = G^{1/2} \exp(i\phi) = \tan(\kappa L) \exp(i3\pi/2) \quad 4.15$$

for the operator associated with the conjugated wave, where for convenience we have assumed $\kappa^* = \kappa$. Thus, $[F, F^+] = \sec^2(\kappa L) [a_3, a_3^+] = [1 + \tan^2(\kappa L)] = 1 + G$, as predicted in Section 4.2. Assuming $a_3(L)$ to be a vacuum state ($\langle a_3 \rangle = \langle a_3^+ \rangle = 0$), we obtain for the variances in each of the quadratures of the output conjugate:

$$\Delta X_3(0)^2 = \langle X_3(0)^2 \rangle - \langle X_3(0) \rangle^2 = \sec^2(\kappa L) \Delta X_3(L)^2 + \tan^2(\kappa L) \Delta Y_4(0)^2 \quad 4.16a$$

$$\Delta Y_3(0)^2 = \langle Y_3(0)^2 \rangle - \langle Y_3(0) \rangle^2 = \sec^2(\kappa L) \Delta Y_3(L)^2 + \tan^2(\kappa L) \Delta X_4(0)^2 \quad 4.16b$$

Hence, even if a_4 is in a number state ($\langle a_4 \rangle = 0$), and both input fluctuations are in a minimum uncertainty state ($\Delta X^2 = \Delta Y^2 = 1/4$ in units of number of quanta), the input variances are amplified by the FWM PC process, to obtain:

$$\begin{aligned}\Delta X_3(0)^2 &= \Delta Y_3(0)^2 \\ &= [\sec^2(\kappa L) + \tan^2(\kappa L)]/4 = [1 + 2\tan^2(\kappa L)]/4 = (1 + 2G)/4\end{aligned}\quad 4.17$$

The total output conjugate variance for each quadrature is formed by a contribution from the empty port associated with $\Delta X_3(L)^2$ equal to or larger than $(1+G)/4$, and a contribution from the amplified input probe fluctuations $(\Delta Y_4(0)^2)$ and proportional to $G/4$, in agreement with the results from the previous section. It should be noted that the ratio of the amplified input noise (multiplicative noise) to the output conjugate intensity (for $\langle n_4(0) \rangle \gg 1$) is independent of gain, depending only on the input noise to signal ratio. On the other hand, the ratio of the additive noise to the output conjugate intensity becomes infinite as the gain $\rightarrow 0$ and it approximates the input empty port noise to signal ratio for high gains.

The variance in one of the quadratures relative to the classical reflectivity or gain is plotted in Figure 4.2 versus the nonlinear coupling coefficient κ times the cell length L to further illustrate the region of minimum noise for maximum gain. In particular, the figure illustrates that $\Delta X_3(0)^2 \rightarrow 1/2$ for $G \rightarrow \infty$, which occurs for $\kappa L = \pi/2$ if the input noise is in a minimum uncertainty state. A comparison of curves a and b show the relative importance of the additive to multiplicative noise (or amplified input probe noise).

4.3.2 Action of a Non-Degenerate FWM PC

A schematic diagram of a NDFWM PC is shown in Figure 4.3. The same formalism developed in Section 4.2 and applied in 4.3.1 can now be applied to nondegenerate FWM PC. Although the minimum limitation for high gain is still the same (the added noise number $A \rightarrow 1/2$), this example shows that the quantum noise limitation can be controlled by appropriate pump-probe detuning. Further, for the case where the noise is no longer ideal (absorption and spontaneous emission are included), a non degenerate FWM PC might present a parameter region where the noise introduced by the medium can be minimized.

The propagation equations for the NDFWM PC and the corresponding solution that determine the evolution equations for the operators are given in Reference 4.5. By inspecting the evolution equations (that include boundary conditions for the input conjugate at $z=L$), we find:

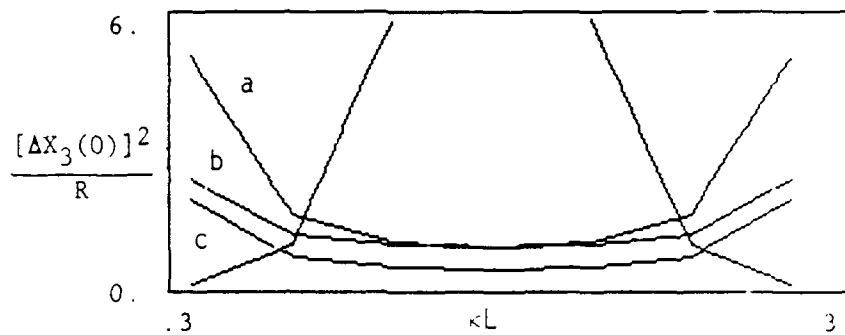


Figure 4-2. Relative variance in the output conjugate quadrature $(\Delta X_3(0))^2/R$ and reflectivity (or gain) R versus the nonlinear coupling coefficient κL .

Curve a: $[\Delta X_3(L)]^2 = 0.7$ $[\Delta Y_4(0)]^2 = 0.25$

Curve b: $[\Delta X_3(L)]^2 = 0.25$ $[\Delta Y_4(0)]^2 = 0.7$

Curve c: $[\Delta X_3(L)]^2 = 0.25$ $[\Delta Y_4(0)]^2 = 0.25$

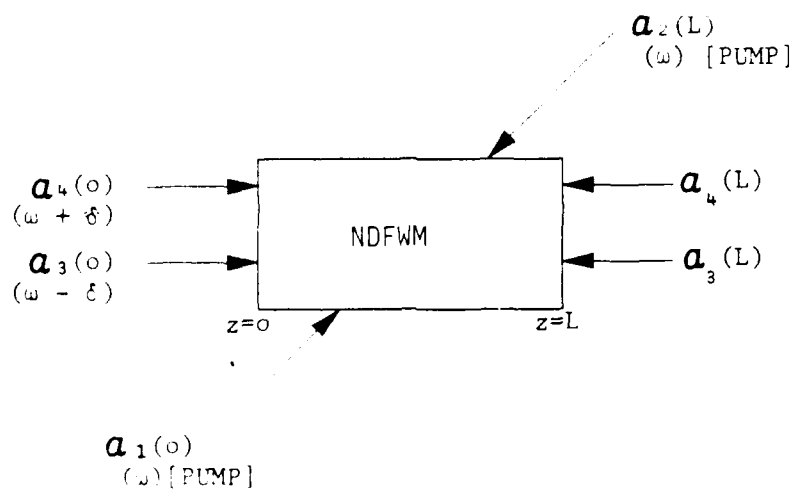


Figure 4-3. Schematic diagram of non-degenerate four wave mixing.

$$R = G^{1/2} \exp(i\phi) = -i\kappa_c^* \sin(\alpha L)/D \quad 4.18$$

$$F = [\exp(-i\Delta k L/2) \alpha/D] a_3(L) \quad 4.19$$

where $\kappa_c^* \approx (\omega - \delta) I_{\text{pump}}$ and $\kappa_p^* \approx (\omega + \delta) I_{\text{pump}}$ are the nonlinear coupling coefficients for the conjugate and probe, $\alpha = [(\Delta k^2/4) + \kappa_c^* \kappa_p^*]^{1/2}$, $D = \alpha \cos(\alpha L) - i\Delta k \sin(\alpha L)/2$, and $\Delta k = k_p - k_c = 2n\delta/c$ is the phase mismatch due to nondegenerate frequencies. Again, $[F, F^\dagger] = 1 + G$ for $\Delta k/\kappa \ll 1$ since the evolution equations are valid to that order, and we find that the quadratures variances can be written in terms of G as

$$\begin{aligned} \Delta X_3(0)^2 &= \langle X_3(0)^2 \rangle - \langle X_3(0) \rangle^2 \\ &= [(\alpha/D)^2 \Delta X_3(L)^2 + (|\kappa_c| \sin(\alpha L)/D)^2 \Delta Y_4(0)^2] \end{aligned} \quad 4.20a$$

$$\begin{aligned} \Delta Y_3(0)^2 &= \langle Y_3(0)^2 \rangle - \langle Y_3(0) \rangle^2 \\ &= [(\alpha/D)^2 \Delta Y_3(L)^2 + (|\kappa_c| \sin(\alpha L)/D)^2 \Delta X_4(0)^2] \end{aligned} \quad 4.20b$$

The normal ordering average intensity is $\langle W \rangle = \langle a_3^\dagger a_3 \rangle = G(\langle n_4(0) \rangle + 1) = (\kappa_c \sin(\alpha L)/D)^2$ and again we have assumed for convenience the input conjugate to be in a vacuum state.

The behavior of the relative output conjugate quadrature variance $(\Delta X^2/G)$ with the detuning parameter $\phi = \Delta k L/2\pi$, and the nonlinear coefficient κL is illustrated in Figures 4.4 and 4.6 respectively. Figure 4.4a and Figure 4.5 illustrate the relative roles of the additive and multiplicative noise. The variation of the reflectivity (or gain) $R = G$ with the detuning parameter is shown in Figure 4.4b. A comparison of Figs. 4.4a and 4.4b demonstrates the increase in noise from its minimum value (.5) as the reflectivity becomes < 1 , which occurs quite rapidly when either ϕ becomes $\neq 0$ or $\kappa L \neq \pi/2$.

An increase in the empty port fluctuations introduces an increase in the output noise that is larger than the one produced by the same increase in the input probe noise. This can be observed by comparing the various curves in Figures 4.4a and 4.5. The effect is negligible for large gain ($\phi \rightarrow 0$, or $\kappa L \rightarrow \pi/2$) as can be seen from the curve indicated with diamonds and the one indicated with crosses in Figure 4.5. The variation of the output

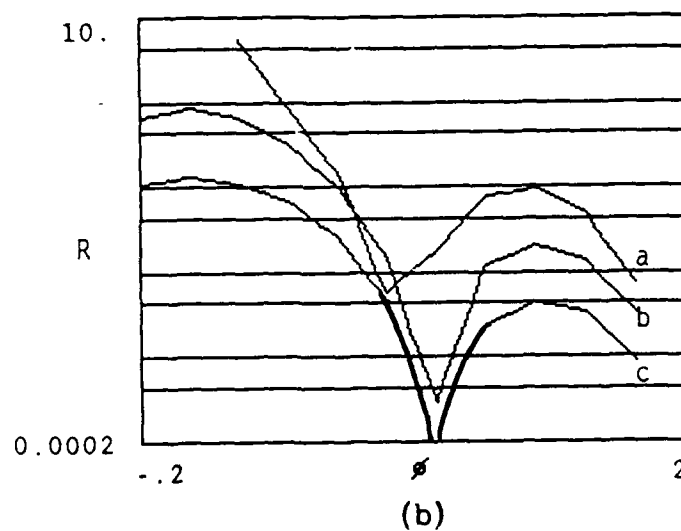
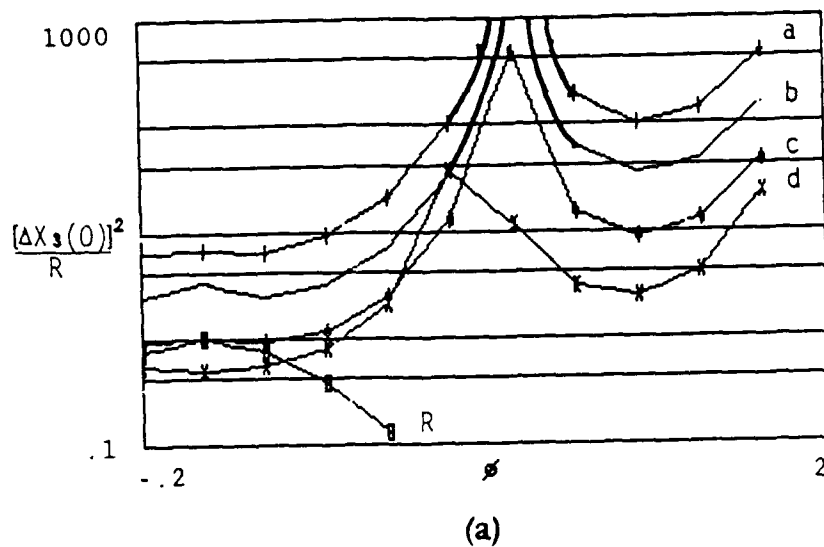


Figure 4-4(a). Relative variance of one output conjugate quadrature versus detuning parameter $\phi = \Delta kL/2\pi$ for various values of nonlinear coupling coefficient κL .
 Curve a: $[\Delta X_3(L)]^2 = .75$, $[\Delta Y_4(0)]^2 = .25$, $\kappa L = \pi/8$.
 Curve b: $[\Delta X_3(L)]^2 = .25$, $[\Delta Y_4(0)]^2 = .25$, $\kappa L = \pi/8$.
 Curve c: Same as curve b except $\kappa L = \pi/4$.
 Curve d: Same as curve b except $\kappa L = \pi/2$.
 Highest gain case.

(b). Reflectivity versus detuning parameter ϕ for various values of nonlinear coefficient κL .
 Curve a: $\pi/8$.
 Curve b: $\pi/4$.
 Curve c: $\pi/2$.

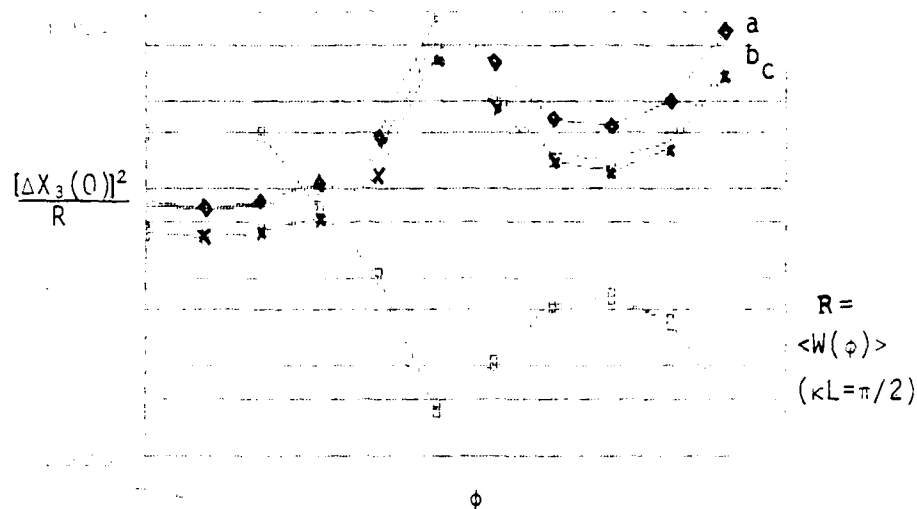


Figure 4-5. Relative variance of one of the output quadratures versus detuning parameter ϕ for $\kappa L = \pi/2$ and various values of input noise.
 Curve a: $[\Delta X_3(L)]^2 = .75$, $[\Delta Y_4(0)]^2 = .25$
 Curve b: $[\Delta X_3(L)]^2 = .25$, $[\Delta Y_4(0)]^2 = .75$
 Curve c: $[\Delta X_3(L)]^2 = .25$, $[\Delta Y_4(0)]^2 = .25$
 The reflectivity $\langle W(\phi) \rangle$ versus ϕ is also shown for comparison purposes.

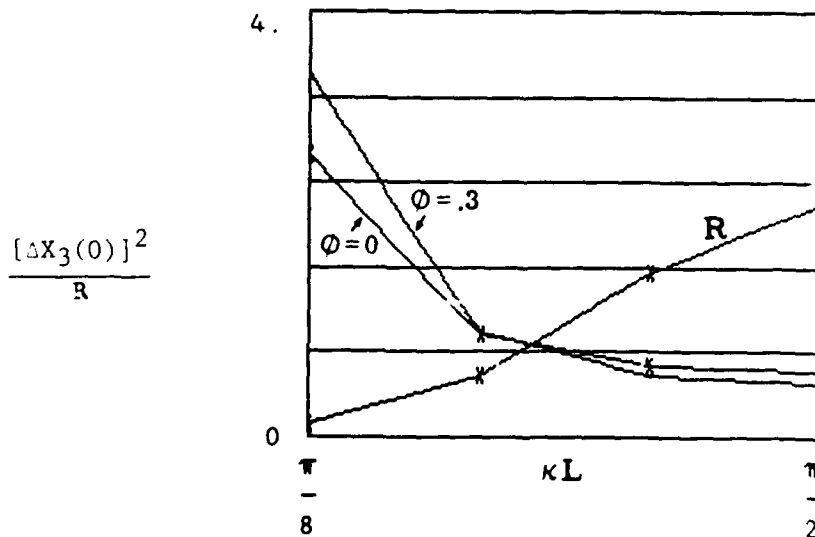


Figure 4-6. Variance of one output conjugate quadrature as a function of the nonlinear coupling κL for $\phi = 0$ (DFWM) and $\phi = 0.3$. Shown is reflectivity for $\phi = 0$.

noise with the nonlinear coupling coefficient is shown in Figure 4.6 where the results obtained in the previous section on degenerate FWM are recovered for $\phi = 0$.

4.4 Quantum Noise in a Lossy Medium

In the previous sections the noise has been assumed "ideal" and the medium lossless. In most actual cases, however, not only absorption occurs but other medium related effects such as spontaneous emission or radiative decay must be taken into account. In particular, quantum noise terms associated with atomic fluctuations (spontaneous emission or radiative decay) are required in the quantum mechanical description of the evolution equations for a lossy medium and add to the noise fluctuations associated with the empty port and the FWM PC process itself. These terms do not appear in the classical or even semiclassical descriptions of References 4.5 or 4.6.

We start the description by assuming a lossy medium and the prescription from Section 4.2 for obtaining the evolution equation of the output operators in term of the input operators. We demonstrate afterwards that non-zero quantum noise terms associated with atomic reservoir operators describing radiative decay or spontaneous emission are necessary for a self consistent description (References 4.2, 4.4). The "semiclassical" propagation equations (Reference 4.6) for the creation and annihilation operators can be written as:

$$\frac{da_3}{dz} = \alpha a_3 + i\kappa_L^* a_4^+ \quad 4.21a$$

$$\frac{da_4^+}{dz} = -\alpha^* a_4^+ + i\kappa_L a_3 \quad 4.21b$$

where α is the absorption or attenuation coefficient, and κ_L is the nonlinear coupling coefficient proportional to the input pump intensity. Again we assume that the pumps can be treated classically. For the case of a Kerr like media where α is independent of the pump intensity, $\kappa_L = \kappa \exp(-\alpha L)$, with κ the lossless nonlinear coupling coefficient previously described. It is straight forward to solve Equations 4.21 for α and κ independent of z (Reference 5) and obtain the semiclassical (Refer-

ence 6) evolution equations for the output operators, as follows:

$$a_3(0) = T \exp(i\alpha_1) a_3(L) - i R a_4^+(0) \quad 4.22a$$

$$a_4(L) = T \exp(i\alpha_1) a_4(0) - i R a_3^+(L) \quad 4.22b$$

where the transmission and reflection coefficients T and R are defined as:

$T = x/D$, $R = \kappa_L \sin(xL)/D$, with $D = \alpha_r \sin(xL) + x \cos(xL)$, $\alpha = \alpha_r + i\alpha_i$, and $x = (\kappa_L^2 - \alpha_r^2)^{1/2}$.

The imaginary part of the absorption coefficient relates to the intensity dependent refractive index of the medium and does not alter the minimum value of the output conjugate fluctuations. It only alters the relative phase between the two quadratures of the input fluctuations associated with the empty port. The output operators must satisfy the boson commutation relations (Equations 4.2); they do not as defined by Equations 4.22. The commutation of the output operators, if we make use of Equations 4.22 yields:

$$[a_3, a_3^+] = T^2 - R^2 = 1 + G - \Delta - G = 1 - \Delta \quad 4.23$$

The factor $\Delta = [\alpha_r^2 \sin(xL)^2 + \alpha_r x \sin(xL) \cos(xL)]/D^2$ can be associated with the missing quantum noise terms. In fact, in order to describe properly the lossy medium it is necessary to add a "noise" term in each propagation Equation 4.21.

An appropriate quantum theory that includes the quantization of the medium (non-ideal atomic noise) and loss, predicts the necessary noise terms. It assumes an infinite reservoir boson system to represent the radiative decay or stimulated emission with a Langevin force operator \hat{l} .

These operators have the property that $\langle \hat{l}(z), \hat{l}^+(z') \rangle = \alpha \delta(z - z')$. When the propagation equations are solved including the appropriate Langevin noise terms, we obtain (Reference 2):

$$a_3(0) = a_3(0)^{sc} + L_3 \quad 4.24a$$

$$a_4(L) = a_4(L)^{sc} + L_4 \quad 4.24b$$

where a_i^{sc} refers to the semiclassical solution and the terms L_3 and L_4 are appropriate integrals of the noise terms \hat{L}_3 and \hat{L}_4 . The solutions L_3 and L_4 satisfy $[L_3, L_3^+] = \Delta$, so that the appropriate commutation relations for the output operators are obtained :
 $[a_3(0), a_3^+(0)] = 1 + G - \Delta - G + \Delta = 1$. It is remarkable but not surprising to note that the solutions predicted by the full quantum mechanics treatment are the same that would have been obtained by the simple requirement of an extra noise term to satisfy the commutation relations.

From the evolution equations we can derive expressions for the variances of the output quadratures. In particular we find that the variance of the output conjugate quadratures is given by:

$$\Delta X_3(0)^2 - T^2(\Delta X_3(L)^2 \cos(\alpha_1 L)^2 + \Delta Y_3(L)^2 \sin(\alpha_1 L)^2) + R^2 \Delta Y_4(0)^2 + \langle L_3 L_3^+ \rangle / 2 - \Delta / 4 \quad 4.25$$

where the term $\langle L_3 L_3^+ \rangle = \Delta$ is defined in Equation 4.23. In the equation above the first two terms proportional to $1 + G - \Delta$ are associated with the added noise from the empty port amplified in an absorptive system, and the third term $-G$ is the noise associated with the amplification of the input signal fluctuations. The last two term are associated with the atomic fluctuations and their sum has the total value $+\Delta/4$. Thus, for the case where the empty port state is vacuum and the probe is in a number state, so that the input fluctuations satisfy $\Delta X = \Delta Y = 1/4$, the output variance for each quadrature is the minimum predicted in Section 4.2: $(1 + 2G)/4$. This result should have been expected once we obtained evolution equations of the form given by Equation 4.3 and that satisfy the commutation relations since in that case the formalism developed in Section 4.2 becomes valid.

The total noise is in part due to the empty port and in part due to the medium and therefore $\langle FF^+ \rangle$ is no longer 0 even for an empty port vacuum state. Thus, the main difference in the results for a lossy medium reside in the fact that the medium noise modifies the output intensity. For the mean value of the number operator n_3 we obtain :

$$\langle n_3 \rangle = G(\langle n_4 \rangle + 1) + \langle L_3 L_3^+ \rangle \quad 4.26$$

Hence, the noise generated by the medium imposes stronger requirements on the input intensity to avoid the unwanted noise fluctuations of the output conjugate intensity but does not alter the limit for avoiding output conjugate phase noise.

Figures 4.7 to 4.10 illustrate the results discussed in this section. In Fig. 4.7 we have plotted the variation with the absorption coefficient ($\alpha_r L$) of the ratio of the total output variance (added noise due to the empty port plus input probe fluctuations plus medium fluctuations) to the gain (G), the classical reflectivity. Curve a, b and c correspond to the values .2, .5 and 1 of the nonlinear coupling coefficient κL respectively. We note that as κL increases towards $\pi/2$ and hence the gain $\rightarrow \infty$ the noise decreases towards the predicted value of .5. The imaginary part of α has been assumed 0 in these figures for convenience.

The variation of the relative output conjugate variance with the nonlinear coefficient for 0 absorption coefficient (solid lines) and $\alpha_r L = .5$ is illustrated in Figure 4.8. In this figure we also show the increase in noise that occurs with a decrease in gain. The lossless result agrees with the one shown in Figure 4.2. The presence of absorption for the case of low pump intensity (no saturation) and no detuning from atomic resonance results in a decrease in gain and hence an increase in total noise.

Figures 4.9 and 4.10 show the relative contributions of the empty port, input fluctuations and medium fluctuations to the total variance. The noise associated with the medium fluctuations is shown in the curve marked with crosses. Figure 4.10 shows that for moderate absorption ($\alpha L \approx 0.5$) the effect of the noise on the intensity due to the medium fluctuations becomes much larger than on the variance of each quadrature for minimum input fluctuations.

At this point it should be noted that the above results can be easily generalized to include saturation and pump detuning from resonance as long as pump absorption can be neglected. In this case, and again because of the beauty of the formalism described in Section 4.2, the total added noise will be given by A defined in that section. The interest of course resides in the analysis of the regions of high and low gain versus detuning and the direct effect of the noise on the output intensity. This is of importance in the design of an experiment to determine the source of non ideal noise, as described in the next section.

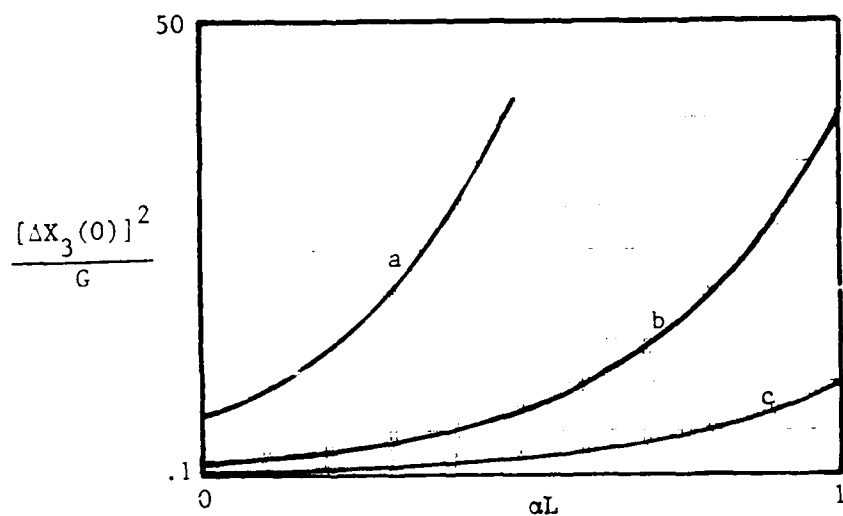


Figure 4-7. Relative variance of the output conjugate quadrature as a function of the real absorption coefficient, αL . Shown are curves for different values of the nonlinear coupling coefficient, κL : a) $\kappa L = 0.2$, b) $\kappa L = 0.5$, c) $\kappa L = 1.0$

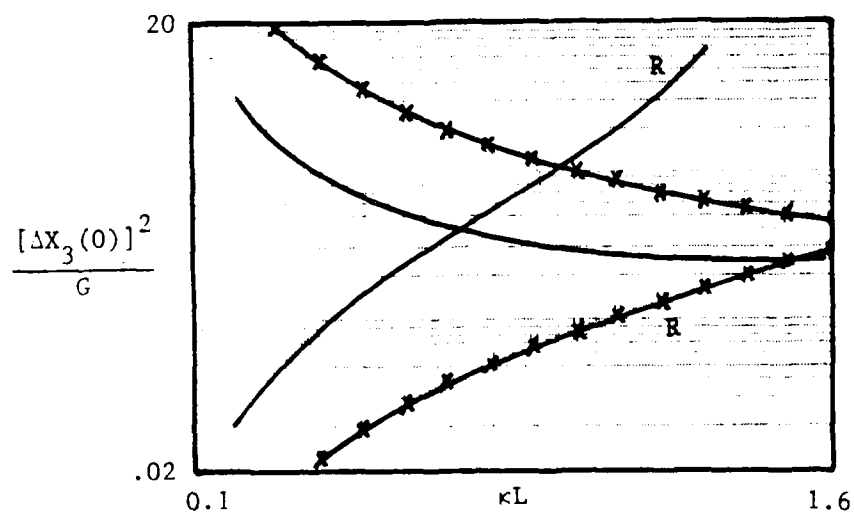


Figure 4-8. Relative variance of the output conjugate and FWM reflectivity as a function of the nonlinear coupling coefficient, κL for two values of real absorption. The solid lines are for $\alpha L = 0$ and the crossed lines are for $\alpha L = 0.5$.

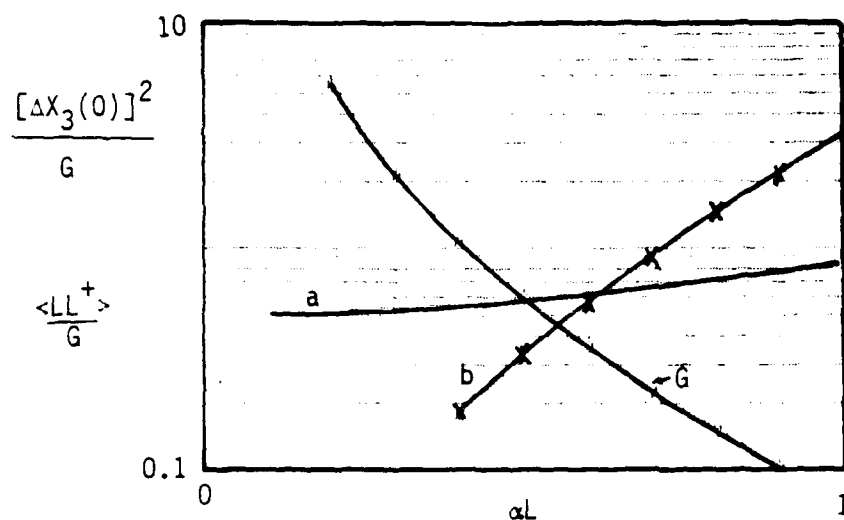


Figure 4.9. Comparison of contribution to the output conjugate quadrature variance from amplified input noise (empty port plus probe) and atomic fluctuations. Curve a): contributions to the relative variance from the empty port and input probe fluctuations assuming minimum input quantum fluctuations; curve b): relative atomic fluctuation noise. Also shown is the gain behavior, G .

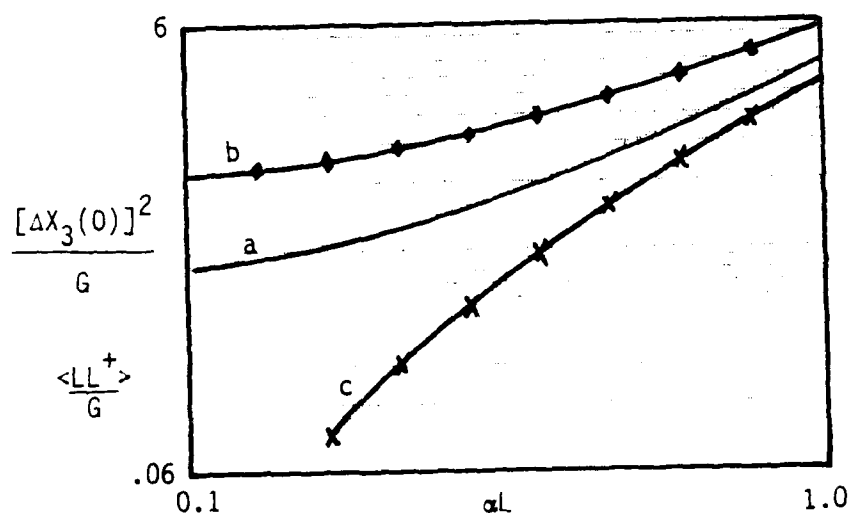


Figure 4.10. Relative contributions to the output conjugate quadrature variance from the amplified empty port noise, the amplified input probe, and the atomic fluctuations for a system where the empty port is not in a vacuum state. Curve a): total relative variance for minimum input fluctuations, b): for empty port input variance ~ 1 , Curve c): the relative contribution of the atomic fluctuations.

The results of Section 4.2 are no longer valid if the noise introduces terms proportional to a_4 rather than to a_4^+ in the evolution equation for a_3 . This might occur if pump absorption and depletion plays an important role.

4.5 Mode Combination as a Noise Source Detector

Recently, a great deal of attention has been given to a type of combination states, "squeezed states", that permit the reduction of noise below the quantum limit in one of the quadratures. One of the approaches that has been proposed and demonstrated to achieve squeezed states is FWM PC (Reference 4.7). Hence, the question arises if these combination states can be utilized to either create a conjugate with a lower noise in one of the quadratures or as a source of noise detection mechanism.

The new mode must be constructed by combining the phase insensitive output modes. Figure 4.11 illustrates how this is accomplished. The conjugate and probe output are combined by means of a delay line, a mirror and a beam splitter. The latter plays the dominant role in creating a squeezed mode.

In fact, following the same formalism as in the previous sections, we can write the combined modes operators b_{\pm} , that occur after an ξ transmissive, β reflective beam splitter as

$$b_{\pm}(1+L) = \xi a_3(0) \pm i\beta a_4(L) \quad 4.27$$

By using the evolution equations of Section 4.3, the combined output modes can be written in terms of the input operators $a_3(L)$ and $a_4(0)$ as follows:

$$b_{\pm}(1+L) = \mu b_{\pm}(L) \pm (\nu\xi/\beta) b_{\pm}(L)^+ \pm \nu a_3(L)^+ [\xi^2 - \beta^2]/\beta \quad 4.28$$

where ν and μ depend on the FWM PC characteristics. In particular, for DFWM we have $\nu = \tan\kappa L$ and $\mu = \sec\kappa L$. Equation 4.28 shows that the noise operator F defined in section 4.2 is 0 for $\xi = \beta$, i.e., a 50/50 beam splitter. As we change the beam splitting ratio noise is added to the system that is proportional to the empty port fluctuations.

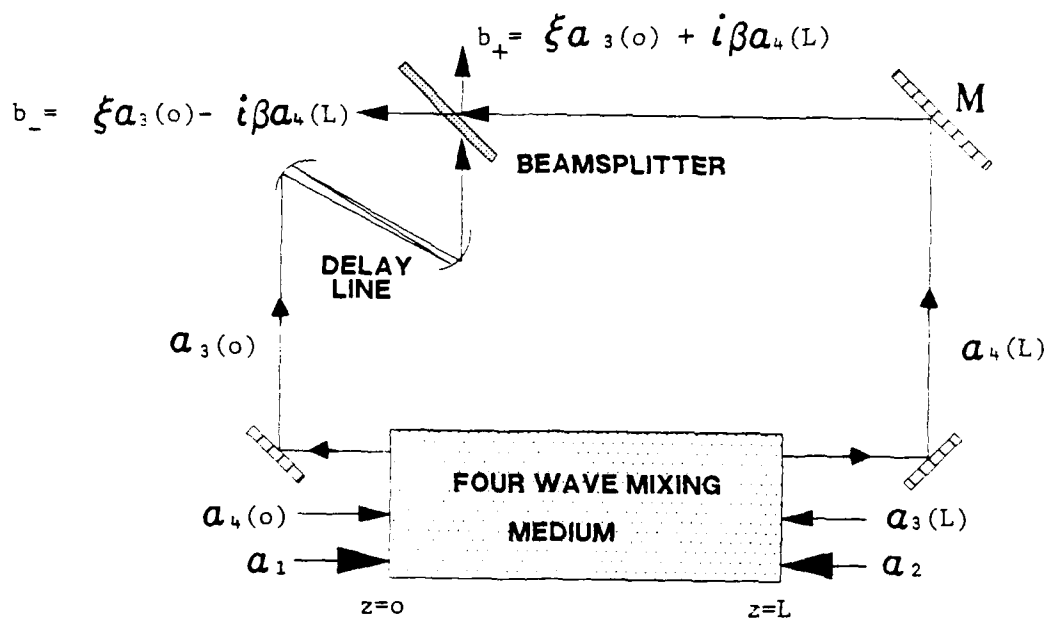


Figure 4-11. Mode combination scheme for characterizing noise sources in FWM media. A combination of probe and conjugate can lead to squeezed states where the variance of one quadrature can be reduced below the quantum limit.

A calculation of the quadrature variances for the combined modes $b_{\pm} X_{\pm} + Y_{\pm}$ yields for the minus mode:

$$\Delta X(1+L)_-^2 = |\mu - \nu\xi/\beta|^2 \Delta X(L)_-^2 - \Delta X_3(L)^2 \nu(\xi^2 - \beta^2)/\beta \quad 4.29$$

$$\Delta Y(1+L)_-^2 = |\mu + \nu\xi/\beta|^2 \Delta Y(L)_-^2 + \Delta Y_3(L)^2 \nu(\xi^2 - \beta^2)/\beta \quad 4.30$$

with $|\mu|^2 - |\nu|^2 = 1$ due to the commutation properties. Equations 4.29 and 4.30 show that squeezing is obtained in one of the quadratures for a 50/50 beam splitter.

Unfortunately, because the combination mode is formed by part conjugate and part probe output it is not useful in most of the relevant applications (if the mode is uncombined, the reduction in the variance in one of the quadratures is lost). On the other hand, this mode can be utilized to characterize the noise that is proportional to $\Delta X_3(L)$ or the empty port. In fact, a measure of the empty port noise can be obtained by varying the ξ/β ratio and measuring the combined mode variances.

The generalization of the previous results to a non ideal medium with losses and spontaneous emission shows that the combined mode can also provide a degree of information about the atomic fluctuations. In fact in the non ideal case, the calculation of the quadratures gives :

$$\Delta X(1+L)_-^2 = \Delta X(1+L)_-^2_{\text{ideal}} + (\xi^2 + \beta^2) \langle L_3 L_3^+ \rangle / 2 - \xi\beta \langle L_3 L_4^+ \rangle \quad 4.31$$

where we have assumed $\alpha_1 = 0$ for convenience. Hence by varying κ (but keeping the absorption constant) only the empty port contributions are varied whereas by varying the beam splitting ratio, the empty port and the atomic fluctuations contributions are varied. Further noise identification could be obtained by using pump probe detuning as well as detuning from resonance which might identify contributions from resonance fluorescence. We have not investigate these possibilities in detail, but the previous discussion shows that it might be worth investigating in the future if atomic fluctuation noise proves a strong limitation to the investigation of interest.

4.6 References

- 4.1 C. M. Caves, Phys. Rev. D 26, 1817 (1982).
- 4.2 P. Kumar and H. Shapiro, Phys. Rev. A 30, 1568 (1984); Seng-Tiong Ho, P. Kumar and H. Shapiro, "Quantum Theory of Nondegenerate Multiwave Mixing", preprint, sent for publication to Phys. Rev. A, 1988; M. D. Reid and D.F. Walls, Phys. Rev. A, 31, 1622(1985).
- 4.3 "Physical Interpretation of Squeezed States", R. W. Henry and S. C. Glotzer, submitted for publication to Phys. Rev. A XX, 1988, TRW preprint (1987).
- 4.4 Jan Perina, Quantum Statistics of Linear and Nonlinear Phenomena, D. Reidel Publ. Co., Dordrecht, Holland 1984.
- 4.5 Robert Fisher, ed., Optical Phase Conjugation, Acad. Press., NY, 1983, pgs. 44-47.
- 4.6 P. Kumar and J.H. Shapiro, Phys. Rev. A 30, 1568 (1984).
- 4.7 R.M. Shelby, M.D. Levenson, D.F.Walls, G.J. Milburn, A. Aspect, Phys. Rev. A 33, 4008 (1986).

NLOT AREA II: PHASE CONJUGATED
SOLID STATE LASER TECHNOLOGY

Sections 5 - 8 of this report describe technical effort in the area of phase conjugated solid state lasers. TRW subcontracted approximately one-half of the effort to Spectra Technology, Inc. of Bellevue, Washington, to characterize a new phase conjugated oscillator/amplifier configuration. Their final report is presented as Section 5, Ring Oscillator Power Amplifier (ROPA). The rest of this report, Sections 6 - 8, present experimental work and analysis performed by TRW.

5.0 RING OSCILLATOR POWER AMPLIFIER

A Final Report Submitted by:
Spectra Technology, Inc.
Bellevue, Washington

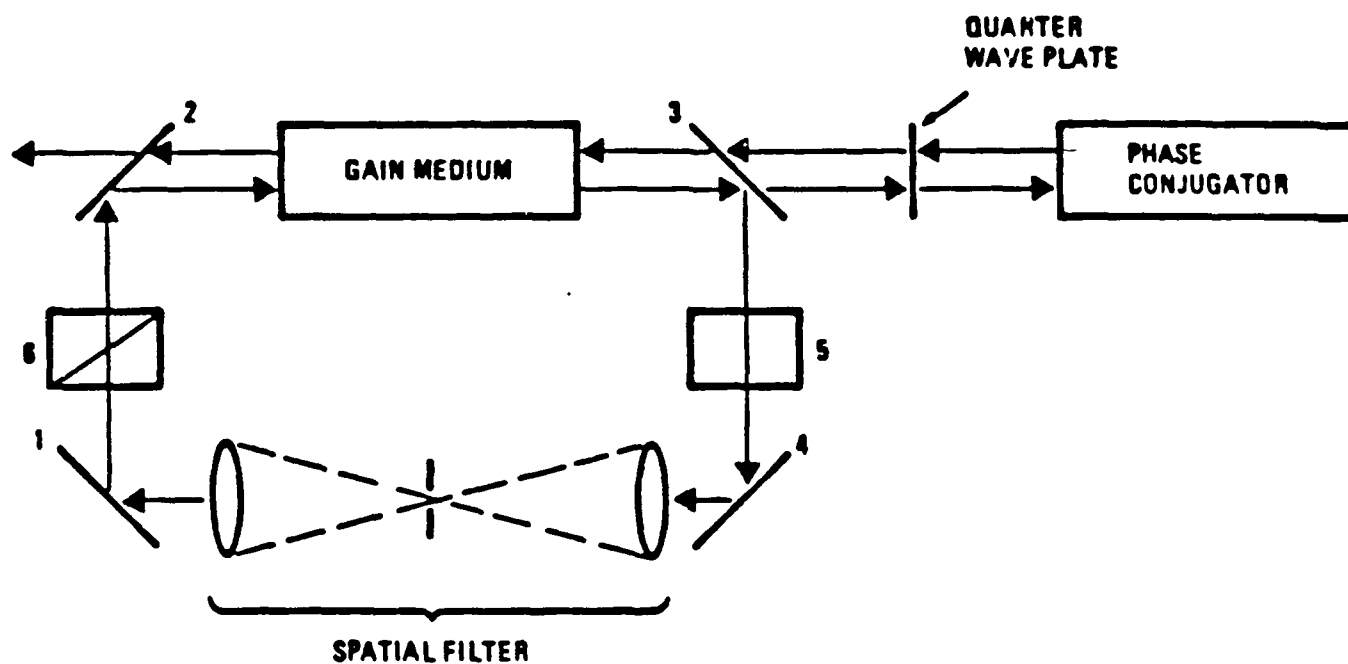
5.0 RING OSCILLATOR POWER AMPLIFIER

5.1. INTRODUCTION

The most critical factor determining the beam quality of the solid state laser is the geometry of the energy deposition and dissipation, which results from the gain medium temperature gradients. From the wave front quality point of view, the slab gain geometry has a number of advantages. It provides a large surface to volume ratio and thus the heat dissipation can be very efficient. Secondly, it is possible to propagate the wave along a zig-zagged path using the slab walls as a total internal reflection surfaces. As a result, the optical path differences across the slab aperture can be reduced. This approach, although very productive in reducing the wave front distortion, still leaves a residual aberration due to end effects. Therefore, the wave fronts emerging from the slab lasers still show some degree of aberration.

One approach for correcting these residual aberrations involves non-linear optical phase conjugation. This approach has the advantage that the correction is independent of the amount of distortion (5.1), and can correct for real time changes in the magnitude and nature of the aberrations. Thus, it is possible to use phase conjugation to correct for the gain medium aberrations over a large and varying energy loading range. The combination of a slab gain medium and NLO phase conjugation make possible a novel concept for a master oscillator that provide good beam quality output at pulse energies in the 100 mJ range. This chapter will detail the experimental studies involving this ring oscillator SBS phase conjugator system. This configuration is known as a Ring Oscillator Power Amplifier (ROPA).

The ROPA device is conceptually simple in its principle of operation. A schematic of the device is shown in Figure 5-1. To understand the principle of operation of the ROPA let us follow the path of the light around the system. Starting at the gain medium, the wave first



1. HIGH REFLECTIVITY MIRROR
2. POLARIZER 100% TRANSMISSION FOR P POLARIZATION 100% REFLECTIVITY FOR S POLARIZATION
3. MIRROR/POLARIZER 100% TRANSMISSION FOR P POLARIZATION, 50% REFLECTIVITY FOR S POLARIZATION
4. HIGH REFLECTIVITY MIRROR
5. FARADAY ROTATOR
6. PCKELS CELL Q-SWITCH

Figure 5-1. Schematic of ROPA Identifying All Major Components.

encounters a special out-coupling optic. It is 50% transparent to S polarized light and 100% transparent to P polarized light. Since only S polarized light is fed back into the resonator, the resonator will run in the S polarized mode. Moving farther around the ring, the light is focused into a tight spatial filter. The aperture is designed to clean up the beam which at this point carries all the aberration from thermal induced media inhomogeneities, allowing only pristine, diffraction limited light on the other side of the aperture. This light now passes through the gain medium, reacquiring the wavefront aberration. When it arrives at the out-coupler, half of it passes out of the resonator into the phase conjugating portion of the device.

In this leg a $\lambda/4$ plate converts the beam to circularly polarized light and focuses it into an SBS cell containing 1400 psi of methane. The SBS process produces a time reversed phase conjugate replica of the input wave. This wave proceeds backwards along the same path, once again encountering the $\lambda/4$ wave plate which produces P polarized light. This polarization passes cleanly through the out coupling optic and retraverse the aberrated gain medium. At the end of its traverse, it is returned to the pristine condition of the original input wave via the well known beam clean-up process. The next optic encountered on its path, also has a polarization dependent coating that is 100% reflective for S and 100% transmitting P polarization. Therefore, it passes through the optic and out of the system. The end result is that the last pass through the gain media both cleans up and amplifies the phase conjugated replica of the original oscillator output. This is the Power Amplifier portion of ROPA.

The central portion of the ROPA is the ring master oscillator. In many ways this is a conventional oscillator which takes advantage of the angular stability enhancement found in ring type systems (5.2). This stability is essential to the ROPA, because of the two lenses and the aperture which make up the spatial filter. The lens in their concentric configuration produce an oscillation which occupies the line between stable and unstable optical oscillators. Therefore, without the ring geometry,

the slightest angular deviation would cause the optic axis to walk away leading the unacceptable cavity losses.

5.2. EXPERIMENTAL CONFIGURATION

The actual experimental configuration developed in the course of the studies presented here is shown on Figure 5-2. The gain medium used during the experiments was STI's Centurion laser head (5.3). This head is a zig-zag Nd:YAG slab capable of providing approximately 70 W of average power with the pump efficiency of the order of half percent. Aberration averaging provided by zig-zagging of the beam in the volume of the slab resulted in about one wave of aberration (full aperture) under the 100 J/pulse of the energy loading while operating the laser at the repetition rate of the order of one Hz. A ring oscillator was built around the Centurion head.

5.2.1. Ring Oscillator Power Amplifier

The ROPA oscillator, as previously noted is a ring. To assure the unidirectional oscillation, an optical diode consisting of a Faraday rotator and a $\lambda/2$ plate was used. This diode provided counter-propagating beam discrimination of the order of 3 to 4 percent which was enough to assure the unidirectionality of the ring (5.4). It also kept the polarization non-uniformities across the diode aperture at the very low level, critical for low voltage hold-off of the cavity Q-switch. (A KD*P Pockel cell driven by a Krytron driver was used as a Q-switch.) The cavity also included a spatial filter whose function was twofold: it controlled the amount of the aberration of the wave oscillating in the cavity, and it controlled the transverse mode content of the oscillator. The filter consisted of two lenses with a focal length of 30 cm. The relative separation of the lenses defined the waist of the fundamental cavity mode (5.5). The spatial filtering was accomplished by inserting a hard aperture into the waist of the spatial filter. To control the axial mode content, a solid (BK7) etalon was inserted into the cavity. The thickness of the

etalon was 5 mm and reflectivity of both surfaces was around 60%. Thus, the bandwidth of the etalon was of the order of 3 GHz.

It was necessary to provide the oscillator with good polarization discrimination, as was dictated by the chosen Q-switching technique (e.g. Pockel Cell), the use of a Faraday rotator as the intracavity optical diode, and the shared aperture configuration of the oscillator-amplifier system. To ensure a well defined polarization of the oscillating wave, two out of six intracavity mirrors were thin film polarizers. The polarization discrimination was also aided by the oscillator output coupler which was 50% reflective for S polarized wave and over 80% transmissive for P polarization.

The aperture of Centurion is a rectangle of 6 by 20 mm. To conduct the studies reported here a smaller oscillator aperture was established. This was necessary because of the limited size of the available pieces of FR-5 glass, (high Verdet constant material used as active medium in the Faraday rotator). The rotator aperture was approximately 6 mm and it was the smallest aperture outside of the spatial filter (the filter aperture was approximately 250 micron). In addition, the cavity included a number of other elements whose apertures were smaller than that of the slab. Among these were the aperture of the half wave plate and the aperture of the Pockel cell (both approximately 12 mm in diameter).

The oscillator output coupled fraction was approximately 50%, with a cavity length approximately 2 meters. This provided a cavity lifetime of the order of 16 ns and the cavity mode separation of the order of 0.15 GHz. The oscillator bandwidth was measured with an air-spaced 10 mm thick Fabry-Perrot etalon comprised of mirrors with 80% reflective coating, thus the bandwidth of the measuring etalon was of the order of 1.1 GHz. Using this etalon as the output analyzer it was shown that the oscillator output had the bandwidth less than 3 GHz. The bandwidth resulted from the intracavity etalon transmission and the mode competition which contributed to narrow-banding.

5.2.2 The Oscillator Wave Front

The intracavity filter performed the role of controlling the transverse mode content, and reducing the amount of the wave front aberration at the filter exit aperture. The oscillator cavity was configured in such a way that the aberrator (gain medium) was positioned between the spatial filter and the output coupler. This assured that the aberrating of the output wave was dominated by a single (the last) pass through the medium. However, the spatial filter was not the only element controlling the wave front. As it turned out, the other apertures of the cavity also participated in preventing multi-pass propagation of the aberrated part of the beam in the oscillator cavity. Thus, the spatial coherence of the output wave was primarily controlled by the hard aperture of the spatial filter while the amount of the wave front aberration as controlled primarily by the sequence of the intracavity apertures positioned outside of the spatial filter (this effect is discussed in greater extent in Section 5.3.2 of this report).

5.2.3 SBS Cell Characteristics

To demonstrate the aberration correction in the slab gain medium, as SBS cell (filled with methane under the pressure of 1400 psi) was used as the phase conjugator. The SBS reflectivity threshold was reached at the oscillator output value of 13 mJ. Figure 5-3 presents the reflectivity data of the SBS cell used during the studies of ROPA. At the value of the output energy of 30 mJ, which resulted from the operation of the oscillator at low repetition rate, the SBS cell conjugated the light with an efficiency of approximately 30% of the initial energy.

5.2.4 Diagnostics

The primary purpose of ROPA is to generate near diffraction limited light at energy levels and repetition rates which exceed the normal limits. To determine if this is possible the main quantities of interest

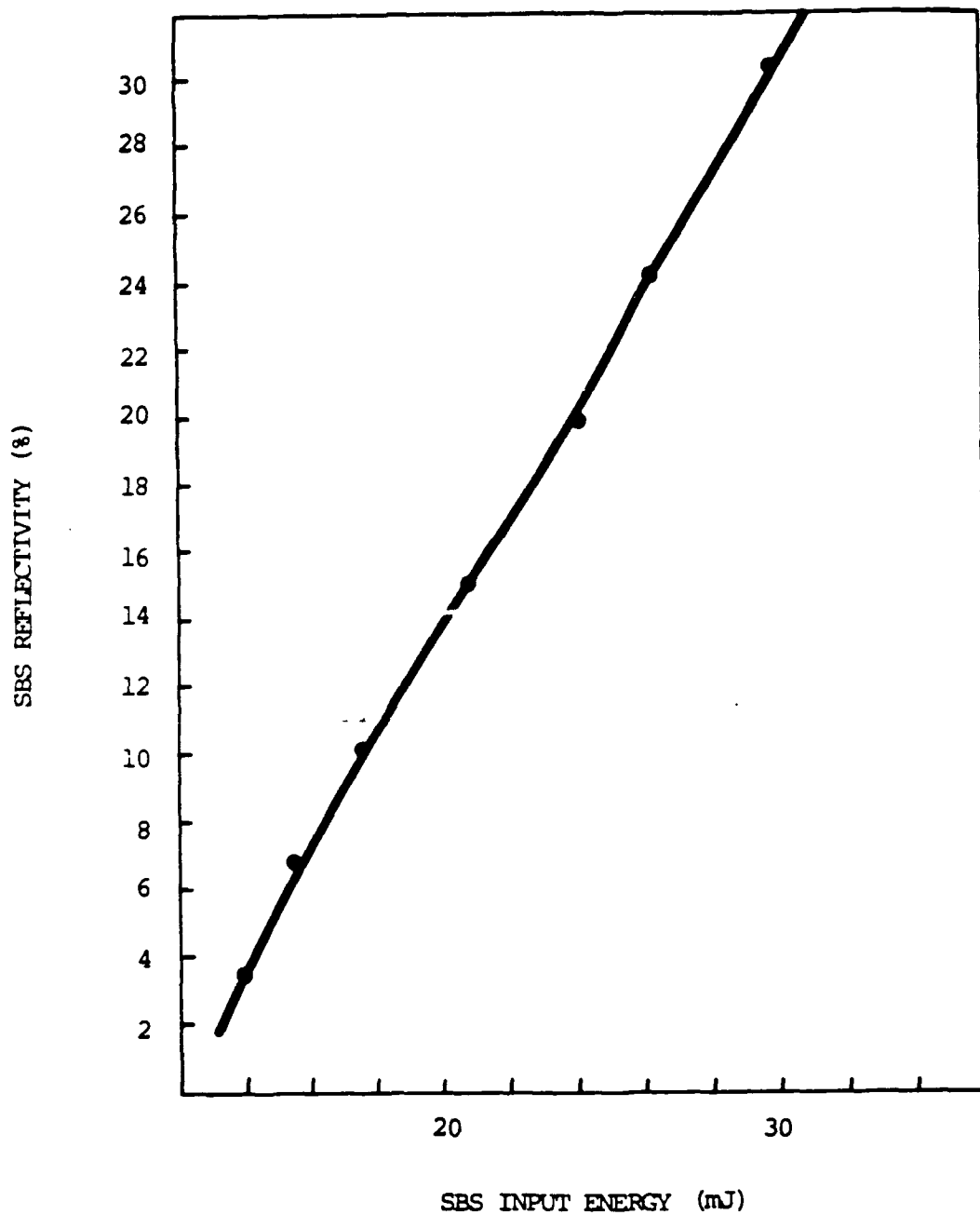


Figure 5-3. The Reflectivity of the SBS Cell Filled with Methane Under 1400 psi Pressure. The 6 mm Beam Diameter was Focused with the Lens of the Focal Length of 300 mm. The Pulse Length at the 30 mJ Input was 30 ns.

are wavefront quality and pulse energy as a function of repetition rate. The studies of ROPA focused on the following aspects of the system: energy extraction characteristics of the oscillator and the amplifier, wave front characteristics of the oscillator and the amplifier output, Strehl ratio characteristics of the oscillator and the amplifier output (the Strehl ratio measurements were undertaken to collaborate the wave front studies), and the system angular sensitivity studies.

The extraction efficiency data, important for anchoring future scaling calculations, was obtained by monitoring the output energy while controlling conditions of operation of the gain medium. To do this, a pyroelectric detector was used as an energy monitor.

To monitor and record the wave front shapes, a Mach-Zender type point diffraction interferometer was used. The interferometer set-up is presented in Figure 5-4. Along one of the paths, the reference wave was filtered by a subdiffraction limited spatial filter. Following this, the reference wave was interfered with original wave at the CID sensor array. In this way a wave front interferogram was created and recorded.

The interferometer included an imaging lens which played a double role. First, it created the far field image at the hard, diffraction limited aperture of the interferometer spatial filter which resulted in generation of the aberration-free reference beam. Second, it imaged an aperture under study on the CID array. Therefore the distance between the lens and the CID array defined the position of the aperture where the wave front was recorded. Thus, it was possible to select the positions in the ROPA configuration at which the wave fronts were recorded.

Data on the Strehl ratio was obtained by measuring the transmission of the pulse through a subdiffraction limiting aperture (5.6). During this experiment the total pulse energy and the energy of the transmitted beam were monitored and recorded. Both the total and the transmitted energies were averaged over the 100 shots and the Strehl ratio was computed for a

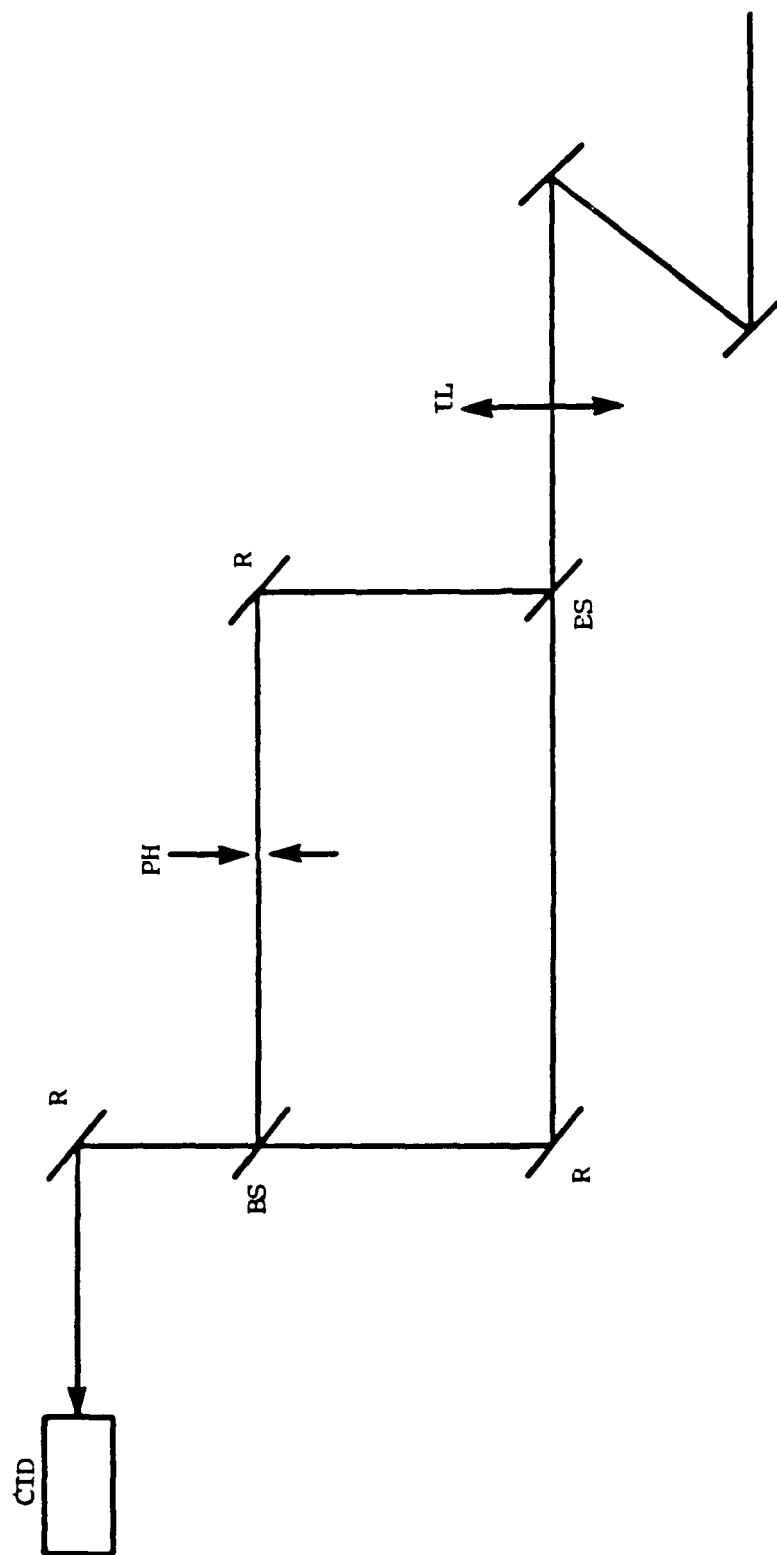


Figure 5-4. The Point Diffraction Interferometer Used to Diagnose the Wave Fronts. The Symbols in the Figure Designate: IL-imaging lens, BS-beam splitter, R-reflector, PH-pinhold, CID-the image sensor.

15710

set of conditions of the gain medium operation.

The data on the angular sensitivity of the oscillator was obtained by monitoring the output energy while changing the detuning angle. The pyroelectric detector was used to monitor the energy, while the detuning angle was controlled by observing the walk-off of the reference HeNe beam bouncing off the detuned cavity mirrors. During these studies, the output energy was monitored while detuning the angle of reflection of one of the cavity mirrors. Thus it was possible to assess the detuning angle for which the output energy decreased to the half of the maximum value.

5.3. SYSTEM PERFORMANCE

During the course of the studies reported here, the oscillator, the amplifier and the ROPA were characterized. The results of the experiments are presented in the following paragraphs.

The alignment of the oscillator, the amplifier, and the ROPA was conducted while operating the gain medium at the repetition rate of 7.5 Hz and driving the flash lamps at the voltage of 1.6 KV. Under these conditions, the power loading of the slab was close to its lower limit. Thus, the conditions of the head operation were conducive to the generation of a good quality, stable output. At this level of the flash lamp energy, the gain medium was loaded with 100 Joules per shot, and the laser head was capable of providing 50 watts of average power from its full aperture while driven at 100 Hz repetition rate. (The operation of Centurion at 140 Joules per shot at 100 Hz yielded 70 Watts from the full aperture.)

5.3.1 Oscillator Performance

The oscillator energy extraction data is presented in Figures 5-5 and 5-6. The figures present the extraction data obtained while operating the laser at the repetition rate of 7.5 Hz. Figure 5-5 a shows the data on the oscillator operating in a free running mode without the hard aperture in the spatial filter. Figure 5-6 a shows the data on the Q-switched oscillator without the hard aperture in the spatial filter. This data showed how much energy could be extracted in the oscillator volume and it defined the baseline for the extraction experiments. It should be noted that the result is consistent with the fact that free-running operation of the Centurion head inside of the linear cavity with a 50% output coupler yielded 370 mJ per pulse at 100 Joules of energy loading. It was expected that the operation of the oscillator with the aperture equal to 1/4 of the full aperture should yield the output energy in the neighborhood of 90 mJ. Thus, the free running oscillator data obtained in the course of these studies is consistent with the previously reported performance of

87 15765

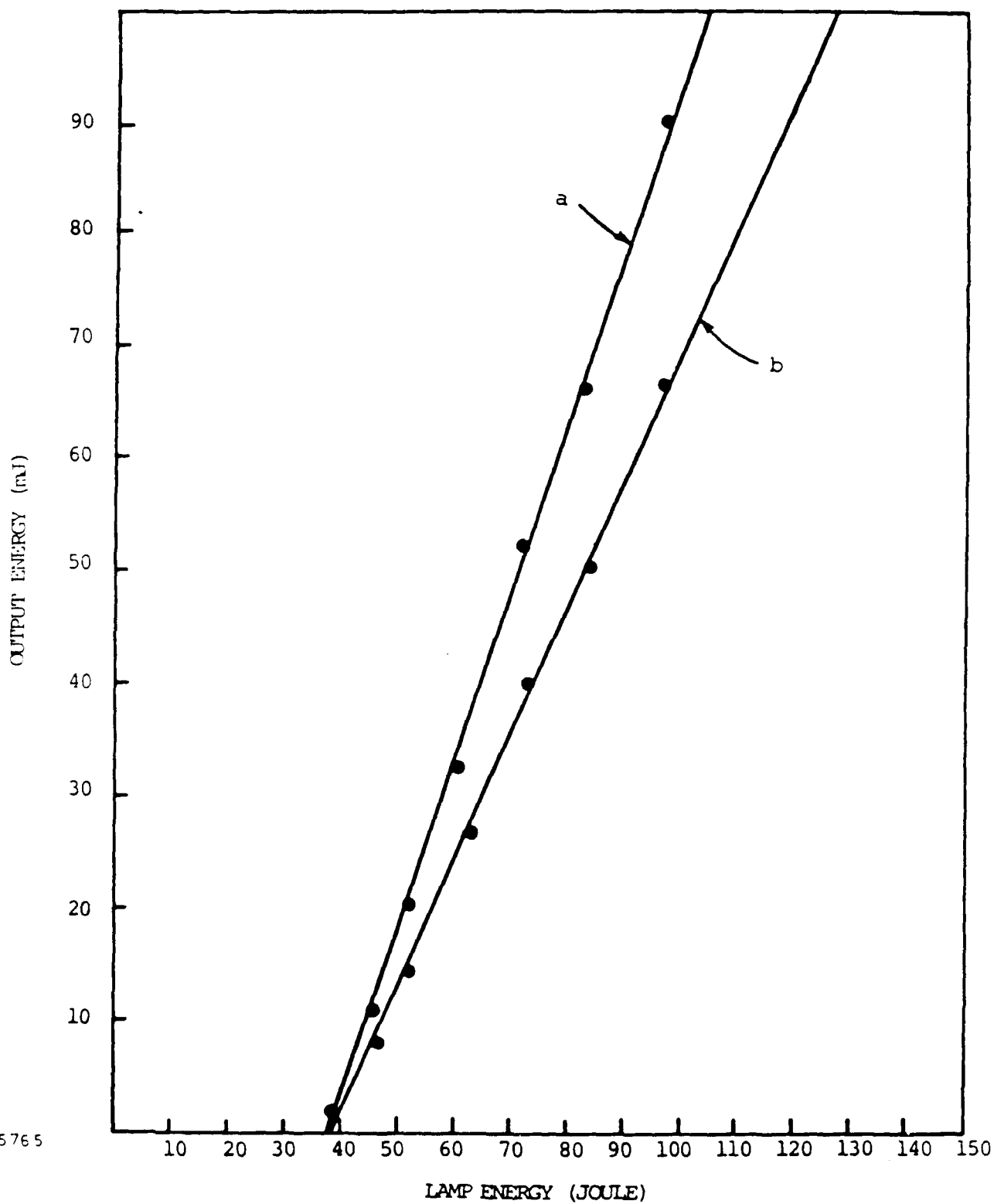


Figure 5-5 . The Extraction of the Energy from the Ring Cavity Defined by the 6 mm Aperture. The Line a Shows the Energy Extracted in Free-Running Mode. The Line b Shows the Energy Extracted During Q-Switching of the Cavity.

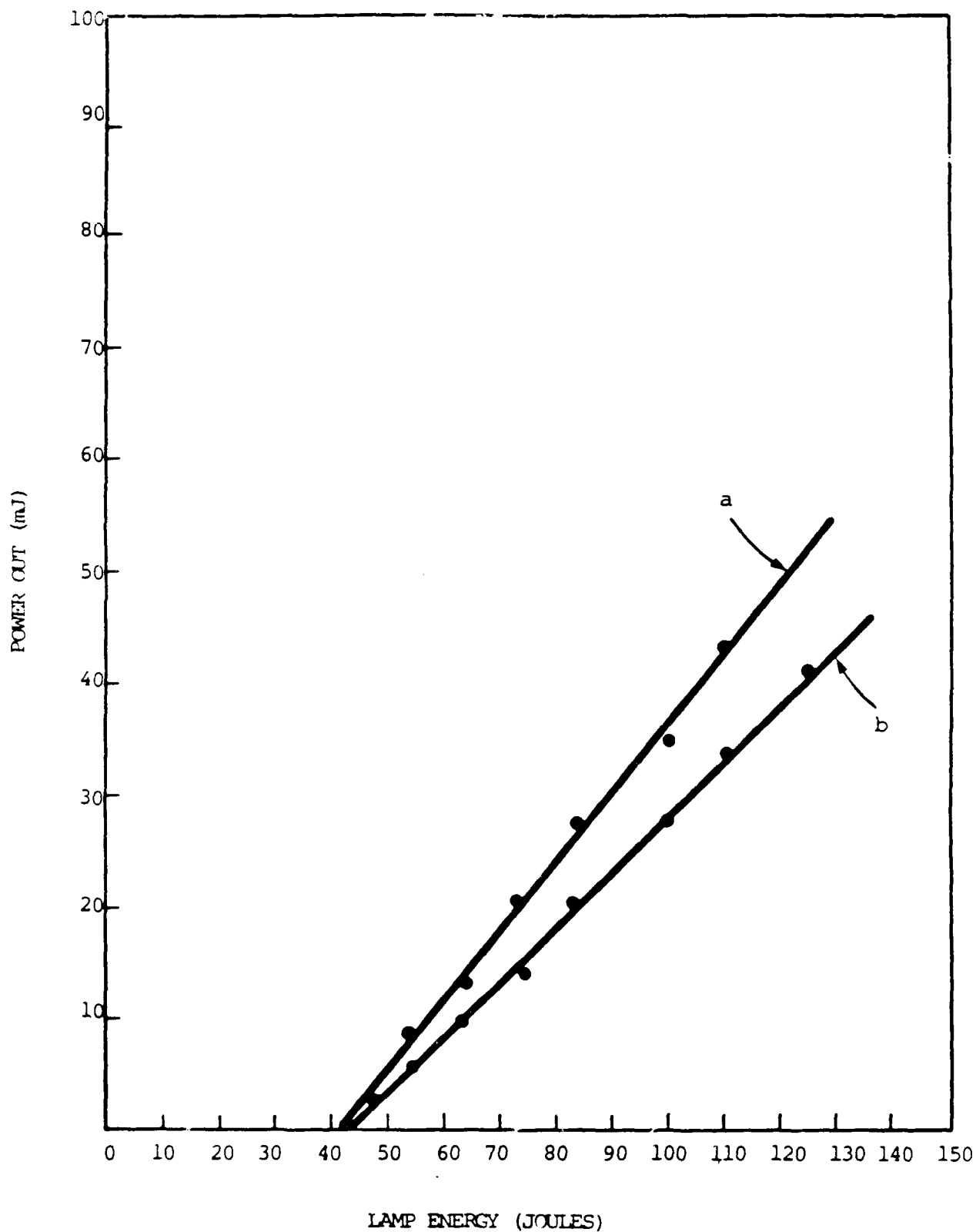


Figure 5-6. The Extraction of the Energy From the Ring Cavity Defined by the 6 mm Aperture and the Spatial Filter. The Line a Shows the Energy Extracted in Free-Running Mode. The Line b Shows the Energy Extracted During Q-Switching of the Cavity.

Centurion.

The extraction of the energy from the oscillator after inserting the filter aperture is shown in Figures 5-5 b (free running operation) and 5-6 b (Q-switched operation). As can be seen from the data, the spatial filtering entailed 75 % loss in the oscillator output. The reduction of the output energy is consistent with the results on the energy content of different cavity modes (5.7).

The operation of the oscillator under the Q-switching is presented in Figures 5-5 b and 5-6 b. As shown by this data, the operation of the Q-switch entailed 23% polarization loss. This was consistent with the observation of the increased transmission through the intracavity polarizers while operating the oscillator in the Q-switch mode. The resulting pulse shape is presented in Figure 5-7. The pulse length of the oscillator output was of the order of 45 to 50 ns and was limited primarily by the cavity lifetime which was around 16 ns. As presented in the figure, the oscilloscope traces of the fast photodiode looking at the oscillator output showed the evidence of the mode beating. This was manifested by the presence of the oscillatory structure superimposed on the Q-switched pulse profile. The frequency of the mode beating was 0.13 GHz, which was consistent with the cavity mode separation. From the pulse shape it can be inferred that the oscillating wave included 3 to 4 axial modes.

The Q-switched, specially filtered oscillator operating at the repetition rate of 7.5 Hz was delivering 28-30 mJ per pulse under the flash lamp loading of 100 Joules. The energy in the counterpropagating mode of the ring was less than 1%. The output had S polarization with S to P energy ratio better than 20. Table 5-1 summarizes the performance of the ring oscillator at 7.5 Hz.

The extraction of oscillator energy at different repetition rates is presented in Figure 5-8. During this experiment, the flash lamp energy loading was kept constant at the level of 100 Joules per shot for which the

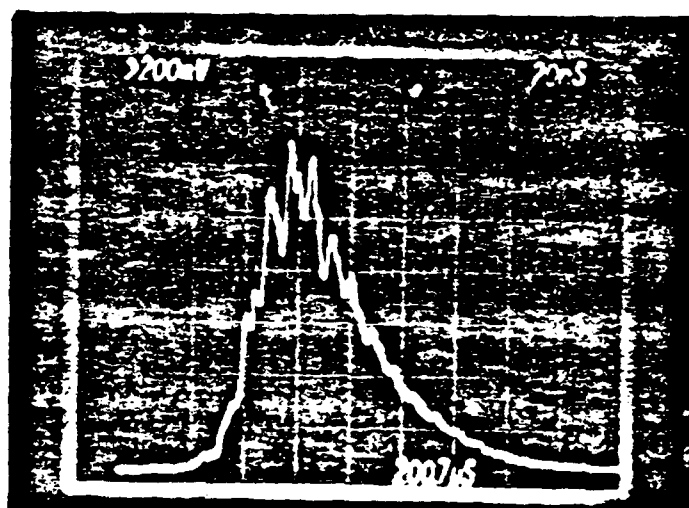


Figure 5-7.

The oscillator trace from a fast photodiode looking at the oscillator output. The time scale was 20 ns per division.

Table 5-1.

Oscillator performance 7.5 Hz repetition rate, 100 J of the energy loading

Pulse Width	-45 ns
Pulse Energy	-30 mJ
Band Width	-3 GHz
Wave Form Distortion	$\lambda/4$
Ration of S to P Polarization	>20
Energy in Counter Propagating Mode	<1%
Spatial Filter Loss	75%
Q-switch Loss	23%

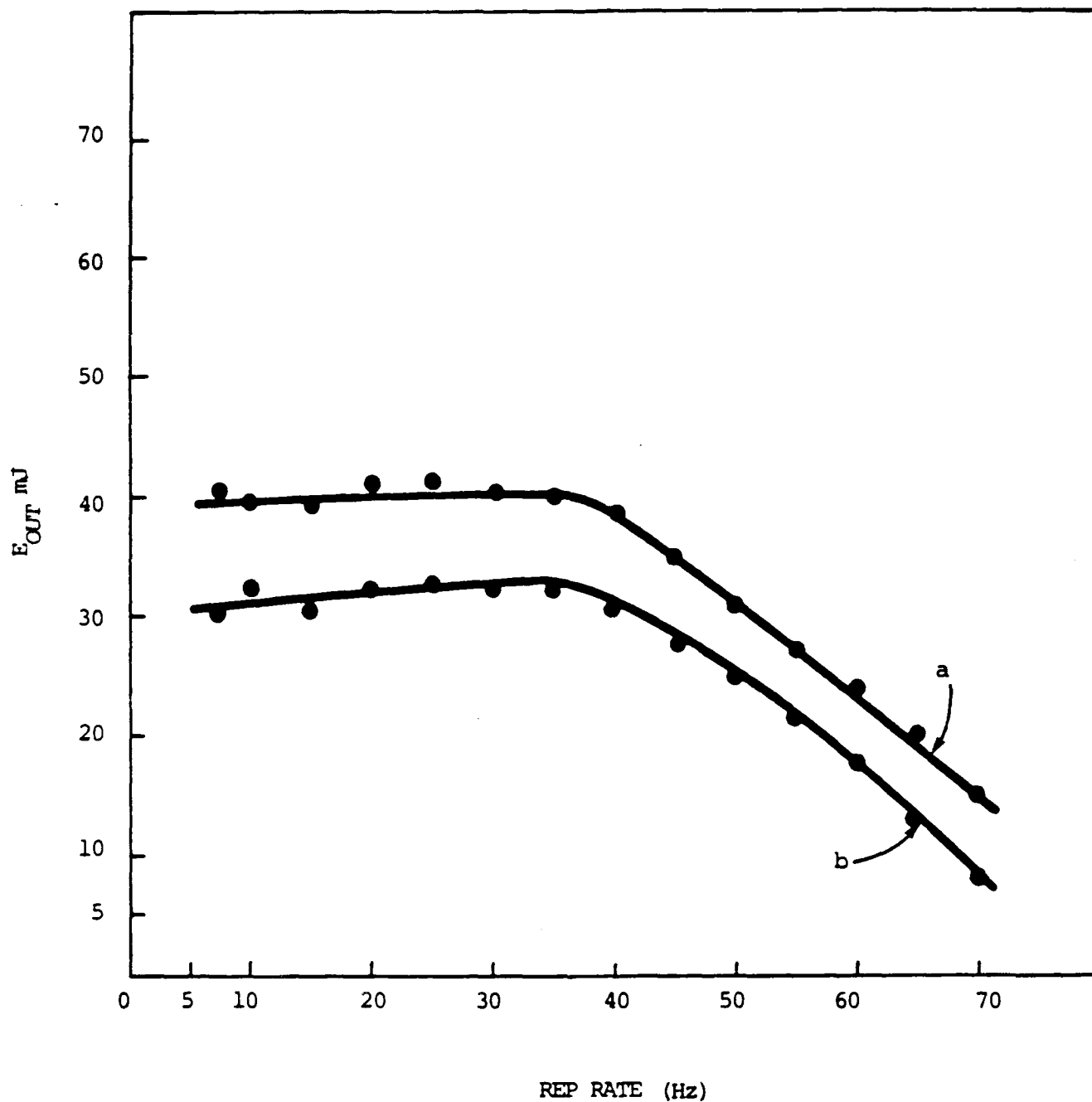


Figure 5-8. The Extraction of the Energy from the Oscillator vs. the Repetition Rate. The Line a Designates the Isle for the Free Running Oscillator. The Line B Designates the Data for the Q-switched Oscillator.

cavity was aligned. As demonstrated by the figure, the higher repetition rate reduced the amount of the energy per pulse extracted from the oscillator.

The second effect contributing to the reduced extraction had to do with the presence of the thermal waves propagating across the slab aperture. The presence of these waves was clearly visible while observing the direction of the output propagation. Under the heavy thermal loads, the pointing stability of the output deteriorated. The time constant of this instability was comparable with the time constant of the thermal lens build-up and relaxation, which is consistent with a thermal origin of the instability.

The thermal waves were diffracting the oscillating wave away from the cavity axis defined during the alignment. The diffraction provided the cavity with a loss mechanism. Thus in a long, small aperture oscillator, such as the one developed during the course of the studies presented here, the pointing instabilities had a detrimental influence on the extraction energy stability. It should be stressed, however, that the pointing instabilities were not of fundamental nature. They could be reduced and eliminated by more careful design of the slab cooling scheme.

Both effects, the thermal lensing of the slab and the pointing instability resulted in an average decrease of the output energy of the order of 40% while changing the oscillator repetition rate from 7.5 to 60 Hz. The most dramatic decrease occurred in the frequency range above 35 Hz repetition rate.

The oscillator wave front was recorded at the output of the spatial filter and at the oscillator output. The results are presented in Figure 5-9. The figure shows the wave front at the output of the spatial filter before (a) and after inserting the filter aperture (b). A comparison of these two interferograms shows clearly that the aperture of 250 microns was adequate to clean up the aberration of the wave front.

a



b

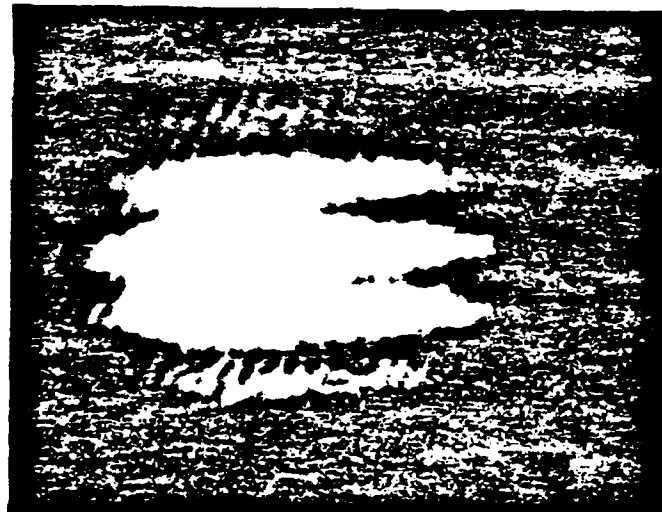


Figure 5-9.

The wave front interferograms at the output aperture of the intracavity spatial filter. Part a represents the result obtained without the filter hard aperture. Part b represents the result after the aperture was inserted.

Similar results recorded at the oscillator output are presented in Figure 5-10 a (without the hard aperture in the spatial filter) and 5-10 b (with the aperture inserted). By comparing Figures 5-9 b and 5-10 a, it can be seen that the wave front distortion at the output was primarily established during the last pass of the wave through the gain medium. This aberration was spatially filtered by the cavity apertures during the previous passage around the ring. Thus, the aberrated component of the field was taken away from the cavity by a sequence of the cavity stops and did not get amplified. However, operation of the oscillator without spatial filtering resulted in the loss of the spatial coherence of the wave, which was manifested by the reduced contrast in the interferogram. Therefore, another impact of the spatial filter was to define the spatial coherence of the output wave while the wave front aberration originated from a single pass propagation of the wave through the gain medium.

A comparison of the wave fronts recorded at the repetition rate of 7.5 Hz to this of 60 Hz is presented in Figure 5-11. It clearly shows the thermal lens build-up. As can be inferred, the lens has primary a cylindrical symmetry. The amount of the wave front distortion changes from $\lambda/4$ at 7.5 Hz to $3 \lambda/4$ at 60 Hz. This is consistent with previously recorded data on Mach-Zender interferometry of Centurion.

The results of the Strehl ratio experiment of the oscillator output are presented in Figure 5-12. This result, in essence, confirmed the observation of the wave front studies. However, it was difficult to quantify the observations, mainly because of the low signal to noise ratio of the results. This low ratio was primarily due to the output pointing instability as discussed above.

Figure 5-13 presents the results of the oscillator output vs. the oscillator detuning angle. This result illustrates the angular sensitivity of the oscillator. As presented by the figure, the output energy decreased by half while detuning of the cavity by ± 0.4 mrad in case of 7.5 Hz operation. The results of similar experiment conducted at 60 Hz repetition

a



b



Figure 5-10.

The wave front interferograms at the output aperture of the oscillator. Part a represents the result obtained without the filter hard aperture. Part b represents the result after the aperture was inserted.

a

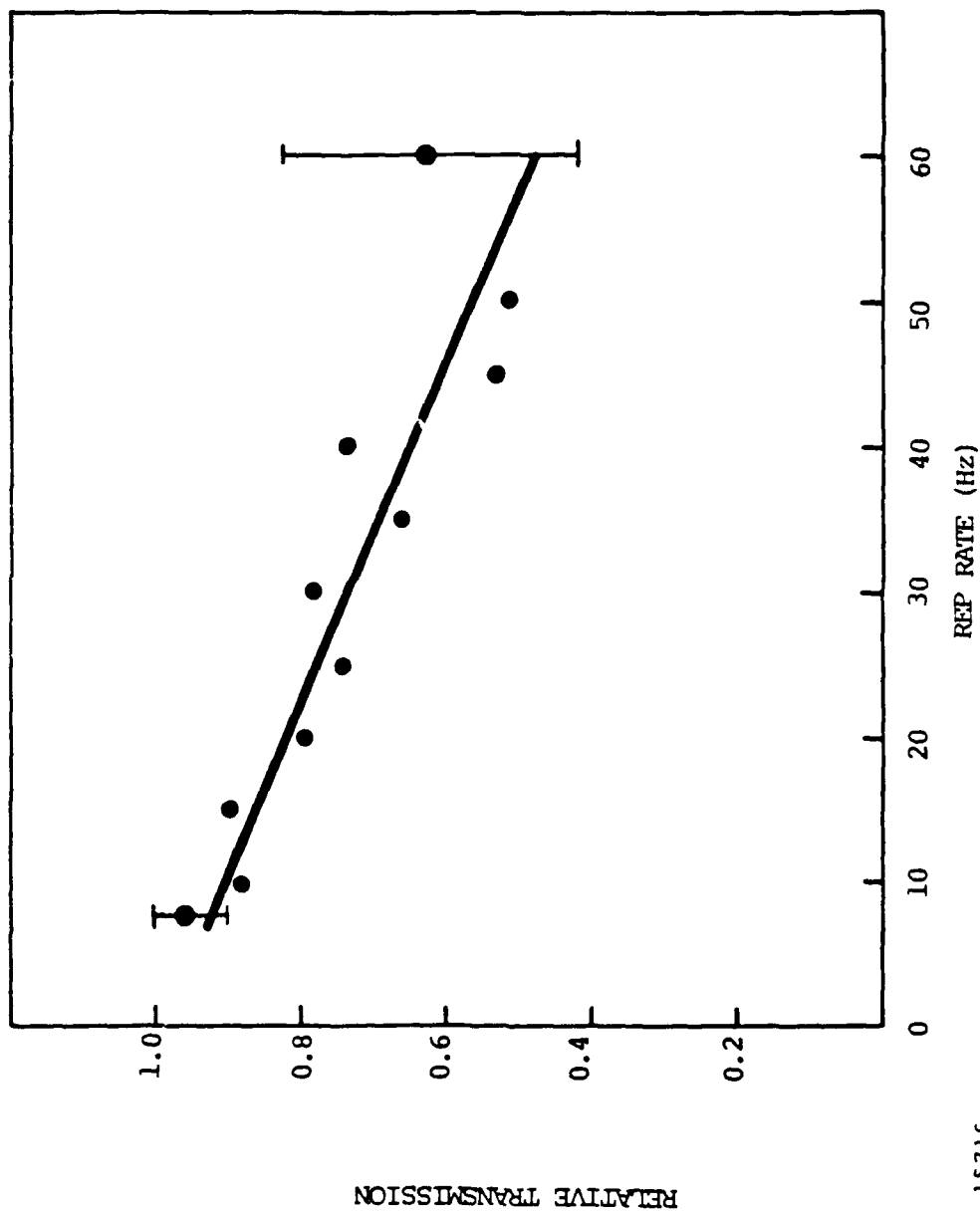


b



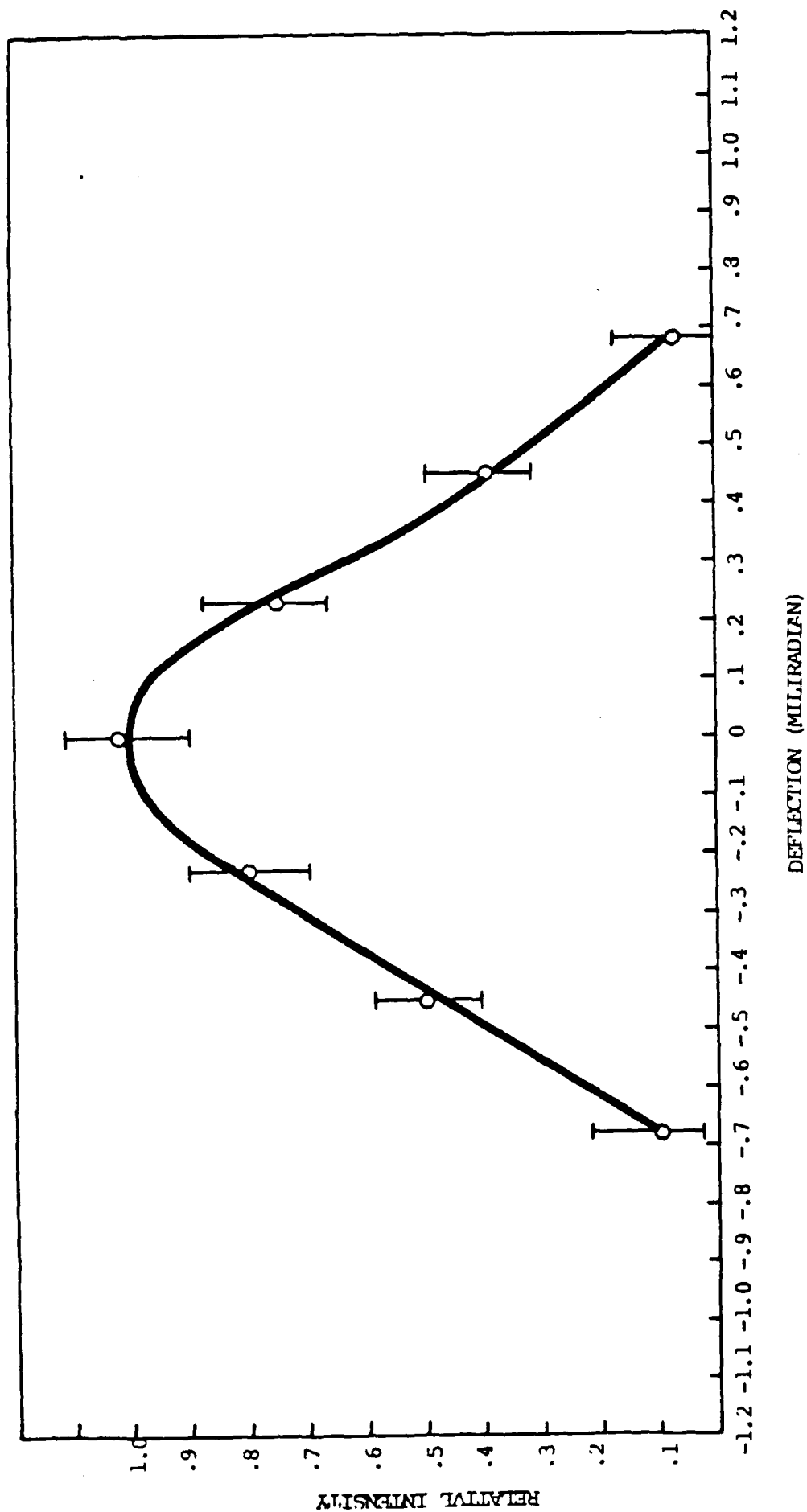
Figure 5-11.

The wave front interferograms at the output aperture of oscillator. Part a represents the result obtained for the system repetition rate of 7.5 Hz. Part b represents the result for the system repetition rate of 60 Hz.



15716

Figure 5-12. The Relative Transmission of the Oscillator Output Through the Subdiffraction Limited Pinhole vs. the System Repetition Rate. The Results were Scaled as to Yield the Transmission Equal 1 at the Repetition Rate of 5 Hz.



15723

Figure 5-13. The Oscillator Output vs. the Cavity Detuning Angle. The Results Were Scaled as to Yield the Output Equal 1 at the Angle for which the Output was at the Maximum. The Data was Obtained of the Repetition Rate of 7.5 Hz.

rate showed that the detuning angle was approximately 10% smaller. The stability resulted from the relay imaged ring nature of the cavity and the presence of the spatial filter. Such relay imaged rings reduced by a factor of six the walk-off of the beam at the output of the cell as compared with the wave propagation not modified by the cell.

The oscillator studies provided the basis for further understanding of the ROPA system. We were able to prove that the spatial filter was indeed successful in providing beam clean-up so that the wavefront distortion seen at the SBS cell were only those accumulated during one pass of the gain medium. This condition is essential to the diffraction limited operation of the entire ROPA device. In addition we were able to ascertain performance characteristics and limitations of the oscillator which directly influence the performance of ROPA itself. In particular the pulse width and pulse energies determine the efficiency of the SBS process.

5.3.2 Amplifier Performance

In order to investigate the performance of the conventional equivalent of the ROPA, a number of amplifier experiments were conducted. In these experiments, the pulses from the oscillator were reflected back into the oscillator aperture by a mirror. The oscillator output on its way back propagated twice through a $\lambda/4$ plate so that the wave entering the oscillator was P polarized. Therefore, it was transmitted through the oscillator output coupler and another cavity mirror which was S polarization reflecting (it was a thin film polarizer). Thus, the returning wave could propagate through the same segment of the gain medium from which the oscillator wave originated. Of course, the returning wave suffered loss on both of the oscillator surfaces. It was also amplified by the remaining gain which was not depleted by the oscillator wave.

To prevent the saturation of the oscillator extraction with the amplifier field, the position of the turning mirror was set to provide a delay between the oscillator pulse generation and the amplifier pulse

extraction. This delay was around 30 ns (30 feet long), and was chosen as a compromise between the requirements of the experiment and the available space on the experimental bench.

The amplifier energy extraction data is presented in Figure 5-14. The figure presents the extraction data obtained while operating the laser at the repetition rate of 7.5 Hz. Figure 5-14 a shows the oscillator with amplifier operating in free running mode while Figure 5-14 b graphs the Q-switched operation. This data showed how much energy could be extracted from gain volume (notice that the here the energy loading range extends to 135 lamp Joules). The amplifier data presents only 25 percent improvement as compared with the oscillator output. These results include 20% loss of the returning wave on the oscillator output coupler and 15% loss on the cavity mirror. Taking these two losses into account results in a value of 2 for the gain of the amplifier pulse. The oscillator-amplifier set-up provided around 37 mJ of energy while operating at 7.5 Hz with 100 Joules per shot of energy loading. Table 5-2 presents details of the system losses and gains.

The extraction of amplifier energy at different repetition rates is presented in Figure 5-15. During this experiment, the flash lamp energy loading was kept constant at the level of 130 Joules per shot, for which the cavity was aligned. As demonstrated by the figure, the higher repetition rate reduced the amount of the energy per pulse extracted from the amplifier by 25%. Most of the reduction occurred in the frequency range above 35 Hz. This resulted from the fact that the thermal lens which built in the gain medium under the heavy energy loading contributed to the increase in oscillator losses. In addition, the thermal lens increased the divergence of the amplifier beam and thus the additional loss was due to mismatch between the gain aperture and the returning beam cross section. However, the reduction was not as dramatic as in the case of the oscillator. This was due to the fact that the energy from the amplifier was extracted under saturated gain conditions.

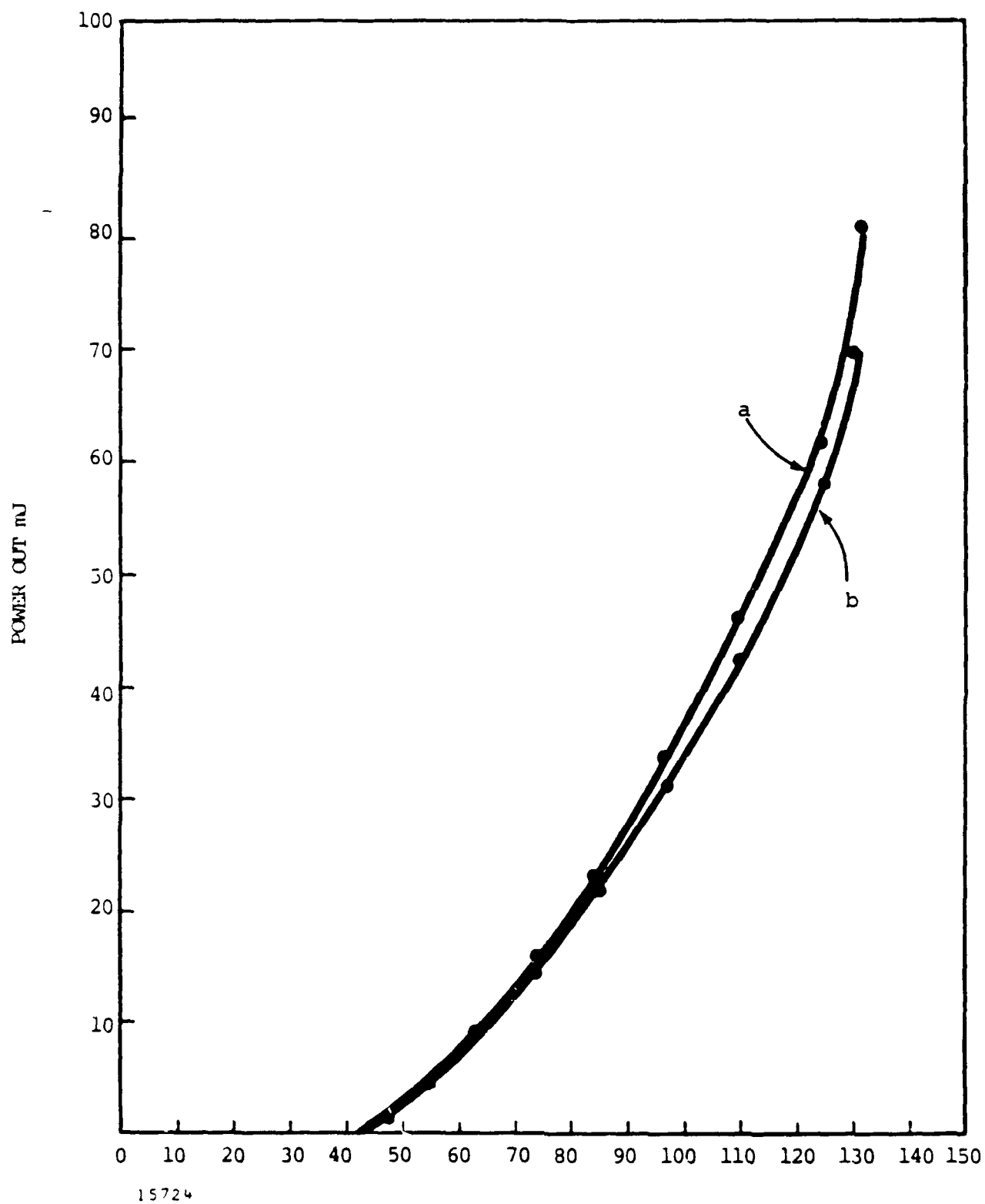


Figure 5-14. The Extraction of the Energy From the Amplifier. The Line a Shows the Energy Extracted in Free-running Mode. The Line b Shows the Energy Extracted During Q-switching of the Cavity.

Table 5-2. System performance.

OSCILLATOR-AMPLIFIER

System Component	Loss/Gain (%)	Resulting Energy (mJ)
Energy for the Oscillator		30
Oscillator Output Coupler	-20	24
Gain Medium	+200	48
Oscillator Mirror	-15	37

ROPA

System Component	Loss/Gain (%)	Resulting Energy (mJ)
Energy for the Oscillator		30
SBS Cell	-70	9
Oscillator Output	-20	7
Gain Medium	+450	35
Oscillator Mirror	-15	27

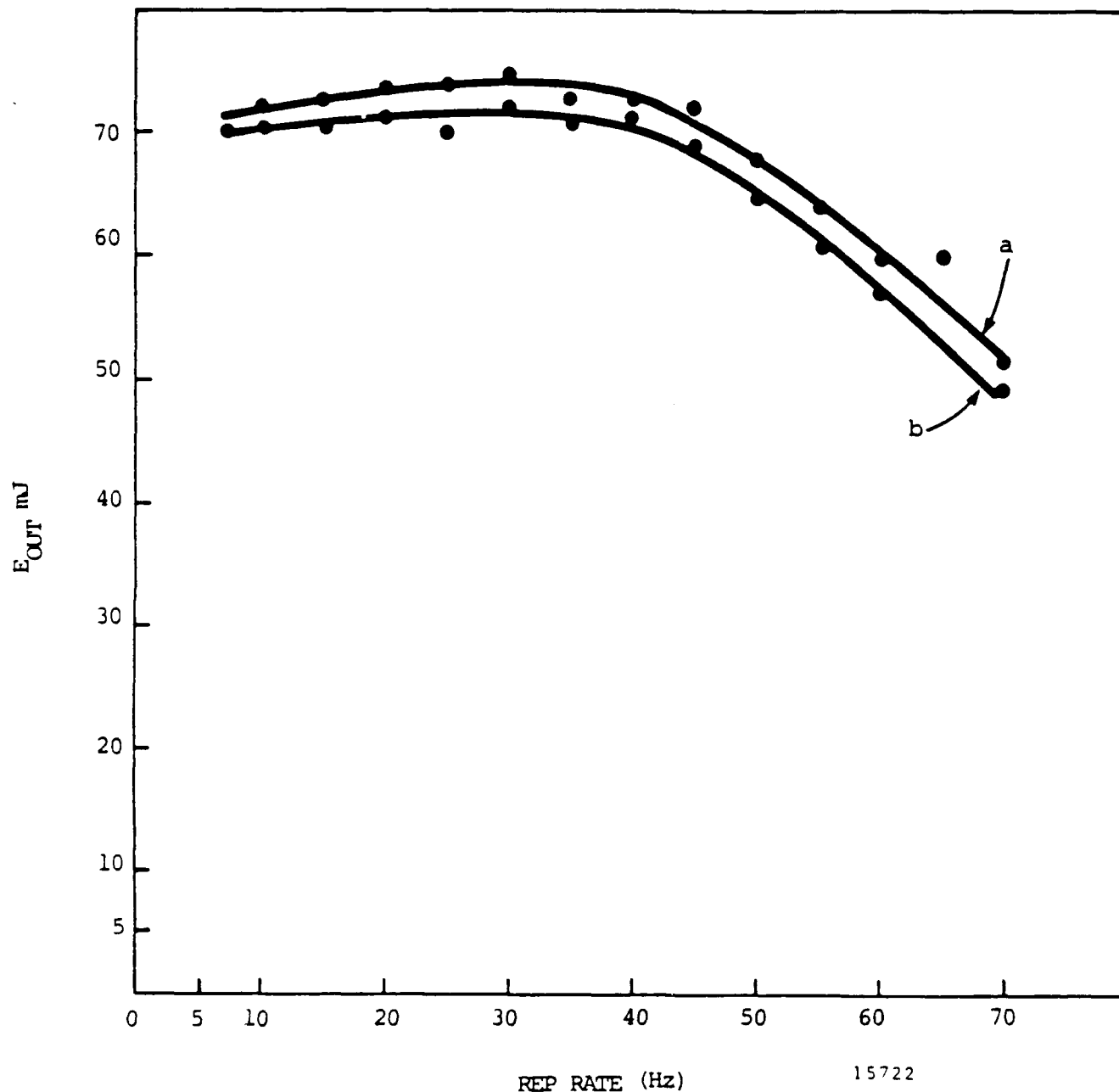


Figure 5-15. The Extraction of the Energy from the Amplifier vs. the System Repetition Rate. The Line a Shows the Energy Extracted in Free-Running Mode. The Line b Shows the Energy Extracted During Q-switching of the Cavity. (The Results were Recorded at the Energy Loading of 130 Joules per Shot).

The amplifier wave fronts were recorded at the output of the system. The results are presented in the Figure 5-16. A comparison of the data recorded at the repetition rate of 7.5 Hz to this of 60 Hz shows the thermal lens build-up. As can be inferred, the lens has primarily a cylindrical symmetry. The amount of the wave front distortion changes from $0.25\text{--}0.5 \lambda$ at 7.5 Hz to around 1.5λ at 60 Hz. This is consistent with the oscillator data and shows that the amplifier distortion is roughly twice as large as that of the oscillator. This result showed that the gain medium aberration distorted the wave front additively in the oscillator-amplifier configuration as expected.

The results of the Strehl ratio experiment of the amplifier output are presented in Figure 5-17.

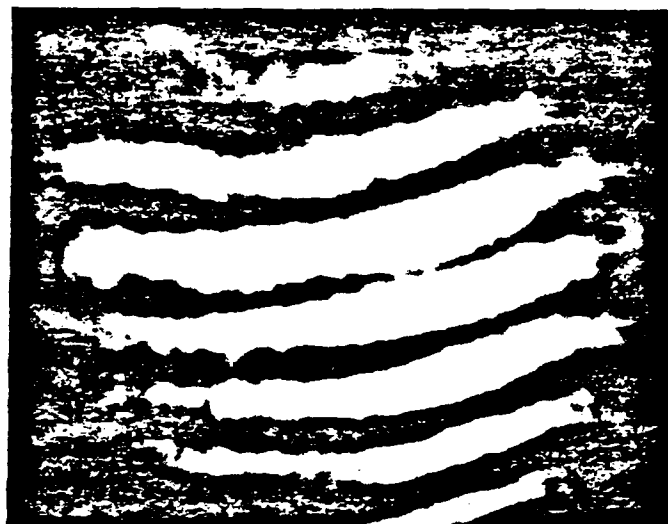
The result confirmed the observation of the wave front studies. Once again, it was difficult to quantify the observations mainly because of the low signal to noise ratio of the results. This low ratio was primarily due to the output pointing instability as discussed in the part of this report dealing with the oscillator performance.

Figure 5-18 presents the results of the amplifier output vs. the oscillator detuning angle, illustrating the angular sensitivity of the oscillator-amplifier system.

As presented by the figures, the output energy decreased by half while detuning the cavity by ± 0.57 mrad in case of 7.5 Hz operation (the result for 60 Hz repetition rate was approximately 10% smaller). The data showed broadening and flattening of the system sensitivity curve. The improved detuning performance of the amplifier stemmed from the fact that the system operated as a saturated amplifier. Therefore, the output variation was reduced as a result of the saturated amplification of the input.

The amplifier studies provided a baseline for comparison of the SBS ROPA device. Here, the optical configuration is very similar to the final ROPA but the reflector is not phase conjugating; this enabled us to establish the reduction in beam quality with average power and to note the

a



b



Figure 5-16.

The wave front interferograms at the output aperture of the amplifier. Part a represents the result obtained for the system repetition rate of 7.5 Hz. Part b represents the result for the system repetition rate of 60 Hz.

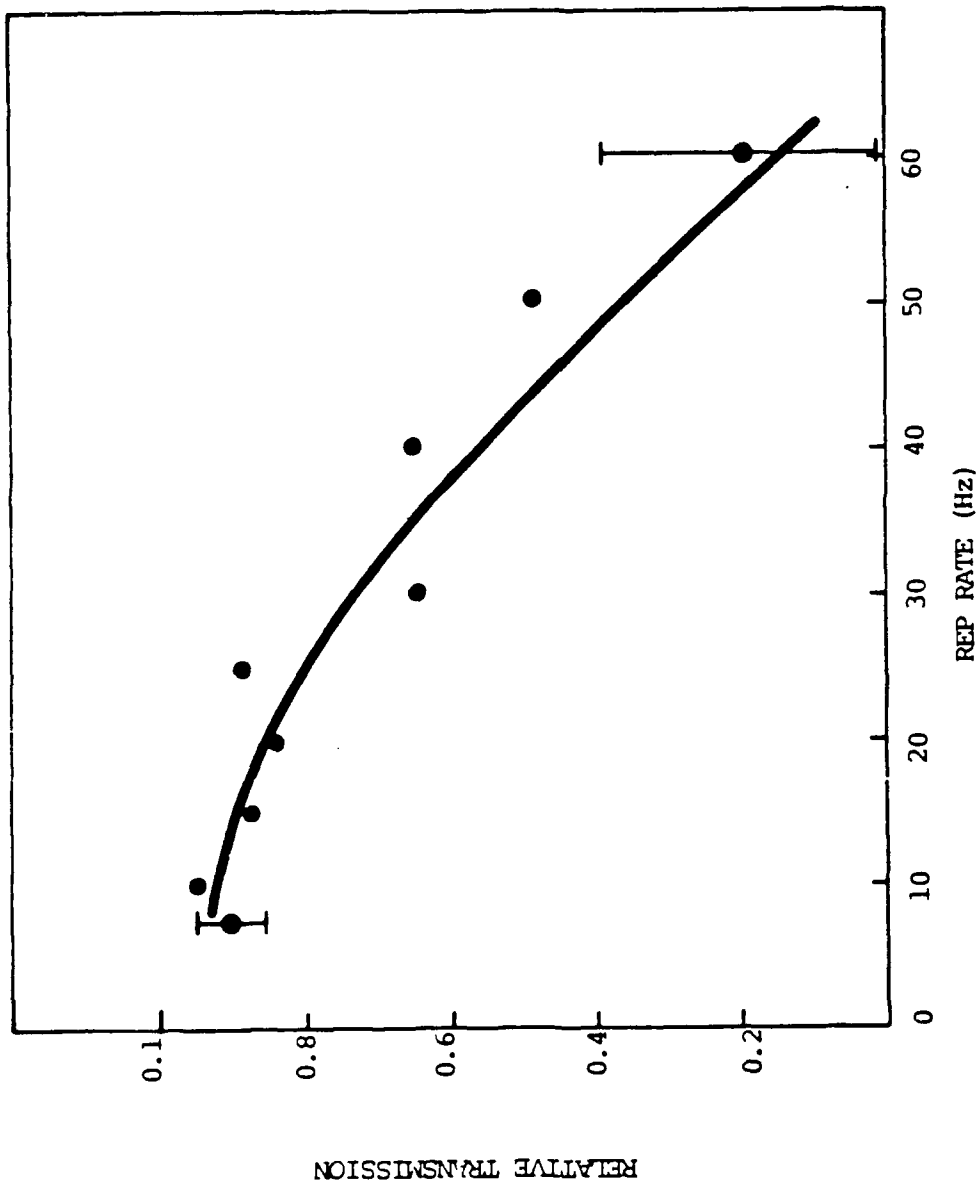


Figure 5-17. The Relative Transmission of the amplifier Output Through the Subdiffraction Limited Pinhole vs. the System Repetition Rate. The Results were Scaled as to Yield the Transmission Equal 1 at the Repetition Rate of 5 Hz.

15717

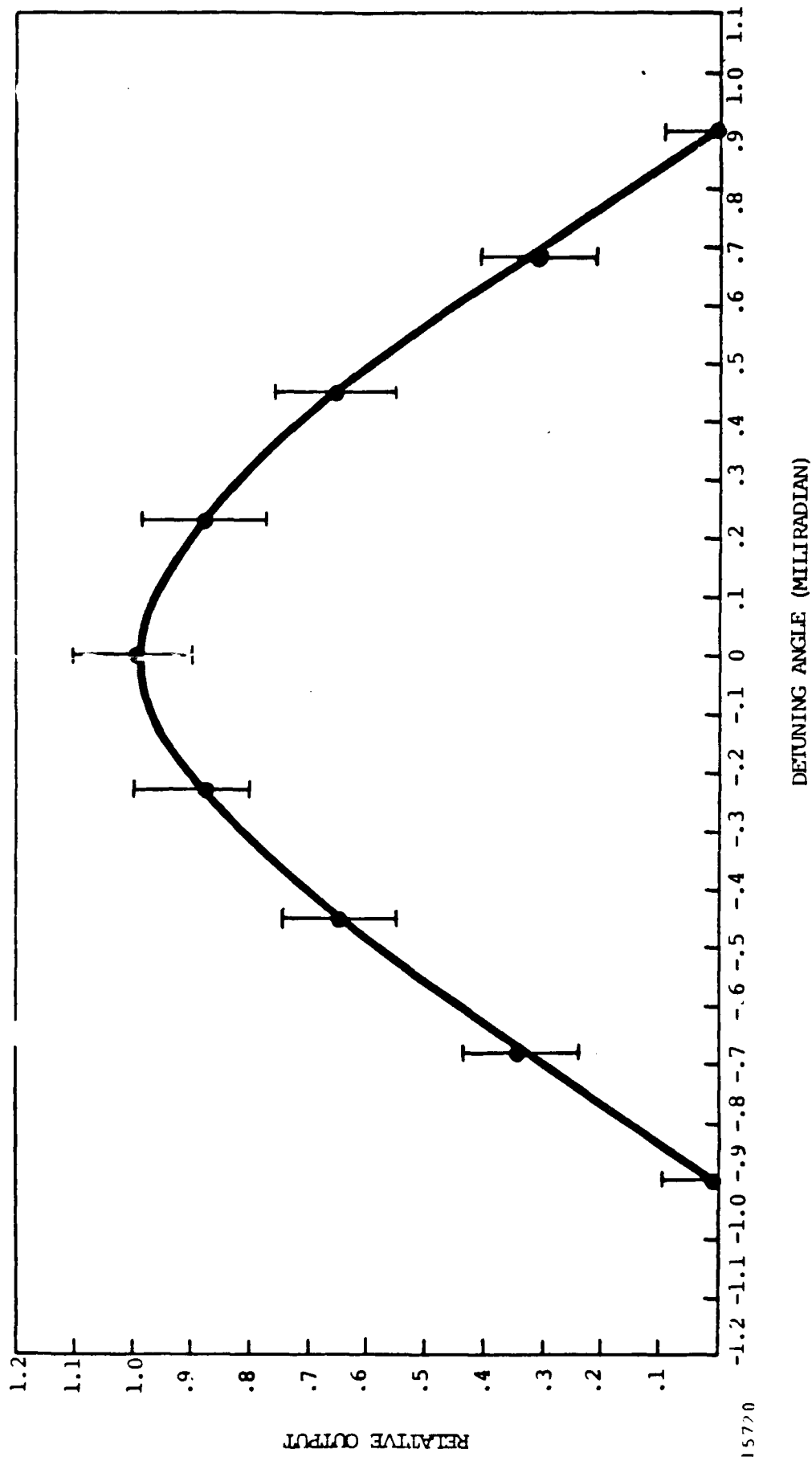


Figure 5-18. The Amplifier Output vs. the Cavity Detuning Angle. The Results were Scaled as to Yield the Output Equal 1 at the Angle for Which the Output was at the Maximum. The Data was Obtained of the Repetition Rate of 7.5 Hz.

total energy limitations of this particular experimental device.

5.3.3 ROPA Performance

To investigate the aberration correction of the slab medium, a number of ROPA experiments were conducted. In these experiments, the pulses from the oscillator were reflected back to the gain volume by the SBS cell. The beam was focused by a 300 mm focal length, which established the Rayleigh range around 5 mm, a distance much shorter than 0.5 m of coherence length of the available laser output.

During the ROPA studies, the $\lambda/4$ retarder was positioned in such a way that the wave reentering the oscillator was P polarized as before. The wave propagated through the same volume of the gain medium from which the oscillator wave originated but with a conjugated phase front. Therefore, the return pass through the gain aberrating volume resulted in distortion compensation. The wave was also amplified by the rest of the gain non-depleted by the oscillator wave.

The ROPA energy extraction data is presented in Figure 5-19. The figure presents the extraction data obtained while operating the laser at the repetition rate of 7.5 Hz. This data showed that the ROPA output was determined as a result of the energy extraction by the oscillator, SBS losses, losses on different optics, and the second pass amplification. The operation of the ROPA at 7.5 Hz repetition rate with the energy loading of 100 Joules per shot resulted in 27 mJ of the ROPA output. The result obtained for 125 Joule loading was approximately 44 mJ of the ROPA output. A detailed account of the ROPA energy gains and losses is presented by Table 5.1. Taking into account 70% SBS loss and 20% oscillator coupler loss, the amplification of the returning wave was of the around 4.5.

The extraction of ROPA energy at different repetition rates is presented in Figure 5-20. The flash lamp energy loading was kept constant at the level of 100 Joules for which the cavity was aligned. As

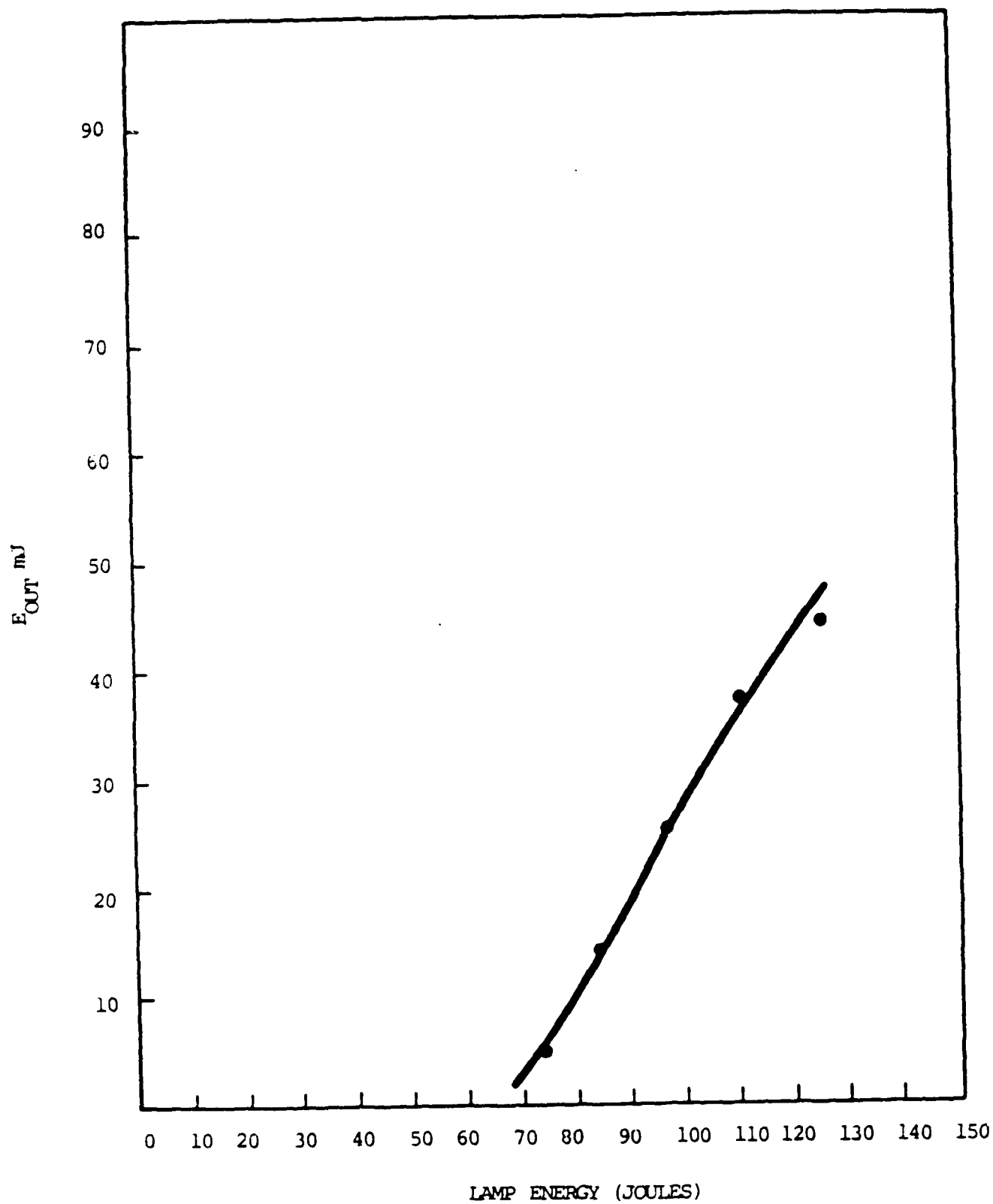


Figure 5-19. The Extraction of the Energy From the ROPA System.

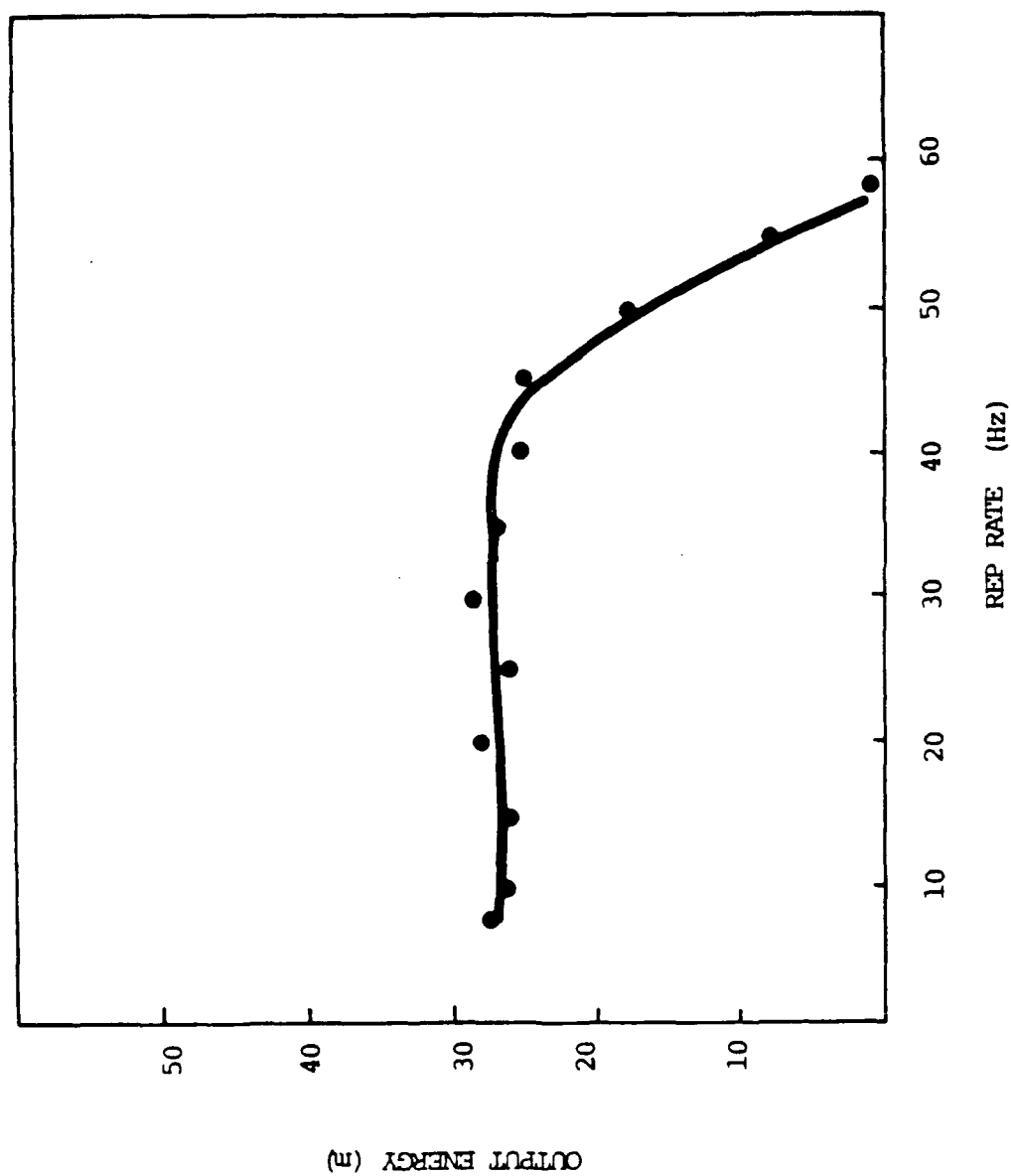


Figure 5-20. ROPA output energy as a function of system repetition rate

15721

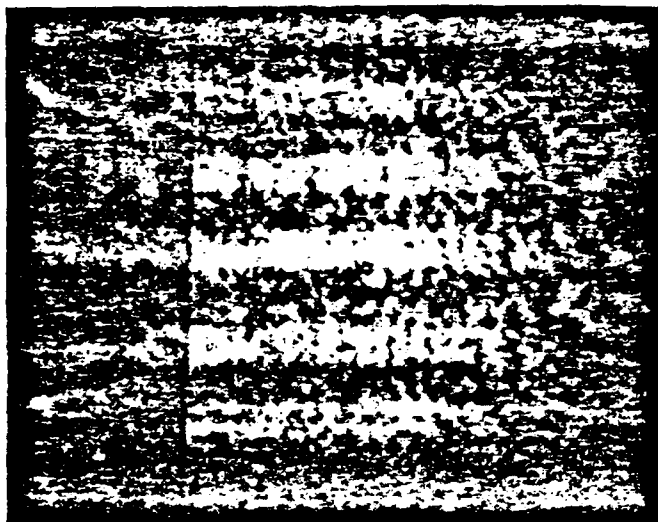
demonstrated by the figure, for the repetition rates up to 40 Hz the extraction curve was flat. However, for the repetition rates above 40 Hz the ROPA output was rapidly decreasing. This resulted from the fact that at the higher repetition rates the oscillator output decreased. It, in turn, caused the phase conjugator to operate at the higher losses, and thus the ROPA efficiency was reduced. Therefore, the reduction in the output energy, intensified by the increase in the SBS loss, was more rapid than that of the oscillator. At the repetition rate between 50 to 60 Hz the oscillator output was barely reaching the SBS threshold, resulting in a deteriorating beam quality of the output. The reduction of the oscillator output continued to decrease to the point where the energy was too small to reach the SBS threshold, at which point the ROPA output was zero.

The ROPA wave fronts were recorded at the output aperture of the gain medium. The results are presented in Figure 5-21. The comparison of the data recorded at the repetition rate of 7.5 Hz to this of 60 Hz clearly shows the aberration correction. As can be seen, the wave front was flat up to 50 Hz repetition rate. At 60 Hz the beam quality became inconsistent and showed the first sign of aberration, consistent with a decreased in oscillator energy reaching the SBS threshold. The wave fronts of the ROPA at 60 Hz are presented in Figure 5-22. This point of the operation, i.e. 100 Joules of the energy loading at 60 Hz repetition rate, defined the limit of the ROPA operation. However, this limit was not of the basic, fundamental nature. Rather, it was defined by a particular design of the laser head used in the course of this demonstration.

The results of the Strehl ratio experiment of the ROPA output are presented in Figure 5-23. This result confirmed the observation of the wave front studies.

Figure 5-24 presents the results of the ROPA output vs. the oscillator detuning angle. This result illustrates the angular sensitivity of the ROPA. As presented by the figures, the output energy decreased by half while detuning the cavity by ± 0.4 mrad in case of 7.5 Hz operation.

a



b

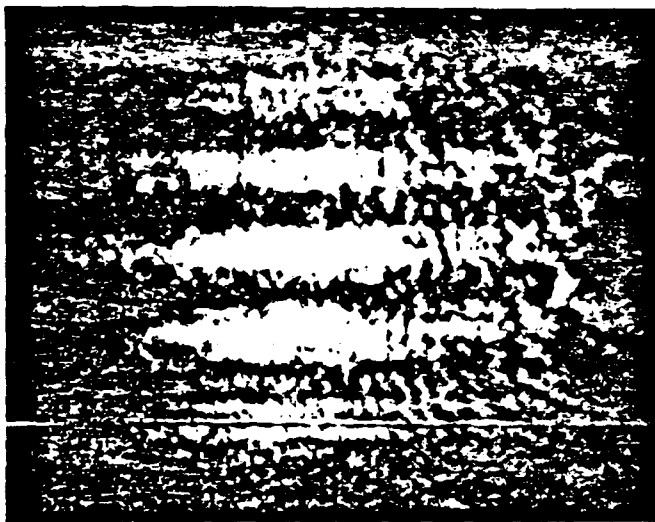
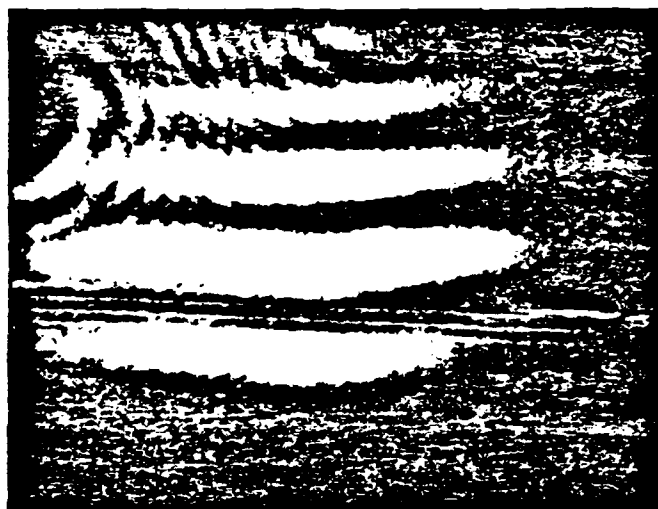


Figure 5-21.

The wave front interferograms at the output aperture of the ROPA. Part a represents the result obtained for the system repetition rate of 7.5 Hz. Part b represents the result for the system repetition rate of 50 Hz.

a



b

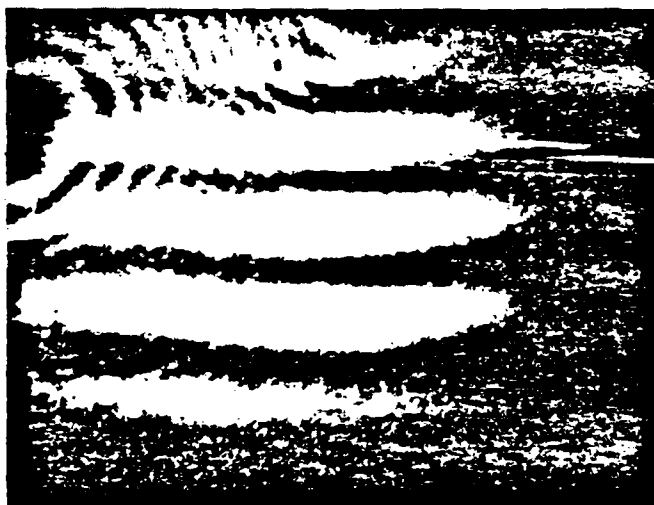


Figure 5-22.

The wave front interferograms at the output aperture of amplifier. Part a b represent the result obtained for the system repetition rate of 60 Hz when the output showed inconsistent performance.

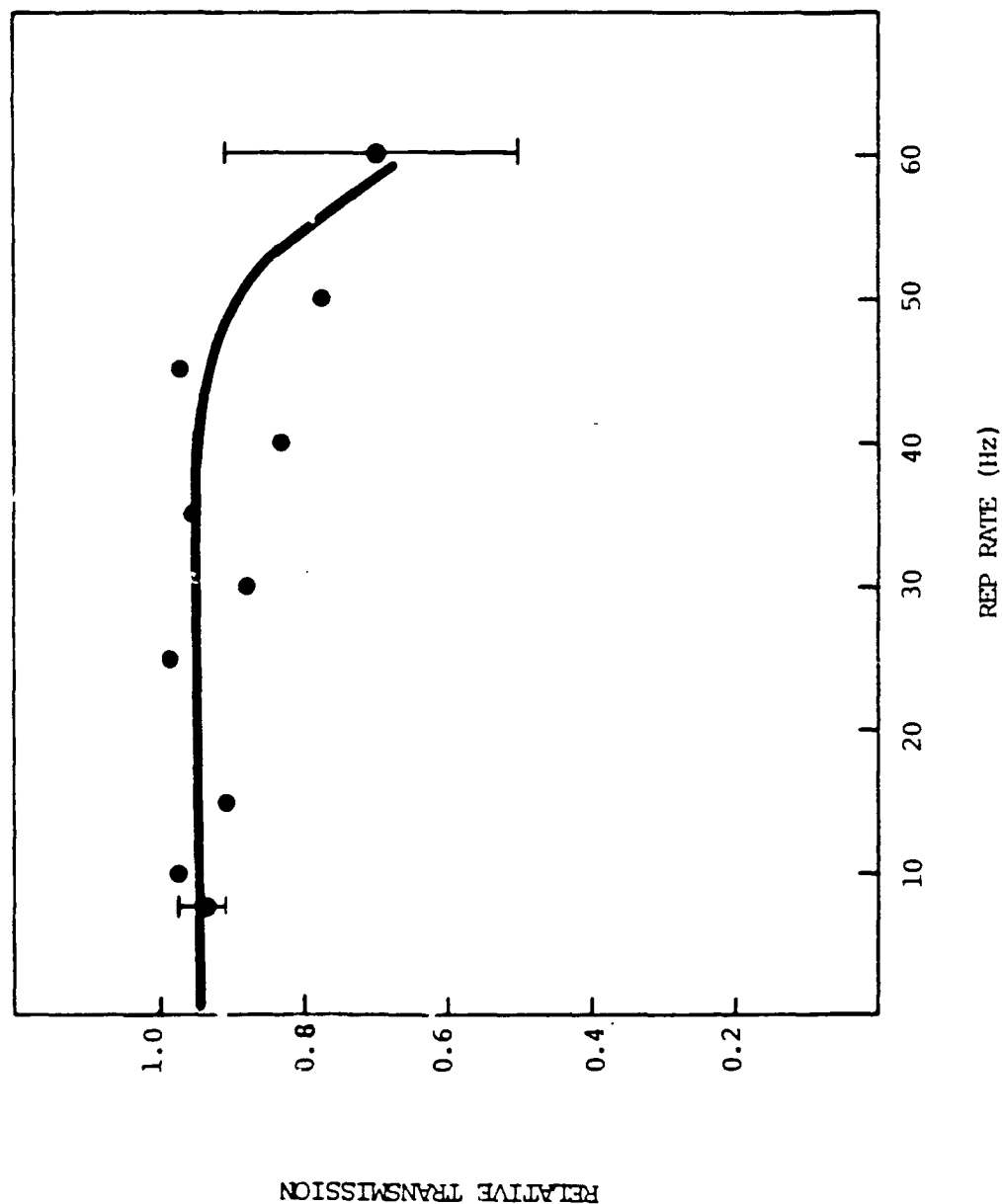


Figure 5-23. The Relative Transmission of the ROPA Output Through the Subdiffraction Limited Pinhole vs. the System Repetition Rate. The Results were Scaled as to Yield the Transmission Equal 1 at the Repetition Rate of 5 Hz.

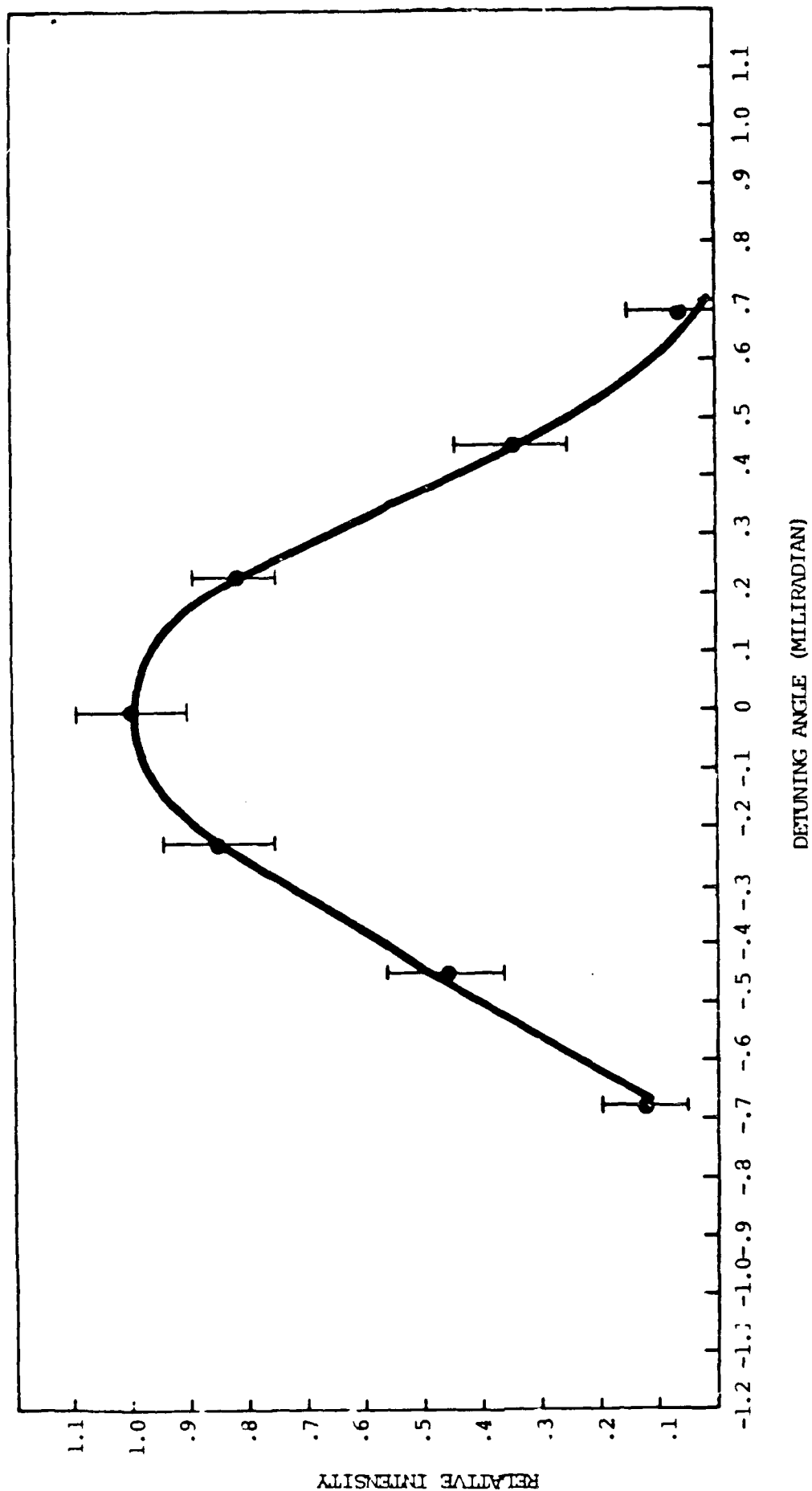


Figure 5-24. The ROPA output vs. the Cavity Detuning Angle. The Results were Scaled as to Yield the Output Equal 1 at the Angle for Which the Output was at the Maximum. The Data was Obtained of the Repetition Rate of 7.5 Hz.

The detuning angle was somewhat narrower (~15%) in case of 60 Hz operation. The good detuning performance of the ROPA as compared with the oscillator alone is very encouraging and stems from the fact that the system operated as an amplifier with the gain relatively close to the saturation level.

5.4 Discussion

The experimental results are sufficient to prove that ROPA systems can be operated as a self-sufficient diffraction limited laser in a situation which would otherwise produce almost a wave of phase aberration. However, there are several aspects which would a priori differ from the expected results. Of primary interest is the low total output power from the ROPA. This is most easily accounted for by studying the total energy balance of the system.

Previous experiments with the Centurion laser head provided a good calibration of the behavior of the YAG slab. Under the flash lamp pumping being used, the Centurion slab could produce 380 mJ of laser output from the full aperture in a free running oscillator with a 50% output coupler. With the energy deposited in the gain medium of 500 mJ it resulted in 75% extraction. We have restricted the available aperture to approximately 1/4 of that available to the original experiments; therefore the total energy stored in the gain volume of the ROPA is approximately 120 mJ. When the system is operated as an oscillator only the output energy per pulse is known to be 30; by measuring input and exit energies we can quantify the losses at the major elements around the cavity. Most elements are not significant but the spatial filter, optical diode, and optics containing specialized polarization dependent coating. The oscillator losses at each one of these elements are listed in the table below:

Spatial Filter	34%
Q-switch	11%
Polarizers, Faraday Rotator	

Etalon

5%

Therefore, the 30 mJ output of the oscillator accounts for 60 mJ stored energy in the YAG slab. (The result on the cavity losses presented above have been assessed for the oscillator in which all the loss elements were operating at once. In this sense they differ from the data, quoted in Table 5-1 paragraph 5.1, which were obtained while testing the loss of separate elements.)

In amplifier experiments, 24 mJ will return to the gain medium as the amplifier extracting pulse. At the exit aperture of the amplifier we observe 48 mJ, the amplification of 2. Given the fact that the oscillator pulse left over 60 mJ of the energy, the amplifier extracts about 40 % of the energy remaining in the gain medium. Such extraction approaches the saturation regime of the amplifier. The summation of the energy required by the oscillator and the energy extracted by the amplifier equals 84 mJ which is 70% of the total energy deposited in the gain volume. Therefore, the output energy extraction limit in the oscillator-amplifier experiment is due to the exhaustion of available energy.

From the calibration of the SBS process we know that an input of energy of 30 mJ will yield a 30% SBS conversion efficiency. This will return 9 mJ to the amplifier phase of the ROPA. At the exit aperture of the amplifier we observe 35 mJ, the amplification of 4. Given the fact that the oscillator pulse left over 60 mJ of the energy, the amplifier extracts about 30 % of the energy remaining in the gain medium. This extraction also approaches the saturation regime of the amplifier. The summation of the output energy and the known lost energy is 78 mJ which is 65% of the total energy deposited in the gain medium. In this case too, the output energy extraction limit in the oscillator-amplifier experiment is due to the exhaustion of available energy.

A primary concern is the fall off in output energy with increasing repetition rate. Unlike the low output energy of the experimental test bed which could be fixed by increasing the gain volume and reducing losses this result represents a potential limitation in the ROPA concept itself. As can be clearly seen in the data, the fall off in output power is a direct results of reduced output power from the oscillator itself with the corresponding loss of SBS efficiency. This is illustrated in Figures 5-3 and 5-20 showing oscillator and ROPA outputs as a function of pulse frequency. Since the output beam quality remains good, what can explain this power reduction which is not seen in the previous Centurion experiments.

To understand this phenomenon let us examine the behavior of a generic ring oscillator as a function of changing spherical aberrations. For aberration below about 1 wave the effect of spherical aberration is nearly identical to that of focus. As can be clearly seen in Figure 5-25 fraction of wave increases in aberration lead to very high losses within the cavity. was 2.5 spot diameters in diameter. The ROPA operates with an aperture much closer to one spot size which exaggerates an already high sensitivity to aberration. A consistent argument accounting for the data can be devised from this behavior. As the thermal loading increases in the slab the amount of thermal lensing increases leading to larger focal aberrations. The focal aberrations cause high passive cavity losses leading to low oscillator outputs at high repetition rates. In principle this can be corrected by the real time movement of optical elements.

5.5 Conclusions

During the course of this program we have investigated the self contained Ring Oscillator Power Amplifier SBS system. In theory this system would be totally self-correcting in terms of thermally induced aberrations. In the laboratory we were able to demonstrate the insensitivity of the output wave front to thermal aberrations in the YAG slab. The correction was evident at both low and high repetition rates,

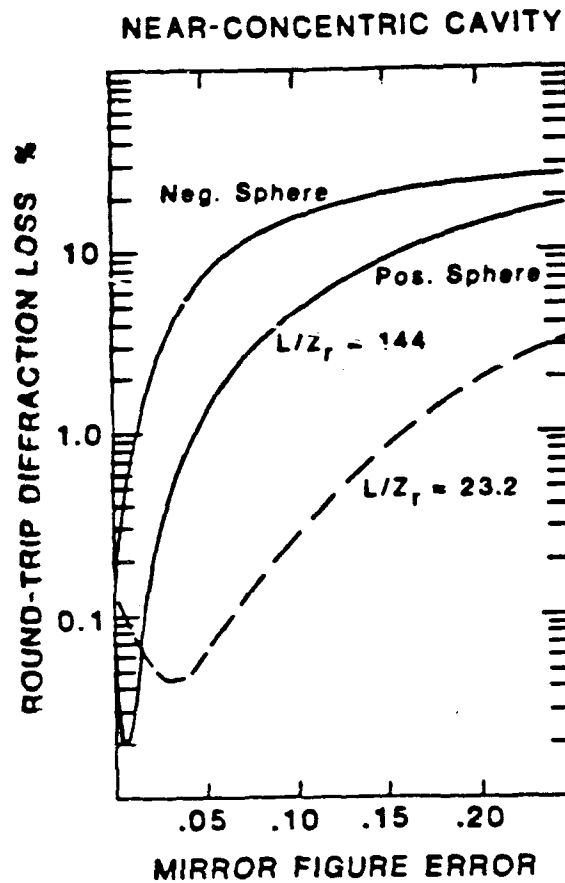


Figure 5-25. Diffractive loss as a Function of Spherical Aberration for Two Generic Ring Cavities. As Can be Seen Nearer the Cavity is the Greater the Effect of Spherical Aberration. The ROPA is Purely Concentric so 1 and Spherical Aberration Effects Large Losses.

but ultimately was limited by the loss of the phase conjugation fidelity when the oscillator output decreased to near the SBS threshold.

The initial output powers of the ROPA were fairly low and it is possible to account for this purely in terms of the limited stored energy. This means that it would be possible to significantly raise the output power by increasing the total available gain volume and adjusted the outcoupling coefficients to maintain cavity fluences at a level suitable for use of a spatial filter. A more significant problem is the drop off in output at higher rep rates. This appears to be an intrinsic part of the devices behavior which would require the introduction of an active focusing system to correct. This adds a level of complexity which can reduce the number of practical application of this particular design.

In the final analysis it is clear, from this series of experiments, that using this basic technique coupled with better utilization of the gain volume will allow us to produce a stand alone laser which could generate at least 100 mJ per pulse at moderate repetition rates (≈ 30 to 50 Hz). Furthermore, and most significantly, the wavefront quality of these output pulses would be on the order of $\lambda/10$ and relatively constant over the operating range. Additionally, due to the self correcting nature of the SBS ROPA there will be no significant variation of wavefront quality during turn on.

REFERENCES

- 5.1. T.R. O'Meara, D.M. Peper, J.O. White, 'Optical Phase Conjugation', ed. R.A. Fisher, Academic Press 1983
- 5.2.
- 5.3. G.E. Alhrecht, J.M. Eggleston, J.J. Ewing, IEEE J. Quant. Electron, QE-22, 2099, 1987
- 5.4. T.R. Kane, R.A. Byer, Opt. Lett., 10, 65, 1984

- 5.5. A. Yariv, Quantum Electronics, Second Edition, J. Wiley and Sons, 1976
- 5.6. M. Born, E. Wolf, Principles of Optics, Sixth Edition, Pergamon Press, 1986
- 5.7. P.W. Smith, Lasers, ed. A.K. Levine, E.G. DeMaria, Marcel Dekker Inc. 1976

6.0 Phase Conjugated Doubling

6.1 Introduction

Phase conjugation is becoming increasingly popular as a method of correcting gain media aberrations in high average power laser resonators. Many applications, however also require harmonic conversion, usually doubling the frequency of a high power near infrared laser beam into the visible region. Thermally induced aberrations in doubling media due to finite absorption is anticipated to be a source of beam distortion. The task of harmonic phase conjugation is to show that aberrations which arise in high power doublers can be corrected by phase conjugation to produce high quality doubled output while relaxing design requirements and making systems more compact by eliminating the need for spatial filtering. It is anticipated in such applications that astigmatism will be the dominant aberration for both zig-zag slab media and high power straight through slab doublers. In response to these anticipations, the work reported here emphasizes astigmatic aberrations and their correction.

6.2 Stimulated Brillouin Scattering Experiment

Stimulated Brillouin scattering (SBS) experiments were performed to observe what effects aberrations had on the SBS process before the doubling step was added. We found that defocus gave good return beam quality, as anticipated, and that astigmatic aberrations gave good return fidelity and beam quality but that the SBS reflectivity degraded for increased astigmatism.

6.2.1 Stimulated Brillouin Scattering Experimental Arrangement

The schematic for the SBS experiments is shown in Figure 6-1. The output of a horizontally polarized q-switched Nd:YAG laser was collimated with a $f=4.0$ m lens. Experiments were performed at a pulse rate of one hertz to minimize the effect of stress-induced birefringence on the laser beam quality. The laser oscillator has a maximum output of 50 mJ per 10 ns pulse which can be amplified by adjusting the voltage on the amplifier flashlamps from 400 to 800 volts increasing the output of the laser to 250 mJ. The bandwidth of the laser was measured and found to vary from one to three GHz shot to shot.

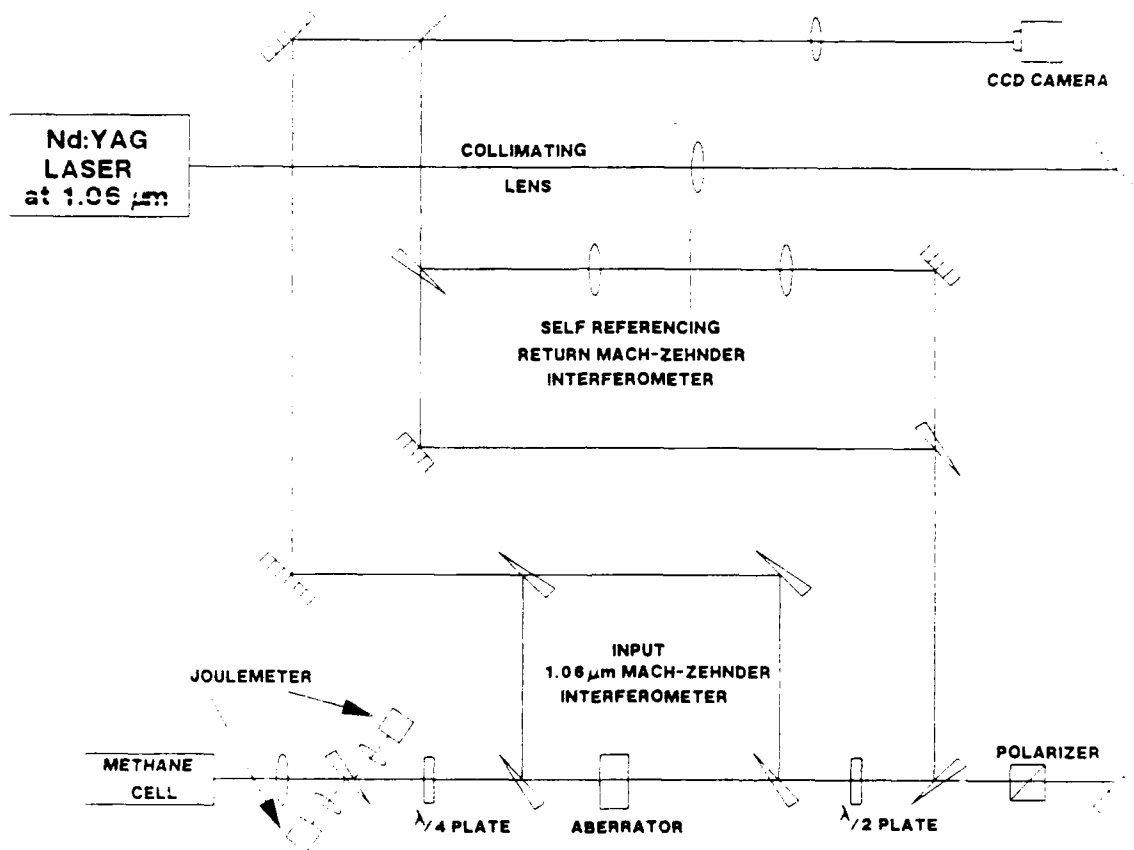


Figure 6-1. Experimental schematic for SBS reflectivity and fidelity in methane.

After reflection from two turning mirrors the laser is incident on a cube polarizer which rejects any vertical polarization component which may be in the beam. The polarization is then rotated by ninety degrees by a half wave plate before beam splitting for the 1.06 μm input Mach-Zehnder interferometer which monitors the beam quality into the SBS cell. This Mach-Zehnder consists of four quartz wedges of almost equal wedge. The wedge angles are placed such that each arm of the interferometer sees the same optical path and astigmatism is kept to a minimum. The test arm of the interferometer contains either a cylindrical lens or a helium jet aberrator. The He-jet aberrator consists of a nozzle placed between two parallel plates. The beam passes over the nozzle between the plates. The He-flow through the nozzle is regulated by adjusting the He pressure behind a small orifice. The parallel plates provide isolation from cross drafts. The index of refraction is reduced in the He channel, creating a mostly astigmatic aberration.

After passing through the interferometer the beam is circularly polarized by a quarter wave plate. The input energy is monitored by a quartz wedge joulemeter combination. A f=30 cm lens focuses the beam into the SBS cell for phase conjugation.

The SBS cell consists of a 21 inch long, 0.5 inch diameter ID, 2.0 inch diameter OD aluminum tube with one half inch thick quartz windows. The windows are slightly angled (three degrees) with respect to the axis of the tube to avoid back reflections. The cell was filled with methane gas as the SBS medium at a pressure of 900 psig.

The reflected beam energy is also monitored by a wedge/joulemeter combination before passing back through the quarter wave plate where it is horizontally polarized. The half wave plate and cube combination can then block any return which may be reflected back into the laser. After horizontal polarization the beam passes back through the sample arm of the Mach-Zehnder containing the aberration. If the wave is exactly time reversed, reverse passage through the aberration should cancel the input aberration for aberrations which are not polarization dependent such as those considered here. A sample of the return beam is then picked off and sent to a second self-referencing Mach-Zehnder where the return beam quality is monitored. The reference arm of this Mach-Zehnder contains a spatial filter so that aberrated beams are filtered to provide a reference

plane wave. The interferogram from this Mach-Zehnder contains any residual aberration which may remain after SBS correction.

Both input and return fringes are displayed simultaneously on a CCD camera. Data analysis is achieved by video taping the camera output and photographing the video display. Fringe patterns can then be digitized and analyzed.

6.2.2 Stimulated Brillouin Scattering Experimental Results

SBS reflectivity and beam quality were monitored for several cylindrical aberrations and input energies. Fixed cylindrical aberrations were obtained by placing cylindrical lenses of low power in the aberrator position in the experiment shown in Figure 6-1. Cylindrical lenses were used to provide a quantifiable amount of astigmatism and to simulate the astigmatic aberrations expected both in solid-state slab lasers and high power doublers. The He-jet aberrator was also placed in this position and the He pressure varied to change the magnitude of the aberration. Figures 6-2 through 6-8 present the results of these experiments.

Figures 6-2 through 6-5 illustrate the results of experiments with cylindrical lens aberrators. The cylindrical lenses used had optical powers of $\pm .12D$, $\pm .25D$, $\pm .50D$, and $\pm .75D$ where diopters (D) are units of inverse focal length in meters⁻¹. Figure 6-2 shows the dependence of reflectivity on aberrator magnitude. As more aberration is introduced, the reflectivity is significantly reduced and the SBS threshold is increased. A table of SBS threshold in methane as a function of aberrator power is given in Figure 6-3. These thresholds were calculated from a linear fit to the input energy versus output energy plot for each aberrator.

Figure 6-4 shows sample fringes from the input and return Mach-Zehnder interferometers at a laser voltage of 750 volts. Even though the input aberration increases dramatically, the return Mach-Zehnder fringes remain fairly constant. A residual of less than .1 wave is apparent in the return beam, even for the higher input aberrations, indicating excellent SBS fidelity and beam quality. The beam quality (BQ) was given a quantitative value by using the definition:

$$BQ = (R_p/R_a)^{-1/2} \quad (6-1)$$

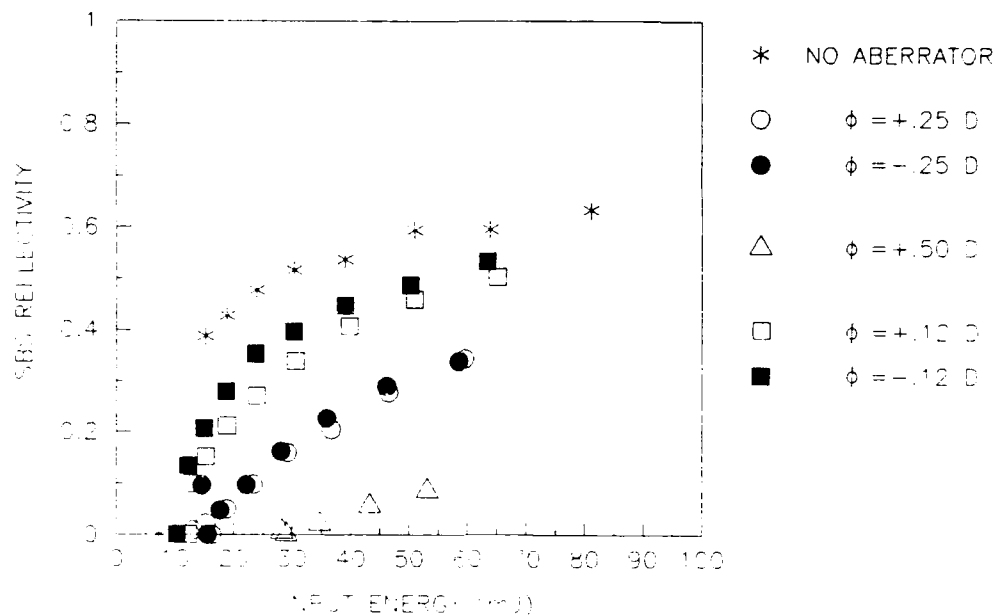
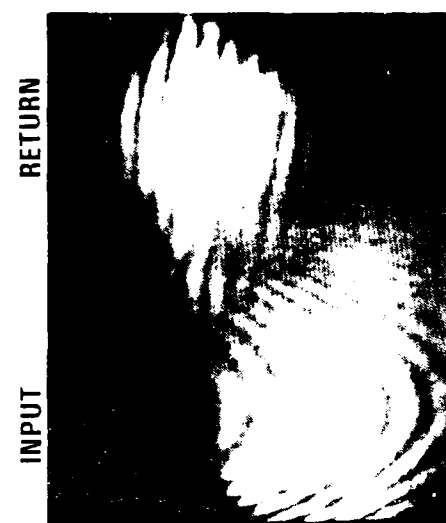


Figure 6-2. SBS reflectivity as a function of input energy for various cylindrical aberrators.

<u>E_{Thresh}(mJ)</u>	<u>ϕ (diopters)</u>	<u>He Jet (psi)</u>
7.25	No Aberrator	
12.17	.12	
10.28	-.12	
16.23	.25	
15.48	-.25	
28.98	.5	
23.11	-.5	
34.32	.75	
27.34	-.75	
5.98		0
10.65		20
14.23		30

Figure 6-3. Table of SBS threshold and aberrator power for cylindrical and helium aberrators.



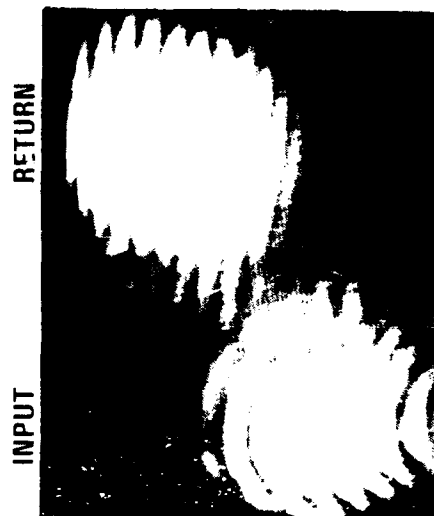
c) $f = -2.0 \text{ m} (-0.5 \text{ D})$



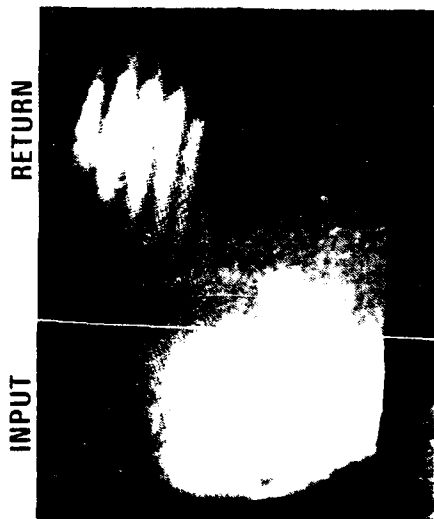
b) $f = -4.0 \text{ m} (-0.25 \text{ D})$



a) $f = -8.3 \text{ m} (-0.12 \text{ D})$



f) $f = 8.3 \text{ m} (0.12 \text{ D})$



e) $f = 2.0 \text{ m} (0.5 \text{ D})$



d) No aberrator

Figure 6-4. Input and SBS Return Fringes for Various Cylindrical Lens Aberrators

CYLINDRICAL ABERRATORS

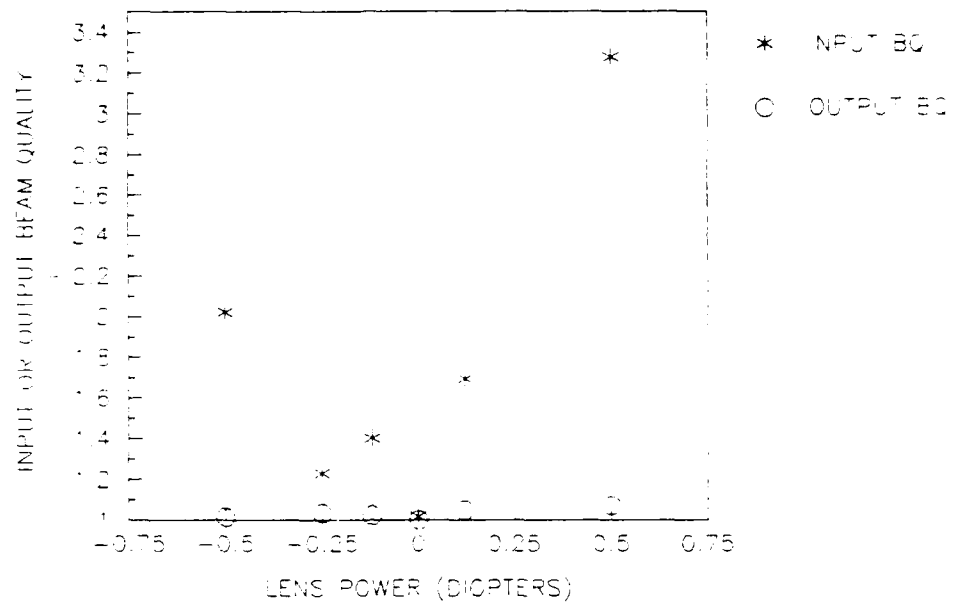


Figure 6-5. Input and output beam quality as a function of lens power for various cylindrical aberrators.

HE-JET ABERRATORS

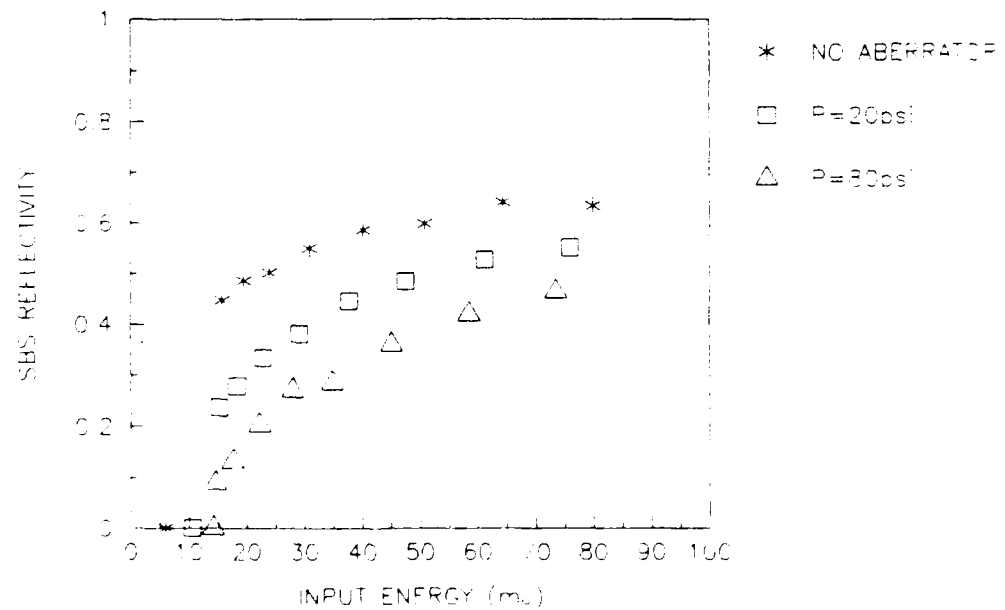


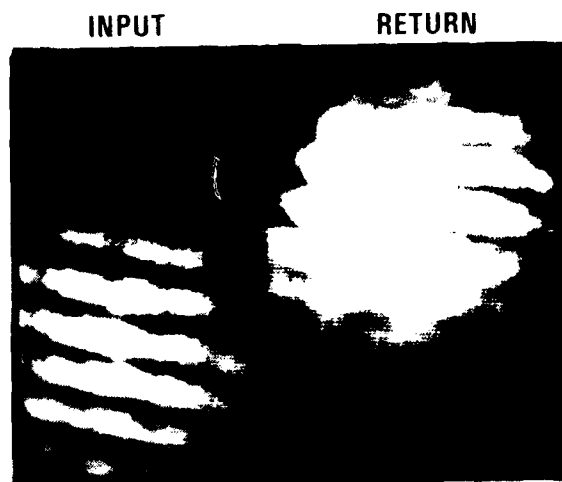
Figure 6-6. Reflectivity as a function of input energy for two helium jet aberrations.

where R_p is the focused beam radius that includes 86% of the energy for a perfect plane wave and R_a is the radius that contains 86% of the energy for an aberrated beam. These radii were determined from a fringe analysis program called WISP (WYCO Interferogram Software Package) available from the WYCO Corporation of Tucson, Arizona. The fringe patterns were digitized and read into the WISP program. The program performs a Zernike polynomial fit to the data and calculates the amount of Seidel aberrations in the beam as well. It also calculates encircled energy, a plot of energy in the focussed beam as a function of radius. The radii for 86% of the encircled energy were used for R_p and R_a to calculate beam quality. Plots of input beam quality and output beam quality as a function of input energy are shown in Figure 6-5 for the cylindrical lens aberrators. Notice that even though the input beam quality may be as bad as 3.25 times diffraction limited that the corrected beam quality is always very close to diffraction limited, $BQ = 1.0$, demonstrating that SBS conjugation fidelity remains excellent over this range of astigmatism.

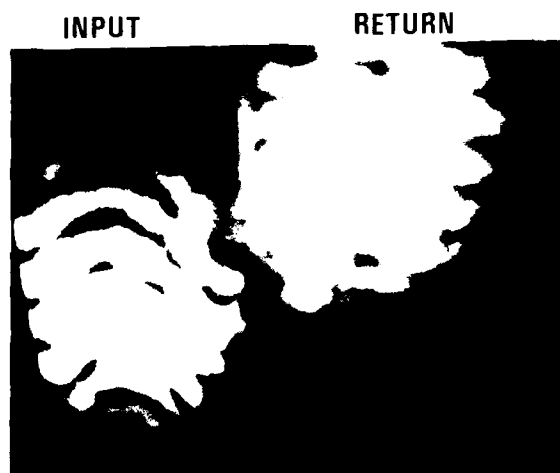
The same type of experiments were performed with the He-jet aberrator as for the cylindrical lens aberrators and the results are shown in Figures 6-6 through 6-8. Figure 6-6 shows the SBS reflectivity as a function of input beam energy for two helium pressures. Here again, as pressure increases (increasing aberration) reflectivity goes down and threshold goes up (see Figure 6-3). Figure 6-7 shows input and return Mach-Zehnder fringes for He-jet produced aberrations. The He jet produces aberrations which are not purely cylindrical in nature. WISP analysis shows that this type of aberrator produces increased amounts of defocus, coma and spherical over cylindrical lenses with the same astigmatism. Figure 6-8 shows that beam qualities of greater than 2.45 times the diffraction limit are corrected to less than 1.10 times diffraction limited by the SBS process.

6.3 Phase Conjugated Doubling Experiment

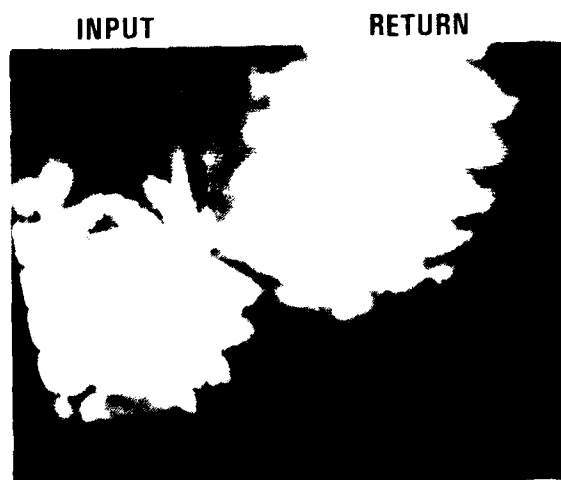
After phase conjugation in methane was characterized, a harmonic generator was inserted into the experiment to demonstrate phase conjugated doubling (Figure 6-9). The polarization properties of the beam were the same as in the previous experiment. Thus, incoming $1.064\mu\text{m}$ radiation



a) No aberration



b) He gas pressure is 20 psi



c) He gas pressure is 80 psi

Figure 6-7. Input Fringes and SBS Return Fringes for the He-Jet Aberrator

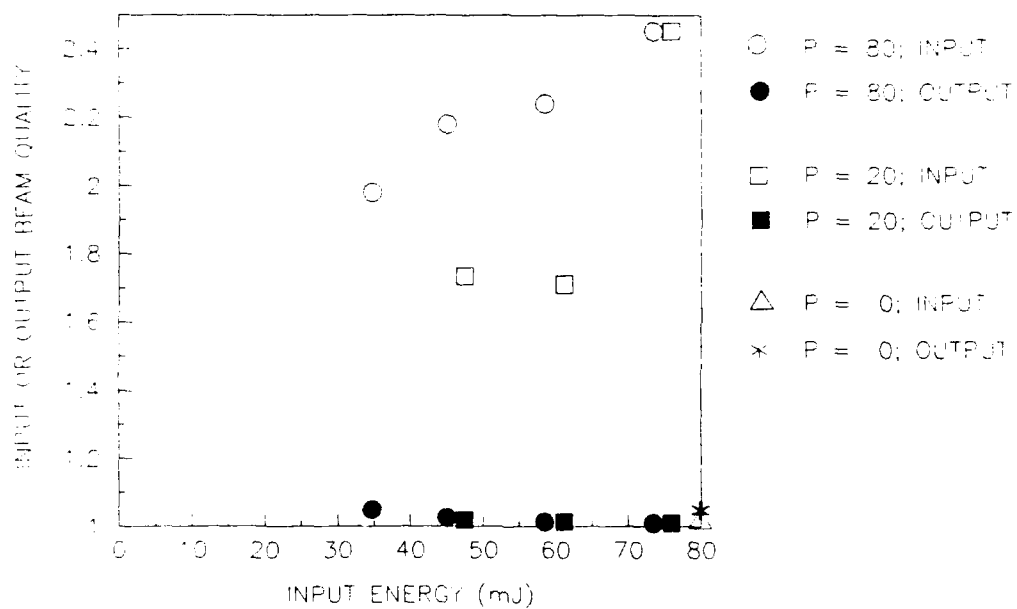


Figure 6-8. Input and return beam quality as a function of energy for helium-jet aberrators.

passed through the doubler and aberrator with vertical polarization. The doubling crystal was oriented so that this polarization was not phase matched; the incoming beam reads optical aberrations but is not frequency converted. Part of this beam was picked off and interfered with a reference beam in a Mach-Zehnder configuration as before. The input beam was phase conjugated via SBS in methane and returned through the doubler with a phase matched polarization. After conversion to $.532\mu\text{m}$ radiation the beam passed back through the aberrator where the aberrations were undone. Phase variations $\phi_f(x)$ sensed at the fundamental are time reversed by SBS and come back to the doubler with equal but opposite phase as $-\phi_f(x)$. When the frequency is doubled these phase variations are also doubled giving $-2\phi_f(x)$ since the field of the harmonic wave is proportional to the square of the amplitude of the generating wave (see Appendix B). When the conjugated wave passes back through the doubler and is converted, each wave of optical path difference (OPD) that was read on the input pass is now read as two waves of OPD at the harmonic thereby cancelling the $-2\phi_f(x)$ of the conjugated phasefront. This corrected return was monitored by sending a sample of the beam into the return self-referencing Mach-Zehnder interferometer.

6.3.1 Phase Conjugated Doubling Experimental Setup

Prior to setting-up the phase conjugated harmonic conversion experiment (PCHCE) the conversion efficiency of the CD*A doubler was characterized. The data from this experiment is shown in Figure 6-10. The peak efficiency observed was 5% at 340 mJ input energy. However, for the PCHCE typical efficiencies were on the order of 2.5%, limited by the input available from our laser and optical losses on the many experimental components.

We noticed early on in the PCHCE that the SBS reflectivity was reduced when the doubler was inserted in the experiment. Evidence of this is shown in Figure 6-11, where the SBS reflectivity is monitored with and without the doubler in place. This change in SBS performance can be explained by the existence of a significant amount of polishing error on the doubler's optical surfaces. An interferogram of the doubler aberration is shown in Figure 6-12. WISP analysis has shown that the doubler added $-.67$ waves of defocus, $-.09$ waves of astigmatism, $+.25$ waves

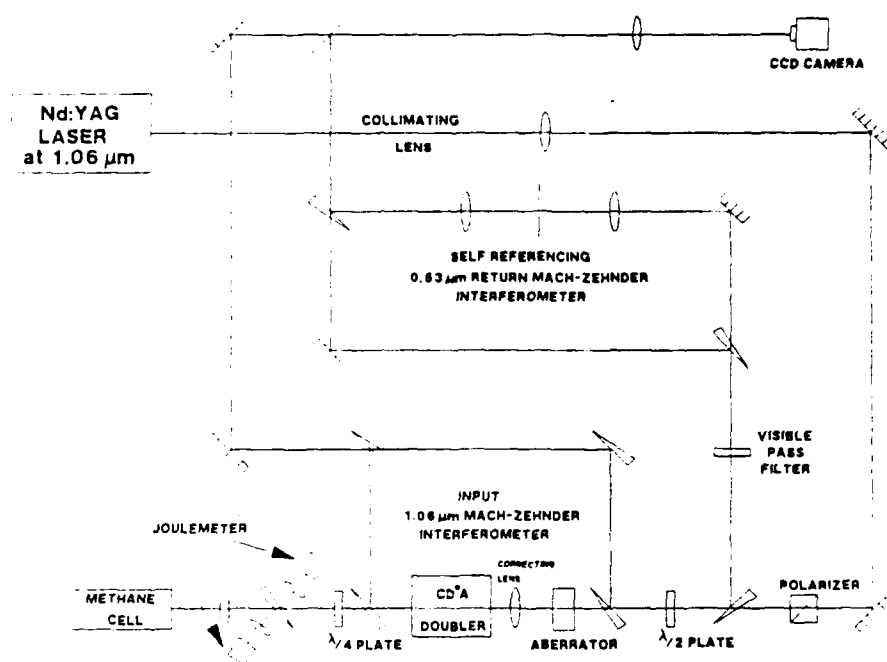


Figure 6-9 Schematic for harmonic doubling experiments.

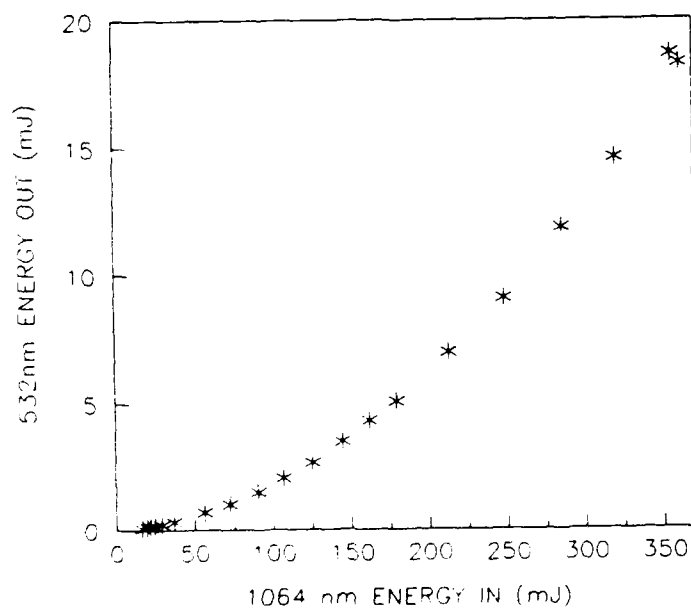


Figure 6-10. Type I Doubling efficiency for CD * A. .532 μm energy out as a function of 1.064 μm input energy.

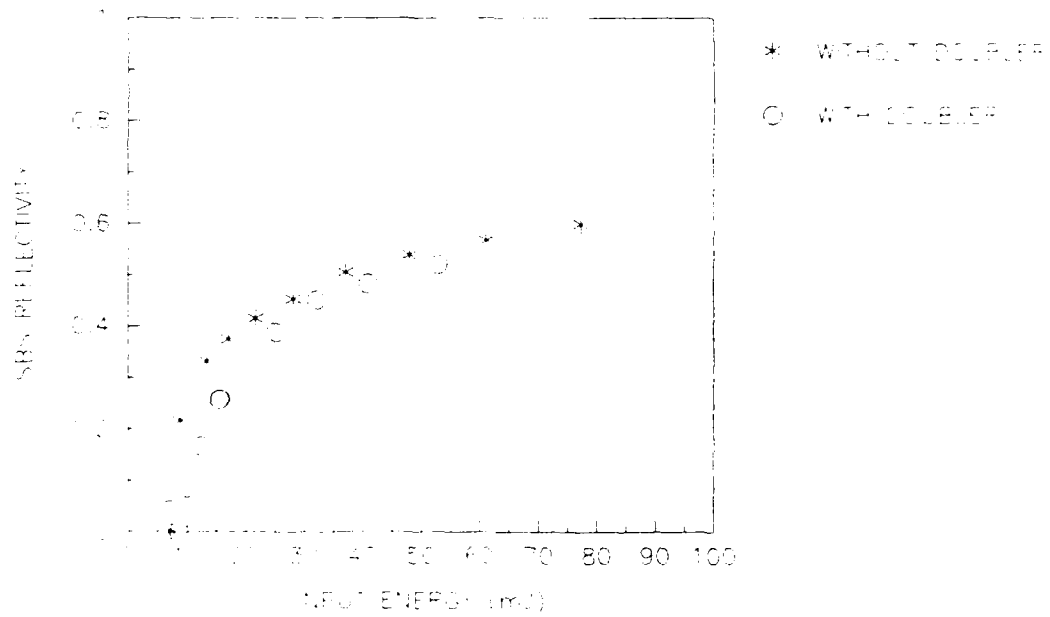


Figure 6-11. SBS reflectivity as a function of input energy with and without CD*A doubler.

a) No aberrations,
bare interferometer



b) CD*A crystal



c) CD*A crystal with
corrector lens
($f = 8.33$ m)

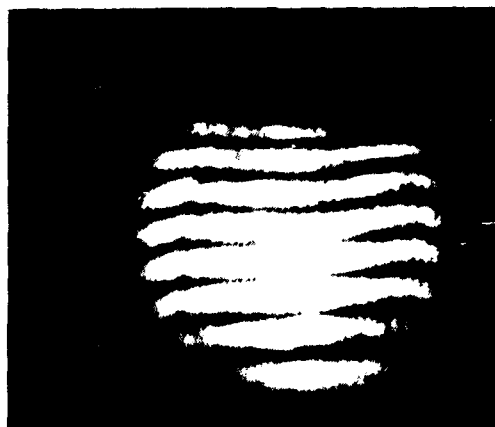


Figure 6-12. Correction of Doubler Aberration

of coma and $+0.21$ waves of spherical aberration, decreasing the beam quality of the input from 1.0 times diffraction limited to 1.25 times diffraction limited. Addition of a spherical corrector lens of -0.12 diopters, shown in Figure 6-9 decreased the defocus by $.33$ waves, the coma by $.04$ waves, and the spherical by $.12$ waves, increasing the beam quality to 1.08 times diffraction limited. The corrected interferogram is shown in Figure 6-12c. All following measurements were made with the corrector lens in place since the reflectivity returned to a higher level even though not all aberrations were completely corrected.

The phase conjugated doubling experiment is very similar to the SBS experiment described in section 6.2.1. The aberrator was moved upstream to make room for the doubler and its correcting lens but kept close to the doubler to simulate aberrations that reside in the doubler. The return sampling arm was modified to pass only visible radiation, blocking the infrared radiation that was not doubled. The mirrors of the return Mach-Zehnder were originally chosen to have high reflectivity in the visible and infrared so that realignment was minimized. The self-referencing spatial filter aperture was reduced to compensate for the shorter wavelength.

6.3.2 Phase Conjugated Doubling Experimental Results

SBS reflectivity and fringe patterns for phase conjugated harmonic doubling were recorded for various cylindrical aberrators ($\pm 0.12D$, $\pm 0.25D$, $\pm 0.5D$). The reflectivity data is shown in Figure 6-13. As the power of the cylindrical aberrator was increased the reflectivity was significantly reduced and the threshold increased as expected from our previous SBS experiments. Threshold numbers were obtained from linear least-squares fits to the input energy versus output energy plots. The threshold data is presented in Figure 6-14. Reflectivity for aberrations higher than $.50$ diopters was so low that doubling was not observed. The same lack of doubling was observed when the He-jet aberrator was tried.

Notice that the reflectivity plot for no aberrator and for $\phi = +0.12D$ almost lie on top of each other and that negative aberrators always have lower reflectivities than their positive counterparts. This can be explained by the existence of a residual astigmatic doubler aberration after correction. The corrector lens, being spherical could not correct

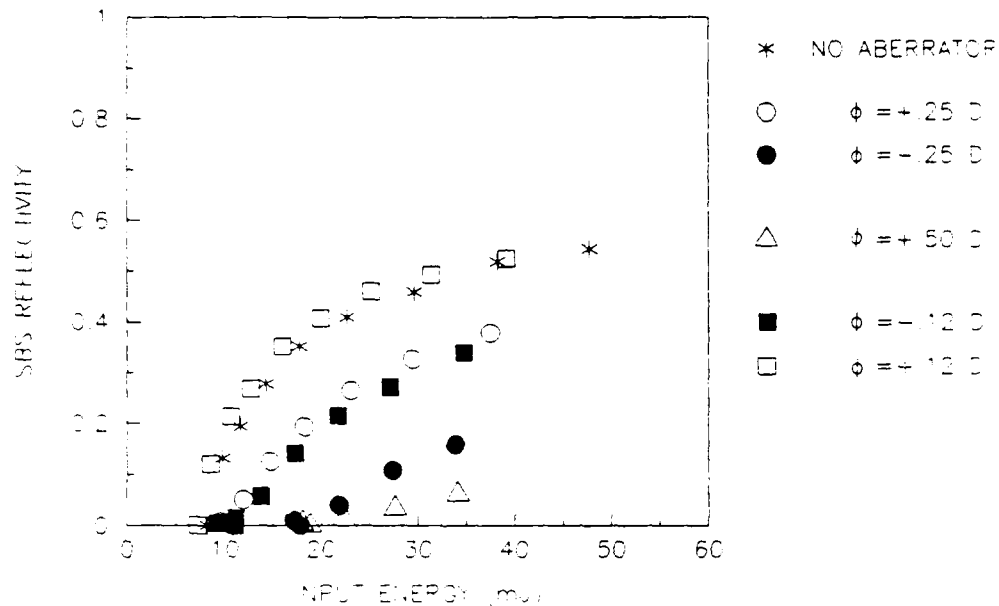


Figure 6-13. SBS reflectivity, doubler with corrector in place, as a function of input energy for various cylindrical aberrators.

<u>E_{Thresh} (MJ)</u>	<u>ϕ (Diopters)</u>
8.22	No Aberrator
10.70	.25
17.74	-.25
18.86	.5
18.19	-.5
7.20	.12
11.06	-.12

Table 6-14. Table of thresholds for various cylindrical aberrators obtained during phase conjugated doubling experiment.

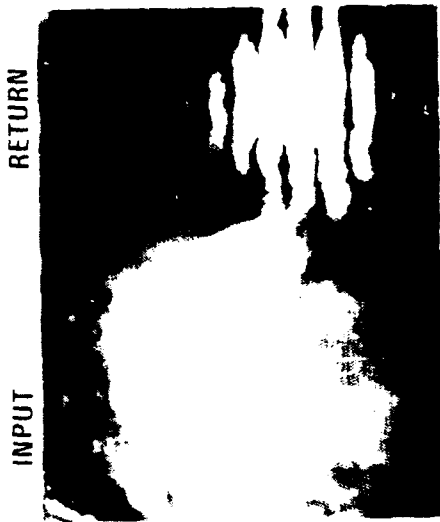
astigmatic doubler aberrations. The WISP analysis shows a $-.09$ wave astigmatic aberration after correction. Such a residual would be additive for negative aberrators reducing reflectivity and subtractive for positive aberrators increasing reflectivity.

Interferometer fringes were also recorded for the phase conjugate doubling experiment; representative samples are shown in Figure 6-15. These types of fringes were digitized and analyzed using the WISP program, which calculated beam quality as previously described. Figure 6-16 shows how input and return beam quality vary with input energy for $\phi = \pm .12D$. There is not a significant increase in beam quality for the $\pm .12 D$ cases shown until ≈ 1.5 times SBS threshold is reached. Similar plots for increased aberrator power are not shown because the threshold became high enough that few return data points could be obtained over a range of input energies. Data shown in Figure 6-17 was obtained for a laser amplifier voltage of 700 volts which was near the maximum capability for our system. Figures 6-17a and b show beam quality as a function of aberrator power in diopters for both cylindrical and spherical lens aberrators. These plots show that for cylindrical aberrators producing input beam qualities of up to 2.7 diffraction limited, return beam qualities of less than 1.2 times diffraction limited were obtained and spherical lens aberrators resulting in beam qualities of up to 7.0 diffraction limited were almost perfectly corrected.

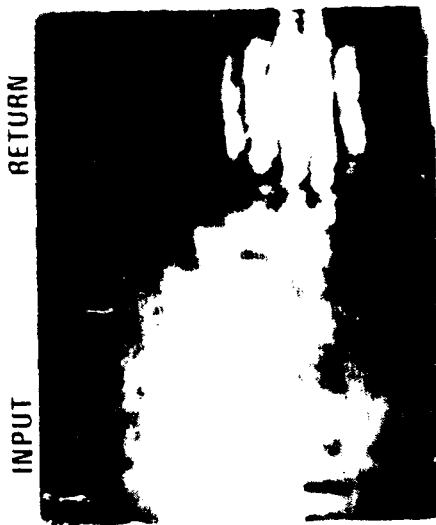
6.4 Stimulated Brillouin Scattering Modeling of Astigmatic Beams.

6.4.1 Model Description

Stimulated Brillouin scattering of astigmatic waves was modeled using the BRIWON code. Since BRIWON is a two dimensional code (1 transverse and 1 propagation) and astigmatism is a 3-dimensional effect, the code was modified to simulate an astigmatic beam by decoupling focusing along the two transverse axes. This was achieved by employing the regular wave-optic focus and creating a second geometric focus in the transverse dimension orthogonal to that used to calculate fidelity. The separation between the two foci was varied to simulate different amounts of astigmatism. The intensity at the geometric focus was calculated based on a spot size equal to that calculated from diffraction theory and the depth



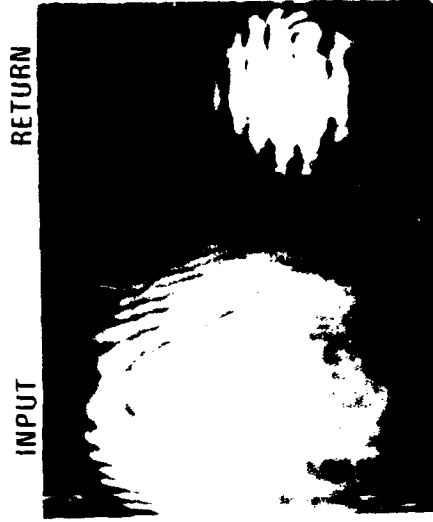
c) $f = -8.33 \text{ m}$



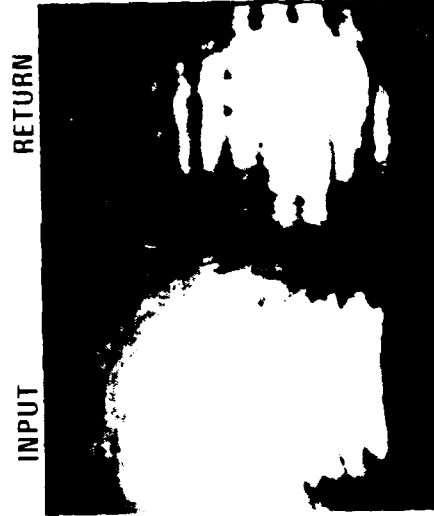
b) $f = -4.0 \text{ m}$



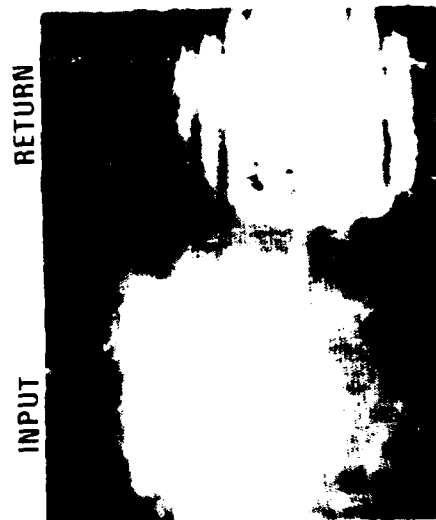
a) $f = -2.0 \text{ m}$



f) $f = 2.0 \text{ m}$



e) $f = 8.33 \text{ m}$



d) $f = 0.0 \text{ m}$

Figure 6-15. Input and Doubled Return Fringes for Various Cylindrical Lens Aberrators

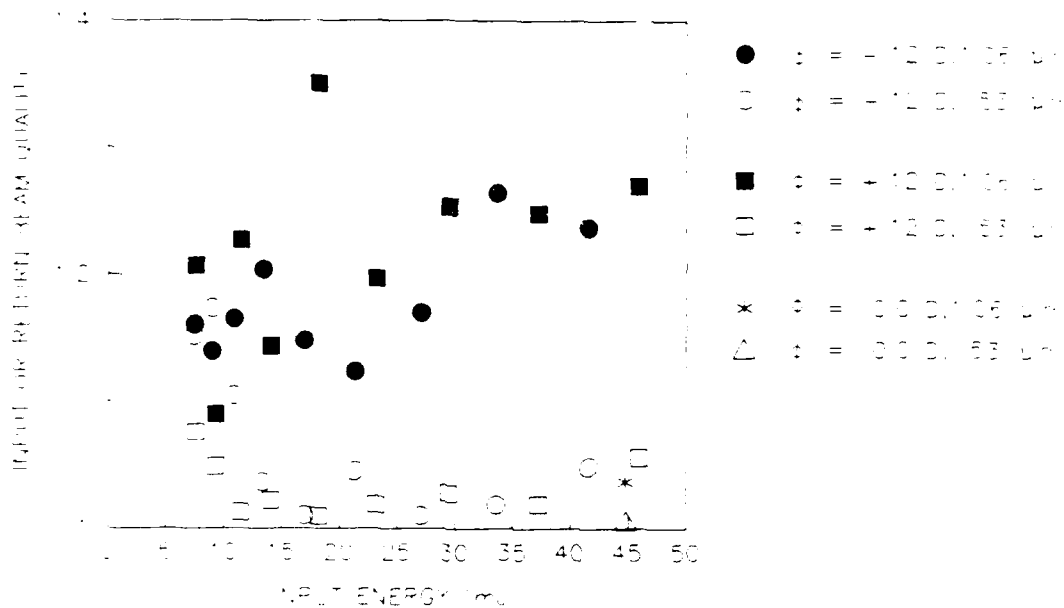


Figure 6-16. Input and output beam quality as a function of input energy for two cylindrical aberrators.

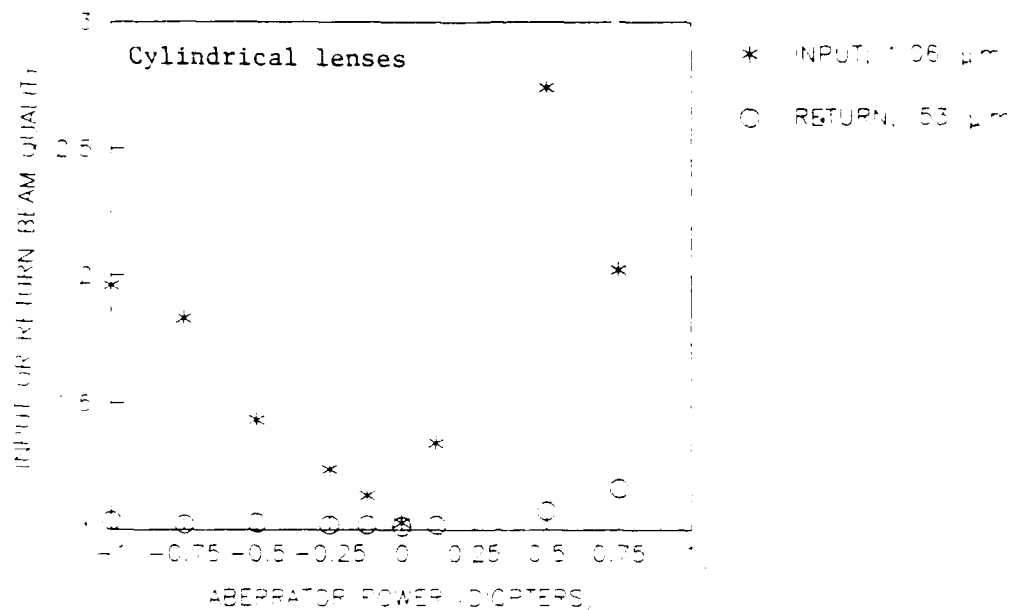


Figure 6-17a. Input and Return Beam Quality for Various Cylindrical Lenses

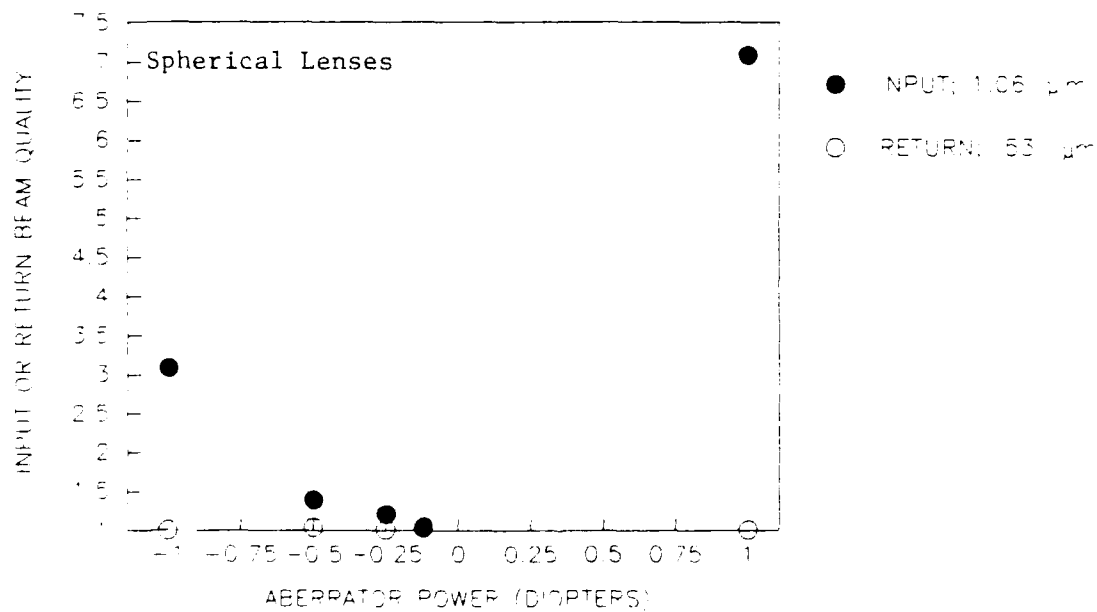


Figure 6-17b. Input and Return Beam Quality for Various Spherical Lenses.

of focus was chosen to be equal to the Rayleigh range. Figure 6-18 shows a sketch of the modeled beam geometry at the focal region, and a three dimensional plot of the intensity in the SBS cell (the SBS gain has been set to zero to eliminate pump depletion). Note that the intensity diagram indicates that the model has a tendency to underestimate the peak intensity at the geometric focus as compared to the wave optics focus, but the respective gIL products which determine the overall gain in the focal regions are comparable.

Another limitation of BRIWON is the fact that it is a steady state code. Thus, the threshold power predicted by the code may be significantly lower than that measured experimentally if the phonon lifetime of the SBS medium is comparable to the pump pulse width (transient regime). At 60 atmospheres of methane, where most of the experiments were performed, the phonon lifetime is approximately 10 ns, and is roughly equal to the pump pulse width. Under these conditions the anticipated threshold energy can be approximated by:

$$E_{th} = N \cdot r_{ph} \cdot P_{ss} \quad (6-2)$$

where N is a number on the order of 5-10 for $BQ < 1.5$, r_{ph} is the phonon lifetime and P_{ss} is the calculated steady-state SBS threshold power. Since r_{ph} is roughly equal to the pulse width, the ratio of $P_{transient}/P_{ss}$ should be approximately N . Thus, when comparing the threshold powers calculated by the model to those observed experimentally, the factor N should be incorporated. The threshold power observed experimentally was .6-.7 MW (6-7 mJ), and the calculated steady state threshold power was 80 KW; this corresponds to a value for N of approximately 8.

6.4.2 Modeling Results

Two sets of experimental conditions were modeled. The first was a series of runs calculating the reflectance, beam quality and threshold power of an incident beam with varying amounts of astigmatism ranging from .1 to .4 diopters. The second was a calculation of the beam quality as a function of input power for a fixed astigmatism of .37 diopters. For the latter case the maximum power level used was roughly 10 times the

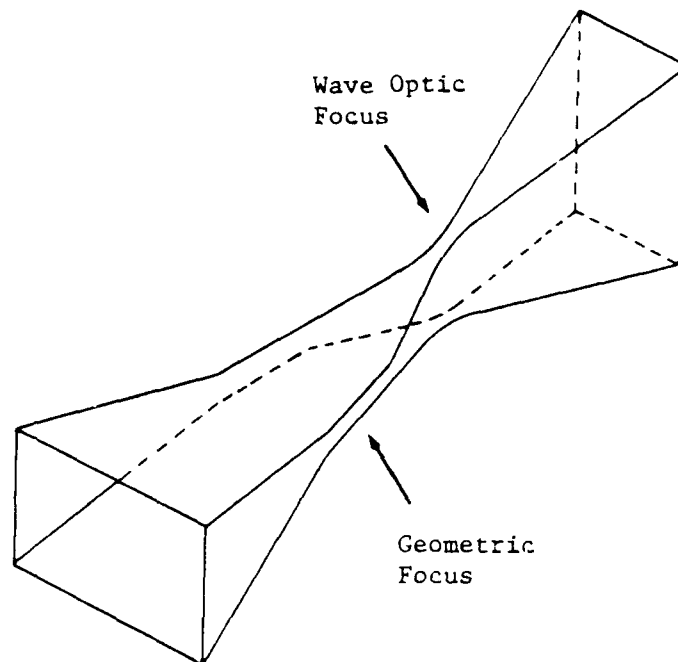


Figure 6-18a. Focussing geometry simulated by BRIWON model.

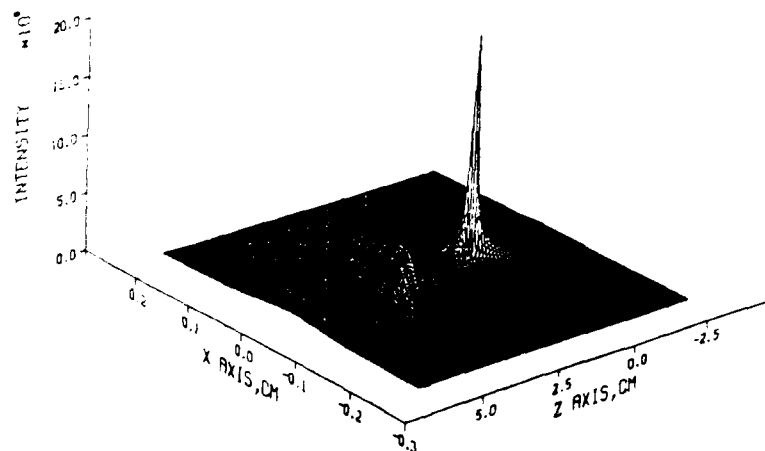


Figure 6-18b. Pump beam intensity profile in the focal region.

threshold, beyond which the code diverged. Where possible, the parameters used for the model calculations matched those used for the experiments.

Figure 6-19 shows a representative output from BRIWON for a case with .37 diopters of astigmatism, and at a power level four times the unaberrated threshold. It consists of the nearfield and farfield intensity profiles for both pump and Stokes beams, and a phase profile of the Stokes beam. It shows a virtually flat wavefront over the large majority of the Stokes beam aperture and an increase in the farfield spot size of the Stokes beam primarily due to the reduction in Stokes aperture size. In addition, BRIWON calculates the SBS reflectance and the threshold power (power transmitted through the cell), which for this case are .17 and 270 KW respectively.

Figures 6-20, 6-21 and 6-22 summarize the model calculations. Figure 6-20 shows the calculated SBS reflectance and the change in threshold power as a function of astigmatism. The reduction in reflectance is a direct result of the increase in the threshold, and correlates well with the experimental results (see section 6.5). Figure 6-21 shows the Stokes beam quality as a function of astigmatism; it predicts excellent beam quality for all cases with a slight trend toward decreased beam quality at higher aberrations. As mentioned above, the increase in the far field spot size of the Stokes beam is primarily due to a reduction in aperture size while the wavefront remains virtually flat over most of the Stokes aperture for all cases. Since the main experimental diagnostic used for measuring fidelity has been interferometry (wavefront OPD), the experimental results are expected to be unaffected by such an effect. Figure 6-22 shows the beam quality for .37 diopters of astigmatism as a function pump energy. It shows an initial improvement in beam quality as the process moves away from threshold also followed by a trend toward decreased beam quality at higher powers. This is expected because of the high intensities at the front focus (geometric focus) which is in the near field of the wave optics dimension of the beam. If the overall gain in this region is high enough ($g_{IL} > 25$), a Stokes beam can grow without benefit of all the phase information that would ordinarily be coded in the far field intensity profile. Higher energy runs are expected to show more dramatic effects but this requires substantial code modifications and is beyond the scope of this effort.

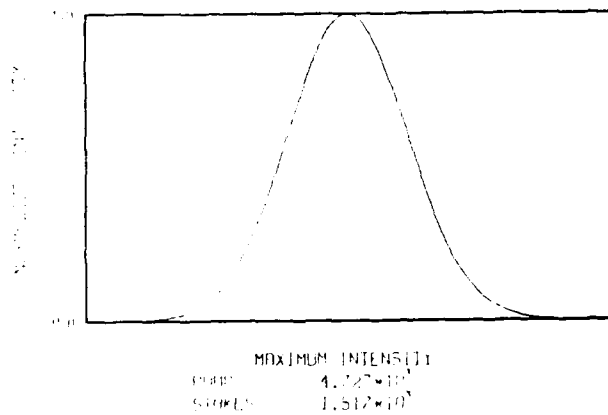


Figure 6-19a. Normalized intensity at the input lens for pump and return Stokes beams.

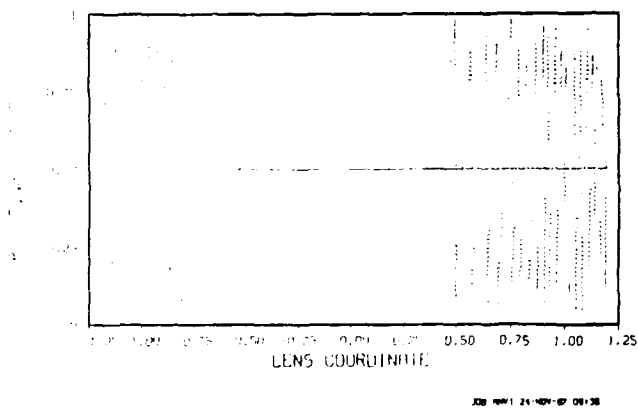


Figure 6-19b. Phase plot of Stokes beam.

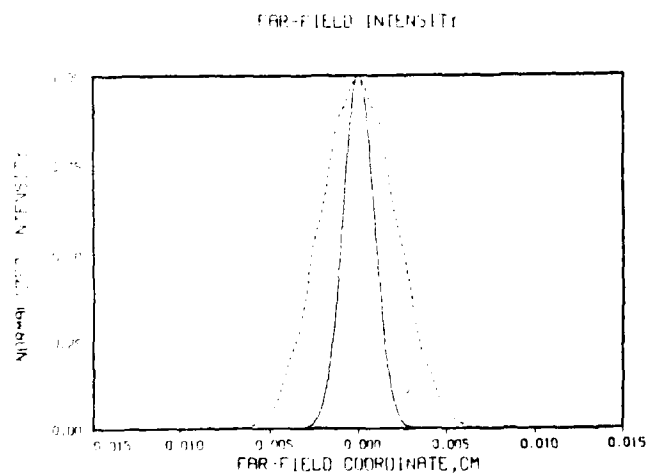


Figure 6-19c. Farfield intensity distribution for input and Stokes beams.

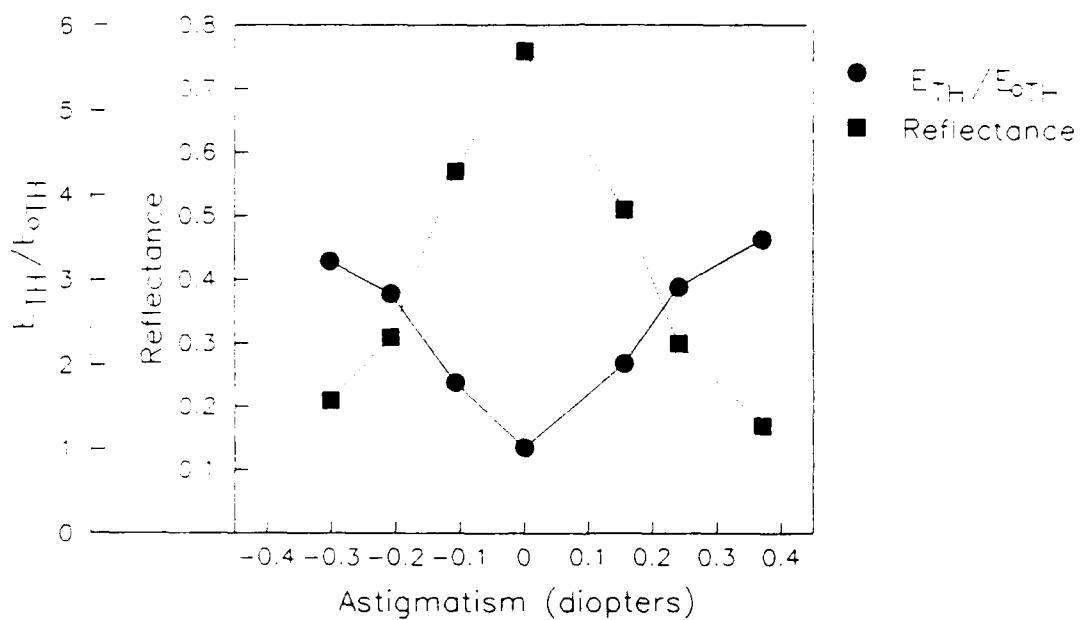


Figure 6-20. Reflectance and Relative Increase of SBS threshold as a function of Astigmatism.

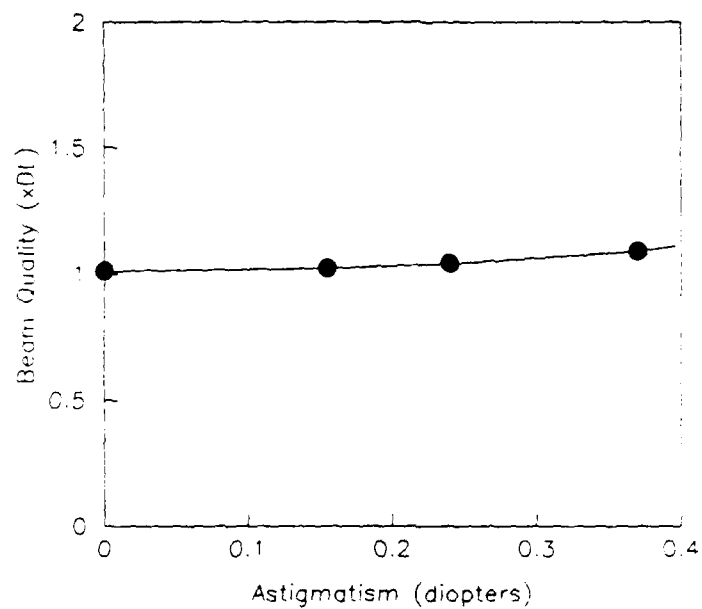


Figure 6-21. Stokes Beam Quality as a function of Astigmatism.

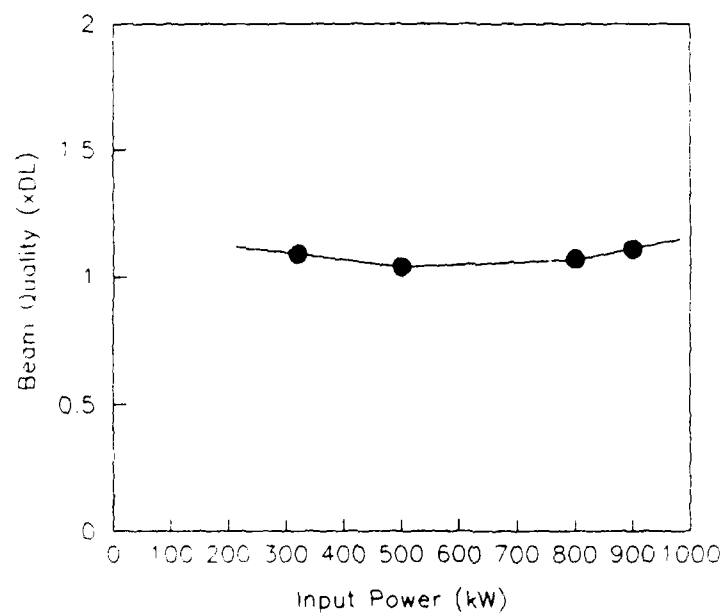


Figure 6-22. Stokes Beam Quality as a function of Input Power.

6.5 Conclusions

The PCHCE has demonstrated that phase conjugated doubling is a viable process i.e. that doubler aberrations sensed at the fundamental wavelength can be phase conjugated and corrected on the doubling pass. We have also shown that SBS and PCHC can handle up to one diopter of defocus and one diopter of astigmatism. The major problem uncovered in the PCHC process is the reduction of SBS reflectivity with increasing astigmatism.

This reduction in reflectivity has been successfully modeled with the BRIWON code. Figure 6-23 shows a comparison of reflectivity as a function of aberrator power as predicted by BRIWON and as observed in the experiment. Trends in the data are accurately predicted by BRIWON, however there is discrepancy in reflectance magnitude. Since the model assumes strictly monochromatic light and the experiment is performed with some finite frequency bandwidth, we would expect the model to predict a higher reflectivity. Figure 6-24 compares experimental results and theoretical predictions of return beam quality as a function of astigmatism. Again, there is good agreement between BRIWON's predictions and experimental observations.

BRIWON also predicts that for higher energy beams than available in our experiments that near field conjugation may reduce SBS fidelity. If conjugation occurs in the near field, then not all the phase information has been converted into intensity information when reflection occurs and the return beam will not be time reversed. If this occurs then aberrations cannot be completely corrected. Our experiment has never been able to reach these conditions because of limited laser power. The predicted fidelity reduction due to near field conjugation may limit the expected correctable aberration in high power laser beams unless the coherence length of the laser is substantially longer than the separation of the two foci.

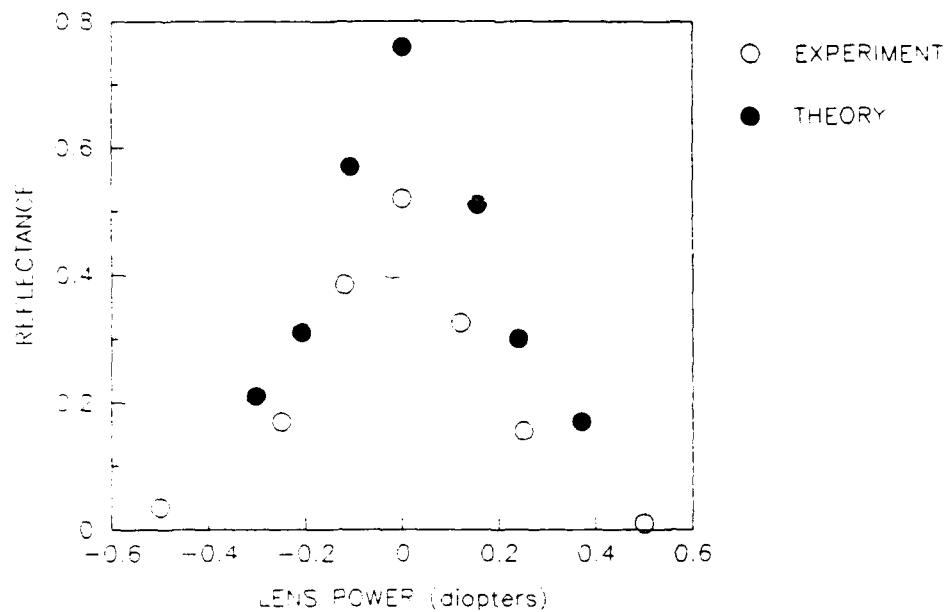


Figure 6-23. Comparison of Theoretical and Experimental Results:
Reflectance as a Function of Cylindrical Abberator Power.

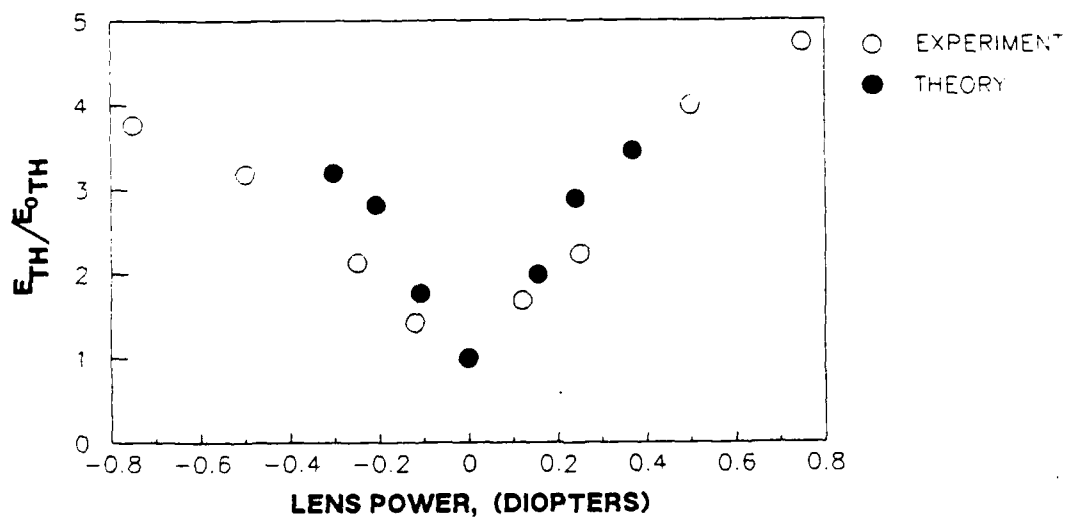


Figure 6-24. Comparison of Theoretical and Experimental Results:
Relative Threshold as a Function of Cylindrical
Aberrator Power.

7.0 50 WATT WAVELENGTH AGILE Nd:YAG LASER RAPID TURN-ON ANALYSIS

Wavelength agile solid state lasers in the 50 watt range (1 J @ 50 Hz) are transmitter candidates for a variety of tactical applications. These lasers are typically Nd:host lasers where wavelength agility is provided through a combination of harmonic conversion and Raman shifting. Many of these application require rapid turn-on (<2 seconds) from a standby condition to full performance and all components must be designed to meet this requirements.

In this section we analyze the thermal response of a 1 J, 50 Hz, Nd:YAG laser equipped with a frequency doubler and a D_2 Raman converter to provide output at $1.06\mu\text{m}$, $.53\mu\text{m}$, and $.62\mu\text{m}$. A thermal analysis of each component has been performed to determine the medium temperature variations as a function of time (particularly for time greater than 2 s) and the corresponding optical path differences (OPD). An assessment is made whether these OPDs can be corrected with fixed aberrator plates, or dynamic aberration correction techniques such as phase conjugation are needed. A target residual OPD of $\lambda/10$ has been selected for times longer than 2 seconds.

The system analyzed contains three primary components that are susceptible to thermally induced optical aberrations: the laser slab, the frequency doubling crystal, and the Raman cell. In addition, temperature nonuniformities in the doubling crystal can cause a change in the refractive indices resulting in a phase mismatch and reduction in conversion efficiency. The system under consideration already incorporates design features that minimize thermal degradation of the beam and the start up transient time. The laser slab is 0.6 cm thick by 2.5 cm wide by 15 cm long. The large thermal diffusivity of Nd:YAG and the small thickness keep this slab nearly isothermal, with a short time to steady state. A zig-zag beam path through this slab averages the OPD in the pump (thickness) direction, so that the residual OPD is reduced by more than an order of magnitude.

CD*A and KD*P were evaluated as doubling crystals candidates. CD*A was chosen as the primary candidate because it reaches steady state faster and has a lower maximum OPD than KD*P. However, KD*P is retained as a

candidate because it has a lower equivalent acceptance angle (relative phase mismatch) than CD*A, so that conversion efficiency is less sensitive to thermal variations. To minimize thermal gradients, the doubling crystal dimensions were selected to be only slightly larger than the 0.6 cm by 2.5 cm beam dimensions, with a 50% conversion efficiency (3.0 cm long for CD*A or 4.9 cm long for type I KD*P).

The Raman cell is designed for a conversion efficiency of 50% and has a pumped region 0.6 cm by 0.625 cm by 50 cm long. The inside wall dimensions of the cell are also slightly larger than the pumped region to promote efficient heat removal. The Raman medium is 10 atmospheres of D₂, which has large thermal conductivity and diffusivity.

Each of these components would have minimal amounts of aberration at the start time that build up to the maximum aberration at steady state. Fixed phase plates can be used to correct the steady state aberrations so that in the presence of the plates, it is the initial isothermal standby condition that has the largest amount of aberrations. The optical quality improves as the system approaches steady state from standby mode. For system components where steady state is not reached within 2 s of turn on, the aberrations are minimized when the fixed phase corrector plates are selected to correct for the aberration that is halfway between that at 2 s and that at full steady state.

The following are time dependent temperature and OPD calculations for each of the components described above, as well as a calculation of the phase mismatch in the doubling crystal. The results are tabulated in Figure 7.1.

7.1 Thermal Gradient Analysis

The maximum temperature difference (center to beam edge) for both the laser slab and the doubling crystal, and an upper bound temperature difference for the Raman cell, is given by

$$\Delta T_{\max} = \frac{Q_v b^2}{2k}$$

and the temperature profile in the x direction at steady state is

$$\Delta T = \Delta T_{\max} \left[1 - \left(\frac{x}{b} \right)^2 \right]$$

	Nd:YAG	CD*A	KD*P	D ₂
Total heat load, Q (W)	125	0.68	1.5	2.3
Heat per unit volume, Q _v (W/m ³)	5.6E6	front: 2.0E5 back: 1.0E5	2.7E5 1.3E5	1.2E5
Maximum temperature difference (K)	thickness: 1.92 width: 0.03	front: 0.45 back: 0.23	0.63 0.32	2.4
Time to 90% of steady state temperature (s)	1.9	6.5	9.0	0.73
Percent of steady state at 2 s	92%	50%	40%	99.7%
Maximum refractive index difference	thickness: 1.4E-5 width: 2.2E-7	8.7E-6	2.0E-5	1.0E-5
Equivalent acceptance angle due to temperature variations (mrad)	--	0.929	0.016	--
Optical path difference (nm)	34	260	750	5194
Maximum OPD after fixed correction and t > 2 s (nm)	1.4	65	225	7.8

Figure 7-1. Predicted thermal performance of various components of 50 W solid state laser.

where Q_v is the heat per unit volume, $b = 3$ mm is the beam half thickness, and k is the thermal conductivity. The thermal profile from center to beam edge at various times is shown in dimensionless form in Figure 7-2 (from Reference 7.1, page 131). The dimensionless times numbered on these curves are $\kappa t/b^2$, where κ is thermal diffusivity. The thermal properties of the component materials are tabulated in Figure 7-3.

7.2 Thermal Profiles in the Laser Slab

The Nd:YAG slab uses a zig-zag path to eliminate the optical path differences through the 6 mm thickness. However, there are also temperature variations along the 2.5 cm width. These edges are insulated from the heat sink with RTV. The solution to this conduction problem, a volumetrically heated slab with cooled sides and cooling exterior to insulation along the edges, is given in Reference 7.1, page 171. For the present Nd:YAG slab with 1/16 or 1/8 inch of RTV on the edges, the steady state center to edge temperature profile, shown in Figure 7-4, is a small fraction (2-3%) of the maximum temperature difference of 1.9 K through the thickness (Figure 7-1). The temperature variations penetrate about 3 mm in from the edges. The center to edge OPD is only 34 nm ($\lambda/30$) for the Nd:YAG slab, and most of this OPD is easily corrected.

7.3 Thermal Effects in the Doubling Crystal

The CD*A and KD*P doublers studied are Type I cut, uniaxial crystals. The doubling crystal is phase matched (IR to green) by aligning the beam along one ordinary axis, and rotating the crystal about this axis by an angle θ , so that

$$n^{2\omega}(\theta) = n_o^\omega$$

where

$$\frac{1}{[n^{2\omega}(\theta)]^2} = \frac{\cos^2 \theta}{(n_o^\omega)^2} + \frac{\sin^2 \theta}{(n_e^\omega)^2}$$

so that

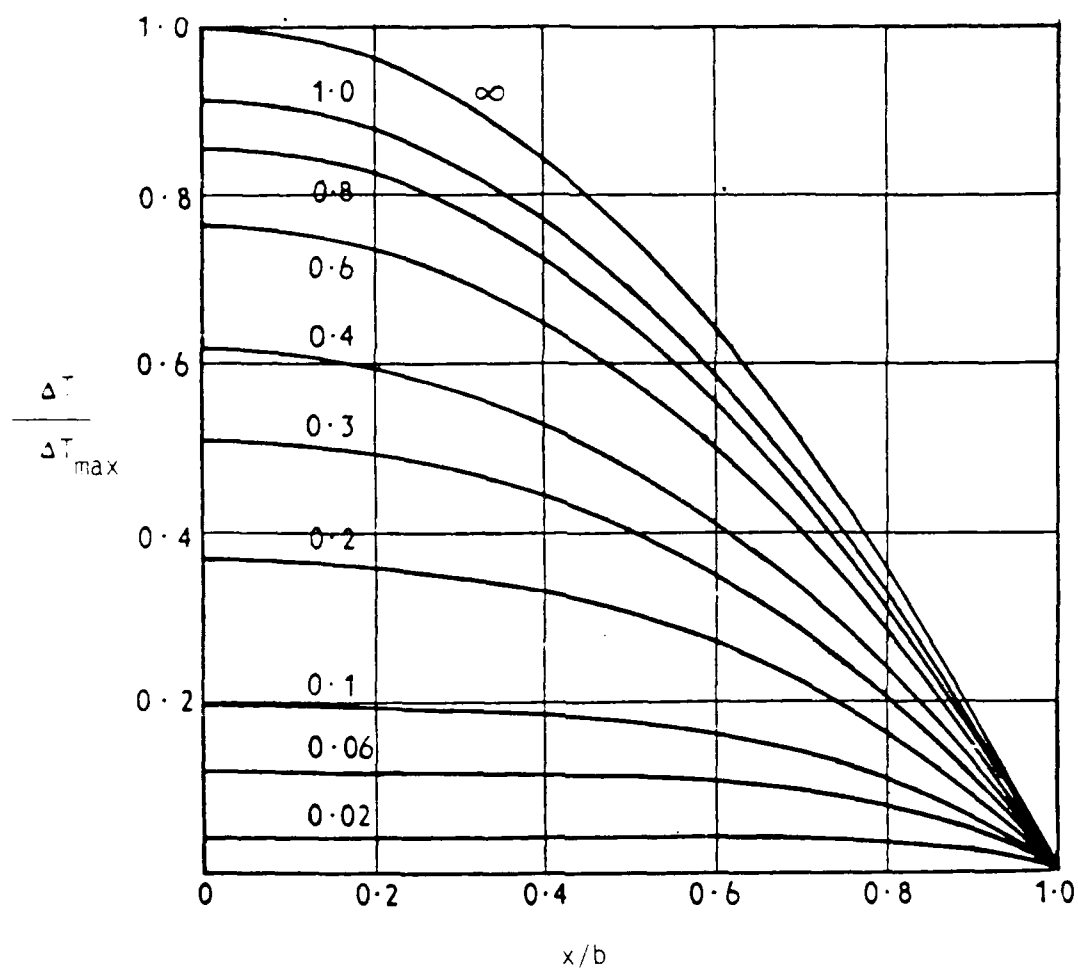


Figure 7-2. Temperatures in the slab $-b < x < b$ with constant heat production at the rate A_0 per unit volume and zero surface temperature. The numbers on the curves are values of $\kappa t/b^2$. (from reference 7.1)

	Nd:YAG	CD*A	KD*P	D ₂
Thermal conductivity (W/mK)	13	2.0	1.9	0.139
Thermal diffusivity (m ² /s)	4.6E-6	1.3E-6	9.4E-7	1.15E-5
Absorption coefficient (m ⁻¹)	--	0.6	0.8	--
dn/dT (K ⁻¹)	7.3E-6	-2.6E-5	-3.3E-5	-4.36E-6

Figure 7-3. Thermal properties of component materials.

EDGE COOLING EFFECT ON TEMPERATURE RTV Insulating the Edges

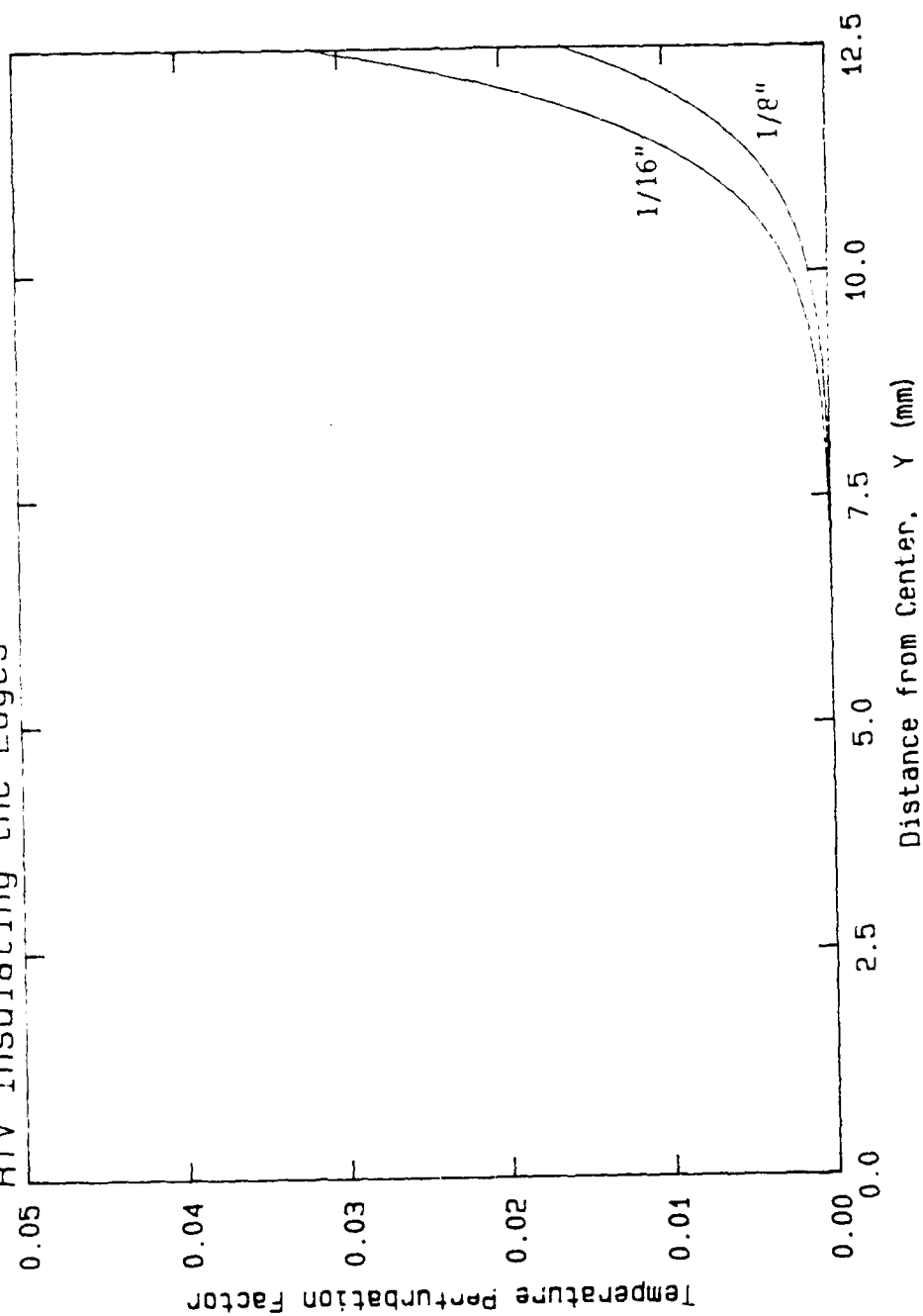


Figure 7-4. Center-to-edge thermal profile in steady state for an edge-cooled slab with two different thicknesses of RTV insulation.

$$\theta = \sin^{-1} \left(\sqrt{\frac{(n_o^\omega)^2 - (n_o^{2\omega})^2}{(n_e^{2\omega})^2 - (n_o^{2\omega})^2}} \right)$$

This angle is 84.9° for CD*A and 36.8° for KD*P. The refractive indices and their temperature derivatives are given in Figure 7-5.

The doubling crystals absorb at 1.06 μm , but not at 0.53 μm . Thus, the volumetric heating at the front end (before conversion) is much greater than at the rear. The volumetric heating rate profile is given by

$$Q_v(x) = I_0 \gamma (1 - \eta)$$

where I_0 is the slab laser output intensity, γ is the absorption coefficient, and η is the cumulative conversion efficiency up to length x . The conversion efficiency is given in Figure 7-6. The temperature variations across the thickness of the crystal cause peak-to-valley optical path differences of 0.26 μm for CD*A or 0.75 μm for KD*P; these OPDs can be reduced by a factor of 3 or 4 with fixed aberrator plates. The temperature variation also causes a maximum (front end) refractive index mismatch (IR to green) equivalent to a 0.929 mrad acceptance angle for CD*A or 0.016 mrad for KD*P. CD*A is better in terms of OPD, but KD*P is better in terms of refractive index mismatch (IR to green), an important consideration for efficiency.

7.4 Thermal Gradients in the Raman Cell

The 0.6 cm by 2.5 cm beam is collapsed to 0.6 cm by 0.625 cm before entering the Raman cell. This increased intensity results in $gIL = 13.3$ for a $L = 50$ cm cell length, where g is the Raman gain coefficient ($g = 2 \times 10^{-9}$ cm/W for 10 atmospheres of D_2), and I is the intensity corresponding to a 10 ns pulse duration.

The Raman cell is heated by the energy defect between the 0.53 μm input and the 0.63 μm output radiation. Thus, the heat load is 18% of the converted output energy. With a conversion efficiency of 50% (optical output of 0.25 J/pulse at 50 Hz), this heat load is 2.25 W. The cell is cooled from four sides. This conduction problem, a volumetrically heated

		CD*A		KD*P	
		1.06 μm	0.53 μm	1.06 μm	0.53 μm
n	ordinary	1.54995	1.5694	1.49314	1.5075
dn/dT	ordinary	-2.54E-5	-2.56E-5	-3.17E-5	-3.32E-5
n	extraordinary	1.53413	1.5498	1.45824	1.4685
dn/dT	extraordinary	-2.27E-5	-1.84E-5	-2.24E-5	-2.66E-5

Figure 7-5. Refractive indices of the two candidate doubling materials at the fundamental and second harmonic wavelengths.

η	x (cm)	
	CD*A	KD*P
0.0	0.00	0.00
0.5	3.00	4.92
0.6	3.51	5.75
0.7	4.12	6.75
0.8	4.91	8.06
0.9	6.19	10.15

Figure 7-6. Conversion efficiency as a function of interaction length in the two candidate doubling materials. This efficiency is important for calculating heating due to absorption at the fundamental wavelength.

rectangle with cooled sides, is solved in Reference 7.1, page 171. The maximum temperature difference is 2.4 K. However, 99.7% of the steady state temperature is reached at 2 s, so that the resulting OPD is almost completely correctable with fixed aberrator plates.

Natural convection is not expected in the Raman cell, because the heating rate is very low. For horizontal fluid layers, the onset of natural convection occurs at an internal Rayleigh number of 583 (see Reference 7.2). The internal Rayleigh number in the Raman cell would be 44, and thus would be stable (stagnant gas with the conduction solutions being valid) by a wide margin. However, the stability to natural convection is not presently known for other, non-horizontal Raman cell orientations. The occurrence of natural convection would reduce the temperature variations slightly and shift the temperature profile. This temperature shift would be orientation dependent and may be difficult to predict. The Raman cell OPD correction with fixed aberrator plates would be limited by the uncertainty or the variability of this temperature profile shift. However, it would still be possible to reduce the OPD by about an order of magnitude. A conclusion of this work is to either keep the Raman cell horizontal or investigate whether natural convection exists in this system and determine its influence on the temperature profile for other Raman cell orientations.

7.5 Conclusions

In summary, the analysis has shown that the turn-on time of the system studied is limited by the transient response of the doubling crystal resulting in residual OPD of $\lambda/8$ at $.53\mu\text{m}$. This OPD is the maximum expected when an appropriate phase corrector plate is used. The laser slab and the Raman cell reach 92% and 99% of steady state within 2 s respectively, and can therefore be well corrected by using fixed phased plates if there is a fixed mode of operation. In Section 6 we showed that aberrations in the doubler can be dynamically corrected by using SBS phase conjugation. This is an option that can be used if the residual aberration calculated above is unacceptable or if higher or variable repetition rates are desired.

The single element that cannot be corrected through phase conjugation is the temperature induced phase mismatch in the doubling crystal. The

results shown in Figure 7.1 indicate that while the induced mismatch in $CD \cdot A$ is barely within the acceptance angle of the crystal (1 mrad), $KD \cdot P$ has a significant margin in this area and can be used in conjunction with phase conjugation to provide efficient, near diffraction limited beams at power levels even higher than that assumed here.

Finally, it should be pointed out that the predicted performance summarized in Figure 7-1 is a function of the average heat load, and therefore applies to any reasonable energy/repetition-rate combination yielding the same average power. In addition, the calculated OPDs are directly proportional to the heat load so performance at higher powers can be directly scaled from these results.

7.6 References

- 7.1 H.S. Carslaw and J.C. Jaeger, Conduction of Heat in Solids, 2nd ed., Oxford University Press, London, (1959).
- 7.2 K.S. Ning, R.E. Faw, and T.W. Lester, "Hydrodynamic Stability in Horizontal fluid Layers with Uniform Volumetric Energy Sources," J. Heat Transfer, 100, 729-730 (1978).

8.0 10 JOULE Nd:GLASS MOPA DESIGN

In this section we present the preliminary design of a 10 J, 5 Hz, phase conjugated, Nd:glass MOPA system. The design consists of a one dimensional analysis using modified versions of the Frantz-Nodvik equations suitable for zig-zag slab amplifiers. The main goal of the analysis is to provide a preliminary estimate of size and shape of the amplifier stages as well as the overall extraction efficiency. Phase conjugation is incorporated to improve the beam quality, but is included in the analysis only to the extent that it introduces some losses and makes the the system into a 2-pass MOPA; the issue of beam quality is not addressed explicitly.

To minimize the number of amplifier stages, we have assumed that the amplifier chain includes a Nd:YLF preamplifier. Because of the relatively high gains and low saturation fluences available in crystalline hosts, the Nd:YLF allows quick and efficient amplification of the beam to the 1 Joule level and provides the high fluence input necessary for saturating the Nd:glass amplifiers. Figure 8-1 illustrates the MOPA system analyzed.

To provide high repetition rates (5 Hz) and minimize the thermally induced aberrations, the preamp and amplifier gain media were designed to be zig-zag slabs. To describe the growth of the fluence as it passes through these amplifiers, a modified version of the Frantz-Nodvik equation (Reference 8.1) is needed which incorporates the folded propagation geometry characteristic of zig-zag slabs.

To be able to produce this equation in closed form, the propagating beam must fill the slab gain volume. This can be achieved by the appropriate selection of the angle at which the ends of the slabs are cut, and adjusting the angle of the input beam relative to the horizontal to maintain Brewster angle at the slab entrance. This is illustrated in Figure 8-2. The ray is incident at the Brewster angle ϕ , and the angle θ is chosen so that it is the same as the total internal reflection (TIR) angle at the bottom slab surface. α is the angle of the internal ray with the normal to the slab face. Inverting Snell's law gives

$$\alpha = \sin^{-1}\left(\frac{\sin \phi}{n}\right) \quad (8-1)$$

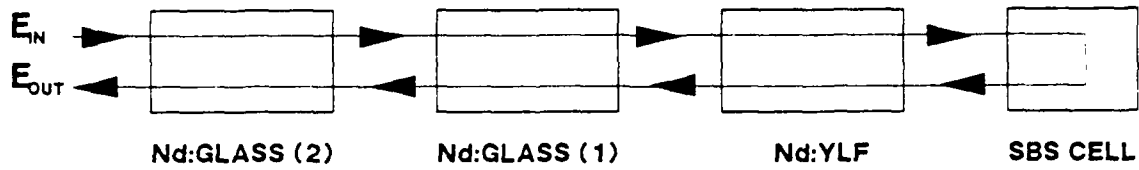


Figure 8-1. Schematic layout of 10 J Nd:glass MOPA analysis.

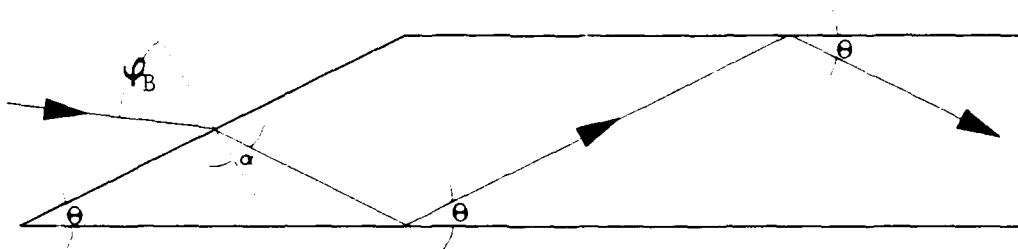


Figure 8-2. Input and propagation geometry of the optical beam through a zig-zag slab medium.

where n is the refractive index of the slab material. Figure 8-2 shows that

$$2\theta + \alpha + \pi/2 = \pi \quad \text{or}$$

$$\theta = \frac{\pi}{4} - \frac{1}{2} \sin^{-1} \left(\frac{\sin \phi}{n} \right) \quad (8-2)$$

From this equation, we find that θ for Nd:YFL is 29 degrees, and θ for Nd:glass is 28 degrees.

The slab is pumped only over an interior region with vertical faces, of area, A , given by the transverse dimensions of the slab, as illustrated in Figure 8-3. This geometry is equivalent to a vertically infinite gain region, with overlapping rays propagating at an angle $\pm\theta$ relative to the horizontal. This geometry can be analyzed in closed form because it is in essence a one-dimensional problem. The derivation of the modified Frantz-Nodvik equation corresponding to this geometry is presented in Appendix C. The result is

$$W_{\text{out}} = E_s A \cos \theta \ln \left[1 + e^{g_0 L / \cos \theta \left[e^{W_{\text{in}} / E_s A \cos \theta} - 1 \right]} \right] \quad (8-3)$$

where W_{in} and W_{out} are the input and output energies, E_s is the saturation fluence, A is the area of the vertical face of the pumped region (Figure 8-4), g_0 is the unsaturated (small signal) gain, L is the length of the pumped region, and θ is the TIR angle made by the rays with the top or bottom faces of the slab, as in Figure 8-2.

We start the analysis by assuming that the energy gained on the input first pass to the SBS cell through the amplifiers is negligible, i.e., the population inversions are unaffected by this pass. We will start the analysis with the outgoing second pass, then later go back and calculate what the initial input energy had to be for consistency. We will further make reasonable assumptions on the unsaturated gain in each slab medium and a damage threshold for the input fluence. These assumptions are tabulated along with other fundamental parameters in Figure 8-5.

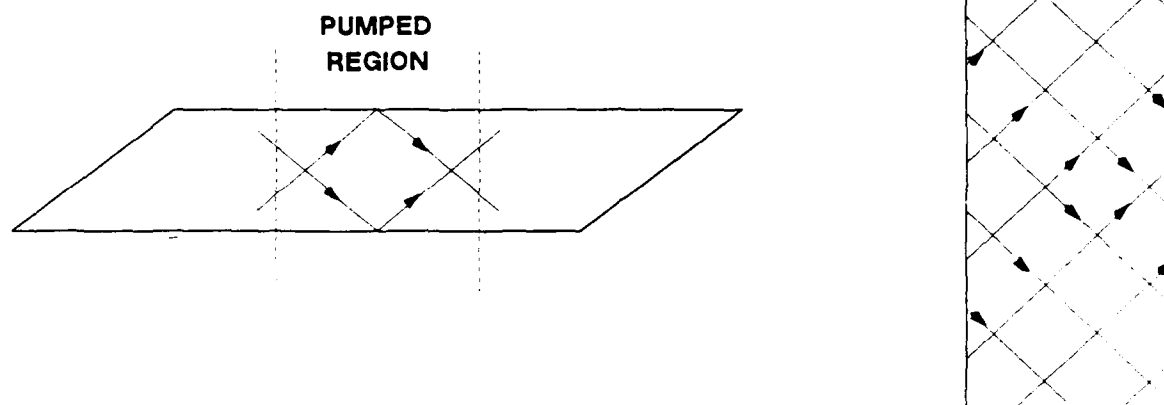


Figure 8-3. Ray propagation in the slab and the equivalent geometry used for the derivation of a modified Frantz-Nodvik equation.

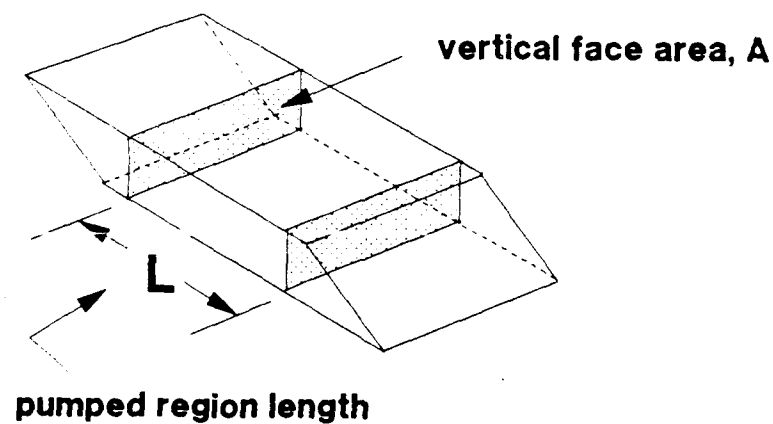


Figure 8-4. Geometry of the pumping region showing the vertical face area, A , and the pumping length, L .

<u>Parameter</u>	<u>Nd-Glass</u>	<u>YLF</u>
Stimulated emission cross section		
σ (cm ²)	3.9×10^{-20}	1.8×10^{-19}
Unsaturated gain		
$g_0 = N_0 \sigma$ (cm ⁻¹)	.05	.20
Wavelength		
λ (cm)	1.05×10^{-4}	1.05×10^{-4}
Photon Energy		
$h\nu = hc/\lambda$ (J)	1.91×10^{-19}	1.91×10^{-19}
Saturation Fluence		
$E_s = h\nu/\sigma$ (J/cm ²)	4.90	1.06
Damage Fluence		
E_d (J/cm ²)	10	10

Figure 8.5. Table of Parameters Used for the 10J MOPA Design

For the high gain Nd:YLF preamplifier, we first require that there be no amplified spontaneous emission (ASE), a condition usually satisfied when $g_0 L \leq 3$. If we assume that $g_0 L = 2.4$ (80% of the ASE limit), the pumped length L is 12 cm based on the gain assumed in Figure 8-5. For the Nd:YLF section to operate as a true preamplifier, we require that it provide nearly exponential growth. Using Equation 8-3 above, we can calculate W_{out} as a function of the cross-sectional area, A , of the slab for a given input energy, in this case 0.1 J at the entrance of the Nd:YLF slab on the outgoing pass. This input energy is the return from the SBS cell and represents 1% of the final output of the MOPA. Thus, it is consistent with the assumption that no significant energy depletion occurs on the input pass through the amplifier chain.

The results are shown in Figure 8-6, which shows signal gain and also shows the extraction efficiency. A slab with a very large A would give truly exponential growth but would have very low efficiency and would not be practical in terms of crystal growth; a small A would give excellent efficiency but no signal growth and would be difficult to pump. An area of 1 cm² was chosen as a reasonable compromise with a corresponding output energy of 0.94 J and an efficiency of 0.33.

We want maximum efficiency for the two Nd:glass stages, and so their dimensions will be adjusted to achieve this end. We define

W_n = the input energy for the n th stage

W_n' = the output energy for the n th stage

where $n = 1$ and 2 represent the first and second amplifiers respectively. The overall efficiency of the glass amplifiers is

$$\epsilon = \frac{W_2' - W_1}{h\nu N_0 (L_1 A_1 + L_2 A_2)} \quad (8-4)$$

where L_n and A_n are the length and area of the n th stage, $h\nu$ is the photon energy, and N_0 is the inversion density (assumed the same in both stages). From Equation 8-4, we see that to maximize ϵ we need to minimize $L_1 A_1 + L_2 A_2$. Toward this end we invert equation 8-3 to find

$$L = \frac{\cos \theta}{g_0} \ln \left[\frac{\exp[W_{out}/(E_s A \cos \theta)] - 1}{\exp[W_{in}/(E_s A \cos \theta)] - 1} \right] \quad (8-5)$$

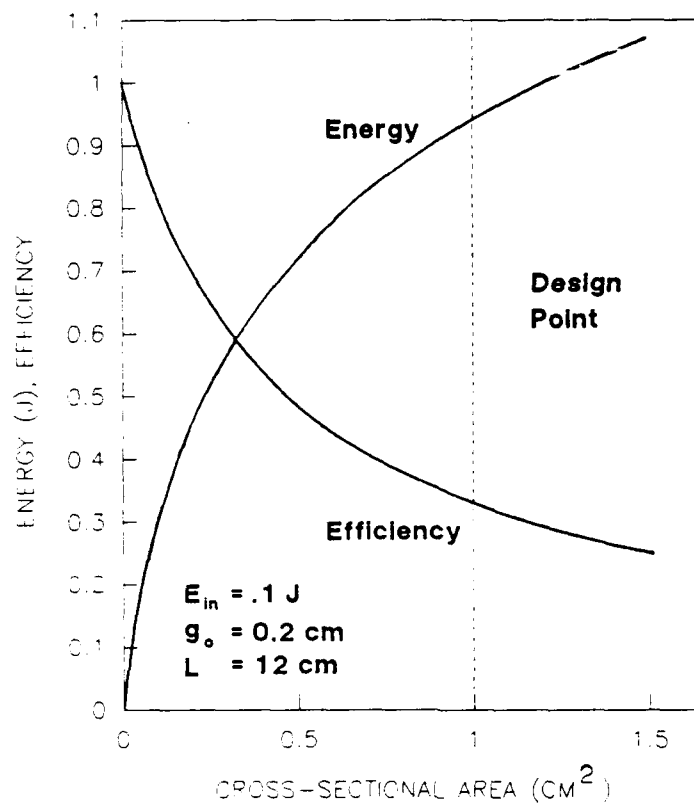


Figure 8-6. Extracted energy and extraction efficiency in the Nd:YLF preamplifier as a function of the slab cross-sectional area.

Next, to achieve maximum efficiency, it is desirable that the fluence E_s be as close to the damage fluence, E_d , as possible to maximize the stimulated emission. Therefore, we impose on the output energies the additional requirement,

$$W_n' = \xi E_d A_n \quad (8-6)$$

with $\xi = 0.8$ providing a 20% safety margin. Using Equation 8-6 in 8-5 to eliminate A_n in favor of W_n' , we obtain

$$\frac{\xi E_d g_0}{W_2' \cos \theta} (L_1 A_1 + L_2 A_2) = \chi \ln \left[\frac{K}{e^{\kappa/\chi} - 1} \right] + \ln \left[\frac{K}{e^{\beta\chi} - 1} \right] \quad (8-7)$$

where

$$\begin{aligned} \chi &= W_1' / W_2' \\ \beta &= \xi E_d / (E_s \cos \theta) \\ \kappa &= \beta (W_1 / W_2') \\ K &= e^{\beta} - 1. \end{aligned}$$

To maximize the overall efficiency, we need to minimize the right hand side of this equation as a function of χ . By using the parameters in Figure 8-5, and evaluating the above as a function χ , we find that the minimum occurs for $\chi = .40$. From Equations 8-5 and 8-6 we also find

$$L_1 = \frac{\cos \theta}{g_0} \ln \left[\frac{K}{e^{\kappa/\chi} - 1} \right] = 40.4 \text{ cm}, \quad (8-8)$$

and

$$L_2 = \frac{\cos \theta}{g_0} \ln \left[\frac{K}{e^{\beta\chi} - 1} \right] = 28.0 \text{ cm} \quad (8-9)$$

From the definition of χ , we have

$$W_1' = \chi W_2' = 4 \text{ J}$$

and from Equation 8-6 we get

$$A_1 = \frac{W_1'}{\xi E_d} = 0.5 \text{ cm}^2 \quad (8-10)$$

$$A_2 = \frac{W_2'}{\xi E_d} = 1.25 \text{ cm}^2, \quad (8-11)$$

where we have taken W_2' to be 10 J, the desired final output. The gain requirement to avoid ASE is satisfied for these two stages: $g_0 L_1$ and $g_0 L_2$ are 2.0 and 1.4 respectively, both well below the limit of 3.

Once the appropriate design parameters for the final pass are established, the required initial energy input on the first pass must be calculated. Solving Equation 8-3 for W_{in} , we find

$$W_{in} = E_s A \cos \theta \ln \left[1 + e^{-g_0 L / \cos \theta} \left(e^{W_{out} / E_s A \cos \theta} - 1 \right) \right] \quad (8-12)$$

Using Equation 8-12 and the numbers calculated above, we find that the required (first pass) input energy for the Nd:YLF stage is 9.7 mJ (which accounts for an SBS reflectivity of .7), for the 1st Nd:glass stage it is 1.0 mJ, and, finally, the required input energy from the master oscillator to the 2nd Nd:glass stage is 0.20 mJ.

The stored energy in any stage is

$$W_{sto} = h\nu N_0 LA \quad (8-13)$$

Using Figure 8-5 and the calculated values of L, A , we find

$$W_{sto}(Nd:YLF) = 2.57 \text{ J}$$

$$W_{sto}(Nd:glass1) = 4.93 \text{ J}$$

$$W_{sto}(Nd:glass2) = 8.54 \text{ J}$$

From the stored energies calculated above, we see that the fractional energy removed from the Nd:YLF on the input pass is less than 4% and that from the Nd:glass stages is less than 1%. Thus, the approximation of neglecting the first pass energy depletion when calculating the second pass results is satisfactory.

The overall efficiency of the system is

$$\begin{aligned} \epsilon' &= \frac{W_2'}{W_{sto}(Nd:YLF) + W_{sto}(Nd:glass1) + W_{sto}(Nd:glass2)} & (8-14) \\ &= \frac{10}{2.57 + 4.93 + 8.54} = 0.62 \end{aligned}$$

which is a reasonable value for such a system.

Finally we should examine these results to see if they are practical enough to be implemented in an actual system. The first issue at hand is the aspect ratio of the TIR surfaces of the two glass amplifiers. If we assume that thermal dissipation requirements limit the thickness of the slab to approximately 0.5 cm, the width of the glass slabs are 1.0 cm and 2.5 cm for the first and second stages respectively, corresponding to aspect ratios of 40 and 11. This type of a geometry is very hard to polish to the surface figures required by typical zig-zag slabs. Furthermore, the small width makes it nearly impossible to efficiently pump at the energy levels required. These problems are eliminated if the amplifiers are folded as shown in Figure 8-7. If the first amplifier is folded twice (three sections), the length of the slab becomes 13.5 cm and the width becomes 3 cm which is very typical of slab dimensions commonly used. Similarly, the second amplifier can be folded once, requiring a 14 x 5 cm slab. Except for minor losses in turning optics to accomplish the folding process, the folded geometry preserves the g_0L product of each amplifier and does not change the extraction efficiency.

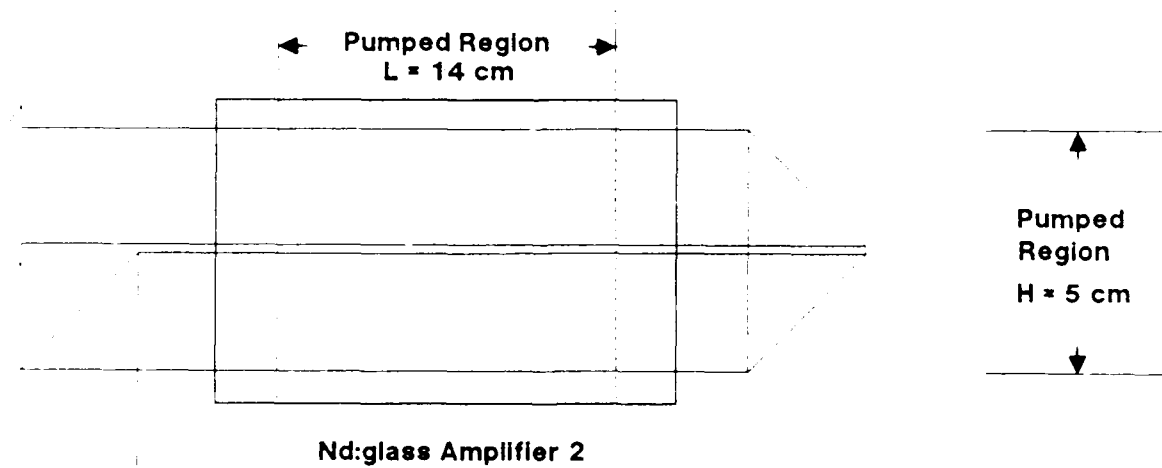
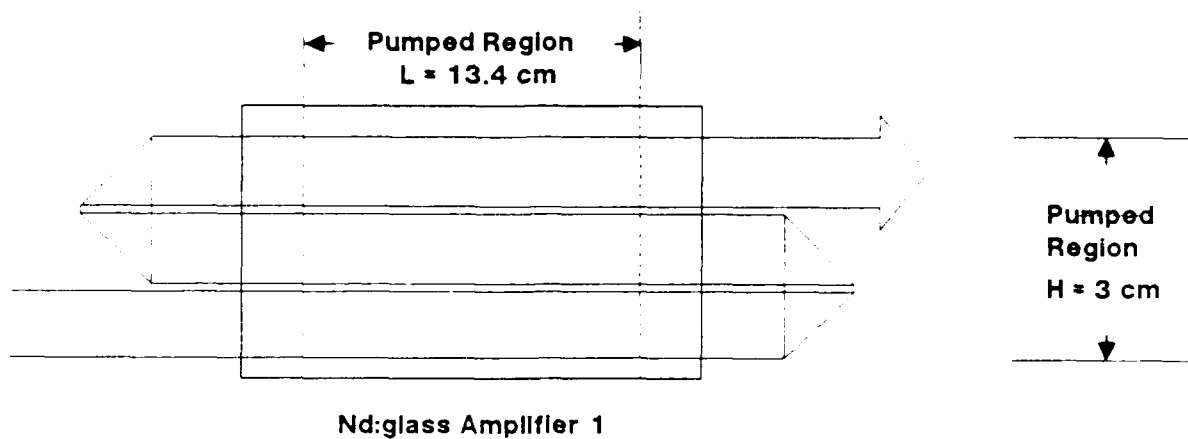


Figure 8-7. Folding geometries of the two Nd:glass slab amplifiers.

Not addressed in the above analysis are losses at the various optical surfaces which are necessitated by such a system. Since the above analysis is intended to provide a preliminary estimate of the design parameters, assumptions were made regarding the gain and the damage threshold, and the input energy was calculated to provide 10 J of output energy. In reality, both the input energy and the gain in the amplifiers can be varied over a wide range, and the assumed damage threshold is conservative. Therefore, losses in the optical elements can be compensated by introducing small changes in these parameters without significantly changing the overall performance of the system. Figure 8-8 summarizes the results of the analysis and the key parameters in the 10 J MOPA design.

References:

8.1 L. M. Frantz and J. S. Nodvik, J. Appl. Phys. 34, 2346 (1963).

<u>Parameter</u>	<u>Preamplifier</u>	<u>Amplifier 1</u>	<u>Amplifier 2</u>
Medium	Nd:YLF	Nd:glass	Nd:glass
Slab dimensions (cm)	.5 X 2 X 12	.5 X 3 X 13.5	.5 X 5 X 14
# passes (non overlapping)	1	3	2
Gain length (cm, unfolded)	12	40.4	28
Stored Energy (J)	2.6	4.9	8.5
E_{in} 1st pass (J)	9.6×10^{-3}	9.8×10^{-4}	2.0×10^{-4}
E_{out} 1st pass (J)	.14	9.6×10^{-3}	9.8×10^{-4}
SBS reflectance	.70	-	-
E_{in} 2nd pass (J)	.1	.94	4
E_{out} 2nd pass (J)	.94	4	10
Efficiency	.33	.62	.71
Overall efficiency	-	-	.62

Figure 8-8. Summary of 10 J MOPA design parameters.

APPENDIX A: ABSTRACTS AND SUMMARIES OF
OTHER NLOT FINAL REPORT VOLUMES

This appendix reproduces the DD Form 1473 and summaries of the other two volumes comprising the Nonlinear Optics Technology program final report. The first volume, Nonlinear Optics Technology Area I: FWM Technology, has already been submitted and is available through the Defense Technical Information Center as report number ADA174112. The work reported here is closely related to that reported in this other volume.

Because its contents are largely unrelated to the effort described in this volume of the report, the second volume, Nonlinear Optics Technology, Phase I, Area 2, is being submitted under separate cover at the same time as this report.

NONLINEAR OPTICS TECHNOLOGY

AREA I: FWM TECHNOLOGY

**J. BROCK, G. HOLLEMAN, F. PATTERSON,
J. FUKUMOTO, L. FRANTZ, M. VALLEY**

**PHASE I FINAL REPORT
JUNE 1985 - JUNE 1986**

**SPONSORED BY:
DEFENSE ADVANCED RESEARCH PROJECTS AGENCY
DARPA ORDER 5369, AMENDMENT #1**

**MONITORED BY:
OFFICE OF NAVAL RESEARCH
ARLINGTON, VA 22217-5000
CONTRACT #N00014-85-C-0257**

The views and conclusions contained in this document are those of the authors and should not be interpreted as necessarily representing the official policies, either expressed or implied, of the Defense Advanced Research Projects Agency or the U.S. Government.

**TRW
APPLIED TECHNOLOGY DIVISION
ONE SPACE PARK
REDONDO BEACH, CA 90278**

Unclassified

SECURITY CLASSIFICATION OF THIS PAGE

REPORT DOCUMENTATION PAGE

1a. REPORT SECURITY CLASSIFICATION Unclassified		1b. RESTRICTIVE MARKINGS	
2a. SECURITY CLASSIFICATION AUTHORITY		3. DISTRIBUTION/AVAILABILITY OF REPORT Unclassified/Unlimited	
2b. DECLASSIFICATION/DOWNGRADING SCHEDULE			
4. PERFORMING ORGANIZATION REPORT NUMBER(S)		5. MONITORING ORGANIZATION REPORT NUMBER(S)	
6a. NAME OF PERFORMING ORGANIZATION TRW Space and Technology Group	6b. OFFICE SYMBOL (If applicable)	7a. NAME OF MONITORING ORGANIZATION Office of Naval Research	
6c. ADDRESS (City, State and ZIP Code) One Space Park Redondo Beach, CA 90278		7b. ADDRESS (City, State and ZIP Code) Arlington, VA 22217-5000	
8a. NAME OF FUNDING/SPONSORING ORGANIZATION DARPA	8b. OFFICE SYMBOL (If applicable)	9. PROCUREMENT INSTRUMENT IDENTIFICATION NUMBER N00014-85-C-0257	
8c. ADDRESS (City, State and ZIP Code) Arlington, VA 2209-2308		10. SOURCE OF FUNDING NOS. PROGRAM ELEMENT NO. PROJECT NO. TASK NO. WORK UNIT NO.	
11. TITLE (Include Security Classification) Nonlinear Optics Technology, Area I:FWM Technology			
12. PERSONAL AUTHOR(S) J. Brock, G. Holleman, F. Patterson, J. Fukumoto, L. Frantz, M. Valley			
13a. TYPE OF REPORT Phase I Final	13b. TIME COVERED FROM June '85 to June '86	14. DATE OF REPORT (Yr., Mo., Day) 1986 September 22	15. PAGE COUNT 143
16. SUPPLEMENTARY NOTATION			
17. COSATI CODES FIELD GROUP SUB GR.		18. SUBJECT TERMS (Continue on reverse if necessary and identify by block number) Four-wave Mixing, Na Vapor, Phase Conjugation, Reflectivity, Imaging Fidelity, Noise Crosstalk	
19. ABSTRACT (Continue on reverse if necessary and identify by block number) Four wave mixing (FWM) performance in Na vapor was evaluated in the strong pumping regime ($I \gg I_{sat}$) required for typical applications related to point-to-point optical links. Gain (= reflectivity), imaging fidelity, and noise crosstalk were measured and analyzed under several conditions to obtain an engineering data base for potential tactical applications such as communications, surveillance, and guidance systems. Results include >230% reflectivity and 15 lines pair/mm imaging resolution, both the highest reported to date with cw pumping in low density Na vapor. The observed resolution was limited by the pixel spacing of our video camera. Ten lp/mm resolution was obtained after passing the input image through a 65 λ aberrator. Noise crosstalk was observable only when the combined signal/noise powers were large enough to saturate the phase conjugate return signal via pump depletion. Under these conditions, a degenerate, coherent noise beam 3x stronger than the signal beam produced only a 21% reduction in the intensity of the phase conjugate signal, and this degree of crosstalk decreased rapidly as the pump/noise angle increased.			
20. DISTRIBUTION/AVAILABILITY OF ABSTRACT UNCLASSIFIED/UNLIMITED <input checked="" type="checkbox"/> SAME AS RPT <input type="checkbox"/> DTIC USERS <input type="checkbox"/>		21. ABSTRACT SECURITY CLASSIFICATION Unclassified	
22a. NAME OF RESPONSIBLE INDIVIDUAL R. E. Behringer		22b. TELEPHONE NUMBER (Include Area Code) 818.795.5971	22c. OFFICE SYMBOL ONR - Pasadena

The experiments were performed with pump and probe beams that were derived from a single, 800 mW, CW ring dye laser (Coherent 699-21) operating narrowband (1 MHz) or broadband (2 GHz) near the 589 nm D₂ resonance line in Na. Pump intensities ranged from 60-130 W/cm²; focused beam diameters of 0.2-1 mm 1/e² produced intensities of 10³-10⁴ I_{sat} which power broadened the Na linewidths to 30-100x of their collision-free width of 62.5 MHz. An on-line Lamb Dip diagnostic monitored laser frequency relative to the resonance line with 50 MHz accuracy. Vapor densities in the 10¹²-10¹³/cm³ range were tested in quartz and pyrex cells with path-lengths varying from 1 mm to 10 cm. Highest reflectivity was obtained with no buffer gas; He buffer pressures up to 50 torr were used.

Existing FWM models for homogeneously broadened systems were adapted to the high-intensity, high reflectivity regime. 1-D analytical and numerical models were implemented to survey FWM situations involving nonresonant and resonant nonlinearities, and a 2-D numerical model was prepared to address wave optic considerations such as conjugation fidelity. A physical picture was developed to interpret experimental results and provide the basis for future development of a quantitative model for strongly pumped, inhomogeneously broadened media. Intensity crosstalk due to a combination of nonlinearity saturation and pump depletion can be predicted quantitatively for arbitrary noise/probe beam intensity ratios.

1.0 EXECUTIVE SUMMARY

Four wave mixing (FWM) performance in Na vapor was evaluated in the strong pumping regime ($I \gg I_{\text{sat}}$) required for typical applications related to point-to-point optical links. Gain (= reflectivity), imaging fidelity, and noise crosstalk were measured and analyzed under several conditions to obtain an engineering data base for potential tactical applications such as communications, surveillance, and guidance systems.

Results include $\geq 230\%$ reflectivity and 15 line pair/mm imaging resolution, both the highest reported to date with cw pumping in low density Na vapor. The observed resolution was limited by the pixel spacing of our video camera. Ten lp/mm resolution was obtained after passing the input image through a 65λ aberrator. Noise crosstalk was observable only when the combined signal/noise powers were large enough to saturate the phase conjugate return signal via pump depletion. Under these conditions, a degenerate, coherent noise beam 3x stronger than the signal beam produced only a 21% reduction in the intensity of the phase conjugate signal, and this degree of crosstalk decreased rapidly as the pump/noise angle increased.

The experiments were performed with pump and probe beams that were derived from a single, 800 mW, CW ring dye laser (Coherent 699-21) operating narrowband (~ 1 MHz) or broadband (2GHz) near the 589 nm D_2 resonance line in Na. Pump intensities ranged from 60-130 W/cm^2 ; focused beam diameters of 0.2-1 mm $1/e^2$ produced intensities of 10^3 - $10^4 I_{\text{sat}}$ which power broadened the Na linewidths to 30-100x of their collision-free width of 62.5 MHz. An on-line Lamb Dip diagnostic monitored laser frequency relative to the resonance line with 50 MHz accuracy. Vapor densities in the 10^{12} - $10^{13}/\text{cm}^3$ range were tested in quartz and pyrex cells with path-lengths varying from 1 mm to 10 cm. Highest reflectivity was obtained with no buffer gas; He buffer pressures up to 50 torr were used.

The reflectivity of DFWM in Na vapor was measured versus frequency offset from resonance, pump intensity, pump/probe angle, and pump bandwidth. With a 300 mW, 1 MHz pump two reflectivity peaks were observed on the Na D_2 line, one on the low frequency side of the 2-3 hyperfine transition and one on the high frequency side of 1-0 transition. Their

FWHMs were ~ 2.2 GHz and 1.4 GHz respectively; the 2-3 reflectivity peak was about 20% of the 1-0 maximum. Little or no reflectivity was observed on the other four hyperfine transitions of the D_2 line because optical pumping depletes the ground state populations of these lines. The strong linear absorption of the medium ($\alpha_0 L \approx 200$) eliminated a conjugate return in a 2.5 GHz frequency range that overlaps the line centers of the 2-3 and 1-0 lines which are separated by 1.7 GHz. An increase of pump power from 300 to 450 mW increased the 2-3 and 1-0 reflectivity maxima by 20% and 12% respectively, the corresponding bandwidths went up by 18% and 50% respectively, and the gap between the two peaks narrowed to 1.2 GHz. The latter result is due to increased saturation of the linear absorption in that region. A maximum reflectivity of 230% was obtained on the 1-0 hyperfine transition with the peak occurring 0.9 GHz on the high frequency side of the transition line center.

Self action effects were observed as increases in the divergences of both the transmitted pump beams and the phase conjugate return. Self focusing, which occurs on the high frequency side of a transition, increases the effective pump intensity on the 1-0 line and is the reason the reflectivity there is higher than on the 2-3 line. The low frequency side of the 2-3 line is subject to self defocusing, which reduces the effective pump intensity there. As expected, the 2-3 line, which has a larger oscillator strength and degeneracy factor, exhibits the higher reflectivity at lower pump intensities where self action effects are negligible.

The reflectivity FWHM versus pump/probe angle was measured to be ~ 2.2 mrad with $1/\sin^2 \theta$ dependence for angles greater than 13 mrad. This dependence, which is predicted for a homogeneously broadened system, is also shown to be expected for angles $\leq \Delta\omega_{pb}/\Delta\omega_D$, the ratio of the power-broadened homogeneous width to the inhomogeneous width (≈ 0.2 at our test conditions). With 2 GHz bandwidth pumps, reflectivities as high as 20% were measured and the FWHM vs pump/probe angle doubled to ~ 4.5 mrad. Simultaneous degenerate and nondegenerate FWM interactions are believed to contribute to the broadband response.

An active tracking demonstration showed automatic tracking over a 50 mrad field of view at angular scan rates in excess of 100 rad/s. Residual tracking error was less than our detection limit of 1 μ rad.

Noise mechanisms intrinsic to the FWM process were studied by introducing a second probe (noise) beam into the phase conjugation region. Intensity crosstalk, which occurs when the presence of a noise beam changes the phase conjugate reflectivity of the signal beam, was observed and characterized. Saturation of the nonlinearity and/or pump depletion produce intensity crosstalk when high probe intensities are used ($I_{\text{probe}} \geq 0.1 I_{\text{pump}}$). A maximum 21% reduction in the phase conjugate signal was observed at a noise/signal intensity ratio of 3:1 and noise/signal angular separation of 13 mrad. Variation of signal, noise, and pump polarizations had no effect on the degree of crosstalk. Reflected phase conjugate power saturates as the probe/pump intensity ratio is increased from 0.02 to 0.3; this saturation curve can be used to predict intensity crosstalk levels. Our analysis indicates there is no mechanism for phase crosstalk between a signal and noise beam, and none was observed.

Spatial crosstalk is defined as the transfer of transverse intensity patterns from a noise beam to the phase conjugate signal wave. This was studied by imprinting a 2.8 line pair/mm, three bar image from an Air Force resolution target onto a 6 mW noise beam, and looking for that image pattern in the phase conjugate return of a 1 mW signal; none was observed. Intensity crosstalk reduced the contrast in the phase conjugate signal image, a three bar image orthogonal to that in the noise beam, by 46%, but there was no reduction in the sharpness of the edges and there was no evidence of an orthogonal pattern overlaid onto the original signal. The noise and signal inputs were focused into the Na cell so the intensity patterns in the conjugation region were the Fourier transforms of the orthogonal bar images. Only the central lobes of the signal and noise inputs, which contain the low spatial frequency components of the original images, were coincident. Thus the crosstalk led to contrast reduction with no loss of edge definition. Our image fidelity for these experiments was limited by the pixel resolution of our video camera to about 15 lp/mm; pump beam $1/e^2$ diameters were about 1100 μm . These measurements were made at pump intensities where self action effects were negligible and phase conjugate reflectivities were 10-25%.

The operating region of interest for field applications involves strong pumping to obtain high reflectivity of weak signals. In general the theory in this regime is not amenable to available analytical or

numerical treatments. Therefore an analytical framework for understanding FWM in a strongly pumped, Doppler-broadened, saturable absorber was established. This was supplemented with development of simple models for homogeneously broadened, nonresonant and resonant systems that can later be upgraded to incorporate inhomogeneous broadening and wave optics considerations. For high reflectivity cases where there is strong linear absorption and strong optical saturation we show that the laser frequency for maximum nonlinearity is shifted off resonance by an amount dependent on optical intensity and on the ratio of signal and pump beam intensities.

The frequency offset for maximum FWM reflectivity in a strongly pumped saturable absorber is explained as follows. The intensity contrast in the alternating spatial regions where the input pump and signal waves interfere produces spatial variations in the nonlinear susceptibility χ of the medium. Fringe contrast is high when beams of equal intensity interfere, but the dark regions remain strongly illuminated when beams of unequal intensity interfere. In a strongly saturated system with equal intensity beams, high fringe contrast produces large spatial variations in χ that are maximized near resonance. When weak signal beams are combined with a strong pump intensity that is $> I_{\text{sat}}$, fringe contrast is low and both the light and dark regions remain strongly saturated near resonance with a result that χ variations are also small. Then maximum nonlinearity is obtained by moving off resonance to a frequency where the effective $I/I_{\text{sat}} \approx 1$, because this is the regime where χ is most sensitive to small changes in illumination intensity.

Doppler broadened media can be understood by estimating the effects of experimental parameters on the population of the velocity group in which the interference grating is written. Key parameters are frequency offset, relative pump and signal angles, and optical intensities. A procedure for identifying the velocity group that is simultaneously resonant with the input optical waves has been outlined.

The optical field interacts resonantly only with absorbers that have velocity components that shift their (stationary) resonance frequency to that of the optical field. In the standard, degenerate FWM geometry with weak, counterpropagating pumps; maximum reflectivity occurs on resonance and only the $v=0$ velocity group can contribute to the nonlinearity. When strong pumping is used, the fringe contrast considerations mentioned above move the maximum nonlinearity to a nonresonant frequency. Now the various

input waves, which typically enter at different angles, optimally interact with velocity groups moving in different directions. One result is that maximum reflectivity can occur with nondegenerate rather than degenerate FWM in this case if the frequency of one of the counterpropagating pumps is shifted by an amount equal to $-\Delta\omega$ when the frequencies of the other pump and the signal are $+\Delta\omega$ from resonance.

In general, FWM performance tends to optimize when frequency offsets and angles are set so that the velocity group involved is near the thermal velocity. The situation becomes very complex, however, when the details of Na hyperfine spectroscopy, hyperfine optical pumping, power broadening, and fringe contrast considerations are included.

The Na hyperfine transitions are closely spaced relative to the Doppler line width, so each transition can be interacting resonantly through separate velocity groups. Under low intensity illumination the hyperfine separations are greater than the homogeneous linewidths, but in our strong pumping regime the homogeneous widths become greater than the hyperfine spacings. The increased homogeneous bandwidth increases the rate at which thermal washout of the interference grating occurs, because it permits interaction with more velocity groups that are moving perpendicular to the grating lines. In the pure Doppler limit only velocities parallel to the interference grating lines are permitted. Finally thermal diffusion counteracts the optical pumping that occurs in 4 out of 6 of the Na D₂ hyperfine transitions. The preceding phenomena have variable, opposing impacts on the net nonlinearity observed. Our physical picture, which provides an outline for qualitatively understanding these effects, can serve as the basis for further development of a comprehensive model.

The contract SOW called for experimental measurements that address technical issues relating to phase conjugated optical links. No analysis beyond that required to empirically relate results to possible application scenarios was specified. The required reflectivity, crosstalk, and fidelity experiments that were performed are presented in this report. During the program it was determined that analysis of FWM physics beyond that required by the contract was desirable. In particular, noise crosstalk mechanisms were investigated on TRW IR&D, and this theoretical description is included in Section 5 because it substantiates our conclusion that crosstalk will not seriously impact FWM applications.

TRW Inc.
One Space Park, 01/1270
Redondo Beach, CA 90278



Nonlinear Optical Technology, Phase I, Area 2 (NLOT I/Area 2)

Final Report 10 June 1985 to 31 March 1987

1 July 1987

S.G. Meisenholder, et al.

Prepared for:
Defense Advanced Research Product Agency
1400 Wilson Blvd.
Arlington, VA 22209
and
Office of Naval Research
800 N. Quincy St.
Arlington, VA 22217

Unclassified

SECURITY CLASSIFICATION OF THIS PAGE

REPORT DOCUMENTATION PAGE

1a REPORT SECURITY CLASSIFICATION Unclassified			1b RESTRICTIVE MARKINGS Per clause H-9		
2a SECURITY CLASSIFICATION AUTHORITY OPNAVINST 5513.8 (7)			3 DISTRIBUTION AVAILABILITY OF REPORT Unlimited		
2b DECLASSIFICATION/DOWNGRADING SCHEDULE OADR					
4 PERFORMING ORGANIZATION REPORT NUMBER(S) AP-1306			5 MONITORING ORGANIZATION REPORT NUMBER(S)		
6a NAME OF PERFORMING ORGANIZATION Applied Technology Division Space & Technology Group, TRW			6b OFFICE SYMBOL <i>(if applicable)</i>		7a NAME OF MONITORING ORGANIZATION Office of Naval Research
6c ADDRESS (City, State and ZIP code) One Space Park Redondo Beach, CA 90278			7b ADDRESS (City, State and ZIP code) 759 E. Walnut Pasadena, CA.		
9a NAME OF FUNDING SPONSORING ORGANIZATION DARPA			8b OFFICE SYMBOL <i>(if applicable)</i>		9 PROCUREMENT INSTRUMENT IDENTIFICATION NUMBER
8c ADDRESS (City, State and ZIP code) 1400 Wilson Blvd. Arlington, VA 22209			10 SOURCE OF FUNDING NOS		
11 TITLE (Include Security Classification) Nonlinear Optics Technology, Phase I, Area 2 (NLOT I/Area 2)			PROGRAM ELEMENT NO	PROJECT NO	TASK NO
12 PERSONAL AUTHOR(S) TRW: S.G. Meisenholder, J.W. Doyle, R.C. Hilyard, C.G. Koop, D.A. Sower; OCLI: S.P. Fisher			WORK UNIT NO		
13a TYPE OF REPORT Final		13b TIME COVERED FROM 06-10-85 TO 06-30-87		14 DATE OF REPORT (Yr, Mo, Day) 87,07,01	
15 PAGE COUNT 51		16 SUPPLEMENTARY NOTATION			
17 COSATI CODES			18 SUBJECT TERMS (Continue on reverse if necessary and identify by block number)		
FIELD	GROUP	SUB GR	HF/DF pulsed chemical laser experimental facility, high energy laser, nonlinear optics, stimulated Brillouin scattering, phase conjugation.		
19 ABSTRACT (Continue on reverse if necessary and identify by block number) <p>The final report for Area 2 of the Nonlinear Optics Technology, Phase I (NLOT I/Area 2) project presents the detailed design for an experimental facility for use in future phase conjugation experiments that will be conducted under a separate project. The objective of the NLOT I/Area 2 program was to design a facility that (1) is compatible with the use of an existing 50-liter DF repetitively pulsed chemical laser (RPCL-50) device and (2) would allow design flexibility/growth potential for other more complex experiments.</p> <p>The detailed design of the experimental facility experiment is described. Phase conjugation is developed by the nonlinear optical process wherein the high energy chemical laser beam is focused within a stimulated Brillouin scattering (SBS) cell, which is filled with xenon at 40 atm. The experimental facility is described relative to the design of the high-energy optical train required to transmit the beam from the RPCL-50 device to the SBS cell. Design issues such as oscillator isolation are described. The design of the beam diagnostics subsystem is also defined. Finally, the report describes certain risk reduction measurements and hardware design/procurement.</p>					
20 DISTRIBUTION AVAILABILITY OF ABSTRACT UNCLASSIFIED/UNLIMITED <input checked="" type="checkbox"/> SAME AS RPT <input type="checkbox"/> DTIC USERS <input type="checkbox"/>			21 ABSTRACT SECURITY CLASSIFICATION Unclassified		
22a NAME OF RESPONSIBLE INDIVIDUAL R. E. Behringer			22b TELEPHONE NUMBER (Include Area Code) (818) 795-5971		22c OFFICE SYMBOL

1. INTRODUCTION AND SUMMARY

1.1 INTRODUCTION

Area Two of the Nonlinear Optics Technology, Phase I (NLOT I/Area 2) project deals with the design of a nonlinear optics experiment to demonstrate a phase conjugation approach which could be applied to a high-energy chemical laser weapon system. Tactical defense systems, using high energy lasers (HELs), will require high-performance, highly reliable system designs. To ensure operational success, the HEL systems must also meet these objectives with adequate performance margin. Use of a nonlinear optics approach for beam control, rather than a complex conventional adaptive optics approach, offers the promise of a much simpler and more reliable laser system.

The key advantage of utilizing a nonlinear optics approach to phase conjugation laser system design for a tactical defense system is a substantial improvement in design and performance margins. Using the stimulated Brillouin scattering (SBS) process, in conjunction with a bidirectional master oscillator, power amplifier (MOPA) configuration, system design requirements can become considerably more flexible while yielding substantial improvements in system beam quality, alignment, and jitter performance. Preliminary assessment of the impact of going to a longer wavelength suggests that repetitively pulsed DF lasers are particularly well suited to the needs of this technology, making the use of SBS phase conjugation a very practical design choice for such lasers.

The objective of NLOT I/Area 2 was to provide test planning, hardware design, and critical/long-lead hardware fabrication needed to support a future deuterium fluoride (DF*) chemical laser phase conjugation demonstration experiment. The initial demonstration, using a hydrogen fluoride (HF*) pulsed chemical laser, will be conducted on a project sponsored by the Strategic Defense Initiative Organization (SDIO). Therefore, the design of the experimental facility must be flexible since it must operate at either DF* or HF* wavelengths.

The NLOT I/Area 2 work discussed in this report was done in close concert with similar work on the Chemical Laser Phase Conjugation Technology (CLPCT) program, sponsored by the Naval Research Laboratory (NRL). The difference between the two projects was that NLOT I/Area 2 concentrated on the design

of an SBS experiment using a xenon gas cell at DF* wavelengths and CLPCT concentrated on the design of an SBS experiment using a xenon gas cell at HF* wavelengths.

1.2 SUMMARY

This final report describes the design of an experimental facility that could be used to obtain parametric data on nonlinear optics phase conjugation, using the SBS process with a pulsed DF* chemical laser. The existing 50-liter repetitively pulsed chemical laser (RPCL-50), although in a single-pulse mode, will be used as the high energy source. The NLOT I/Area 2 study resulted in the design of an optical train to transmit the RPCL-50 beam to the SBS cell. The preferred SBS medium is gaseous xenon at 40 atm. Design requirements, analysis, and layouts were developed for the high-energy optical train subsystem. The primary design issue was oscillator isolation, i.e., the prevention of excessive power fed back to the RPCL resonator. The design utilizes an optical delay line which ensures that the RPCL cavity gain has decayed by the time the return energy from the SBS cell enters the resonator. This oscillator isolation approach is augmented by the use of a quarter wave plate which rotates the polarization vector of the return beam by 90 degrees relative to the incident beam.

The beam diagnostics subsystem provides for measurements of the characteristics of the incident beam, reflected beam, and transmitted beam relative to the SBS cell. Both near- and far-field characteristics are of interest. In particular, the following measurements will be made for the incident and reflected beam:

- Beam quality, both time averaged and time resolved
- Energy, time averaged
- Temporally resolved power
- Power spectrum, time resolved
- Near-field irradiance, time averaged
- Near-field phase, time averaged
- Polarization, time resolved
- Bandwidth, time averaged (incident only)

Experimental measurements were made as part of the NLOT I/Area 2 investigation for the purpose of characterizing the RPCL-50 device. The test series included the following measurements:

- Beam jitter
- Polarization
- ASE
- Multiline spectrum

The Optical Coating Laboratory, Inc. (OCLI) was involved in the design of thin film optical coatings which could be used for the transmissive optics in the future phase conjugation experiment. OCLI also provided six calcium fluoride windows, which were long-lead hardware required for the future experiment.

APPENDIX B: THEORY OF PHASE CONJUGATED DOUBLING

This appendix presents a working draft of a theoretical paper on phase conjugation correction of aberrations in harmonic doubling. This paper is currently being prepared for publication. It discusses in detail the physical basis for the successful experimental demonstration of phase conjugated doubling presented in Section 6 of this report.

Theory of Phase Conjugation in Frequency Doubling

Lee M. Frantz

TRW Electronics & Defense Sector

It is shown that, in frequency doubling, the phase aberrations due to the crystal's surface unevenness can be removed by phase conjugation, leaving a residue that is insignificant in most practical cases.

1. Introduction

Ordinarily, frequency doubling leads to beam quality degradation. For conversion efficiency, it is desirable to reduce temperature variation in the crystal; this can be done by segmenting it longitudinally and flowing a cooling medium between segments. Residual unevenness of the many crystal surfaces, however, then becomes a source of poorer beam quality. We shall show theoretically that, if the beam is phase conjugated and passed back through the crystal, the surface-induced phase aberrations are removed even while the doubling process proceeds, provided certain conditions are satisfied. Experimentally, the removal of the aberrations in this way has already been demonstrated.⁽¹⁾

To see why this effect occurs, we first note that, if there is an amplifier between the crystal and the phase conjugate mirror (PCM), then the aberrations induced by it on the fundamental wave are nullified before any conversion takes place. Furthermore, the surface-induced aberrations are progressively removed from the fundamental as it returns in conjugated form through those surfaces that originally caused them, so they are not transmitted to any part of the harmonic that is generated after their removal.

But what of those aberrations that are still in the fundamental wave when an element of harmonic wave is generated? And what is the effect of the remaining surfaces on this element? We shall show that the aberrations transmitted from the fundamental are nearly cancelled on the harmonic by the unevenness of the remaining surfaces, in much the same way that they are cancelled from the conjugate of the fundamental, itself. Thus, we shall conclude that if the fundamental is incident on the frequency doubling crystal as a nearly plane wave, the harmonic will emerge as a nearly plane wave.

2. Theoretical Basis

To understand the physics underlying this assertion, consider the first crystal segment encountered by the fundamental wave. In Figure 1,

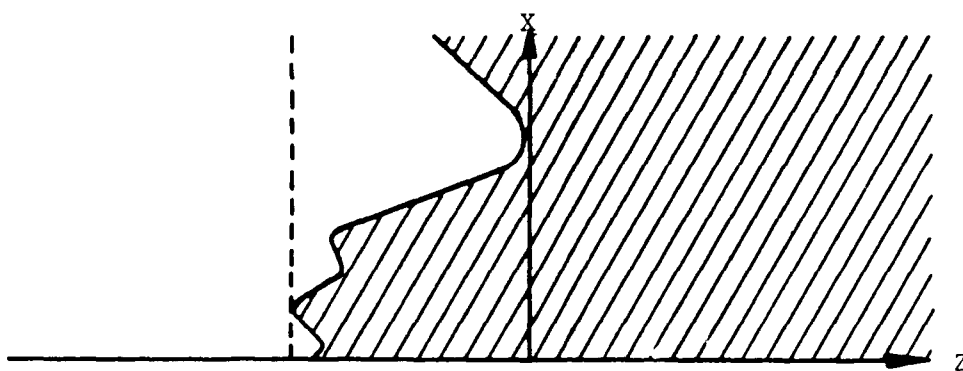


Figure B-1. Uneven surface of a crystal segment. The y-axis is normal to the plane of the figure.

the dashed region represents the segment and the curved line is its left surface. The propagation direction is along the z-axis, and the origin is set so that the x and y axes just touch that element of surface that extends the farthest to the right. At any location $\vec{\rho}$ in the x-y plane magnitude of the surface's distance from $z = 0$ is denoted by $u(\vec{\rho})$, and the maximum distance is $u_m = \max[u(\vec{\rho})]$. We assume, for the moment, that the incident fundamental is a plane wave,

$$E_F(\vec{\rho}, -u_m) = E_0 = \text{const.}$$

In practice, the peak-to-valley unevenness u_m can be held down to the order of 600 angstroms⁽²⁾; this is small enough that the effect of the passage of the wave to $z = 0$ can be described by a phase increment calculated from geometric optics. Ignoring reflection, which is irrelevant to this argument, we have

$$E_F(\vec{\rho}, 0) = E_0 \exp[i\phi_F(\vec{\rho})], \quad (1)$$

where

$$\phi_F(\vec{\rho}) = k_0[u_m - u(\vec{\rho})] + nk_0 u(\vec{\rho}), \quad (2)$$

and where k_0 is the free-space wave number of the fundamental (for this argument we also ignore the presence of the coolant) and n is its refractive index in the crystal. The returning fundamental, having reflected from the PCM, is proportional to the conjugate of (1); if the proportionality factor is ignored, it is

$$E_F^*(\vec{\rho}, 0) = E_0 \exp(-i\phi_F). \quad (3)$$

The theory of harmonic generation shows that the spatial growth rate of the harmonic wave is proportional to the square of the amplitude of the generating wave⁽³⁾, which in this case is the complex conjugate of the fundamental,

$$\frac{dE_H}{dz}(\vec{\rho}, 0) = A[E_F^*(\vec{\rho}, 0)]^2, \quad (4)$$

where A is a constant. From (4), we see that the differential element of harmonic wave created in the differential element of length dZ at $Z = 0$ is

$$dE_H(\vec{\rho}, 0) = A[E_F^*(\vec{\rho}, 0)]^2 dZ, \quad (5)$$

or, using (3),

$$dE_H(\vec{\rho}, 0) = AE_0^2 \exp[-i2\phi_F(\vec{\rho})] dZ.$$

On leaving the crystal through the surface, the harmonic wave element acquires an additional phase factor, just as the fundamental did on entering it,

$$\begin{aligned} dE_H(\vec{\rho}, -u_m) &= dE_H(\vec{\rho}, 0) \exp[i\phi_H(\vec{\rho})] dZ \\ &= AE_0^2 \exp[i(\phi_H(\vec{\rho}) - 2\phi_F(\vec{\rho}))] dZ. \end{aligned} \quad (6)$$

The phase distribution $\phi_H(\vec{\rho})$ is of exactly the same form as that given for $\phi_F(\vec{\rho})$ by (2), except that k_0 is replaced by the free-space wave number of the harmonic wave, and n is replaced by the refractive index of the harmonic. We assume now that the fundamental is incident at precisely the phase matching angle, so that the two refractive indices are identical. We also note that the harmonic's wave number is $2k_0$, so that

$$\phi_H(\vec{\rho}) = 2\phi_F(\vec{\rho}).$$

Inserting this into (6), we find

$$dE_H(\vec{\rho}, -u_m) = AE_0^2 dZ,$$

that is, the emerging harmonic element is a plane wave. The aberrations passed on to it by the fundamental have been removed at the surface in the same way that the conjugate of the fundamental has its aberrations removed.

If the element of harmonic wave were generated on the first pass of the fundamental through the crystal, instead of on the return pass, it would have the form,

$$dE_H(\vec{\rho}, 0) = A[E_F(\vec{\rho}, 0)]^2 dZ.$$

After propagating through the rest of the crystal, picking up phase aberrations, being phase conjugated, then returning through the rest of the crystal, picking up phase aberrations, being phase conjugated, then returning through the crystal and thereby having all these phase aberrations removed, it would arrive at $Z = 0$ in precisely the form shown in (5). The argument would then follow as before.

It should be noted that the same type of argument holds for harmonic conversion of any order.

2. General Case

The above argument applies to an element of harmonic wave generated at the first surface of the first crystal segment. Now we consider the more general case of generation anywhere in any segment; we shall show that for frequency doubling the same conclusion can be drawn, provided, however, that certain conditions are satisfied. The generalization for higher order harmonic conversion will not be considered here.

Let the phase conjugated fundamental wave, on its return pass, be denoted by E_{FC} . It has the form,

$$E_{FC}(\vec{\rho}, Z) = f(\vec{\rho}, Z) E_F^*(\vec{\rho}, Z), \quad (7)$$

where $f(\vec{\rho}, Z)$ describes the effect on E_F^* of gain in the amplifier and loss in the crystal. The factor f may depend on $\vec{\rho}$ because of a non-uniform transverse gain distribution, or because of gain saturation. The latter effect is likely to be the bigger, since the fundamental beam intensity must fall off strongly from its central value to avoid edge diffraction. But f is real, because it describes only an intensity effect. We shall assume that the scale size of the $\vec{\rho}$ variations in f is sufficiently large, and the propagation distance sufficiently small, that f is not altered by diffraction; that is, we shall ignore any changes in f with propagation.

If E_{FC} is known at $Z = Z_g$ inside one of the crystal segments, then at the segment surface, $Z = Z_N < Z_g$, it can be obtained from Fresnel propagation theory as⁽⁴⁾

$$E_{FC}(\vec{\rho}, Z_N) = \frac{k}{2\pi i \delta_N} \int E_{FC}(\vec{\rho}, Z_g) \exp\left[i \frac{k}{2\delta_N} (\vec{\rho}_1 - \vec{\rho})^2\right] d\vec{\rho}_1, \quad (8)$$

where $\alpha_N = Z_g - Z_N$, and k is the wave number. This relationship can be mathematically inverted to give

$$E_{FC}(\vec{\rho}, Z_g) = \frac{-k}{2\pi i \delta_N} \int E_{FC}(\vec{\rho}, Z_N) \exp\left[-i \frac{k}{2\delta_N} (\vec{\rho}_1 - \vec{\rho})^2\right] d\vec{\rho}_1. \quad (9)$$

If at some Z this wave generates an element of harmonic wave, it will be given, (as in (5)), by

$$dE_H(\vec{\rho}, Z) = A[E_{FC}(\vec{\rho}, Z)]^2 dZ.$$

For notational simplicity, we drop the differential symbols, absorb the dZ into A , and rewrite this equation as

$$E_H(\vec{\rho}, Z) = A[E_{FC}(\vec{\rho}, Z)]^2. \quad (10)$$

If this harmonic element is generated at $Z = Z_g$, then at the segment surface it is given, in analogy to (8), by

$$E_H(\vec{\rho}, Z_N) = \frac{k}{\pi i \sigma_N} \int E_H(\vec{\rho}_1, Z_g) \exp\left[i \frac{k}{\sigma_N} (\vec{\rho}_1 - \vec{\rho})^2\right] d\vec{\rho}_1.$$

Now, into the integral we insert the expression (10) for $E_H(\vec{\rho}, Z_g)$. Then we substitute (9) for $E_{FC}(\vec{\rho}, Z_g)$, reverse the orders of integration, identify a formal integral expression for the Dirac delta function, and integrate over it. The result, after a simple transformation of integration variables, is

$$E_H(\vec{\rho}, Z_N) = -\frac{A}{i\pi} \int E_{FC}\left[\vec{\rho} + \left(\frac{\lambda\sigma_N}{2\pi}\right)^{1/2} \vec{\xi}, Z_N\right] \\ \times E_{FC}\left[\vec{\rho} - \left(\frac{\lambda\sigma_N}{2\pi}\right)^{1/2} \vec{\xi}, Z_N\right] e^{-i\xi^2} d\vec{\xi},$$

where λ is the wavelength. Next we introduce (7). Because we are ignoring changes in f with propagation we make the approximation,

$$f\left[\vec{\rho} \pm \left(\frac{\lambda\sigma_N}{2\pi}\right)^{1/2} \vec{\xi}, Z_N\right] \approx f(\vec{\rho}, Z_g),$$

take f out of the integral, and absorb it into the factor A . For notational simplicity, we ignore the new ρ dependence of A , since it will always be assumed unaltered by propagation: we also ignore loss in the crystal and, therefore, drop the new Z_N dependence of A . The result is

$$E_H(\vec{\rho}, Z_N) = -\frac{A}{i\pi} \int E_F^*\left[\vec{\rho} + \left(\frac{\lambda\sigma_N}{2\pi}\right)^{1/2} \vec{\xi}, Z_N\right] \bullet E_F^*\left[\vec{\rho} - \left(\frac{\lambda\sigma_N}{2\pi}\right)^{1/2} \vec{\xi}, Z_N\right] e^{-i\xi^2} d\vec{\xi}.$$

We then expand E_F^* in a power series in ξ_x and ξ_y , keeping only terms up to second order. The integrals can now be done exactly, giving

$$E_H(\vec{\rho}, Z_N) = \Delta [E_F^*(\vec{\rho}, Z_N)]^2 (1 + \epsilon_N), \quad (11)$$

where

$$\epsilon_N = \left\{ \left[\frac{1}{E_F^*(\vec{\rho}, Z_N)} \nabla_{\perp} E_F^*(\vec{\rho}, Z_N) \right]^2 - \frac{1}{E_F^*(\vec{\rho}, Z_N)} \nabla_{\parallel}^2 E_F^*(\vec{\rho}, Z_N) \right\} \frac{i\lambda\sigma_N}{4\pi} \quad (12)$$

where Δ_{\perp} is the transverse component of the gradient.

Now, exactly as at the first surface, the fundamental wave had previously acquired a phase factor due to the surface figure,

$$E_F(\vec{\rho}, Z_N) = E_F(\vec{\rho}, Z_N - U_{mN}) \exp[i\phi_{FN}(\vec{\rho})] \quad (13)$$

where $\phi_{FN}(\rho)$ is understood to be of the same form as given in (2) for ⁽⁴⁾ $\phi_F(\rho)$. U_{mN} is defined as $U_{mN} = \max [U_N(\rho)]$, and $U_N(\rho)$ is generally different for each of the surfaces. Similarly, the harmonic wave gains a phase factor in passing out of the crystal segment.

$$E_H(\vec{\rho}, Z_N) - U_{mN} = E_H(\vec{\rho}, Z_N) \exp[i\psi_{HN}(\vec{\rho})], \quad (14)$$

where, as at the first surface,

$$\psi_{HN}(\vec{\rho}) = 2 \psi_{FN}(\vec{\rho}). \quad (15)$$

Using (13), (14), and (15) in (11) we obtain

$$E_H(\vec{\rho}, Z_N - U_{mN}) = A[E_F^*(\vec{\rho}, Z_N - U_{mN})]^2 (1 + \epsilon_N)$$

Comparing this with (10), and recalling that (10) describes the harmonic element at the point of creation, we see that, to within the error term ϵ_N , the harmonic element has exactly the form it would have if it had been generated at $Z_N - U_{mN}$. Repeating this process to take the harmonic through the intersegment gap and then just through the next surface at $Z = Z_{N-1}$ yields

$$E_H(\rho, Z_{N-1} - U_{m, N-1}) = A[E_F^*(\rho, Z_{N-1} - U_{m, N-1})]^2 (1 + \epsilon_N)(1 + \epsilon_{N-1})$$

In doing this, we have ignored the effect of propagation on ϵ_N , since we shall only be looking for an estimate of the error. Now repeating the process through all of the remaining segments, we finally obtain

$$E_H(\vec{\rho}, Z_1 - U_{m1}) = A[E_O^*(\vec{\rho})]^2 \prod_{j=1}^N (1 + \epsilon_j), \quad (16)$$

where $E_O(\rho)$ is the fundamental wave incident on the first segment, and Z_1 is the location of the first surface. Eq. (12) holds for ϵ_j , except that for $j \neq N$ we have $\alpha_j = Z_{j+1} - Z_j$.

Next, we need to examine and estimate the ϵ_j . In (12), we approximate E_F^* by

$$E_F^*(\vec{\rho}, Z_N) = E_O^*(\vec{\rho}) \exp[-i\psi_N(\vec{\rho})], \quad (17)$$

where

$$\psi_N(\vec{\rho}) = \sum_{j=1}^N \phi_{Fj}(\vec{\rho}) \quad (18)$$

is the sum of the phase disturbances imposed at each of the aberrating surfaces seen by the fundamental on its initial trip to the Nth segment, and each ϕ_{Fj} has the form,

$$\phi_{Fj}(\vec{r}) = k_o [U_{mj} - U_j(\vec{r})] + nk_o U_j(\vec{r}), \quad (19)$$

as in (2). Intuitively, this appears to be a fairly accurate approximation for this system. The number of segments will probably be no more than ten, with probably no more than 10 cm between segments and a 1 cm segment thickness, for a total distance of the order of 100 cm. The wavelength λ is about a micron and the transverse scale size of a surface undulation is of the same order as the aperture diameter D, which is of the order of centimeters⁽²⁾; therefore, the propagation distance for the imposed phase aberrations to be strongly affected by diffraction is above $D^2/\lambda = 10^4$ cm, which is 100 times the propagation distance. Furthermore, the surface gradients⁽²⁾, $du/d\rho \sim 10^{-5}$, are so small that there will be very little refraction.

If we write E_o in terms of its magnitude and phase,

$$E_o = A_o \exp(i\phi_o),$$

and insert this, along with (17), into the expression (12) for ϵ_N , we find

$$\epsilon_N = \left[\left(\frac{1}{A_o} \nabla_{\perp}^2 A_o \right)^2 - \frac{1}{A_o} \nabla_{\perp}^2 A_o + i \nabla_{\perp}^2 \phi_o + i \nabla_{\perp}^2 \phi_N \right] \frac{i \lambda c_N}{4\pi}. \quad (20)$$

We would like to estimate $\nabla_{\perp}^2 \psi_N$ by taking the average over a statistical ensemble of surfaces, but because the average, $\langle \nabla_{\perp}^2 u_j \rangle$, vanishes, so also does the average, $\langle \nabla_{\perp}^2 \psi_N \rangle$. Therefore, we use the square root σ_N of the variance as a measure. Combining (18) and (19), and treating the U_j as independent but identically distributed stochastic variables, we get

$$\sigma_N^2 = \langle (\nabla_{\perp}^2 \psi_N)^2 \rangle = N k_o^2 (n-1)^2 \langle (\nabla_{\perp}^2 U)^2 \rangle, \quad (21)$$

where U is any of the U_j . To estimate this, we think of the slow surface undulations as part of a product of sine waves, $U(\rho) = \omega (\sin 2\pi x/D) (\sin 2\pi y/D)$, where D is the aperture diameter, and find for the maximum value of the transverse Laplacian,

$$|\nabla_{\perp}^2 U|_{\max} = 2\omega(2\pi/D)^2.$$

Using this in (21) as an upper limit estimate then gives

$$\epsilon_N = \sqrt{N} k_0 (n-1) 8\pi^2 \omega / D^2. \quad (22)$$

Returning now to (16) and expanding the product of error terms,

$$\prod_{j=1}^N (1 + \epsilon_j) = 1 + \epsilon_{\text{tot}} + \dots$$

where, with the aid of (20) and (22), we have

$$\begin{aligned} \epsilon_{\text{tot}} &= \sum_{j=1}^N \epsilon_j \\ &= \left[\left(\frac{1}{A_0} \nabla_{\perp}^2 A_0 \right)^2 - \frac{1}{A_0} \nabla_{\perp}^2 A_0 + i \nabla_{\perp}^2 \phi_0 \right] \frac{i\lambda}{4\pi} \sum_{j=1}^N \sigma_j \\ &\quad + \frac{4\pi^2 \omega (n-1)}{D^2 n} \sum_{j=1}^N \sqrt{d} \sigma_j. \end{aligned} \quad (23)$$

We have kept only the linear term in the product expansion, because we are interested only in cases in which the error is small compared to unity. We denote the crystal segment length by a and the intersegment gap length by b . To estimate the maximum error, we take $N + 1$ to be the total number of segment surfaces. We also take

$$\delta_N = Z_g - Z_N = a, \text{ so that}$$

$$\delta_j = Z_{j+1} - Z_j = \begin{cases} a, & j \text{ odd,} \\ b, & j \text{ even} \end{cases}$$

and

$$\sum_{j=1}^N \delta_j = Z_g - Z_1 = Ma + (M-1)b,$$

where M is the number of crystal segments ($N = 2M - 1$). Defining

$$R_M = \sum_{k=1}^M \sqrt{2k-1},$$

$$S_M = \sum_{k=1}^{M-1} \sqrt{2k},$$

we obtain from (23) the final error expression,

$$\begin{aligned} \varepsilon_{\text{tot}} = & \left[\left(\frac{1}{A_0} \gamma_1 A_0 \right)^2 - \frac{1}{A_0} \gamma_1^2 A_0 + i \gamma_1^2 \phi_0 \right] \frac{i\lambda}{4\pi} [Ma + (M-1)b] \\ & + \frac{4\pi^2 (n-1)}{D^2 n} (R_M a + S_M b). \end{aligned} \quad (24)$$

To illustrate conditions under which the error is small, we take the following possible design values: the crystal segment length is $a = 0.4$ cm, the intercrystal gap length is $b = 7.4$ cm, the number of segments is $M = 10$, the wavelength is $\lambda_0 = 1.06 \times 10^{-4}$ cm (Nd:Glass), the crystal diameter is $D = 1$ cm, the surface "undulation" amplitude is⁽²⁾ $\omega = 3 \times 10^{-6}$ cm, and the refractive index is $n = 1.49$ (KDP). For a beam with a Gaussian intensity distribution, $I = I_0 \exp(-\rho^2/\sigma^2)$, the amplitude is $A_0 = \sqrt{I_0 \exp(-\rho^2/2\sigma^2)}$; we then have

$$\left(\frac{1}{A_0} \gamma_1 A_0 \right)^2 - \frac{1}{A_0} \gamma_1^2 A_0 = \frac{2}{\sigma^2}.$$

Using the above design values, we find that for the term in (24) involving this quantity to be small compared to unity, the requirement is: $\sigma > .09$ cm. To avoid edge diffraction effects, we might impose the condition $\rho_{\max} > 3\sigma = .27$ cm, which would lead to the result, $I_{\min}/I_0 = 1.2 \times 10^{-4}$. Both of these conditions can then be satisfied with the chosen crystal diameter of $D = 1$ cm. for the term involving $\nabla_{\perp}^2 \phi_0$, we need $|\nabla_{\perp}^2 \phi_0| \ll 1.7 \times 10^3 \text{ cm}^{-2}$, a requirement easily satisfied by a nearly plane wave. Finally, putting numbers into the last term, we find $[4\pi^2 \omega(n-1)/D^2 n] (R_M a + S_M a) = 8.3 \times 10^{-3}$, so this is already small compared to unity for the design values.

3. Conclusions

Provided that certain reasonable requirements are imposed on the design values of a frequency doubling system, the phase aberrations caused by the surface figure of the crystal segments can be removed by phase conjugation.

References and Footnotes

1. see Section 6 of this report.
2. Laser Program annual Report -1976, Lawrence Livermore Laboratory, P. 2-261.
3. See for example, A. Yariv, "Quantum Electronics," 2nd Edition, (John Wiley & Sons, New York, 1975), P. 421.
4. The subscript N has been added to indicate that we are dealing with the Nth surface.
5. With the proper definition of U, Eq. (19) applies at right as well as left segment edges.

Acknowledgements

The author would like to thank W.W. Simmons for valuable discussions.

APPENDIX C: DERIVATION OF THE FRANTZ-NODVIK EQUATION
FOR A ZIG-ZAG SLAB AMPLIFIER.

We shall analyze the one-dimensional problem of two beams of monochromatic light propagating through a vertically infinite medium occupying the region $0 \leq x \leq L$. The two beams have the same frequency. One, with number density $n_1(x)$, has a direction making a positive angle θ with the axis as in Figure C-1; the other, with number density $n_2(x)$, has a direction making a negative angle θ with the x-axis. The transport equations for these two groups of photons are

$$\frac{\partial n_1}{\partial t} + c \cos \theta \frac{\partial n_1}{\partial x} = \sigma c n_1 N, \quad (C1)$$

$$\frac{\partial n_2}{\partial t} + c \cos \theta \frac{\partial n_2}{\partial x} = \sigma c n_2 N, \quad (C2)$$

where σ is the resonance absorption cross section, c is the velocity of light in the medium, and N is the population inversion density. Since Equations C1 and C2 have the same form and are linear in n_1 and n_2 , we define the total photon number density,

$$n = n_1 + n_2$$

and add Equations C1 and C2 to get the overall photon transport equation,

$$\frac{\partial n}{\partial t} + c \cos \theta \frac{\partial n}{\partial x} = \sigma c n N. \quad (C3)$$

The creation rate of photons, given by the source term, must be the same as the rate of increase of lower level atoms, which in turn is the same as the rate of decrease of upper level atoms. For a 4-level laser whose decay rate out of the lower level is so fast that it can be approximated as infinite relative to the other rates involved, the inversion density rate equation is then

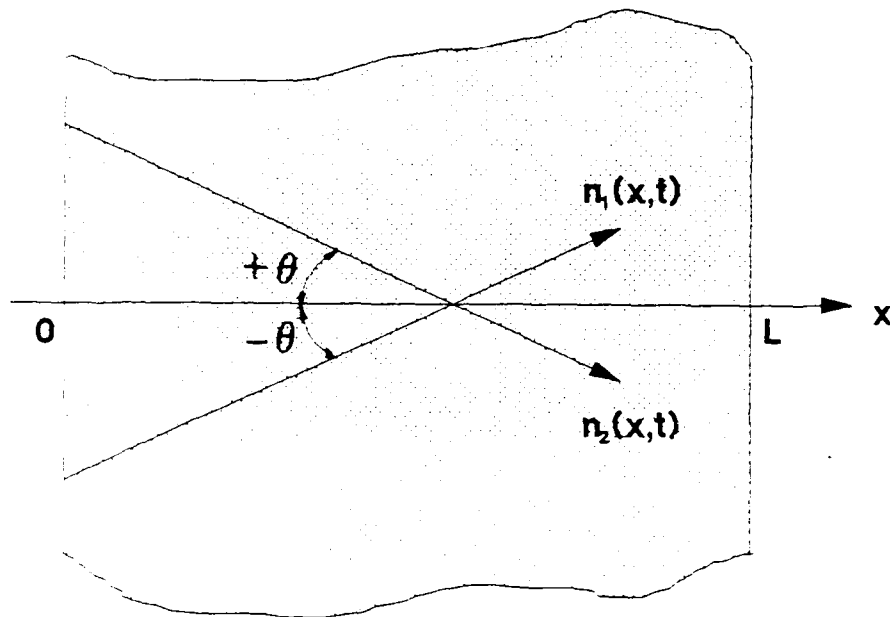


Figure C-1. Geometry of derivation of modified Frantz-Nodvik equation for beam propagation in a zig-zag slab medium. $n_1(x,t)$ and $n_2(x,t)$ are the photon number densities of two beams propagating at $\pm \theta$ relative to the x axis.

$$\frac{\partial n}{\partial t} = -\sigma c n N \quad (C4)$$

For a three-level laser, the rate equations for N_2 and N_1 , the upper and lower level population densities, are

$$\frac{\partial N_2}{\partial t} = -\sigma c n N$$

$$\frac{\partial N_1}{\partial t} = \sigma c n N$$

Since the inversion density is

$$N = N_2 - N_1,$$

we can subtract the lower equation from the upper one to get

$$\frac{\partial N}{\partial t} = -2\sigma c n N \quad (C5)$$

Equations C4 and C5 can be combined into the single equation,

$$\frac{\partial N}{\partial t} = -\alpha \sigma c n N \quad (C6)$$

where

$$\alpha = \begin{cases} 1 & \text{for a 4-level laser} \\ 2 & \text{for a 3-level laser} \end{cases}$$

We now have to solve the coupled pair, Equations C3 and C6. As boundary conditions, we prescribe the population inversion $N_0(x)$ before the beams enter the medium, and the total photon density, $n_0(t) = n_1(0,t) + n_2(0,t)$, at the $x=0$ boundary plane of the medium. The procedure for solving the equations exactly parallels that in the original Frantz-Nodvik paper

(Reference C.1), so it is not reproduced here. The result is

$$n(x,t) = \frac{n_0 \left[t - \frac{x}{c \cos \theta} \right]}{1 - \left\{ \exp \left[-\frac{\sigma}{\cos \theta} \int_0^x N_0(x') dx' \right] \right\} \exp \left[-\alpha c \sigma \int_{-\infty}^{t-x/\cos \theta} n_0(t') dt' \right]} \quad (C7)$$

Next, we restrict our attention to the special case of an input photon density having a square wave temporal shape,

$$n_0(t) = \begin{cases} n_0 & 0 \leq t \leq \tau_p \\ 0 & \text{all other times} \end{cases}$$

and a uniform initial population inversion,

$$N_0(x) = N_0, \quad 0 \leq x \leq L$$

Equation C7 now becomes

$$n(x,t) = \frac{n_0}{1 - \left[1 - \exp \left\{ -\frac{\sigma N_0 x}{\cos \theta} \right\} \right] \exp \left[-\alpha c \sigma n_0 \left[t - \frac{x}{c \cos \theta} \right] \right]} \quad (C8)$$

for $0 \leq t - x/(c \cos \theta) \leq \tau_p$ and $0 \leq x \leq L$. Light entering the pumped region of the amplifier at time t leaves it at time $t + L/c \cos \theta$ so the output pulse shape at $x = L$ is

$$n_L(t) = n(L, t + L/c \cos \theta).$$

According to Equation C8, this is

$$n_L(t) = \frac{n_0 e^{\alpha c \sigma n_0 t}}{e^{\alpha c \sigma n_0 t} - \left[1 - e^{-\sigma N_0 L / \cos \theta} \right]}, \quad 0 \leq t \leq \tau_p$$

This expression can be integrated directly to find the output energy, W_{out} , from a pumped region whose vertical face has area A ,

$$W_{out} = Ah\nu c \cos\theta \int_0^{\tau} N_L(t) dt$$

$$= \frac{Ah\nu c \cos\theta}{\alpha\sigma} \ln \left[1 + e^{\frac{\sigma N_0 L / \cos\theta}{\alpha} \left(e^{a\sigma n_0 \tau} - 1 \right)} \right]$$

The input energy into the same region is

$$W_{in} = Ah\nu n_0 c r \cos\theta,$$

the unsaturated gain is

$$g_0 = N_0 \sigma,$$

and we define the saturation fluence by

$$E_s = h\nu / \sigma.$$

In terms of these quantities, the equation for the output energy is, finally,

$$W_{out} = \frac{E_s A \cos\theta}{\alpha} \ln \left[1 + e^{\frac{g_0 L / \cos\theta}{\alpha} \left(e^{W_{in} / E_s A \cos\theta} - 1 \right)} \right] \quad (8-3)$$

For the Nd: Glass 4-level laser, we set $\alpha = 1$ and get Equation 8-3 of the main text.

Reference:

C. I. L. M. Frantz and J. S. Nodvik, J. Appl. Phys. 34, 2346 (1963).